Characterization and optimization study of Poly(N-isopropylacrylamide) (P(NIPAM)) and β-cyclodextrin (βCD) system for Controlled Release Drug Delivery Systems with NMR and MRI techniques

Master thesis, University of Bergen
Faculty of Mathematics and Natural Sciences
Department of chemistry

Author: Alfonso N. Chiu III
Supervisor: John Georg Seland

Abstract

This project is a direct continuation from my bachelor project that was based off Wisniewska,M (2017), where she investigated the changes in Poly(N-isopropylacrylamide) P(NIPAM) at the Volume Phase Transition (VPT) . The goal of the project was to expand the portfolio and characterization of P(NIPAM), particularly on how β-cyclodextrin (βCD) reacts as it goes through VPT both inside the hydrogel and outside the hydrogel. By using Magnetic Resonance Imaging (MRI), it allows us to monitor the changes of P(NIPAM) as it goes through the Lower Critical Solution Temperature (LCST), the Volume Phase Transition Temperature (VPTT), and 40 °C. Multi-Slice Multi-Echo (MSME) imaging was used to monitor the physical changes of the hydrogel with increasing temperature for comparison to spectral data using Magnetic Resonance Spectroscopy (MRS). Combining MRI with MRS allows for us to combine the macroscopic and microscopic picture of the βCD activity inside and outside the hydrogel. The changes of βCD in the polymer interior and exterior was monitored using STimulated Echo Acquisition Mode (STEAM), and the diffusion of βCD and water inside the hydrogel was recorded using MEshcher-GArwood Point RESolved Spectroscopy (MEGA-PRESS). The release of the βCD inside the hydrogel network was minimal until reaching VPTT, where the change in concentration sharply decreased due to the phase transition. As for the βCD change outside the hydrogel, the change was adherent to the shrinkage kinetics of P(NIPAM), showing delays in release due to restricted diffusion caused by the shrinkage of the P(NIPAM) after VPTT. For the self-diffusion data of the βCD, it was found that the βCD signals were loss using MEGA-PRESS after VPTT as a result of diffusion. The water self-diffusion values were also found to be decreasing consistently after a delay from 40°C.

Acknowledgement

I would like to first extend my sincerest gratitude and pleasure to have been under the guidance of associate professor John Georg Seland. Throughout my time spent as a learning master student for the department of chemistry, John has been there to assist me and devise ways to solve problems with the synthesis, as well as educating me on the dynamics of diffusion, MRI, and NMR. He was always patient with me, and no matter what happened, he always tried to find time to assist me in my project. I could have not asked for a better supervisor. I would also like to thank John's PhD student, Emile Schjeldsøe Berg for helping on the diffusion analysis. His insight and guidance were a tremendous help that saved me from nights of headaches, as well as providing me some encouragement during my last days in the lab. A thousand years would have never prepared me for my master's journey being done in the middle of the pandemic, plagued with multiple setbacks caused by machinery breakdown and synthesis failures. Not to mention, doing all of that while trying to apply for medical school outside of Norway and working as an academic tutor in chemistry for 2 years almost daily. Most importantly, being away from family made these last two years a wild bumpy ride.

Despite the obstacles, I am here still standing on my two feet thanks to the support of everyone closest to me. To Nikita, thank you for being a good friend and always inspiring me to strive for excellence. To my dearest Silje, no amount of "thank yous" can describe how lucky I am to be supported by you during my most intense year yet. In all of those sleepless nights, you were always there to encourage me and make me believe in my ability to do good. Finally, I want to extend my biggest gratitude and dedicate my master thesis to my both my mother and father, Alfonso Jr. and Jessica. The sacrifices you both made for me to be here with all these opportunities can never be repaid in my lifetime or the next. Although science was neither of your profession, you both have taught me the greatest lessons of all in life. A hardworking person with a heart full of integrity is priceless. This is all for you.

Overview of Symbols

- NMR = Nuclear Magnetic Resonance
- MRS = Magnetic Resonance Spectroscopy
- MRI= Magnetic Resonance Imaging
- P(NIPAM)= Poly(N-isopropylacrylamide)
- CD= Cyclodextrin
- βCD = β-Cyclodextrin
- VPT= Volume Phase Transition
- VPTT= Volume Thase Transition Temperature
- LCST= Lower Critical Solution Temperature
- MSME= Multi-Slice Multi-Echo
- STEAM= STimulated Echo Acquisition Mode
- MEGA-PRESS= MEshcher-GArwood Point RESolved Spectroscopy
- CRDDS= Controlled Release Drug Delivery System
- DDS= Drug Delivery System
- $\Delta F_{elastic}$= Elastic contribution to free energy of swelling of dry polymers
- $\Delta F_{mixingl}$= Mixing contribution to free energy of swelling of dry polymers
- ΔF_{total}= Total free energy of swelling of dry polymers
- M_n= Average molecular weight before crosslinking
- M_c= Average chain molecular weight between crosslinks
- V_1= Molar volume of the solvent
- χ_1= Polymer solvent interaction parameter
- $\bar{v}$= Specific volume of the polymer(p_{solv}/p_{pol})
- v_{2s}= Polymer volume fraction in the swollen state at equilibrium
- ρ_s= Density of the solvent
- ρ_p= Density of the dry hydrogel
- Q_m= Swelling ratio
- M_s= Hydrogel mass after swelling
- D_0= Self-diffusion in solution
- D_m= mutual diffusion
- D_s= Self-diffusion
- M_d= Mass of the dry hydrogel

- $\sqrt{\langle \bar{r}_0^2 \rangle}$= Root-mean-square end to end distance of the polymer chain in the undisturbed state
- C_N= Flory characteristic ratio of the polymer
- M_r= Molecular weight of the repeat units
- ξ = Mesh size
- r_s= Radius of the solute
- r_{FV}= Free volume void sizes in the hydrogel
- f= friction coefficient
- k_B= Boltzmann constant
- T= Absolute temperature
- η= Solvent viscosity
- R= Ideal gas constant [8.3145 $J \times K^{-1} \times mol^{-1}$]
- Λ= Geometry parameter of the diffusing material
- R_h= Hydrodynamic radius distribution
- E_A= Activation energy
- D_s^{gel}= Self-diffusion of gel
- D_s^0= Self-diffusion coefficient of solute in solution
- NIPAM= N-isopropylacrylamide
- AAc= Acrylic Acid
- DAT= N,N’-Diallyl L-tartardiamide
- TEMED= N,N,N,N-tetramethylethylenediamine
- Mean-square displacemen(R^2)t= MSD
- ζ= Restriction effect
- t_d=diffusion time
- d_w= Random walk dimension
- α = Time-independent scale
- P= spin angular moment
- I= Spin quantum number
- h= Planck’s constant
- μ= intrinsic spin
- B_0= Static magnetic field
- γ= Gyromagnetic ratio

- γ_H= Gyromagnetic ratio of hydrogen
- ω_L= Larmor frequency
- v= Resonance condition/Precessional frequency
- $\hbar$= Reduced Planck constant
- M_0= Net magnetization
- ΔE= Total energy difference
- N_{upper}/N_{lower}= Ratio of the populations
- B_1= Extra magnetic field
- FID= Free induction decay
- τ_p= Duration of the rf field
- T_2= Transverse relaxation time
- T_1= Spin lattice relaxation time
- $M_z/M_y/M_x$ = Net magnetization on the z/y/x-axis
- T_2^*= Effective transverse relaxation time
- T_{2MS}= Dephasing time due to the magnetic susceptibility differences
- T_{2M}= Dephasing time due to the main field inhomogeneity
- MR= Magnetic resonance
- rf= Radio frequency
- σ= Shielding constant of a proton
- δ= Chemical shift
- B_{local}= Local magnetic field
- PFG= Pulse field gradient
- g= Field gradient
- θ= Position of slice
- $\Delta\omega$= Associated frequency profile
- Δz= Slice thickness
- G_{SS}=Slice-selective gradient
- B_i= Magnetic field strength of position "r_i"
- G_T= Total gradient amplitude
- ω_i= Frequency of the proton in position "r_i"
- G_{RO}= Read-out gradient
- ω_{NQ}= Nyquist frequency

- FOV= Field of view
- S/N= Signal-to-noise ratio
- N_{RO}= Number of readout sample points
- N_{PE}= Number of phase encoding steps in the acquisition matrix
- VOX_{RO}=Spatial resolution in the phase-encoding direction
- G_{PE}= Phase-encoding gradient
- ω_0= Base frequency
- $\emptyset_1$= Phase shift
- k_x= k-space for x data points
- k_y= k-space for y data points
- Δk_i= Separation between points in k-space
- Δi= spatial resolution
- RO= Read out
- ω_i= Central frequency
- VOI= Volume of interest
- SVS= Single voxel techniques
- D= Diffusion coefficient of pure solutions
- CHESS=Chemical Shift Selective
- b= Attenuation factor
- I= Intensity
- D_2O= Deuterated oxide
- $t_{initial}$= Start of the experiment
- FLASH= Fast low angle shot
- TE= Echo time
- TR= Repetition time
- PD= Proton density
- φ= Accquired phase
- φ_0= Initial phase
- DMSO-d_6= Dimethyl sulfoxide-d6
- SDH_2O= Super distilled water

Overview of figures

Overview of equations

	1.2.9	Friction coefficient
	1.2.10	Solvent viscosity
	1.2.11	Self-diffusion of the gel
	1.2.12	Mean-squared displacement (MSD)
	1.2.13	Restriction effect
	1.2.14	Modified MSD (Hindered diffusion)
2.1	2.1.1	Spin angular moment
	2.1.2	Intrinsic spin of the nucleus
	2.1.3	Angular moment on the z-axis
	2.1.4	Alternative definition of intrinsic spin
	2.1.5	Angular frequency
	2.1.6	Resonance condition
	2.1.7	Energy separation of two states of a spin
	2.1.8	Boltzmann distribution
2.2	2.2.1	Pulse angle
	2.2.2	Total magnetization vector
2.3	2.3.1	Transverse relaxation (x-axis)
	2.3.2	Transverse relaxation (y-axis)
	2.3.3	Spin lattice relaxation (z-axis)
	2.3.4	Transverse relaxation (xy-axis)
	2.3.5	Calculating T_2^*
	2.3.6	Transverse magnetization with T_2^*
2.4	2.4.1	Local magnetic field
	2.4.2	Resonance frequency
	2.4.3	Chemical shift
2.5	2.5.1	The precessional frequencies of the nuclei at the various positions
	2.5.2	Position of the slice
	2.5.3	Displacement of vector due to excess precessional frequency
3.1	3.1.1	Magnet field strength with respect to “r_i” and G_T
	3.1.2	Larmor frequency of the magnetic field gradients
	3.1.3	Associated frequency profile of a slice

	3.1.4	Total range of frequencies in the image
	3.1.5	Nyquist frequency
	3.1.6	Spatial resolution of the readout gradient
	3.1.7	Total pixel bandwidth
	3.1.8	Spatial resolution of the phase-encoding gradient
3.2	3.2.1	k-space for G_{RO}
	3.2.2	k-space for G_{PE}
	3.2.3	FID signal received by the coil
	3.2.4	The separation between points in k-space
	3.2.5	Spatial resolution with respect to the direction i
3.4	3.4.1	Stejskal-Tanner equation
	3.4.2	b-value or attenuation factor
	3.4.3	Intensity change in determining the diffusion coefficient
5.3	5.3.1	Mathematical definition of the acquired phase at position "r"
6.1	6.1.1	Variable temperature calibration formula from BRUKER
7.1	7.1.1-7.1.2	Calculating the real temperature of the probe using the temperature calibration curves of parallel 1 and 2 from **figure 7.1.1**

Overview of tables

Contents

(1)Introduction

(1.1) Background on Controlled-Release Drug Delivery Systems (CRDDS)

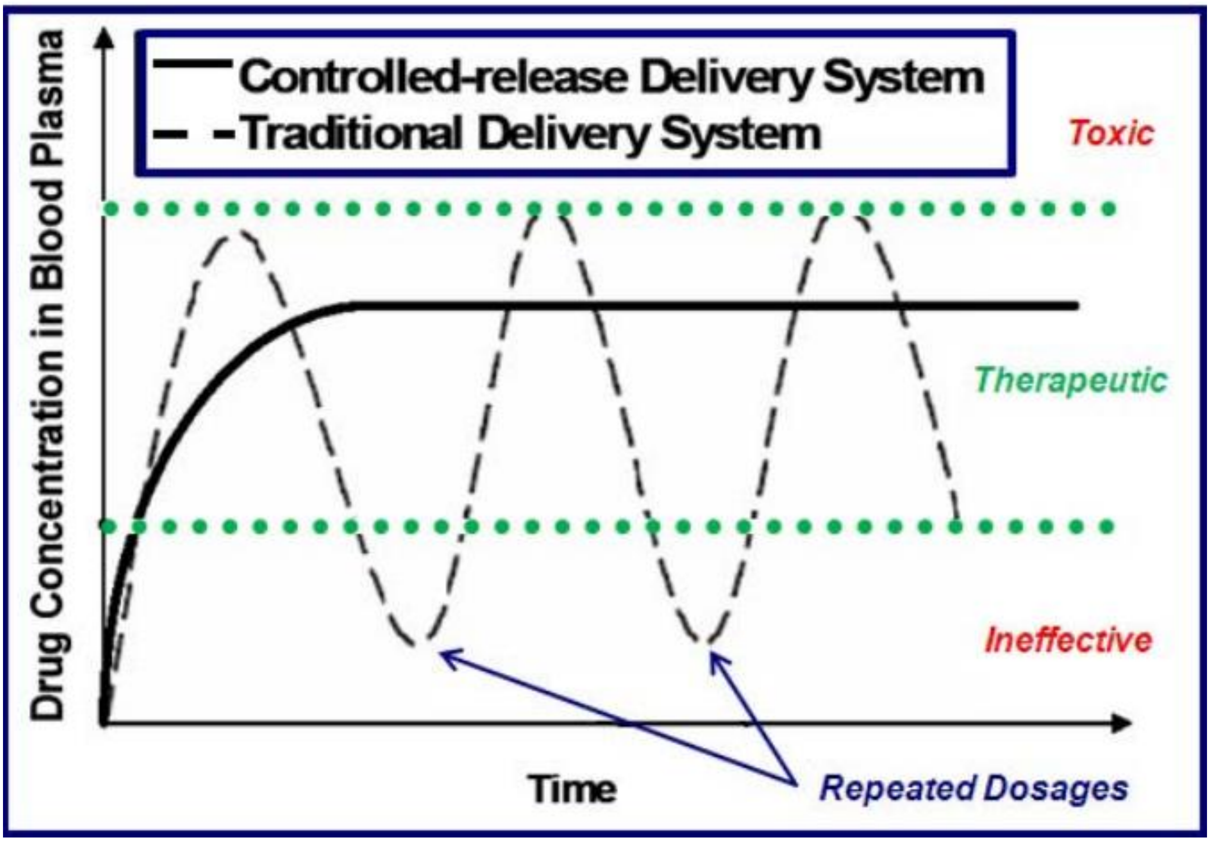

Figure 1.1.1: Comparing typical release profiles for controlled release and conventional drug delivery systems. Controlled release optimizes the therapeutic effect of the drug unlike the traditional system. It can avoid the known issues, such as drug ineffectiveness or toxicity [41, 45].

Customarily, drug administration is administered as a high singular dosage or as a series of small doses to stimulate a therapeutic effect for the drug [38-40]. The therapeutic concentration of a drug can be obtained through syringe injections, oral administration, transdermal administration, or implants [4, 42]. However, the conventional means to administer these drugs can commonly lead to lower efficacy, lower patient compliance, unwanted side-effects, and high levels of toxicity [38-40]. These complications associated with the conventional means are caused by unstable drug concentrations in the blood as it peaks as soon as the drug is administered, but sharply declines after a period of time [43-45].

In order to circumvent the aforementioned complications and obstacles of drug administration, Drug Delivery Systems (DDS) have been developed and employed. A DDS is defined as a pharmaceutical technique that delivers a therapeutic compound with a controlled release rate in a specific time interval at a specific target site in the body [43-44, 46-47]. DDS maintains the drug level in the organism within the therapeutic window as seen in **figure 1.1.1** [41]. Although **figure 1.1.2** shows the different modified classifications of DDS, this project will be on Controlled Release Drug Delivery Systems (CRDDS) [48].

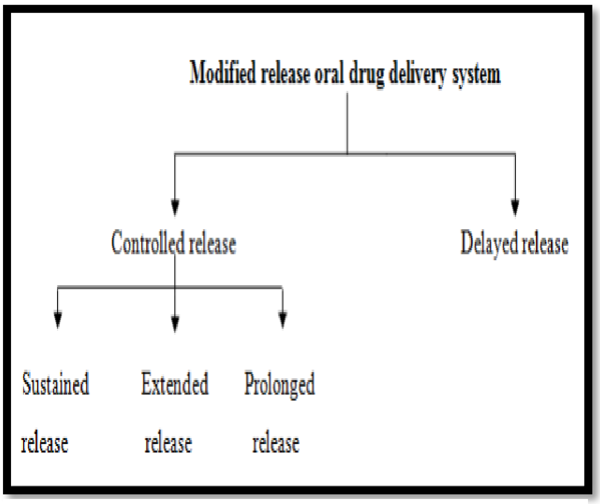

Figure 1.1.2: Various classifications of modified release Drug Delivery Systems. The emphasis will be on Controlled Release Drug Delivery Systems [48].

CRDDS is defined as any delivery system that achieves a slow release of the drug over an extended period of time [49]. CRDDS are not target-specific, so this means that the system is unable to deliver the drug to the target site in a direct manner. Despite this limitation, it is still possible to exclusively deliver the drug to the target site by implementing target delivery systems, which exploit the characteristics of the drug carrier and the target's site, so that it can regulate the biodistribution of the drug. From an optimal perspective, a perfect CRDDS is achieved when the drug is delivered into a therapeutic system, which means to say that the drug is released at a pre-determined rate, locally or systematically at a precise time interval [49,50]. Consequently, this makes it so that the presentation of a drug is limited to the specific body site for its intended release, absorption, or transport of the drug's active component through various biological membranes on its route to the target [51-52]. The release kinetics of CRDDS in a therapeutic system is commonly zero-order. Therefore, the dose of the CRDDS in therapeutic systems are not as significant than the release rate, which makes the release rate of the CRDDS in therapeutic systems the rate-determining step for the absorption, and the drug concentration in the plasma and target site. By design, CRDDS is expected to develop a predictable, but constant plasma concentration without the influence of the biological environment of its intended target system or body part [50]. This system prevents substantial variations in medical dosage, reduces the frequency intake of medicine, and the medicine can be administered locally.

(1.2) Background on Hydrogel dynamics

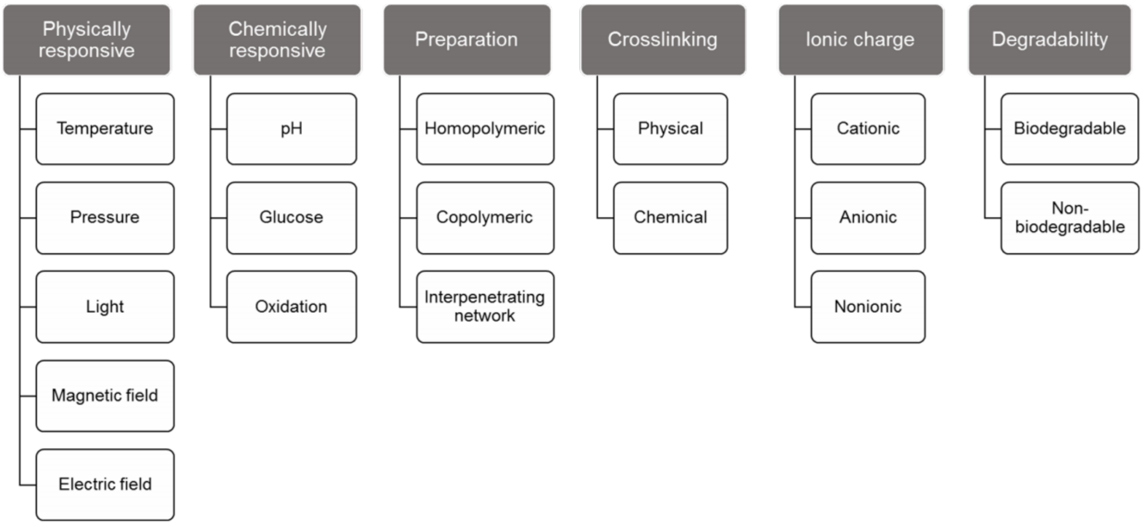

Figure 1.2.1: Diverse classifications of hydrogels based on the type of preparation, stimuli, types of crosslinkers, ionic charge and degradability. Adapted from [54].

Hydrogels have been extensively used in CRDDS acting as drug carrier molecules for therapeutic agents and various drugs in branches of medicine, cardiology, oncology, immunology, wound healing, pain management and tissue engineering [45,53]. Hydrogels are 3D high molecular weight networks that are composed of a polymer backbone, water and a crosslinking agent. Hydrogels can swell and retain a substantial fraction of water within its structure, but it will not dissolve in water at physiological temperature and pH [55-57]. The crosslink interactions in the hydrogel are responsible for maintaining the structural integrity. This crosslink can either be characterized as chemical or physical. When covalent bonds form between polymer chains, this is considered a chemical crosslink interaction. This produces a permanent cross-link junction hydrogel. On the other hand, physical crosslinking is the result of reversible intermolecular interactions between polymer chains, such as ionic interactions, polymerized entanglements, or hydrogen bonds [58-59]. The diverse classifications of the hydrogels are classified in **figure 1.2.1** [60]. Gels exhibiting a phase transition in response to external conditions summarized in **figure 1.2.1** are referred to as "stimuli-responsive" or smart gels [45, 61].

Swelling kinetics

The swelling process of the polymer networks that comprise hydrogels can be described by the Florey and Rehner's equilibrium swelling theory can be used to explain the swelling process of the polymer networks that comprise hydrogels. According to the Flory-Rehner theory, when a non-ionic hydrogel is placed in excess solvent, the polymer chains begin to absorb the solvent and swell until the counteracting forces of osmotic force and elastic force balance each other, thus establishing equilibrium. Once equilibrium is established, the maximum dimensional change has occurred and swelling ceases to continue. The Flory-Rehner equation is one such equation to describe the interaction between the polymer and liquid molecules, particularly the equilibrium of swelling gel polymers [63-64]. It is defined in **equation 1.2.1**. The physical situation of the interaction can be represented below by the elastic ($\Delta F_{elastic}$) and mixing (ΔF_{mixing}) contributions to free energy of swelling of dry polymers (ΔF_{total}) [45]:

$$\Delta F_{total} = \Delta F_{mixing} + \Delta F_{elastic} \quad \textbf{(Equation 1.2.1)}$$

ΔF_{mixing} represents the chain in free energy due to the polymer mixing between the pure solvent and the polymer chains. It can be used to measure the compatibility of the polymer with the solvent molecules. On the other hand, $\Delta F_{elastic}$ is the change in free energy due to elastically effective crosslinks in the hydrogel network [4, 45, 65-66]. **Equation 1.2.1** above can be differentiated with respect to the number of solvent molecules with the two conditions being the system is isothermal and isobaric until the full Flory-Rehner equation is formed. It is defined in **equation 1.2.2** [4, 67].

$$\frac{1}{M_c} = \frac{2}{M_n} - \frac{\frac{\bar{v}}{V_1}\left[\ln(1-v_{2s})+v_{2s}+\chi+V_{2s}^2\right]}{v_{2s}^{\frac{1}{3}}-\frac{v_{2s}}{2}} \quad \textbf{(Equation 1.2.2)}$$

$$\bar{v} = \frac{\rho_{solv}}{\rho_{pol}} \quad \textbf{(Equation 1.2.3)}$$

$$v_{2s} = \frac{\frac{1}{\rho_{pol}}}{\frac{Qm}{\rho_{solv}}+\frac{1}{\rho_{pol}}} \quad \textbf{(Equation 1.2.4)}$$

$$Q_m = \frac{M_s}{M_d} \quad \textbf{(Equation 1.2.5)}$$

In **equation 1.2.2**, M_n represents the average molecular weight before crosslinking. M_c represents the number average chain molecular weight value between cross-links. V_1 is the molar volume of the solvent. χ_1 is the polymer solvent interaction parameter. $\bar{v}$ is the specific volume of the polymer (p_{solv}/p_{pol}) and is showcased in **equation 1.2.3**. v_{2s} is the polymer volume fraction in the swollen state at equilibrium. v_{2s} is defined in **equation 1.2.4**. In **equation 1.2.3**, ρ_s represents the density of the solvent, whilst ρ_p is the density of the dry hydrogel. At

equation 1.2.4, however, the equation showcases the definition of v_{2s}, where Q_m is defined as the swelling ratio and its definition is shown at **equation 1.2.5**. In **equation 1.2.5**, M_s is the hydrogel mass after swelling, whilst M_D is the mass of the dry hydrogel [4, 45, 67-70].

Mesh size

The Flory-Rehner calculated value from **equation 1.2.2** is a preliminary step for the next calculated value, which is the root-mean-square end to end distance of the polymer chain in the undisturbed state $\left(\sqrt{\langle \bar{r}_0^2 \rangle}\right)$ [4, 70]. $\left(\sqrt{\langle \bar{r}_0^2 \rangle}\right)$ is shown in **equation 1.2.6**, and it is a pertinent value for determining the hydrogel mesh size, as described by Canal and Peppas [71]. This is due to $\left(\sqrt{\langle \bar{r}_0^2 \rangle}\right)$ depends on M_n [4, 70], where l is the bond length along the polymer backbone/the average bond length [4, 72-73], C_N is the Flory characteristic ratio of the polymer, and M_r is the molecular weight of the repeat units [4, 45, 72-73].

$$\sqrt{\langle \bar{r}_0^2 \rangle} = l\sqrt{\frac{2C_N M_c}{M_r}} \textbf{ (Equation 1.2.6)} \qquad \xi = \sqrt{\langle \bar{r}_0^2 \rangle} \times v_{2s}^{-\frac{1}{3}} \textbf{ (Equation 1.2.7)}$$

Utilizing a combination of aspects from both **equation 1.2.4** and **equation 1.2.6**, the mesh size of the hydrogel (ξ) can be determined and defined as shown in **equation 1.2.7**. The mesh size of the hydrogel is defined as the linear distance between two adjacent crosslinks [70, 74]. The mesh size can be affected by a variety of variables, such as varying the crosslinking density, polymer concentration, the presence of ionic polymers or changing the conditions of the polymerization reaction. Altering the conditions of the polymerization reaction would mean changing the solvent types, stimuli conditions like pH and/or temperature values. Such changes can influence the mesh size ratio, which is the main factor that determines how quick the drug can be released from the hydrogel network [74]. An example of the reversible reaction of the hydrogel can be seen in **figure 1.2.2**. If the drug molecule is larger than the mesh size, the drug molecule becomes physically entrapped inside the network, and it can only be released via network degradation, deformation or swelling. If the molecule is smaller than the mesh size, diffusion is independent on the mesh size, and the drug molecules migrate freely [45, 75]. **Figure 1.2.3** visualizes the effects of a small or large mesh size [78].

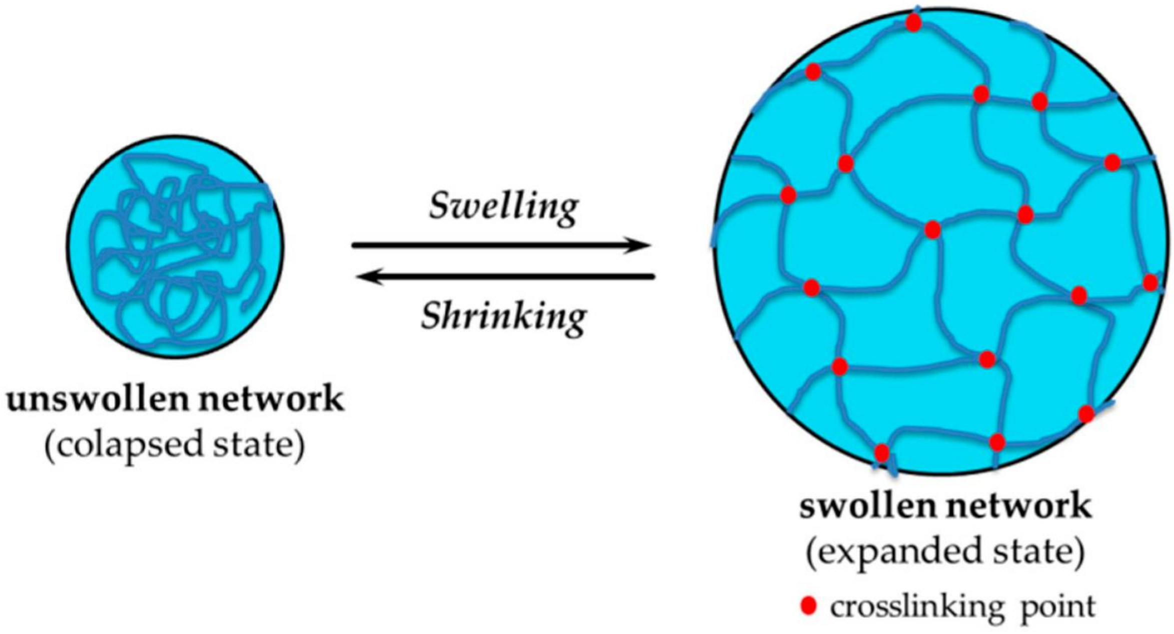

Figure 1.2.2: Schematic diagram showing the hydrogel swelling and shrinkage. In the presence of water, the unswollen network becomes swollen. The swollen hydrogel is interlinked using crosslinkers, which are marked in red here. The mesh size(ξ) in the swollen state is larger, so movement of the drugs are higher in the swollen state. Stimuli conditions can reverse the reaction by causing the network to return to its collapsed state by breaking down the crosslinkers, such as via change in pH, polymer concentration, temperature and etc. This can make it harder for the molecules to move through the network. Adapted from [76].

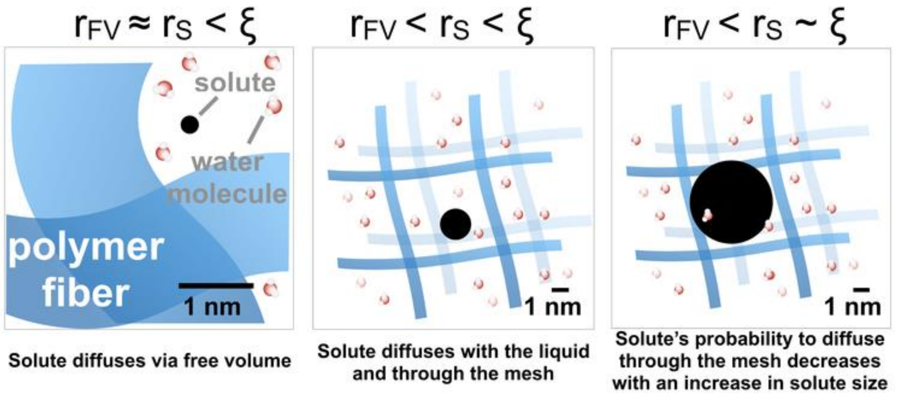

Solute diffuses via free volume

Solute diffuses with the liquid and through the mesh

Solute's probability to diffuse through the mesh decreases with an increase in solute size

Figure 1.2.3: 3 pictures that shows the effects of altering mesh sizes. (1st picture) Shows solute diffusing via free volume as the hydrodynamic radius of the solute(r_s) and free volume void sizes in the hydrogel(r_{FV}) are approximately equal, but are smaller than the mesh size (ξ).(2nd picture) Shows how r_{FV} is less than the r_s, and r_s is still smaller than the ξ, which leads to the solute diffusing with the liquid and through the mesh. (3rd picture) Same conditions as the 2nd picture with the exception that r_s is approximately equal to the ξ, so the probability of the solute diffusing through the mesh decreases as the size of the solute increases [78]

Diffusion

It is vital to know that diffusion dominates the drug release. The effect of steric hindrance becomes more apparent once the mesh size matches the size of the diffusing drug as shown in **figure 1.2.3**. The polymer chains of the hydrogels can act as physical obstructions for the solute, slowing its movement by reducing the average free volume per molecule available to the solute, thus increasing hydrodynamic drag for the solute. Consequently, this increases the path length of the solute. Several models have been proposed to characterize the effects of hydrodynamic drag, physical obstruction and free volume. The suitability of each model is largely dependent on the nature of the polymer. Quoting a statement from Brian Amsden, "*Diffusion in homogeneous hydrogels could not expected to be aptly described by a model which assumes that the polymer chains are rigid, straight, and motionless, and neither would the converse be expected to be true*." These models are summarized in **attachment 1** [45,75].

With that in mind, the controlled release of a drug from the hydrogel is made possible by diffusion. Diffusion is generally defined as the random translation incoherent motion of molecules measured in length^2 time^{-1} [4]. The two main categories of diffusion taking place in hydrogels are self-diffusion and mutual diffusion [79]. Self-diffusion is the type of diffusion that is driven by random Brownian motion of molecules in an uniform solution, which stems from the internal kinetic energy. It occurs in the absence of any concentration gradient [79-80]. On the other hand, mutual diffusion occurs in the presence of a concentration gradient. Mutual diffusion can be described by Fick's laws of diffusion [79, 81-82]. The diffusion coefficient of both mutual and self-diffusion is commonly denoted as D_m or D_s respectively [83, 84]. The D_s of a molecule relates to its molecular size, and it is sensitive to molecular interactions and temperature at infinite dilution [84-85]. At infinite dilution, the diffusion coefficient is denoted by D_0, which is represented in **equation 1.2.8** (Stokes-Einstein equation)**.** This equation describes the hydrodynamic properties of solute transport through gels [45, 86].

$$D_0 = \frac{k_B T}{\mathrm{f}} \textbf{ (Equation 1.2.8)}$$

$$f = \lambda \pi \eta R_h \textbf{ (Equation 1.2.9)}$$

$$\eta = \eta_0 e^{E_a/RT} \textbf{ (Equation 1.2.10)}$$

In **equation 1.2.8**, k_B represents the Boltzmann constant, T represents absolute temperature and f is the friction coefficient. The friction coefficient is defined in **equation 1.2.9**, and it is dependent on η (solvent viscosity). η is defined in **Equation 1.2.10**, where E_a is the activation energy, T is the absolute temperature and R is the ideal gas constant (8.3145 J K^{-1} mol^{-1}). The geometry parameter (λ) of the diffusing particle. The geometry parameter depends on the boundary conditions. If the particle interacts strongly with the solvent molecules, such that the solvent layer that lays closest to the surface moves at similar velocity as the particle (stick boundary condition), the λ parameter is equal to 6. R_h represents the hydrodynamic radius distribution [4, 45, 81-83].

One factor that is vital to consider is the intermolecular interaction between the solute and the polymer network. This can influence the solute diffusion in hydrogels. Numerous models have been proposed as shown in **attachment 14** to describe the relationship between the hydrogel structure and the solute with regards to its transport properties [75]. One example of these models is a simple model proposed by Oston et al, which described self-diffusion of molecules in a porous media. Oston assumed that the medium is composed of random networks of long and straight fibers [54]. The definition for D_s^{gel} is represented by **equation 1.2.11**, where D_s^0 is the self-diffusion coefficient of solute in solution, and ξ is the mesh size [4, 45, 87-89].

$$D_s^{gel} = D_s^0 * exp\left(-\frac{R_h}{\xi}\right)$$ (**Equation 1.2.11**)

If the hydrogel has an absence of hydrogen bonding or hydrophobic interactions in the interior, the D_s^{gel} of the gel will decrease due to the obstruction effect and increase in the hydrodynamic drag on the diffusing molecules by the presence of the polymer chains [45, 75, 86-87].

For polymer networks, diffusion is commonly anisotropic due to the changes in its polymer interior (pH or temperature stimuli). As such, the $<R^2>$ component of **equation** 1.2.12 or also known as the mean-squared displacement (MSD), will be influenced by the changes of the polymer geometry [4,144].

$$< R^2 > = nD_s t_d$$ (**Equation 1.2.12**)

$$\zeta = \frac{D_s t_d}{a^2}$$ (**Equation 1.2.13**)

Restrictive polymer networks can make it so that the self-diffusion of the molecule (water) inside the gel can lose its linear behavior, it and will heavily rely on the time and the geometry of the gel. The restriction effect (ζ) is given in **equation 1.2.13**. If ζ<<1, then the diffusion is unrestricted due to the diffused molecules not being able to reach the boundaries of the restriction, thus following **equation 1.2.12** to be followed. If $\zeta \approx 1$, then the length scale is gradually approaching the restricting geometry condition, and the MSD in **equation 1.2.12** will no longer be linear with t_d. Instead, it will follow a modified form of **MSD** as shown in **equation 1.2.14**, where α is a time-independent scale constant and d_w is the random walk dimension [4].

$$< R^2 > = \alpha n D_s {t_d}^{2/d_w}$$ (**Equation 1.2.14**)

The final possible effect is when $\zeta >> 1$, thus MSD will solely depend on the shape, dimensions and orientation of the of the restricting geometry. It is also completely independent of the t_d. **Figure 1.2.4** shows the MSD trends as a function of t_d as explained by the 3 possible outcomes of the restriction effects that can influence MSD [4,143].

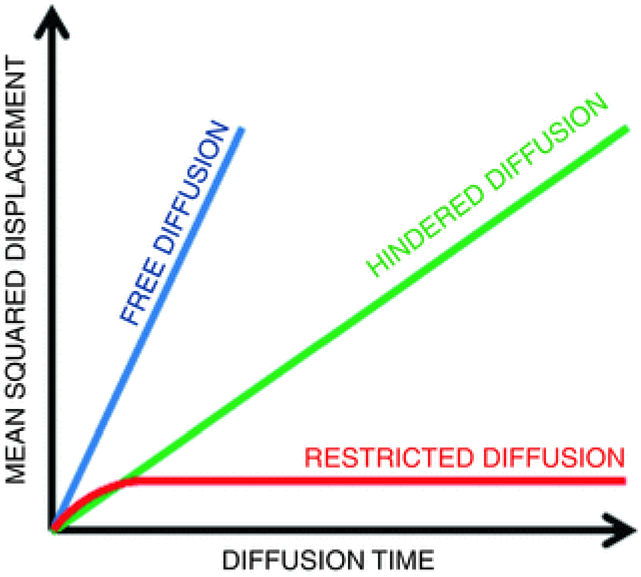

Figure 1.2.4: MSD plotted against t_d. The blue curve represents free diffusion. The green curve represents the hindered diffusion. The red curve represents the restricted diffusion [143].

(1.3) Background on P(NIPAM) and β-Cyclodextrin(βCD)

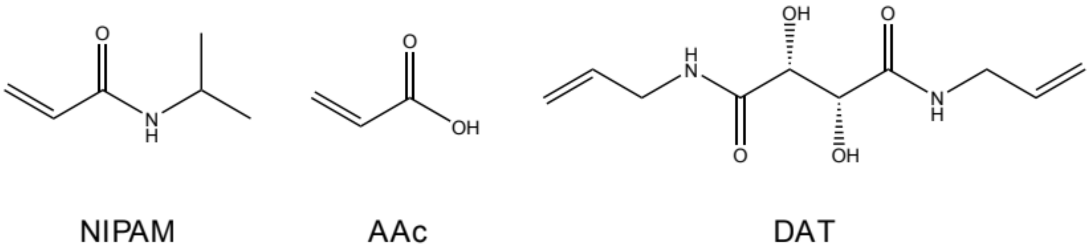

Figure 1.3.1: Chemical structures of NIPAM, AAc, and DAT, which are used to synthesize P(NIPAM) hydrogels. Taken from [4].

The polymer being analyzed in this dissertation is poly-N-isopropyl, also known as P(NIPAM). It can be synthesized using N-isopropylacrylamide (NIPAM), polymerized Acrylic Acid (AAc) and the crosslinker, N,N'-Diallyl L-tartardiamide (DAT). P(NIPAM) is regarded as a smart polymer hydrogel due to temperature responsive nature. Moreover, P(NIPAM) acts as a carrier molecule, which transports loaded medicine onto the desired target through self-diffusion. The diffusion is triggered by a minor temperature change to release the drug in a slow and linear fashion [90-93]. When the Lower Critical Solution Temperature (LCST) at 32 °C is reached, P(NIPAM) in an aqueous mixture can undergo a reversible gelation [95]. This is regardless of the polymer molecular weight and concentration. Small temperature change around LCST can induce the collapse of P(NIPAM) and Volume Phase Transition (VPT). VPT is reached at 34°C. This is referred to as the Volume Phase Transition Temperature (VPTT) [96,97]. Decreasing the temperature below VPTT will cause the hydrogel to swell in the water just as shown in **figure 1.2.2**. This is due to the strong hydrogen bonds formed between water and the hydrophilic amide and hydrophobic carbonyl groups of P(NIPAM) [98-102]. At temperatures above the LCST, hydrophobic interaction between the hydrophobic moieties is strengthened whilst simultaneously weakening the hydrogen bonds between the water, and the amide and hydrophobic carbonyl groups of P(NIPAM). If the temperature reaches VPTT, the hydrogel will aggregate and undergo a coil-globule transition, in which the polymer volume will substantially shrink and extrude water molecules from the aggregates. During the transition, P(NIPAM) will have more gel like properties as the rising temperature will dehydrate the isopropyl groups, the main polymer chain, and the amide groups of P(NIPAM) [103-107]. This thermosensitive trait near body temperature makes P(NIPAM) an excellent choice for biomedical applications, such as drug delivery [108-109].

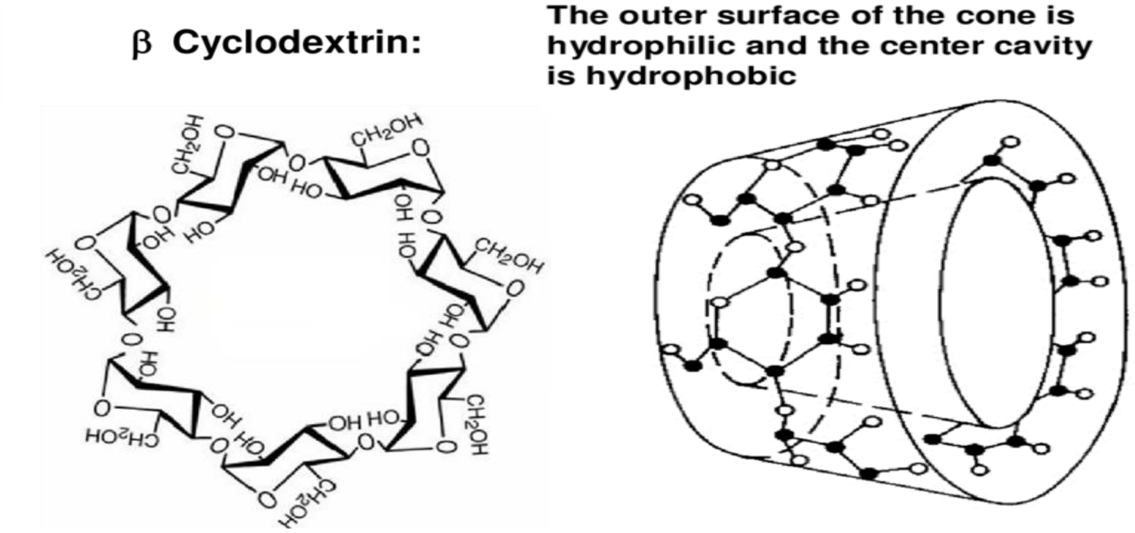

Figure 1.3.2: The chemical structure of βCD (left) and its truncated hollow cone structure(right) [111].

However, it is pertinent to be aware that a majority of hydrogels are limited to the delivery of hydrophilic drugs. Due to this limitation, cyclodextrins (CD) are utilized to act as the carrier molecule for hydrophobic molecules. Specifically, β-Cyclodextrin (βCD) is used. βCD is composed of 7 α-D-glucopyranoside units (**figure 1.3.2**), and are linked together by α−1,4 glycosidic bonds. Cyclodextrins serve as the vehicle for hydrophobic drugs as they can solubilize the hydrophobic components of the incorporated medicine. This is made possible as cyclodextrins are cyclic oligosaccharides with a hydrophilic exterior and a hydrophobic cavity, appearing with a truncated hollow cone accompanied with primary and secondary hydroxyl groups pointed towards the exterior. This structure allows for cyclodextrins to form an inclusion complex with the hydrophobic molecule being entrapped in the hydrophobic cavity. An example of such application is shown in **attachment 2** by Erdos, M et al. In addition, the cavity of the cyclodextrin can host water molecules through the small and large rims that act as entrance into the cavity, thus form hydrogen bonds 9 [198, 200]

(1.4) Earlier research done on P(NIPAM) and CD-systems

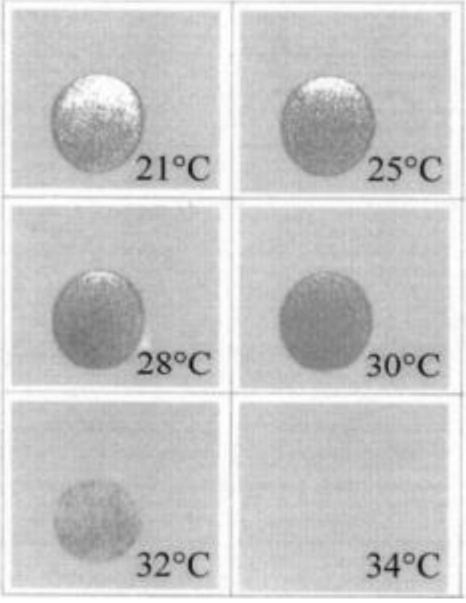

Figure 1.4.1: 2D Fourier imaging of P(NIPAM) swollen in D_2O at various temperature values [113]. Contrast decreased with higher temperatures due to lower mobility of the network chains.

Studies have been undertaken looking into the dynamics of P(NIPAM) and βCD or cyclodextrin using NMR and MRI techniques. Knorgen et al for example investigated the swelling and diffusion of P(NIPAM) infused with D_2O during a heating experiment. As shown in **figure 1.4.1**, Knorgen monitored the deswelling effect with higher temperatures of P(NIPAM) in D_2O. Knorgen noted that the brighter the areas are, the longer T_2 was, and the higher the mobility of the network chains were. However, the T_2 signals of the matrix rapidly disappeared once temperature surpassed VPTT and triggered a coil-to-globule transition [112-113]. Similarly, Tanaka et al found a similar observation, where the best contrast of the gel in relation to the water was observed in the image after 18 min at T_{VPT} because of the large difference in the mobility of the water. The image of the polymer matrix swollen in perdeuterated water supports the idea that the shrinking process is a 2-step process, and the brighter areas signify longer T_2, thus higher mobility in the network chains.

In Wisniewska's paper, which is the paper this project is based on, characterized the change of P(NIPAM) at LCST and VPTT, such as monitoring the change in area, diffusion, and T_2 relaxation at various temperature conditions (temperature jumps and slow heating experiments). She observed that the sample going from room temperature to 31°C in a temperature jump observed constant T_2 relaxation and self-diffusion during the entire experiment. On the other hand, the hydrogel sample that was kept at 40°C after the temperature jump observed a decrease in both diffusion and T_2 relaxation. The last sample was slowly heated from room temperature up to 40°C, and it showed that its T_2 relaxation and self-diffusion were independent from the shrinking kinetics. However, she did also look into how the change of concentration for βCD outside the hydrogel at LCST and VPTT. She concluded that the release of βCD outside of the hydrogel was dependent on the linear shrinkage of the P(NIPAM) before LCST. Samples that went above LCST and VPTT showed that the release of βCD correlated well with the shrinking kinetics [4]. Liu et al found a similar finding, where he found that the proton signal intensity of -$CH(CH_3)_2$ for the NIPAM component in poly(N-isopropylacrylamide) core-shell microgels decreased whilst the CH (1) signal for the βCD component increased at 40°C [114]

(1.5) Goal of the project

The goal of this project is to provide a more extensive portfolio for P(NIPAM) and βCD and how they interact with LCST, VPTT, and at 40°C using various temperature protocols based on Wisniewska's paper about P(NIPAM) and βCD. Particularly, this project will focus on analyzing the βCD concentration changes inside and outside the hydrogel using STEAM, as well as βCD's diffusion during a temperature increase inside the hydrogel using MEGA-PRESS. This project's results hope to provide a better perspective of the βCD behavior to see if it adheres well with the shrinking kinetics of the hydrogel and other literature works done on the P(NIPAM) and CD-system.

(2)NMR Theory

(2.1) Zeeman interaction and NMR signal

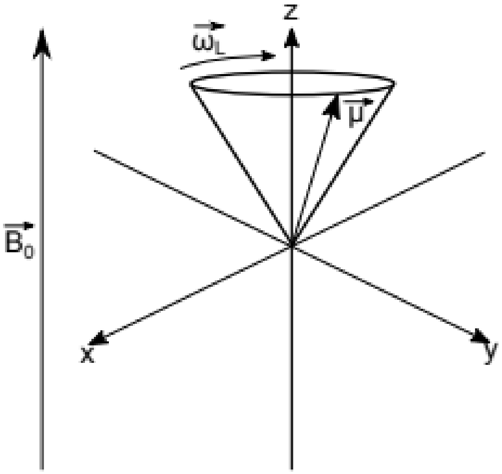

Figure 2.1.1: Precession of a magnetic moment spin (µ) in a static magnetic field (B_0) with Larmor frequency (ω_L) around the xy-plane of the frame of reference. Adapted from [4].

In NMR, nuclei have a spin angular moment (P), which is defined in **equation 2.1.1** [115]. A nucleus with a nuclear spin quantum number (I) may take (2I+1) different orientation relative to an arbitrary axis.

$$P = \sqrt{I(I+1)}\hbar \quad \textbf{(Equation 2.1.1)}$$

The various spins are summarized in **attachment 3**. The integral spins are whole numbers. The fractional spins are fractions, and the zero spins are those nuclei with I=0 [115, 117]. In addition, $\hbar = \frac{h}{2\pi}$, where h is the Planck's constant (6.626×10^{-34} Js). The intrinsic spin (µ) of the nucleus has an associated magnetic moment, which is defined in **equation 2.1.2**, where γ is the gyromagnetic ratio [45, 115].

$$\mu = \gamma P = \gamma\sqrt{I(I+1)}\hbar \quad \textbf{(Equation 2.1.2)}$$

$$P_z = m\hbar \quad \textbf{(Equation 2.1.3)}$$

$$\mu = \gamma m\hbar \quad \textbf{(Equation 2.1.4)}$$

The γ is dependent on the nucleus, so it can be positive or negative depending on if the spin of the nucleus is clockwise or counterclockwise respectively [4, 118]. A high γ indicates that the nucleus is highly sensitive in NMR [119]. The most analyzed nucleus is the hydrogen. It has a value of $\gamma_H = 26.7522 \times 10^7 radT^{-1}s^{-1}$. By applying a nucleus with both an angular moment and magnetic moment along a static magnetic field (B_0) on the z-axis, the angular moment will orient itself along the magnetic field as defined by **equation 2.1.3**. Combining **equation 2.1.2** and **equation 2.1.3** will yield **equation 2.1.4**, where m is the magnetic quantum number [45, 115].

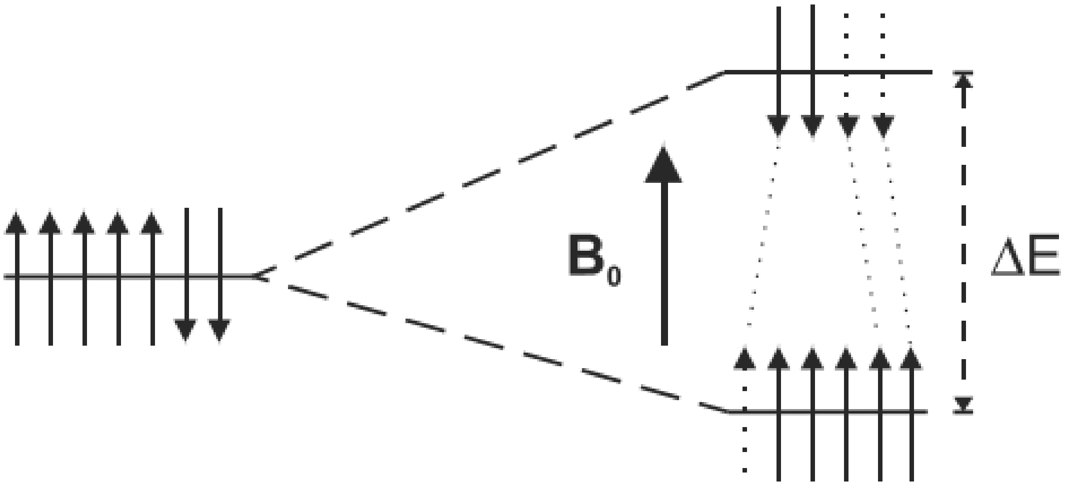

Figure 2.1.2: Energy separation of two states of a spin using a Zeeman diagram. On the left side of the figure, there is no magnetic field present. The protons will adopt the configurations of z-components that is equal in energy, so that there is no preferred alignment between the spin up and spin down orientations. The spins that are pointing up, parallel to B_0*, are of lower energy. Moreover, it contains more protons than the higher energy spins, which are pointing down, perpendicular to* B_0*. This difference in energy between the two levels is proportional to* B_0 *and* ω_L*. Excitations at the Larmor frequency causes the spins from the lower energy state to transition to the upper energy state. For the upper energy states, the stimulations causes the spin to lose its energy and relax to the lower energy state. Due to the higher population of low energy state spins, there is a net absorption of energy by the spins in the sample [13].*

The quantum number may have values m=I, I-1,…,-I. In total, there are (2I+1) possible orientations for the angular and magnetic moment to create a torque on the nucleus, which causes the nucleus to precess around the frame of reference's xy-plane with an angular frequency as represented in **equation 2.1.5** [115,117-118,120]. With that in mind, this angular frequency is referred to as the Larmor frequency (ω_L), and it is visualized in **figure 2.1.1**. If the precessing nucleus is exposed to electromagnetic radiation of frequency (v_1) that is the same as ω_L , then the resonance condition, which is defined in **equation 2.1.6**, is satisfied [45, 117, 119-120].

$$\omega_L = \frac{\gamma B_0}{2\pi} \quad \textbf{(Equation 2.1.5)} \qquad\qquad \omega_L = v_1 = \frac{\gamma B_0}{2\pi} \textbf{(Equation 2.1.6)}$$

A strong coupling between the spins and the electromagnetic radiation is present when the energy is at the Larmor precession frequency. This stimulates the transitions between the spin up and spin down energy levels [13]. The energy separation of the two states of a spin $-\frac{1}{2}$ nucleus is given at **figure 2.1.2**, and it is defined in **equation 2.1.7** [115,117]. This is called a Zeeman diagramIn the direction perpendicular to B_0, the spin orientations are still randomly distributed just as they were outside the magnetic field as there is still no net magnetization(M_0) perpendicular to B_0 [45].

$$E_{total} = \gamma \hbar B_0 = \hbar \omega_L \ \textbf{(Equation 2.1.7)}$$

$$\frac{N_{upper}}{N_{lower}} = e^{-\Delta E_{total}/kT} \textbf{(Equation 2.1.8)}$$

On the other hand, in the direction parallel to the magnetic field, there is a constant nonzero interaction or coupling between the proton and B_0 due to the parallel direction of the magnetic field. This coupling of protons to the magnetic field is what we refer to as the Zeeman interaction. For these protons, more will be oriented parallel to B_0 than will be oriented antiparallel as there is an induced polarization of the spin orientation by the magnetic field. **Figure 2.1.3** demonstrates this induced polarization by the Zeeman interaction at the microscopic and macroscopic perspective. The spins parallel to B_0 (positive z-component) has a higher spin population, and they are the ones creating the M_0 [13].

Consequently, this coupling causes a difference in energy between protons aligned parallel or along B_0 and protons aligned in energy between protons aligned perpendicular or antiparallel to B_0. This energy difference, ΔE is proportional to B_0, and using the Zeeman diagram, the energy difference can be visualized and explained. The stronger B_0 becomes, the higher frequency and energy needs to be used to achieve a spin-flip transition. This is represented by Boltzmann distribution in **equation 2.1.8**, where k is the Boltzmann constant (1.38×10^{-23} J K^{-1}), and the ratio of the thermal equilibrium populations of the N_{upper} and N_{lower} states are given [45,117,120-121].

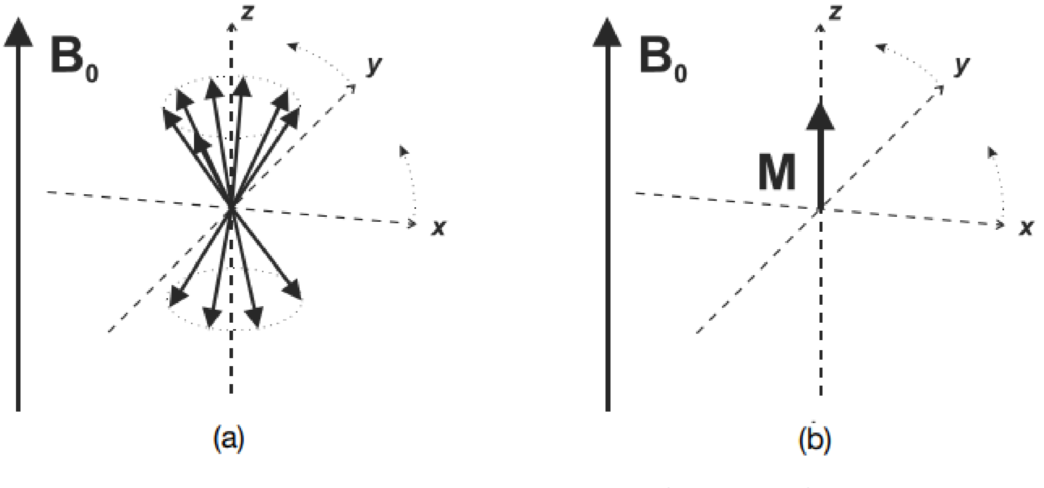

Figure 2.1.3: (a) Microscopic perspective and (b) macroscopic perspective of a collection of protons when B_0 is present. Every proton precesses around B_0. If a rotation frame of reference with a rotation rate that is equal to ω_L is utilized, the protons will appear stationary. The Z-components can have one positive and one negative value, but the x and y components can be any value, regardless if it is positive or negative. The spins will appear to track along 2 cones, with one cone having a positive z-component and the other will have a negative z-component. The higher spin population on the upper cone produces a nonzero vector sum M_0, which is of constant magnitude and parallel to B_0 [13].

(2.2) RF-pulse

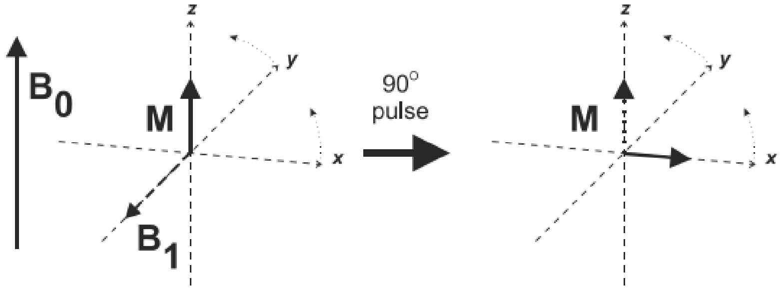

Figure 2.2.1: Energy absorption (macroscopic) after a 90° rf pulse. In a rotating frame of reference, the rf pulse broadcast at ω_L can be treated as an extra magnetic field labeled B_1. The additional magnetic field is oriented perpendicular to B_0. When the energy is applied at the ω_L, the spins absorb it and the net magnetization, M rotates into the transverse plane. The direction of rotation is perpendicular to both B_0 and B_1. The amount of resulting rotation of M_0 is referred to as the pulse flip angle [13].

Given how there are more spins at the lower energy level in the Zeeman diagram and the positive Z-component for **figure 2.1.3**, there will be a net absorption of energy by the tissue. These spins, when excited by the oscillation of the electromagnetic pulse that has a central frequency equal to the ω_L and an orientation perpendicular to B_0 as shown in **figure 2.2.1**, can be used to measure the magnetization strength by rotating M_0 entirely to the transverse plane, which creates a transverse magnetization as a result of a a $90°_x$ pulse. However, a $180°_x$ pulse can be used to cause M_0 to rotate to the negative longitudinal plane. The NMR signal can only be recorded when M_0 is on the transverse plane as the receiver coil is in this plane [13].

In addition, the magnetic part of the electromagnetic radiation, B_1, will oscillate in short time intervals along the x-direction, passing through zero along the way. This creates a weak magnetic field, and the orientation difference created allows a coupling between the RF pulse, B_1 and M_0, so that the energy can be transferred to the spins at the ω_L. Consequently, this change in the orientation cause M_0 to rotate away from its equilibrium orientation. The direction of rotation of M_0 will be perpendicular to both B_0 and B_1, and this is possible even in the presence of a strong B_0. This field is called the rf field and it is created by feeding radiofrequency power to a wounded coil at the x-axis [13, 118].

Once the transmitter is turned off, the spins immediately begin to realign themselves and return to their original equilibrium orientation. The return to its equilibrium position is also accompanied with an emission of energy correspondent to the ω_L. M_0 will precess about B_0. As a result, a free induction decay (FID) is produced when the spins induce a voltage in the receiver coil that is positioned perpendicularly to the transverse plane during precession. The FID will eventually decay with times as more spins release their absorbed energy through relaxation, in which consequently, the coherence and uniformity of the spins are lost [13].

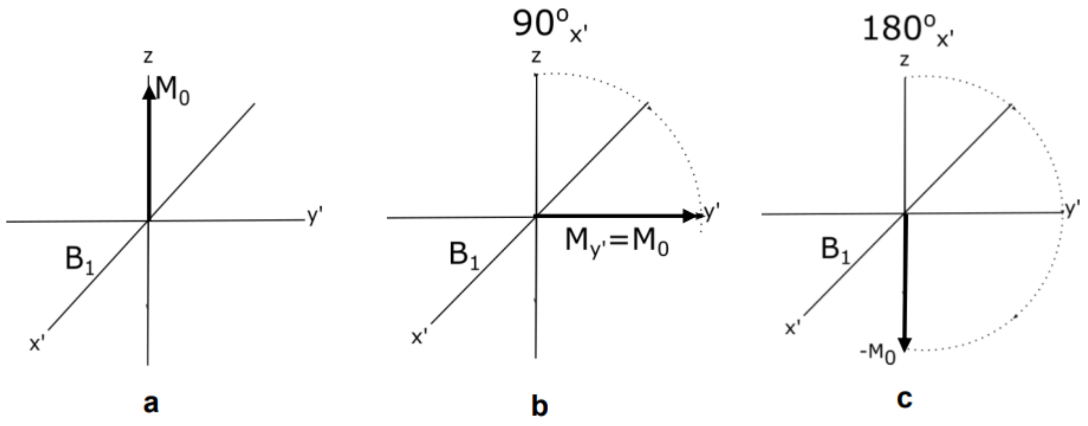

Figure 2.2.2: Direction of different rf pulses in a rotating frame coordinate system. (a) Prior to the pulse application (b) After applying a 90◦ rf pulse. (c) After applying a 180◦ rf pulse [119].

If precession proceeds from x’ towards -y’ as seen in **figure 2.2.2** in a rotating coordinate system, only one oscillating field along the x’-axis is considered. This is due to the other field, which is rotating in the opposite sense to the Larmor precession, has no important interaction with the magnetization, thus should be ignored. The rotation angle or flip angle of μ around B_1 in the y’, z-plane is given by **equation 2.2.1**, where τ_p represents the duration of the rf field pulse and θ is the pulse angle between the z-axis and the total magnetization vector, $\vec{M}$. Summing up all the $\vec{\mu}$-values will give $\vec{M}$, which can be used to replace $\vec{u}$. The equation for $\vec{M}$ is represented in **equation 2.2.2** [4, 45, 115, 118].

$\theta = \gamma B_1 \tau_p$ **(Equation 2.2.1)** $\vec{M} = \sum \vec{u}$ **(Equation 2.2.2)**

The oscillating y-component fields always cancel each other out due to similar magnitudes and frequency. On the other hand, the oscillating fields of the x’-components shrink towards zero as the angle through which the rotating vectors approaches $\frac{\pi}{2}$ or 90◦. The longitudinal magnetization will go to the transverse magnetization. Increasing the angle beyond 90◦ will cause the x’-component to grow until reaching the maximum value of 180◦ or π. When it transitions to the 180◦ rf pulse, the longitudinal magnetization will become negative. This is referred to as the inversion pulse or flip angle. After reaching the flip angle, the rotation will continue, which causes the x’-component to increase back to zero and rise again to the $2B_1$ value. Consequently, the most used flip angles are 90◦ ($\frac{\pi}{2}$) and 180◦ (π) [115,119]

(2.3) Relaxation

As mentioned prior, after M_0 rotates to the transverse plane, the spins that absorbed the energy from an RF pulse will gradually release their absorbed energy and realign themselves back to their original equilibrium. According to the derived Bloch-equations, if the rf field is turned off (turning off the transmitter), the relaxation process can be introduced as shown below in **equation 2.3.1**, **equation 2.3.2**, and **equation 2.3.3** for the x, y and z-axis respectively [115, 122-123]. T_2 is the transverse relaxation time, and it is defined in **equation 2.3.1** and **equation 2.3.2**. T_1 is the spin lattice relaxation time, and it is defined in **equation 2.3.3**. τ is the time after the pulse angle [117], and M_0 is the net magnetization at thermal equilibrium along the z-axis presented in **equation 2.3.3** [122-123]. The derived Bloch equations provides information to describe the motion of the bulk of magnetization after a 90° rf pulse is sent out as a function of time during the return to equilibrium.

$$M_x(t) = M_0 e^{\frac{-\tau}{T_2}} \sin(\omega t) \; (\textbf{Equation 2.3.1})$$

$$M_y(t) = M_0 e^{\frac{-\tau}{T_2}} \cos(\omega t) \; (\textbf{Equation 2.3.2})$$

$$M_z(t) = M_0 \left(1 - 2e^{\frac{-\tau}{T_1}}\right) (\textbf{Equation 2.3.3})$$

Longitudinal or spin-lattice relaxation(T_1)

As mentioned, T_1 is the time required for the net magnetization of the z-component (M_z) to exponentially return to 63% of its original Boltzmann equilibrium distribution after rf excitation. The non-radiative return of the proton from a 90° RF pulse to an equilibrium distribution of populations in a system is an aspect of relaxation [117]. M_0 will rotate as observed in **figure 2.3.1**, and there will be an absence of longitudinal magnetization after the rf pulse is sent. The rf pulse will lead to the saturation of the upper state to match the lower state population [4, 115, 122-123]. After some time, the sample will return to equilibrium, and the component in the xy-plane will decay to zero due to T_2. Furthermore, the z-component (M_z) will build up to its equilibrium value(M_0) via spin-lattice longitudinal relaxation (T_1) [124]. The spin transfers its energy to the surroundings or “lattice” and not to another spin. The energy no longer contributes to spin excitation [13,115, 117, 119, 123]. During this return of magnetization, proton spins will release energy as shown in **figure 2.3.1**. This is referred to as T_1 relaxation. The more energy that is released to the lattice, the more signal that will be generated after the next rf pulse [13,115, 117, 125].

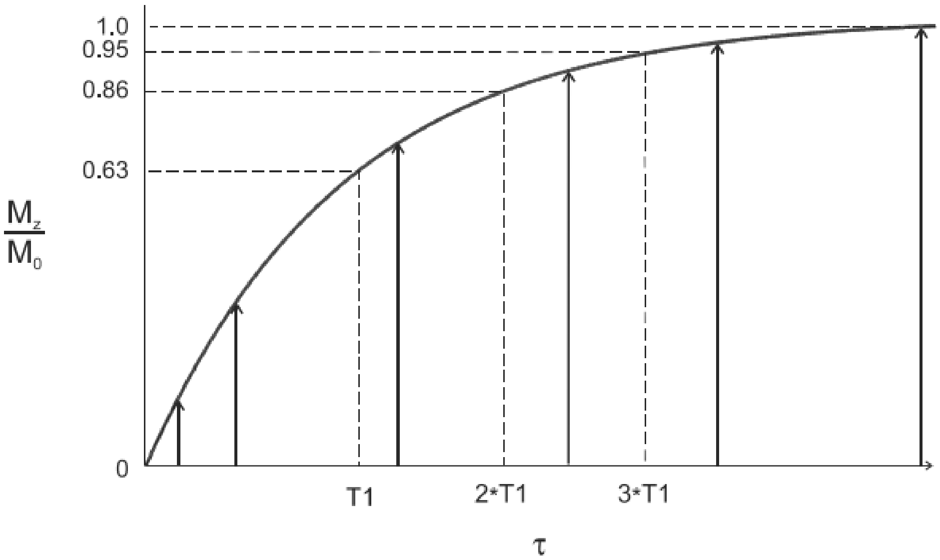

*Figure 2.3.1: T_1 relaxation curve after a 90° rf pulse. There is an absence of M_z until the gradual release of energy from the saturated proton spins are observed through T_1 relaxation. The more protons that release their energy, the larger M_z will be. At some point, $M_z= M_0$ and equilibrium will be completely restored. The change of M_z/M_0 with accordance to τ showcases an exponential growth and is defined in **equation 2.3.3** [13].*

Transverse relaxation(T_2)

T_2 or transverse relaxation is the time required for the transverse component of the net magnetization (M_{xy}) to decay to 37% of its initial value in an irreversible process. T_2 is mathematically given by **equation 2.3.1** and **equation 2.3.2** will define the solution from $M_{x,y}$ to form **equation 2.3.4**, where M_0 is the value of xy-magnetization when τ=0 [4, 118,122-123]. The decay is visualized in **figure 2.3.2**.

$$M_{xy} = M_0 e^{\frac{-\tau}{T_2}} \text{ (}\textbf{Equation 2.3.4}\text{)}$$

Transverse magnetization is comprised of spins in phase, and once the rf pulse is turned off, the phase coherence is gradually lost as relaxation reduces the precession of the spins [115, 126]. After sending a 90° rf pulse, M_0 will rotate into the xy-plane to create M_{xy}, and the coherence will be in the transverse plane at the end of the pulse. The protons with the absorbed energy from the rf pulse will precess at the same frequency ω_0 and is synchronized at the same point or phase of its precessional cycle. Protons with identical molecular environments and ω_0 will readily absorb the energy that is being released by its neighbour via spin-spin relaxations [13].

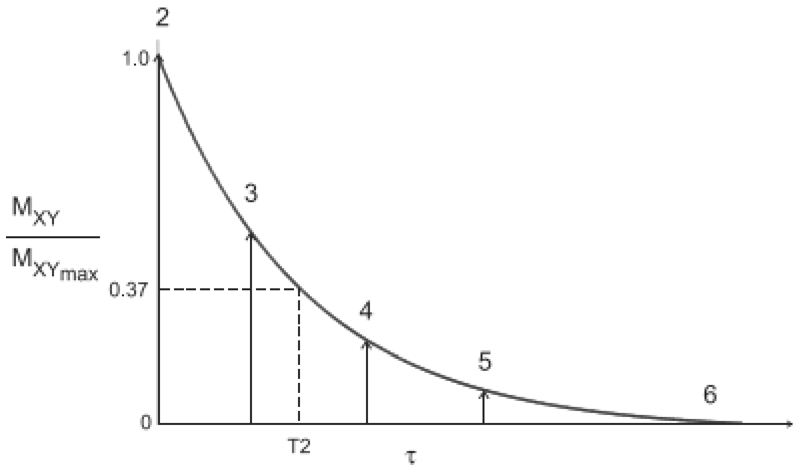

Figure 2.3.2: M_{xy} is plotted against a function of time. The decay for M_{xy}/M_{xymax} is exponential and can be described by ***equation 2.3.4****. T_2 is the time constant in which M_{xy} has decayed to 37% of its original value. This is referred to as the transverse relaxation [13].*

During relaxation back to equilibrium, the coherence in the plane will be lost and the proton spins will release their energy, orienting themselves back along B_0. Phase coherence is when a small fraction of individual spins precesses in phase in double cones, and it can be lost in 2 different ways. Relaxation is one way to destroy phase coherence. The second method is to alter the Larmor frequencies and change the precession of the spins. In addition, the loss of phase coherence is observed to be an entropic process. The coupling of the magnetic and angular moment can produce a variety of orientations, and each of these spins will position at random angles around the direction of the applied magnetic field at thermal equilibrium [82, 92]. The fluctuation of ω_0 will produce a gradual and irreversible loss of phase coherence to the spins during the energy exchange and relaxation. Consequently, the magnitude of M_{xy} diminishes, which inadvertently reduces the generated signal as the receiver coil is located at the transverse plan. Unlike longitudinal relaxation, transverse relaxation does not involve equalizing the upper state population to match the lower state, so the energy of the spin system is unaffected by spin-spin relaxation. After the transverse coherence disappears, it will reform in the longitudinal direction as T_1 relaxation occurs. T_2 cannot be larger than T_1 as T_2 can completely decay before the longitudinal magnetization achieves thermal equilibrium (M_z=M_0). With this in mind, M_z is unable to achieve equilibrium until M_{xy} is zero, hence T_2 is often less than T_1 [13, 118-119].

T_2* and spin echo

During the loss of phase coherence, nonuniformity in B_0 can occur, and this can come from 3 main sources [13]:

1. **Main field inhomogeneity:** Due to the imperfections in the magnet and the immediate surroundings of magnet (building walls and metals), there will be a constant degree of nonuniformity to B_0. The field distortion will be constant during the measurement.
2. **Sample-induced inhomogeneity:** Differences in magnetic susceptibility and magnetic polarization of neighboring tissues can distort the local magnetic field near the interface between the tissues. As a result, this creates a constant magnitude of inhomogeneity as long as the patient or sample is in within the influence of the magnet.
3. **Imaging gradients:** This technique is used for spatial localization, and it creates a magnetic field inhomogeneity that is transient during measurement. However, a well-designed pulse sequence can eliminate imaging gradients as a source of dephasing. Imaging gradients are further described in the MRI subsection.

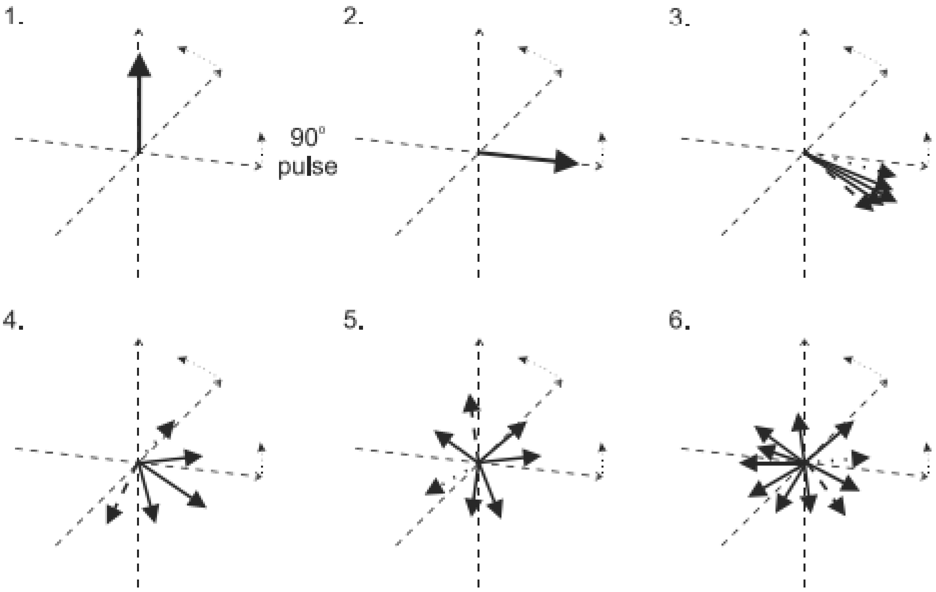

Figure 2.3.3: Effects of T_2^* It is assumed that ω_0 is faster than a rotating frame. (1) M_0 is parallel with B_0 prior to the 90° rf pulse. (2) The 90° rf pulse is sent, and the proton spins begin to precess in phase in the transverse plan. (3) After some time, the proton spins will begin to precess at various frequencies due to fluctuations of ω_0 caused by inter- and intramolecular interactions. This is visualized by the dashed arrow and dotted arrow which showed a faster precession and a slower precession respectively. Therefore, the proton spins become asynchronous with each other. (4,5,6) Slowly, but gradually, the transverse coherence magnitude diminishes until there is complete randomness of the transverse components, and no coherence is no longer observed [13].

T_2^* is defined as the dephasing time or as the effective transverse relaxation time. It is a combination of transverse relaxation and the effect of magnetic field inhomogeneity. **Figure 2.3.3** describes the asynchronous result of inhomogeneities for T_2^*, where the precession rates for the proton spins become non-uniform until coherence completely disappears. Furthermore, $T_2 > T_2^*$ when inhomogeneity is present. A lack of shimming is one common example of inhomogeneity in the magnetic field. It is defined in **equation 2.3.5**, where T_{2M} is the dephasing time due to the main field inhomogeneity and T_{2MS} is the dephasing time due to the magnetic susceptibility differences [13,132]. For tissues and liquids, T_{2M} is an important factor in determining T_2^*. In addition, T_{2MS} predominates T_2^* for tissues with substantial iron deposits or air-filled cavities [13].

$$\frac{1}{T_2^*}=\frac{1}{T_2}+\frac{1}{T_{2M}}+\frac{1}{T_{2MS}}$$ **(Equation 2.3.5)**

The decay of M_{xy} after the 90° rf pulse marks the exponential process of FID with $T_2\times$ instead of T_2. **Equation 2.3.6** defines the net magnetization on the transverse plane with consideration to $T_2\times$ instead of T_2, where $M_{xy(max)}$ is the transverse magnetization immediately after the excitation pulse [161]. **Figure 2.22** shows the difference between T_2 and $T_2\times$ when M_{xy} relaxes after excitation. M_{xy} decays with $T_2\times$ as this relaxation accounts for the factors that causes the dephasing of the proton spins. Seeing to as it is M_{xy} that generates the MR signal, the decaying signal following the rf pulse is referred to as 'free induction decay' (FID) signal.

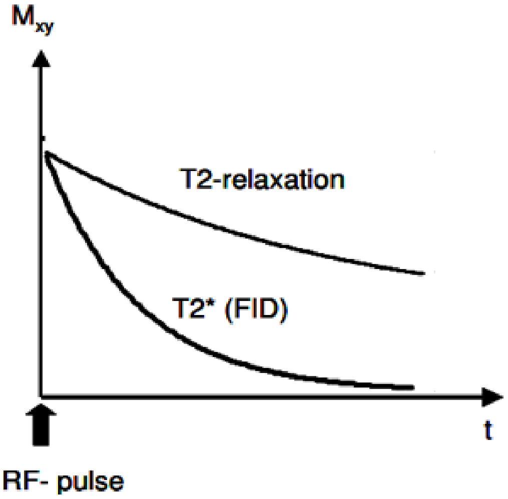

Figure 2.3.4: T_2 relaxation compared T_2 following an excitation pulse [127]*

$$M_{xy}=M_{xy(max)}e^{\frac{-\tau}{T_2^*}}$$ **(Equation 2.3.6**

Difference between T1, T2, and T_2^*

T_1 and T_2 have traits that separate them from one another. The most substantial difference between the 2-time constants is the influence of B_0. T_1 is significantly influenced by the strength of B_0. Longer T_1 times are produced with a stronger or larger B_0. On the other hand, T_2 is generally insensitive to B_0. However, very small B_0 values(B_0<0.05Tesla) will bear a significant change in T_2. $T_2\times$ is influenced by its components, namely T_{2M} and T_{2MS}, and similar to T_1, $T_2\times$ is sensitive to B_0. For T_{2M} to be short, it requires a good magnetic field uniformity. A superb uniformity is generated with a higher B_0, but this is difficult to achieve. Such great values of B_0 will cause apparent disparities in M_0 between 2 tissues with varying magnetic susceptibilities, which leads to shorter T_{2MS} [13].

180° rephasing pulse angle and spin echo

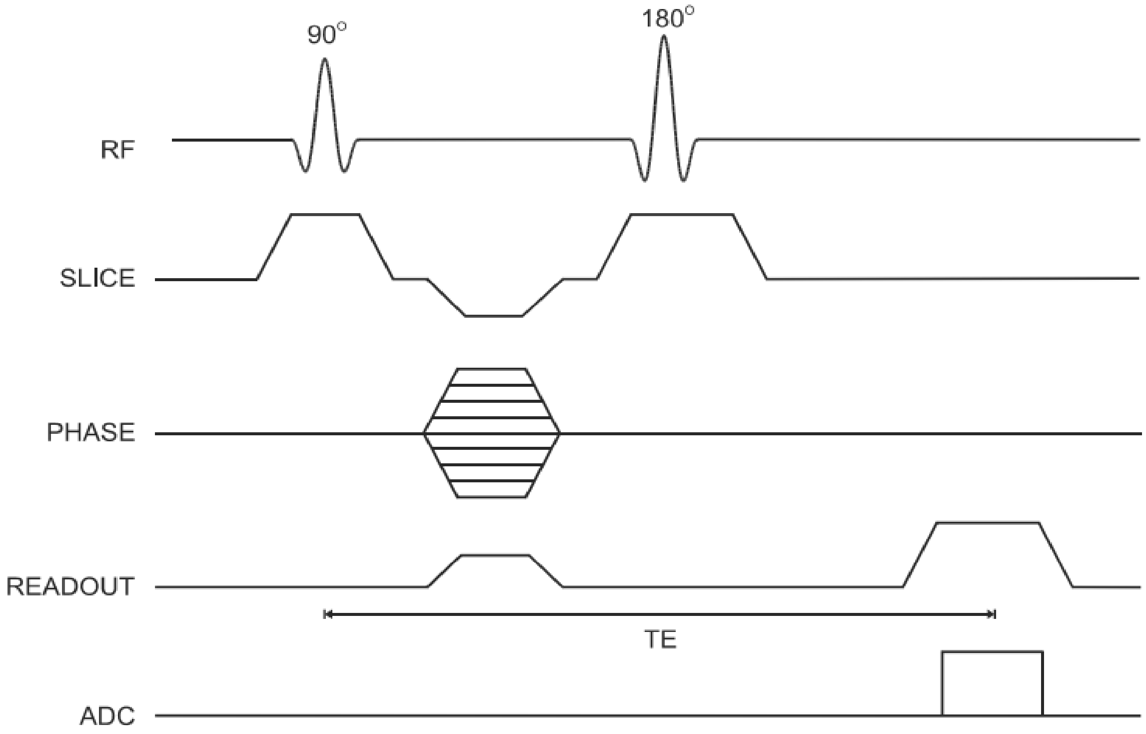

Figure 2.3.5: Standard single echo spin echo sequence timing diagram. The sequences are characterised by a single refocusing 180° rf pulse, a single detected echo, and a single phase-encoding table [13].

The FID signal following the 90° rf pulse is referred to as a “tail,” and it is usually determined by the inhomogeneous external field. As a result of B_0 inhomogeneities, the magnetization vector will contain some slow spins, whilst other spins have faster spins due to some of the spins of the sample to precess at different rates, which leads to phase differences and a loss of M_{xy} faster than expected from only spin-spin interactions alone. The spins with a higher Larmor frequency will precess faster than spins with lower Larmor frequencies, which creates the signal delay after applying a 90° rf pulse [115, 119, 128-130]. However, the artificial decay of the rf signal can be eliminated, so that the natural decay of the nuclear signal can be observed by applying an 180° rf pulse. The rephasing pulse angle is visualized in **figure 2.3.5** and **figure 2.3.6**, where it shows the standard single echo spin echo sequence diagram, and the vector diagram for the spin echo respectively [13, 119].

When the 180° pulse is applied, the magnetization vector is flipped to a mirror image position. This causes the spins to continue to precess, but their motion is now flipped and reversed. The 180° rf pulse can cause the proton spins to reverse their phases relative to the resonant frequency, but the rates and directions of precession for the proton spins do not change. The rephasing causes the main field inhomogeneities and magnetic susceptibility differences to be eliminated as the proton spins will experience an identical interaction before to and following the 180° pulse. Consequently, T_2^* relaxation disappears [13, 119, 131]. It is imperative to remove the T_2^* as water diffusion experiments only affect M_{xy}

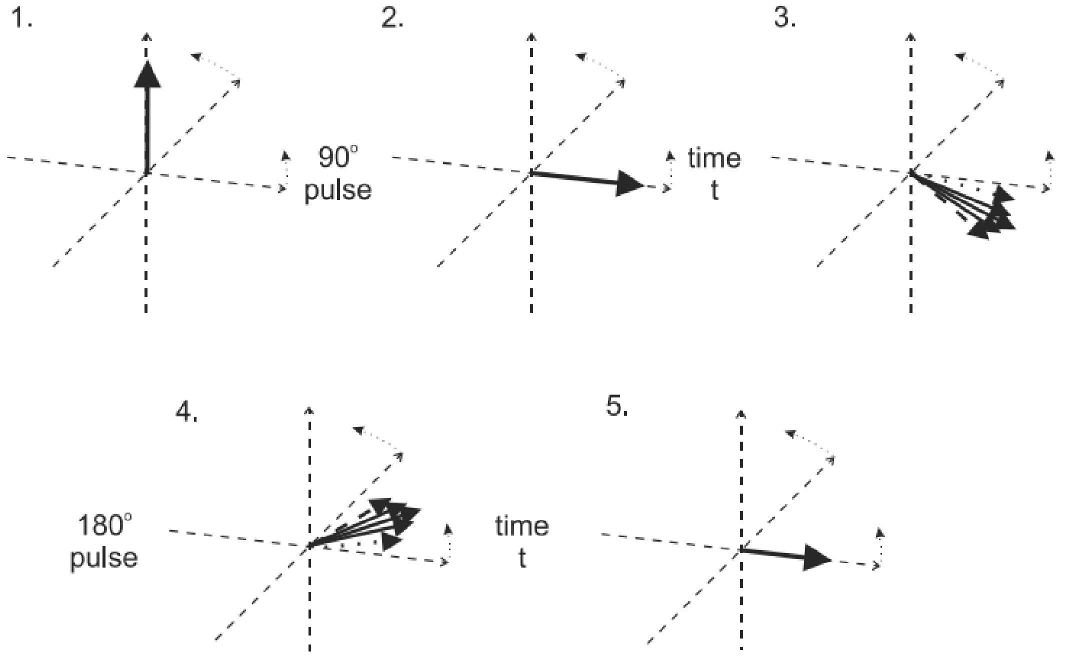

Figure 2.3.6: Vector diagram of a single echo spin echo sequence. (1) Assume that the rotation frame is slower than ω_0. (2) The 90° rf pulse rotates the net magnetization from equilibrium(M_0) down to the transverse plane (M_{xy}). (3) However, the T_2^* relaxation creates asynchronous proton spins during t_1. (4) By applying a 180° rf pulse will cause the protons to reverse their phase relative to the transmitter phase. The dashed arrows represent the faster precessing proton spins, whilst the dotted arrows represent the slower proton spins. (5) The proton spins are given some time(t_2) to regain their phase coherence in the transverse plane after which some time, a signal will be generated in the receiver coil. This is what we refer to as the spin echo. The loss in magnitude of the reformed coherence relative to the original coherence is because of the irreversible processes of T_2 relaxation [13].

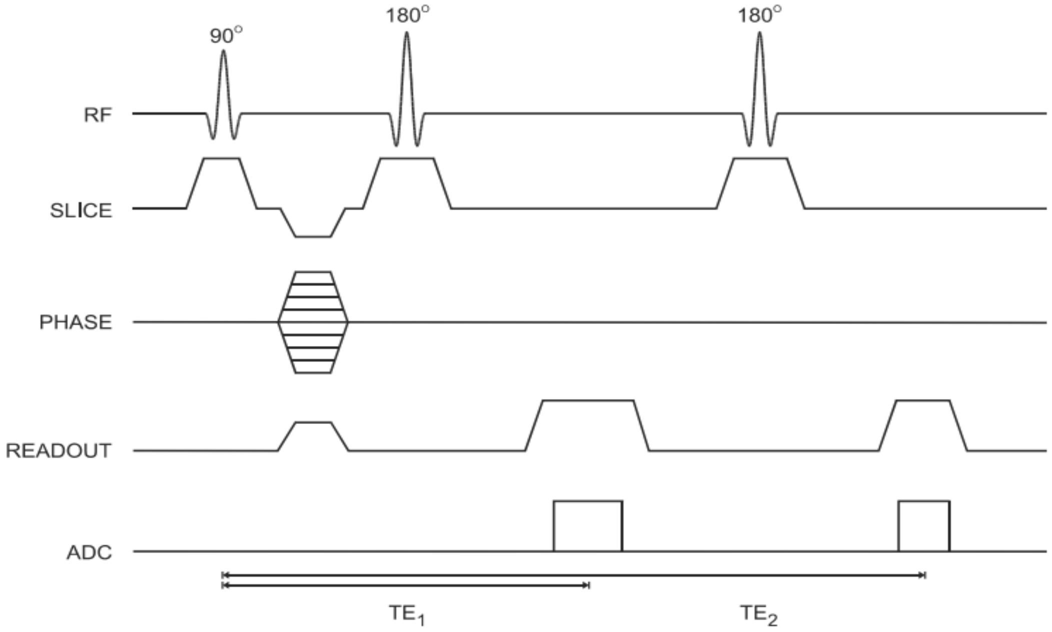

Figure 2.3.7: Standard multiecho spin echo sequence timing diagram. Multiple echoes can be generated by utilizing more 180° rf pulses, as well as utilizing gradient pulses on the slice selection and readout gradient pulses, and ADC sampling times [13].

After the second signal delay (τ_2), the protons will regain their transverse coherence, which induces a spin echo before the faster spins leave again, thus leaving the slow spins behind. This leads to the system to dephase again as the sources of the dephasing continue to influence the spins. Complete refocusing allows an accurate T_2 echo measurement with all T_2^* effects removed. In NMR and MRI, spin echo is fundamental in modern NMR experiments, and the standard multiecho spin echo sequence is a common pulse sequence diagram that is shown in **figure 2.3.7**. NMR signals can be observed after an initial excitation of rf pulses due to both spin relaxation and any inhomogeneous effects. A 2nd 180° rf pulse will reverse the proton spin phases and re-establish coherence to the proton spins, and the key difference between the 1st and 2nd 180° rf pulse is that the 2nd echo has a higher T_2 relaxation that contributes to the signal loss. This process of spin echo formation continues until T_2 relaxation completely dephases the proton spins [83, 119, 125-128].

A higher use of multiple 180° rf pulses maintains the phase coherence to the protons longer than the use of a single 180° rf pulse due to the substantial dephasing that the field inhomogeneity induces over a short space of time. Hence, by applying 180° rf pulses at the instants τ, 3τ, 5τ,…etc., we obtain echoes with shifting phases at intervals of 2τ, i.e. at the times 2τ, 4τ, 6τ. Besides that, the irreversible spin-spin relaxation is unaffected by the 180° rf pulse. This means to say that the loss of phase coherence and signal amplitude for a spin echo is because of the true T_2 relaxation, and it is only T_2 that determines the decay of the echo intensities [13 ,119, 128-130].

(2.4) NMR spectrum

A Fourier Transform of the Free Induction Decay is implemented to produce a spectrum with peaks that correspond accordingly to the resonance frequencies of the spins of the sample. The local magnetic field (B_{local}) is influenced by the chemical environment of a nucleus of the molecule [4]. B_{local} is represented in **equation 2.4.1**, where σ is the shielding constant of a proton. The σ can vary with the environment, thus different nuclei come into resonance at different frequencies [4, 45,117].

$$B_{local} = B_0(1 - \sigma) \text{ (\textbf{Equation 2.4.1})}$$

By modifying **equation 2.4.1**, the resonance frequency (v) can be defined when B_{local} replaces $\overrightarrow{B_0}$ to give **equation 2.4.2** [4, 117].

$$v = \frac{\gamma B_{local}}{2\pi} \text{ (\textbf{Equation 2.4.2})}$$

The resonance frequency (v) varies with $\overrightarrow{B_0}$, and as such, the NMR spectrometers operate with varying $\overrightarrow{B_0}$ fields compared to the signal frequencies. This can consequently can prove challenging. The separation of the resonance of a particular group of nuclei from the standard is specified by measuring its frequency separation from a peak of reference, v_{ref}. For comparison, the frequency separation difference of a peak is divided with v_{ref}. Following this, the chemical shift (δ) is defined in **equation 2.4.3** [4, 45,117].

$$\delta(ppm) = 10^6 * \frac{v - v_{ref}}{v_{ref}} \text{ (\textbf{Equation 2.4.3})}$$

The chemical shifts obtained in **equation 2.4.3** is independent of the applied field. If $\delta > 0$, the nucleus is deshielded. If $\delta < 0$, it means the nucleus is shielded [4, 45, 117].

(2.5) Pulse field gradient(PFG) NMR:

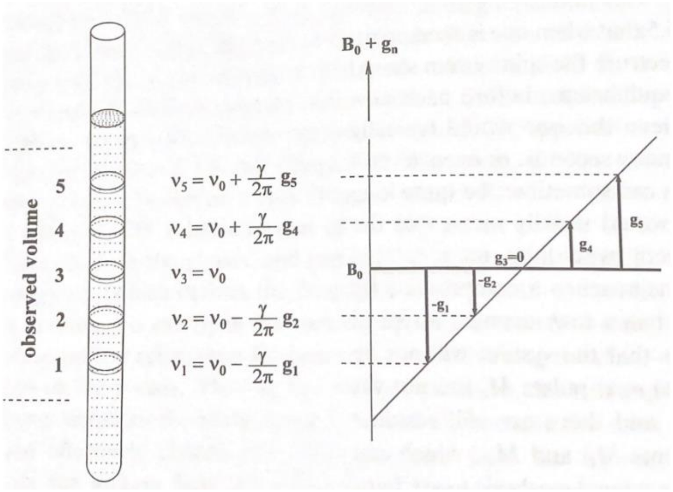

Figure 2.5.1: The application of a linear field gradient parallel to B_0. The contributions of the field gradient with respect to B_0 is represented by g_n, and $v_1 \rightarrow v_5$ are the various resonance frequencies for the 5 randomly chosen slices. Slice 3 is located at the center, and its $g_n=0$ [119].

When accumulating FIDs in order to produce a spectrum, relaxation should be complete, and equilibrium should be established prior to a new rf pulse being sent out. As mentioned before, τ should be adequately long. Commonly, 2 seconds is sufficient, but relaxation can vary from a couple of seconds to minutes. However, in practice, the duration can be unacceptably long, so a compromise is required in order to prevent a rf pulse being sent before the system is fully relaxed and $M_z=M_0$. Incomplete relaxation would mean that residual transverse magnetization components, M_{xy} can create artefacts using 2D methods. In order to resolve such problem, pulse field gradients (PFG) are considered [119-120].

PFG introduces controlled inhomogeneities utilizing a special gradient coil, which applies a linear magnetic field gradient parallel to B_0 on the z-axis. It is worth mentioning that the gradients can be applied to the x and y axis as well. The nuclei in the designated volume experience a nonuniform magnetic field. **Figure 2.5.1** highlights the slices and the contributions of the field gradients to B_0. The applied field gradient is picked, so that the excess field contribution by the cryomagnet at the center of the designated volume for the sample is 0. The upper portion (g_4 and g_5) of the middle part(g_3) of the sample bears a stronger magnetic field, whereas the lower portion ($-g_1$, $-g_2$) has a weaker magnetic field. These variations of magnetic field strengths are created by the additional contributions of the magnetic field gradients. With this in mind, B_0 is found at the middle with g_3, but the magnetic flux densities change depending on where they are with respect to the middle. For example, the upper portion densities are found by B_0+g_4 or g_5. A similar pattern is found for the lower portions via B_0-g_1 or g_2. The precessional frequencies of the nuclei at the various positions are defined in **equation 2.5.1** under with respect to the resonance condition of **equation 2.1.6**. The formula can be used to determine the precessional frequency of the nuclei, in which in this case, can yield 5 different values($v_1 \rightarrow v_5$) [119-120].

$$v_n = \frac{\gamma}{2\pi}(\overrightarrow{B_0} + g_n) \textbf{ (Equation 2.5.1)}$$

These gradients are only active for a certain period of time. Once they are switched off, the nuclei in the sample will only precess at $\overrightarrow{B_0}$ and v_0, in which v_0 is the precession frequency when $\overrightarrow{B_0}$ is present [119].

Gradient interaction with M_{xy}

Refer to the **figure 2.5.2**. (**a**)The magnetic field is homogenous at B_0 and equilibrium is established, meaning that M_0 is present. This is prior to the 90° rf pulse is sent. (**b**) As described before, when the 90° rf pulse is sent, the magnetization rotates from M_z to $M_{y'}$ in the rotating frame, where v_0 is the precessional frequency. The gradients are then added, and it is assumed that the slices are thin enough for the nuclei within each one experience the same magnetic field strength, where difference arises from slice to slice because of field gradient contributions(g_n). Slice 1 and slice 2's vectors will rotate slower and fall behind in the rotating frame, whilst slice 3 and slice 4's vectors will rotate faster and get ahead in the rotating frame. These are indicated by the small arrows. (**c**) Combining the total transverse magnetization yields M_n, where M_n is directed along the y-axis and its sum onto the x and y planes are called the macroscopic transverse magnetization ($M_{y'}$). Taking into considerations the application of gradients, the vectors for M_n will rotate and precess at varying degrees. The angle in which the vectors move in the rotating frame during τ of the gradient pulse depends on the frequency difference Δv, hence the position of the slice is given by **equation 2.5.2**:

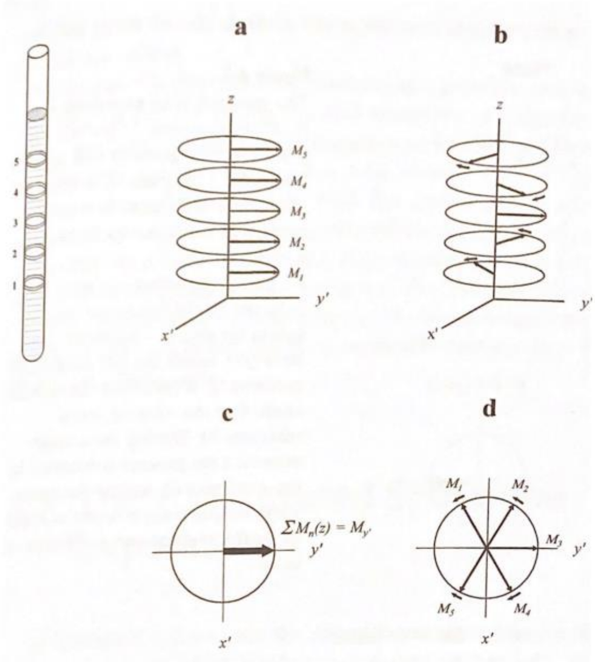

Figure 2.5.2: Behavior of the transverse magnetization in the presence of a field gradient. The sample is divided into 5 random slices, where slice 3 has g_3=0. A 90° rf pulse is sent and creates the transverse magnetization. The field contributions of the gradients(g_1 → g_5) creates a non-uniform pattern of precessional frequencies v_1 → v_5. The exception here is M_3 along the y'-axis in the rotating frame due the magnetization and frame having identical frequencies. Aside from M_3, the fanning-out process for the other slices occurs, hence the macroscopic transverse magnetization for the sample will gradually fall to 0 [110].

$$\theta = 2\pi\tau\Delta v \textbf{ (Equation 2.5.2)}$$

(d) The phase coherence of the vectors are completely lost during τ. After some time, the transverse magnetization component for the sample will relax and decay, thus no signal will be induced in the receiver coil [119].

Pulsed gradient spin-echo

Similar to how a spin echo is characterized, but it has some notable distinctions. One such difference is that the 90_x° rf pulse and 180_y° rf pulse are followed immediately by a field gradient pulse (G_1 and G_2 respectively), both with the same sign, magnitude G, and duration τ. **Figure 2.5.3** shows the pulse sequence and its respective vector diagram in **figure 2.5.4** For simplicity, an assumption is made that the proton spins in H_2O and the nuclei in the sample are in similar environments. Moreover, it is assumed that B_0 is constant throughout the sample volume, so the nuclei precess at v_0 when field gradients are not present. Taking reference from the effect of field gradients on the transverse magnetization, at the instant before recording the FID, it is evident that there is only 1 vector M_H for all the proton spins in the sample [119].

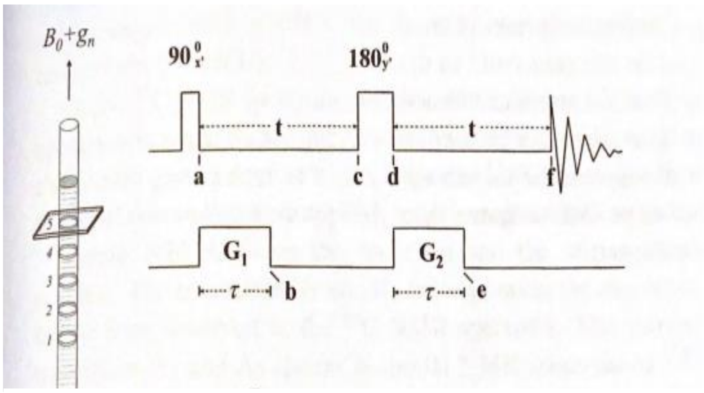

Figure 2.5.3: Spin-echo experiment with pulsed gradient. (A) Spin-echo pulse sequence accompanied by an additional gradient field G_1 shortly after the 90°_x rf pulse and the second, but identical, gradient field G_2 after a 180°_y rf pulse is sent [119].

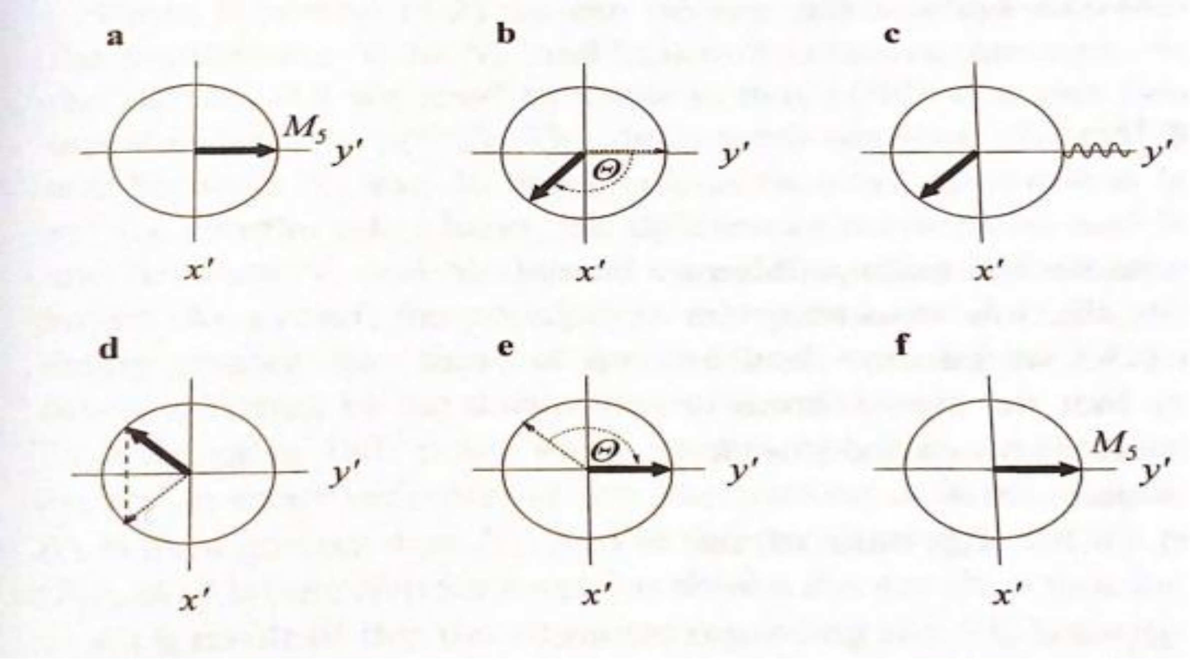

Figure 2.5.4: Spin-echo experiment with pulsed gradient. Vector diagrams show the state of the transverse magnetization referred to as M_5 for slice 5 at each of the instants from (a)→(f) [119]

(a) Using slice 5 as a point of reference to explain PFGSE, M_5 lies on the y-axis after the $90_x°$ rf pulse. **(b)** During the time τ in which G_1 is applied, the field strength goes from $B_0 \rightarrow B_0+g_5$, thus the processional frequency becomes v_5. V_5 excesses the rotating frame by a magnitude of $\frac{\gamma}{2\pi} g_5$, which causes the vector to advance with accordance to **equation 2.5.3** during the time τ.

$$\theta = \gamma g_5 \tau \text{ (\textbf{Equation 2.5.3})}$$

During the remaining time between the end of the gradient pulse and the beginning of the $180_y°$ rf pulse, the angle of M_5 relative to the coordinate system remains unchanged. This is due to both the gradient pulse and $180_y°$ rf pulse rotate with an identical frequency with v_0.

(c, d) Afterwards, the $180_y°$ rf pulse reflects M_5 through the y-axis. **(e)** G_2 follows, and it is identical to the first, giving the same precession frequency v_5, so that after τ the vector M_5, precessing faster than the frequency of the rotating frame, is turned into the direction of the y-axis. **(f)** The orientation stays the same after the gradient is removed. This applies to all of the slices in the sample. Consequently, the M_n are refocused along the y-axis at the beginning of the data acquisition. Finally, an echo is produced [119].

In order to get the best resolution, the sample has to spin. This exempts the latest generation of spectrometers. However, spinning the sample does lead to some mixing in the sample. In order to prevent this, PFG must be done without spinning. This does help alleviate the problem of mixing, but diffusion effects for the molecules are still an issue. Diffusion within the slice has no effect, but diffusion has an influence at the axial direction, which is the direction where the field gradient is positioned. As a result, the value of g_n and v_n can change between G_1 and G_2, which means the affected nuclear spins are not refocused. This then does not contribute to the intensity on the middle part of the echo. Furthermore, the diffusion reduces the magnitude of the echo, and this effect can be used to determine the diffusion coefficients D. In addition, it can also be used to suppress the solvent signal, especially when the solvent molecules diffuse faster than those of the solute, such as seen in polymer solutions [119].

(3)MRI theory

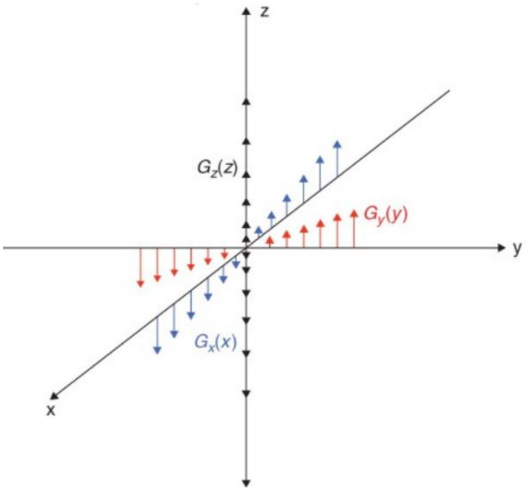

Figure 3.1.1: The magnetic field gradients (G_x, G_y, and G_z) to localize spins in MRI. Adapted from [133].

Using the same physical effects of NMR, Magnetic Resonance Imaging (MRI) can be applied to create radiological images. It creates these radiological images by correlating NMR signals with spatial locations and the use of magnetic field gradients (G_x, G_y and G_z) [4]. 2D or 3D images are formed because of this combination, which provides macroscopic information of the sample. One of the main differences between NMR spectroscopy and MRI imaging is that MRI generates the images using the intensity of the radiation applied, whilst NMR generates its spectrum based on the frequency of the radiation. Darker areas on the image indicates that the number of re-emitted photons are low in that specific area. The low reemission of the protons is a result of protons' tendency to not misalign when the RF waves are applied to the specific area [45,115,134-135].

(3.1) Magnetic field gradients

Magnetic field gradients are variations in the magnetic field (B_0) caused by spatial perturbation with respect to position. The gradients can either be 1D/2D, and these gradients are linear with respect to B_0. This linear dependence of the magnetic field towards the localization of the magnet is defined in **equation 3.1.1**, where B_i is the magnetic field strength with respect to its direction, r_i and G_T is the total gradient amplitude [13, 45, 115, 135-136].

$$B_i = B_0 + G_T * r_i \text{ (\textbf{Equation 3.1.1})}$$

These magnetic field gradients are what are used to localize frequencies and phases in various regions in the sample by applying short periods of it during the scan. These physical gradients are visualized in **figure 3.1.1**. These gradient pulses are found in the x, y, and z directions, and these are labelled G_{RO}, G_{PE}, and G_{SS} respectively. G_{SS} is labelled as the slice-selection gradient. G_{PE} phase encodes the sample, and the G_{RO} reads out or frequency encodes the sample. These gradients together enable the production of 2D or 3D images of the sample [115, 127,133, 137]. During slice selection, a 90° RF pulse and a 1D, linear magnetic field gradient in the direction of which the RF pulse is applied is simultaneously implemented. Couple this 90◦ RF pulse with a magnetic field gradient, the spins on the plane of the sample will rotate accordingly [134, 136-137]. Moreover, using **equation 2.1.6**, the Larmor frequency for the magnetic field gradients can be defined in **equation 3.1.2**, where ω_i is the frequency of the proton in position r_i [4,13, 115, 137].

$$\omega_L = \frac{\gamma B_0}{2\pi} \textbf{ (Equation 2.1.6)}$$

$$\omega_i = \gamma B_i \textbf{(Equation 3.1.2)}$$

Slice-selective gradient (GSS)

The first step to creating the MRI images is 'slice selection,' as it characterizes the inhomogeneous and phase separated samples, so it can provide localized information about the sample's chemical environment [134-135]. This slice selection step goes in tandem with a frequency-selective excitation pulse. Exciting the selected slice will cause the applied rf pulse to have an associated frequency profile ($\Delta\omega$). The $\Delta\omega$ can be used to adjust the slice thickness (Δz) along with the applied magnetic gradients. This is shown in **equation 3.1.3**, where the G_{SS} is the selected slice. A smaller G_{SS} value would mean the selected slice is thick and vice versa. In multi-slice imaging, each slice selected will have a uniform gradient and bandwidth for each slice. However, the central frequency will not be uniform, and this combination excites a variety of regions within the tissues [13]. The process overview for slice-selection is described in **figure 3.1.2**.

$$\Delta\omega = \gamma(G_{SS}\Delta z) \textbf{(Equation 3.1.3)}$$

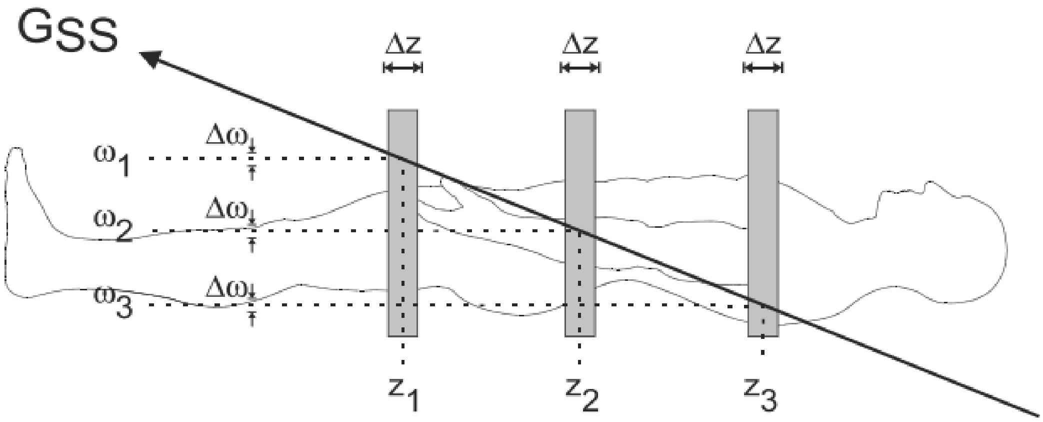

Figure 3.1.2: The slice selection process involves the G_{SS}. The total magnetic field experienced by the proton and its corresponding frequency are dependent on its position based in ***equation 3.1.2****. The tissues located at z_i will absorb the rf pulse energy, whilst it's broadcasting a varying central frequency (ω_i). Therefore, each position will have a unique associated resonant frequency. Both G_{SS} and $\Delta\omega$ can heavily influence the Δz. Adopted from [13].*

For a perfect slice profile, it necessitates an infinite pulse duration. This is to prevent the effects of truncating for the rf-excitation pulse or sinc-pulse. A conventional rf-pulse duration to prevent such an effect is around 40 ms. An rf-pulse duration around 8 ms will substantially deteriorate the slice profile. To counteract the longer experiment time, the gradient strength can be increased because this can reduce the pulse duration by a factor of "n" for the same slice profile and Δz. It is also possible to reduce the duration of the rf-pulse using amplitude and phase modulation or shaped rf-pulses [127].

Read-out gradient (G_{RO})

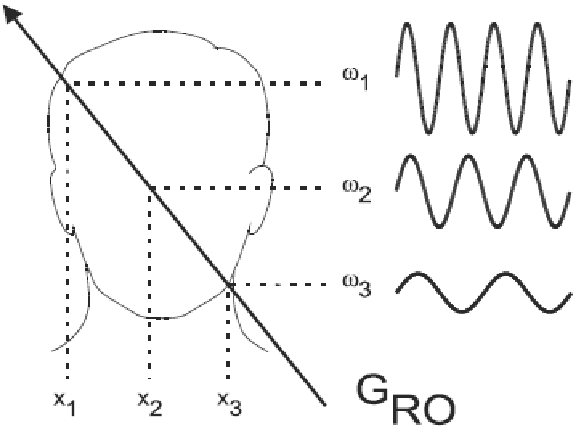

Figure 3.1.3: Readout process. After excitation, the proton spins precess in a uniform manner within the selected slice volume. When the echo is detected, G_{RO} is applied, and the proton spin frequencies become asynchronous, thus generating the echo signal. The ω_i for each proton depends on its position as stated in ***equation 3.1.1*** *and* ***equation 3.1.2****. Frequencies measured from the echo are marked to the corresponding position [13].*

When G_{RO} is applied during the signal acquisition, the frequencies along the x-axis are changed spatially. Typically, the MR signal is detected when the G_{RO} is present, as it produces one of the two visual dimensions of the image on the film when a 90° slice-selective pulse excites the chosen slice region. It is quickly followed by the net magnetization to rotate to the transverse plane, perpendicular to B_0 and precessing at ω_L. T_2^* induces dephasing for M_{xy}, which can be rephased using the 180° rf pulse, gradient pulse, or both. During the echo formation as a result of the rephasing, G_{RO} is applied perpendicular to the slice selection. Consequently, the proton spins will begin to precess asynchronously as determined by **equation 3.1.2**. The varying frequencies are superimposed into the echo before the echo is measured by the receiver coil and digitized for creating the FID. The readout process is visualized in **figure 3.1.3** [127].

G_{RO}'s magnitude and frequency can be detected, which allows for the position of the proton spins to be determined. In addition, the two parameters that determines the magnitude for G_{RO} are: (1) Field of view; FOV_{RO} and (2)Nyquist frequency; ω_{NQ}. This relationship of G_{RO} with the two parameters are defined in **equation 3.4**, where $\Delta\omega_{RO}$ is the total range of frequencies in the image. ω_{NQ} is mathematically defined in **equation 3.5** [13].

$$\Delta\omega_{RO} = 2 * \omega_{RQ} = \gamma(\Delta G_{RO} * FOV_{RO}) \text{ (\textbf{Equation 3.1.4})}$$

$$\omega_{NQ} = \frac{(Total\ number\ of\ data\ points)}{2} * Sampling\ time \text{ (\textbf{Equation 3.1.5})}$$

The proton spins must be positioned at the edge of FOV_{RO} for G_{RO} to precess at ω_L. ω_L can range from 500-500 000 Hz in MR, which are dictated by the number of data points and sampling time. Prior to digitization, frequencies that are higher than the Nyquist limit from the signal are filtered using a low-pass filter. The filtered signal is considered noise, so it can improve the signal-to-noise ratio (S/N). Moreover, it can be improved by increasing the sampling time to match the Nyquist frequency and low-pass filter width. By increasing G_{RO}, the smaller FOV_{RO} becomes. Its mathematical definition is described in **equation 3.1.6.** Maintaining the Nyquist frequency and the total frequency bandwidth. Resolution is vital in MR imaging, and it can be expressed in several ways, namely spatial resolution, or frequency resolution. The spatial resolution of the readout gradient (VOX_{RO}) is expressed as the voxel size[mm/pixel]. This is derived from FOV_{RO} and the number of readout sample points in the acquisition matrix, N_{RO} [13].

$$VOX_{RO} = FOV_{RO}/N_{RO}$$ (**Equation 3.1.6**)

On the other hand, the frequency resolution [Hz/pixel] is based on N_{RO} and the total bandwidth $\Delta\omega_{RO}$. This is defined in **equation 3.1.7.** By improving the total sampling time, the frequency resolution can be improved independent of the spatial resolution. This is because it reduces the Nyquist frequency for the image and the background noise. Moreover, by decreasing G_{RO}, the correct spatial resolution can be maintained with respect to **equation 3.1.4**. **Figure 3.1.4** describes the two resolution parameters and how they are affected by the Nyquist frequency and FOV [13].

$$Pixel\ bandwidth = \frac{\omega_{RO}}{N_{RO}} = 2 * \omega_{NQ}/N_{RO}$$ (**Equation 3.1.7**)

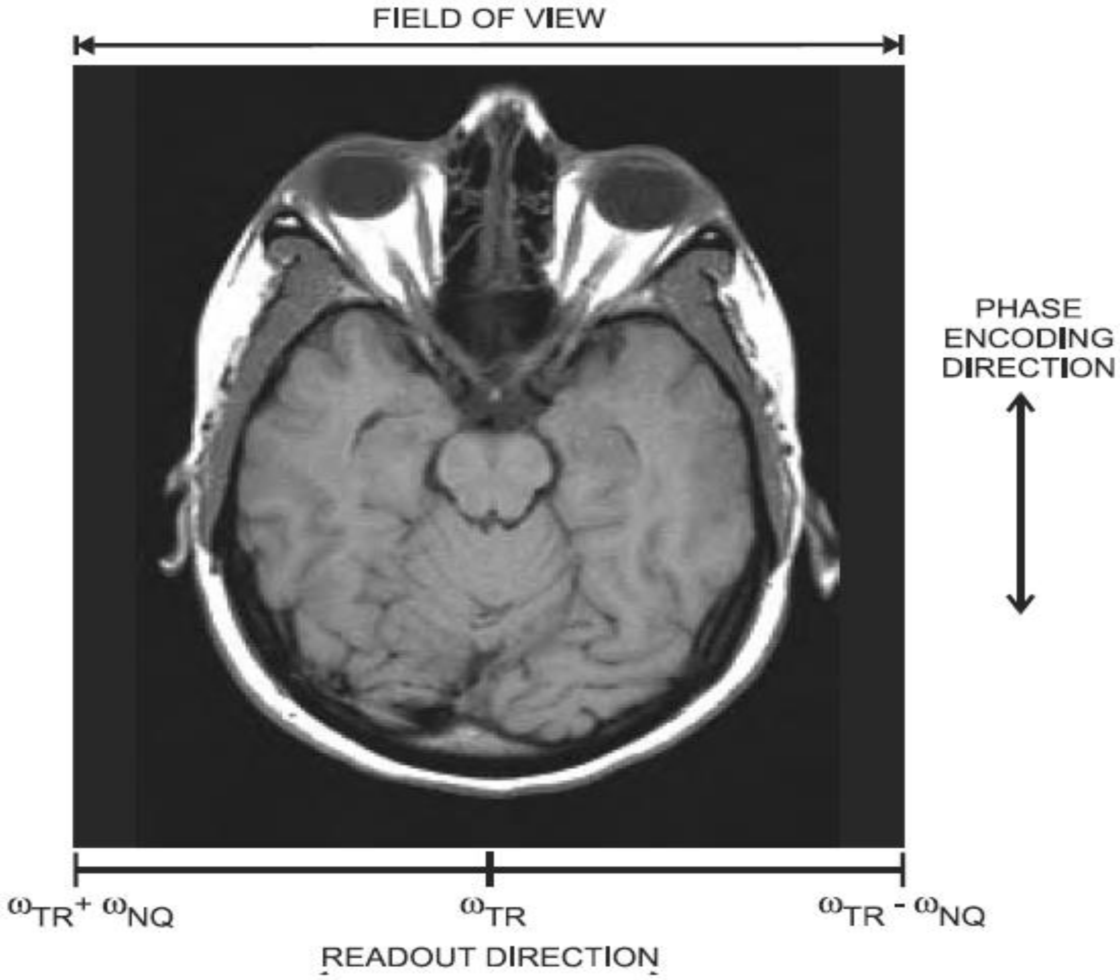

Figure 3.1.4: The readout direction and phase encoding direction are placed on the x-axis and y-axis respectively. By placing a proton spin at the edge of the FOV in the readout direction, the proton spin will precess with accordance to ω_{NQ} above or below the transmitter frequency ω_{TR}. By changing the FOV, the image spatial resolution [mm/pixel] will change, but the frequency resolution [Hz/pixel] will not be affected [13].

Phase-encoding gradient (G_{PE})

The magnetization of G_{PE} and its measured frequency allows the position of the proton to be determined. G_{PE} is positioned perpendicular to both G_{RO} and G_{SS}, and G_{PE} is the only gradient that can change the amplitude during a recording of a 2D image sequence. On the other hand, when G_{PE} is applied, the frequencies along the y-axis are changed spatially, but it is applied before the signal acquisition in contrast to the read-out process via G_{RO}. Before the application of G_{PE}, a proton in the slice region precesses at the base frequency ω_0. However, the application of G_{PE} will change the precessional frequency and cause it to either increase or decrease with accordance to **equation 3.1.2**. Silencing the G_{PE} will cause the proton spins to return to its original frequency, but the proton spins will have an asynchronous manner. Some spins will be ahead or behind in phase relative to the previous state. The magnitude, duration of G_{PE} and the proton spin location will determine the amount of induced phase shift. Protons located at different positions in the phase encoding direction experience different magnitudes of phase shift for the same G_{PE} pulse. The concept is visualized in **figure 3.1.5**, whilst **figure 3.1.6** highlights the process [13].

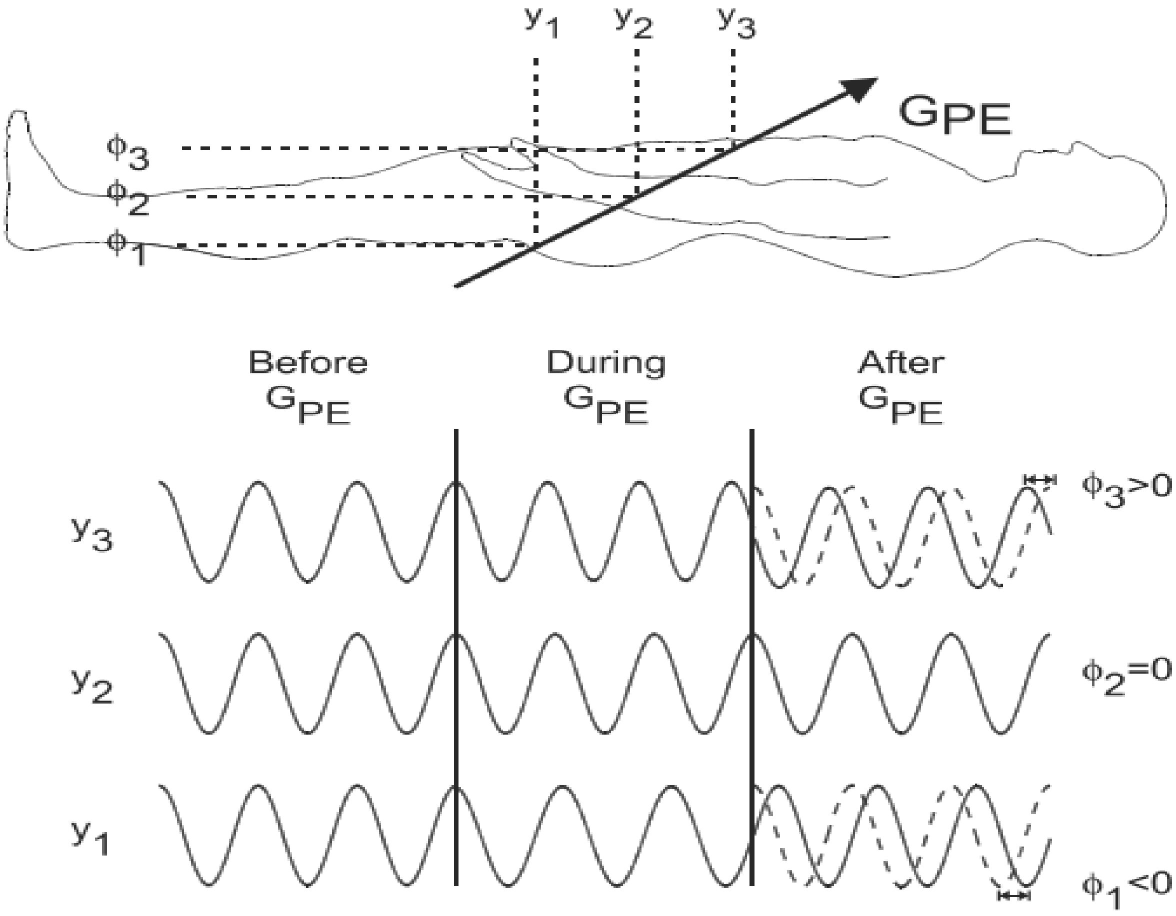

Figure 3.1.5: Phase encoding concept. All the proton spins precess at a uniform frequency prior to the presence of G_{PE}. Only when G_{PE} is applied is when the proton spin precessional frequency will either increase or decrease, which again depend on its position, y_i. Notice how $y_2=0$, and it experiences no effect from G_{PE}, thus experience no change in frequency or phase ($\emptyset_2 = 0$). A proton at y_3 precesses faster while G_{PE} is applied. Turning off G_{PE} will cause the proton spins to precess at its original frequency, but it will be ahead of the reference frequency. The reference frequency is represented by the dashed curve, and the phase shift $\emptyset_3$ is induced in the proton spin by G_{PE}. On the other hand, a proton located at y_1 will experience a decrease in its frequency while G_{PE} is applied. Only when G_{PE} is turned off is when it precesses at its original frequency, but the difference being that the proton spins will precess behind the reference by a phase shift of $\emptyset_1$ [13].

The maximum amount of phase shift for a proton spin is experienced at the edge of the FOV in each phase encoding step. The MR image is formed by repeating slice excitation and signal detection multiple times, but each slice has a different amplitude of G_{PE}. Moreover, the 2nd Fourier transformation in the image converts the signal amplitude at each readout frequency from a function of G_{PE} to a function of phase [13].

When it comes to spatial resolution in the phase-encoding direction, it depends on 2 parameters, which are given in **equation 3.1.8.** The first parameter is filed of view in the phase encoding direction FOV_{PE}. The second parameter is the number of phase encoding steps in the acquisition matrix, N_{PE}. In order to determine the FOV_{PE}, G_{PE} has to be changed from one step to the next. With reference to **figure 3.1.6**, one can observe that a proton located at a chosen FOV_{PE}, each phase-encoding step induces one-half cycle (180°) of phase change relative to the previous phase encoding step. This is possible only if the assumption of constant pulse duration is satisfied. Moreover, the N_{PE} determines the total number of cycles of phase change produced at the edge of the FOV. This in turn determines the ω_{NQ} in the phase encoding direction for a given pulse duration. With that in mind, the spatial resolution [mm/pixel] in the phase-encoding direction is defined [13]:

$$VOX_{PE} = FOV_{PE}/N_{PE} \text{(\textbf{Equation 3.1.8})}$$

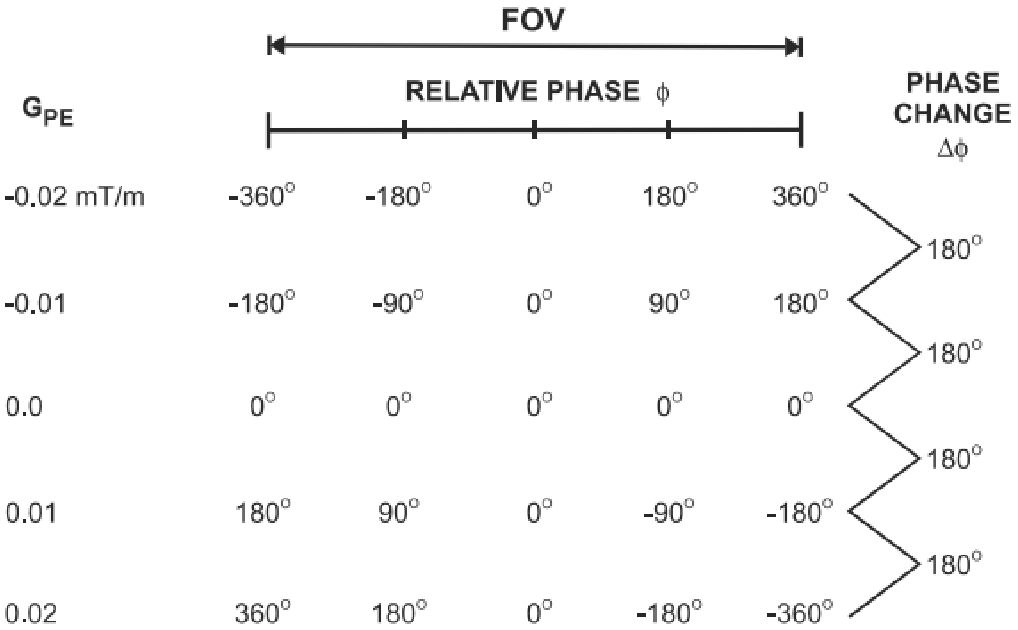

Figure 3.1.6: Phase encoding process. A proton at the edge of the FOV in the phase-encoding direction will undergo phase change Δ∅ after a 90°rf pulse from one step to the next. Every point in the FOV will gradually receive less phase change for the same gradient amplitude. The center proton spin will never experience phase change. In addition, the change in gradient amplitude from one phase-encoding step to the next will be dependent on the particular FOV chosen [13].

By reducing the FOV_{PE} and increasing N_{PE}, the resolution can be improved. To reduce the FOV, the gradient amplitude changes from one G_{PE} to the next needs to be increased. It is also worth noting that the FOV in the phase-encoding direction is not strictly to be identical or similar as the FOV in the readout direction. This also applies for the voxel size [13].

(3.2) Raw data, image data matrices and spatial encoding in k-space

In MRI, there are two formats of data: (1) Raw data and (2) Image data. In a raw data matrix, the amplitude of the detected signals for a given echo correspond to a unique row. Each row differs in its value of G_{PE} that is applied prior to detection. Moreover, the rows are usually displayed in order of increasing phase-encoding amplitudes from the top to bottom. As a result of this, it corresponds to maximum negative and maximum positive amplitudes. It can be described that the raw data matrix is a grid of points with a similar directional pattern as **figure 3.2.1**, where the readout direction is on the horizontal direction and the phase encoding direction is positioned at the vertical direction. Their respective dimensions depend on N_{RO} and N_{PE} as shown in **equation 3.1.6** and **equation 3.1.8** respectively [13].

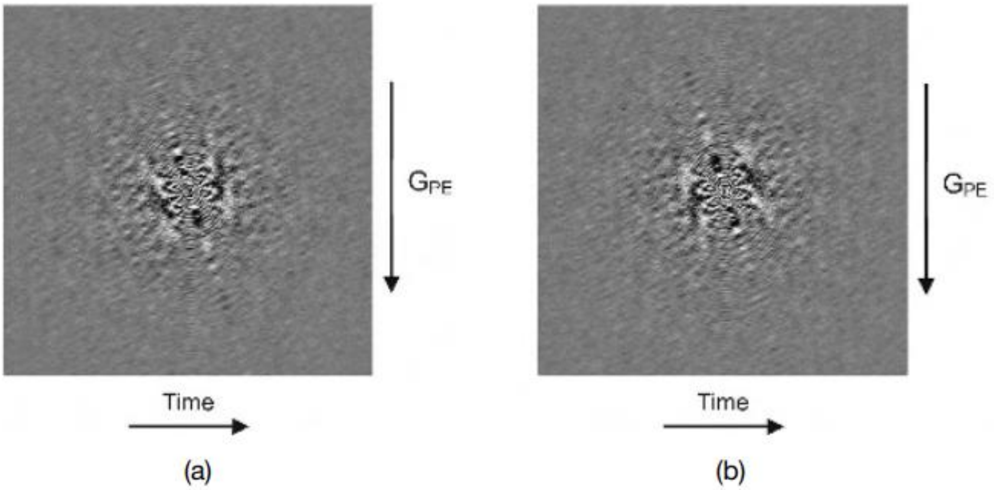

Figure 3.2.1: Examples of raw rata imaging, where (a) is real and (b) is imaginary. The dimensions for the images are $N_{PE} \times N_{RO}$*, and each row is measured with a unique signal at a specific* G_{PE}*. The number of rows corresponds to* N_{PE}*. Signals with a high negative amplitude* G_{PE} *are displayed at the top, and the low amplitude* G_{PE} *are placed in the middle. However, the high positive amplitude* G_{PE} *is positioned at the bottom of the matrix. Each column represents a data point sampled at a different time following a rf pulse excitation [13].*

The second data format is image data or also known as display matrix. It is created when the complex raw data matrix undergoes a 2D Fourier transformation for both the rows and columns. The image matrix is a complex frequency and phase map of the proton signal intensity from a volume element. This volume element is namely weighted by T_1 and T_2 values of the tissues that are within the slice-selected volume. In addition, the specific frequencies and phase are distinct to the location of the volume element, and they are measured with respective to the base transmitter frequency.

Once the slice has been selected by G_{SS}, and the image is spatially encoded by localizing the ^1H signals via G_{RO} and G_{PE}. The two latter gradients are used to differentiate the signals using k-space [13, 127]. K-space is a data matrix where the MR data is stored before it is processed, and the Fourier transformation application can provide a final reconstructed image [138-139]. The k-space represents the spatial frequency information in 2D or 3D of an object, and it is defined by the space covered by the phase and frequency encoding data [140]. The k-space for both G_{RO} and G_{PE} are defined in **equation 3.2.1** and **equation 3.2.1,** respectively [137,141-142]. Each k_x and k_y data point corresponds to the echo signal amplitude influenced by G_{RO} and G_{PE} respectively. In the equations below, G_{RO} or G_{PE} is the maximum strength of the magnetic field gradient, t is the cumulative time for an active gradient and γ=2.675×10^8 rad s^{-1} T^{-1} for ^{1}H. [4, 45].

$$k_x = \frac{\gamma}{2\pi}\int_0^t G_{RO}(t)dt$$ (**Equation 3.2.1**)

$$k_y = \frac{\gamma}{2\pi}\int_0^t G_{PE}(t)dt$$ (**Equation 3.2.2**)

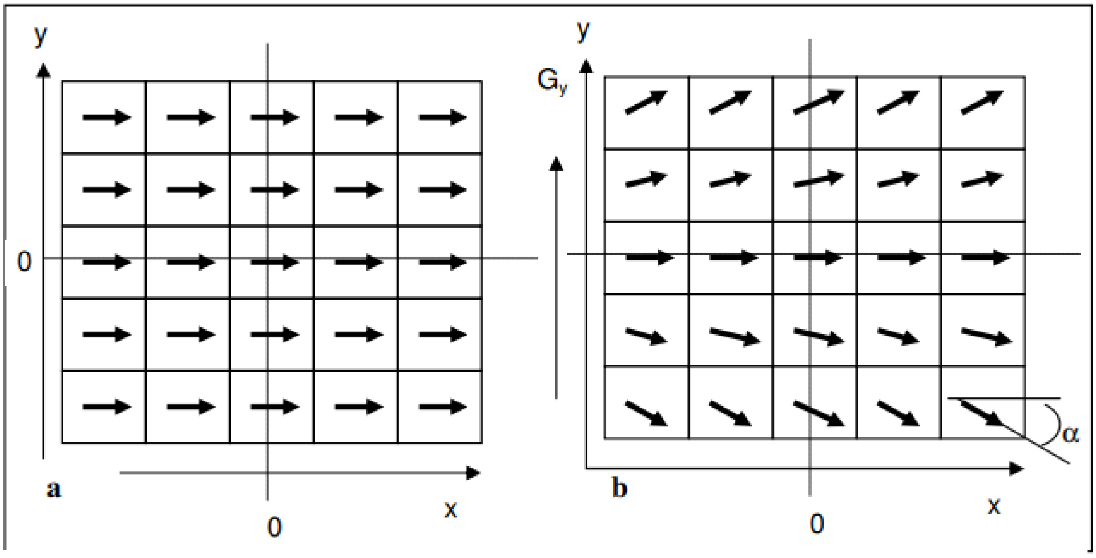

Figure 3.2.2 : k-space showing the phase angle of the transverse magnetization vector before(a) and after(b) the implementing the magnetic field gradient in the y-direction .Adopted from [127]

Combining both the k-spaces for G_{RO} and G_{PE} provide the foundation for the application of the 2D Fourier transform, in which the signal of the 2D image is defined in **equation 3.2.3**, where S(t) is the FID signal received by the coil. **Figure 3.2.2** shows an example on how k-sapce changes when a phase angle is applied due to a transverse magnetization vector. The spins experience a shift, thus move at different positions in the k-space [4, 134,137,140-142],
[4, 45, 134 142-145].

$$S(t)(k_x, k_y) = \iint m\,(x, y)e^{-2i\pi[k_x x + k_y y]}dxdy$$ (**Equation 3.2.3**)

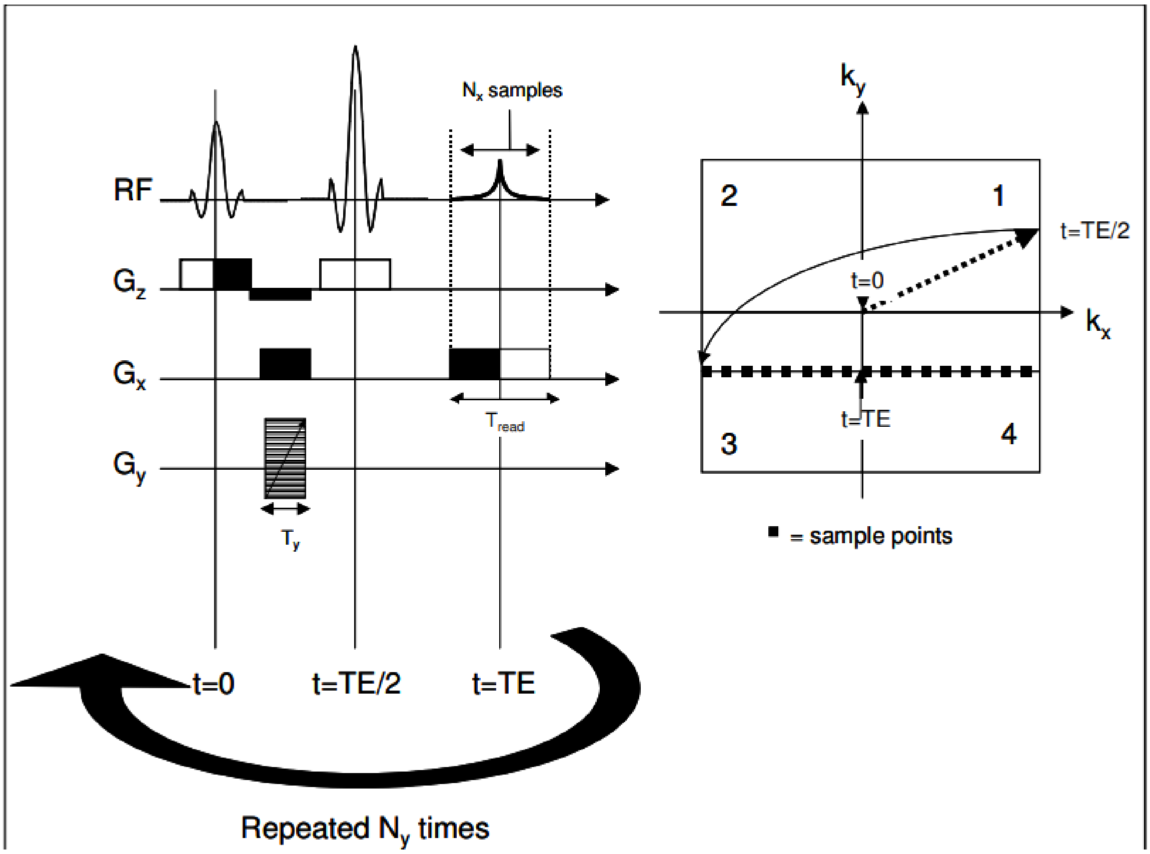

Figure 3.2.3: Spin echo sequence with its k-space trajectory for the RO k-space line. Adopted from [127].

Take the spin echo sequence in **figure 3.2.3** as an example on how the signals from the rf pulse can be spatially encoded in the k-space. Recalling from the NMR section, the 180° rf pulse refocuses the signal and removes the inhomogeneities in T_2. The signal echo is generated by a 2^{nd} RF pulse rather than by switching the polarity of the read-out gradient, which allows a complete k_x-line to be sampled in each T_R or time interval between each 90° rf-pulse. The k-space sequence follows [4, 127]:

1. Both k_x and k_y are both equal to zero, meaning they begin at the center origin of the space.
2. G_x or G_{RO} is applied around k_x, which causes the position to move to $k_{x,max}$ at the 1^{st} quadrant of the space.
3. The k_y value is increased by applying a positive G_y or G_{PE}.
4. A 180 ° rf-pulse is applied after the implementation of G_{PE}, and the position then changes from the 1^{st} quadrant at $k_{x,max}$ and k_y to to $-k_{x,max}$ and $-k_y$ at the 3^{rd} quadrant
5. The line is sampled using G_{RO} along k_x until the k-space is fully covered. Note that G_{PE} is varied steplike manner, which makes it possible to garner information from the entire

k-space during the various repetitions. Once the sampling of k_x at this step is done, the position returns back to $k_{t=}$0 and k_y=0

6. Afterwards, the position either increase or decreases depending on the applied G_y or G_{PE}.

Separation between points in k-space is proportional to the inverse of the Field of View (FOV) in image space, where it is defined in **equation 3.2.4**, where the i is defined as the spatial dimension of x or y. The higher the distance between sampled points in k-space are, the lower the FOV of the resultant image becomes. A sufficient FOV is required in order to ensure ample coverage of the object Moreover, **equation 3.2.5** defines the spatial resolution (Δi) with respect the direction of i [4,45,137, 140-142]

$$\Delta k_i = \left(\frac{1}{FOV_i}\right) \textbf{ (Equation 3.2.4)}$$

$$\Delta i = \frac{1}{2k_{i,max}} \textbf{ (Equation 3.2.5)}$$

An MRI image is composed pixels and voxels, where the pixel intensity is proportional to the number of protons present in the voxel [115]. The voxel dimensions in the resultant image become smaller as the coverage of k-space increases further out from the center. Higher resolution image requires more data samples, which requires longer scan time. Moreover, low spatial frequencies or low amplitude G_{PE} are represented by the center of k-space, and define most of the image contrast, but lack edges or information on small objects. With this in mind, the maximum signal content is located at the central part of the raw data matrix. The variations observed in the signal amplitudes are primarily due to the differences in the inherent tissue signals. These differences are essential to create the contrast in the image. On the other hand, the outer most part of the raw data matrix have a relatively low signal amplitude. This leads to low signal amplitudes that could only be possible if there is a high positive or negative amplitude G_{PE}, so the periphery of k-space contains high spatial frequency information, which provides sharp edges in images [13, 45, 127, 134, 142, 144, 145].

(3.3)Localized spectroscopy

Recalling the effects of magnetic field gradients, they can be used to selectively excite in tandem with gradient pulses for the Volume of Interest (VOI) in the sample to localize the rf energy [4, 13]. Localization techniques can be separated into two categories, namely (1) Single voxel techniques and (2) Multiple voxel techniques. The focus for this project will be solely on single voxel techniques or SVS.

Single voxel techniques (SVS)

Single voxel techniques or SVS for short, are used to acquire spectra from a single small volume of tissue. The most orthodox approach for SVS is to excite the desire tissue volume exclusively via the intersection of three slice-selective rf excitation pulses. With this in mind, there are two rf pulse schemes that come into the picture. The first scheme is Point Resolved Spectroscopy (PRESS). PRESS's pulse sequence is shown in **figure 3.3.1**, where the water is supressed by a CHESS rf pulse or "Chemical Shift Selective" pulse. This SVS technique utilizes a 90° rf pulse, which is followed by two sequential 180° rf pulses. It can be similarly compared to a standard multiecho sequence. A key observation to note here is that each rf pulse has a distinct associated physical gradient as the slice selection gradient. Due to this nature, only the protons located at the intersection of all three pulses will produce the spin echo at the desired echo time TE [13].

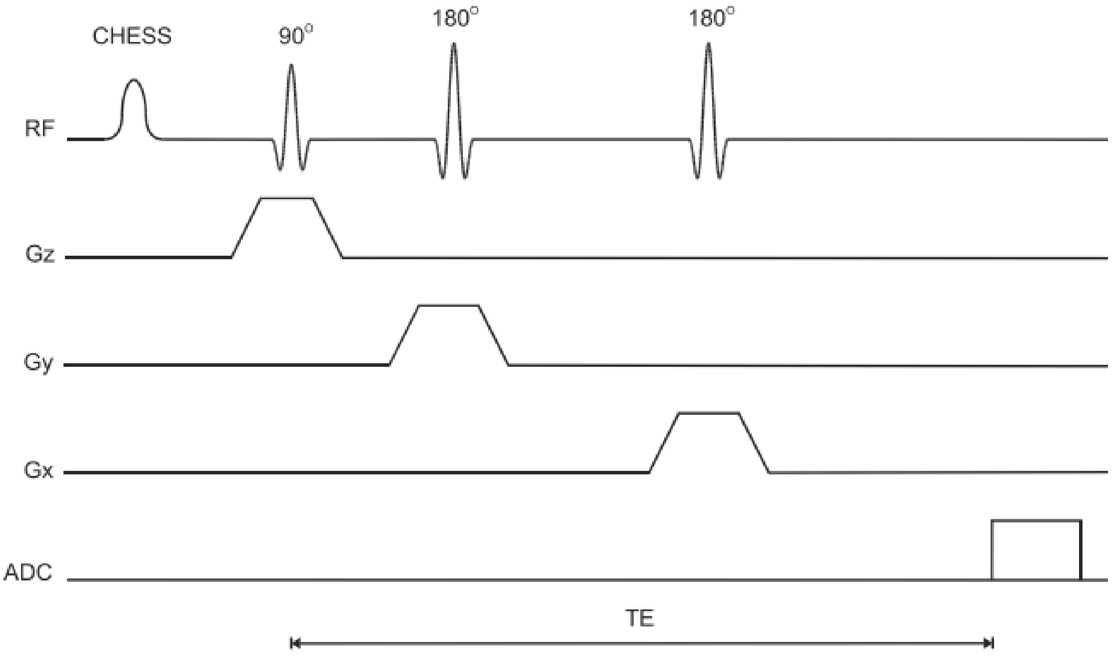

Figure 3.3.1: PRESS pulse sequence timing diagram. The water is supressed by the CHESS rf pulse [13].

Subsequently, the second scheme is referred to as Stimulated Echo Acquisition Method (STEAM). Unlike PRESS, STEAM uses three sequential 90° rf pulses with a different slice selection gradient. This is visualized in **figure 3.3.2**. Likewise, the stimulated echo is produced by the proton spins located at the intersection of the pulses. With these two schemes in mind, there are several key differences between the two localizing techniques. First and foremost, the entire net magnetization from the voxel is refocused by 2 180° rf pulses to refocus and produce the echo signal in PRESS. However, in STEAM, a maximum of ½ of the entire net magnetization generates the stimulated echo, and it does not have a 180° refocusing rf pulse. Apart from this, the S/N ratio of PRESS is substantially larger than its STEAM counterpart when the scan parameters are equivalent with each other. STEAM allows for shorter TE values, which reduce signal losses from T_2. This makes it ideal for analyzing metabolites with a short T_2 value [13].

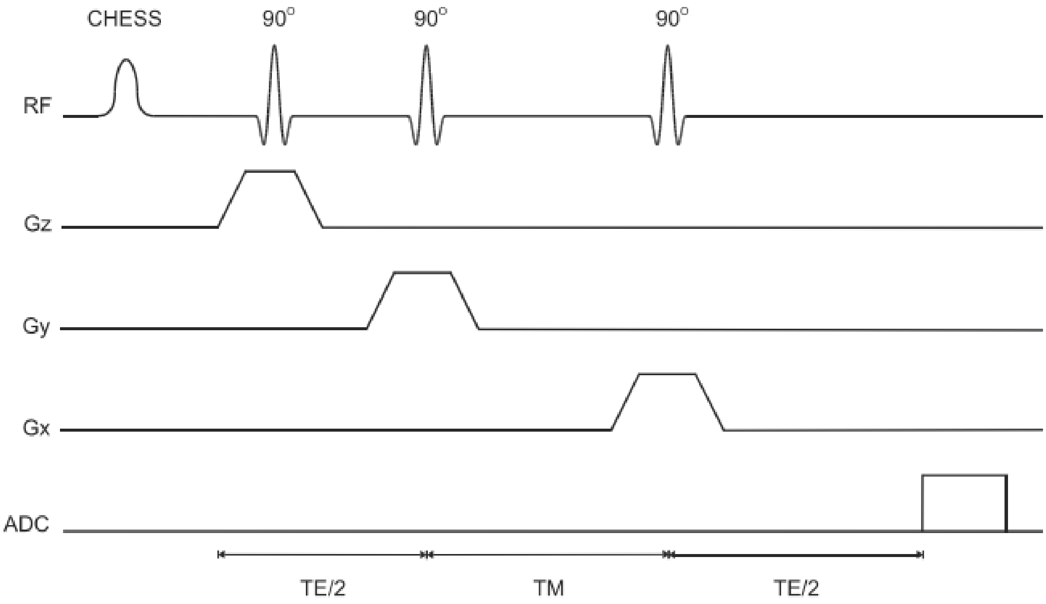

Figure 3.3.2: STEAM pulse sequence timing diagram. Similar to ***figure 3.3.1****, a CHESS rf pulse is used to supress the water signal [13].*

(3.4) Diffusion in MRI and hydrogels

There are two types of movement commonly found in tissues. The first type of movement is referred to as coherent bulk flow. This type of flow occurs when blood or cerebrospinal fluid (CSF) experiences a difference in pressure between two locations. The second type of movement is translational motion. This type of movement occurs when there is a small displacement of the molecule in space. It is the second type of movement that will be focused on as diffusion is one of the most important aspects in biological systems. Due to the nature of the hydrogel being able to swell as a result of temperature change, diffusion will be something to consider during the monitoring process. Diffusion of molecules can occur as a result of concentration difference between two environments, with the most common example being the side of a cell membrane allowing certain compounds to exit the cell or enter the cell. When one talks about diffusion, it is important to remember that diffusion itself is thermodynamic in origin, and it is a nonequilibrium process. This nature makes cells capable of random transportation of gases and nutrients from the extracellular space into the inside part of the cell [13].

Looking into pure solutions, diffusion can be described by the diffusion coefficient D[mm^{2}s^{-1}], which gives information of the amount of material that was transferred from one location to another through the membrane. The most common way to analyze diffusion in magnetic resonance (MR) is using the Stejskal-Tanner method. This method utilizes a symmetric pair of gradient pulses that increase the amount of spin dephasing observed in a spin echo. When the spins move when the gradient pulses are active, the spins will experience unequal effects from the gradient pulses. Moreover, the spins will not rephase during the echo time TE. Consequently, this lack of rephasing will lead to signal amplitude loss from those unphased spins. **Equation 3.4.1** describes **figure 3.4.1** [13].

$$S(TE) \propto \exp\left(-\frac{TE}{T_2}\right) * \exp\left(-b * D\right) \quad (\textbf{Equation 3.4.1})$$

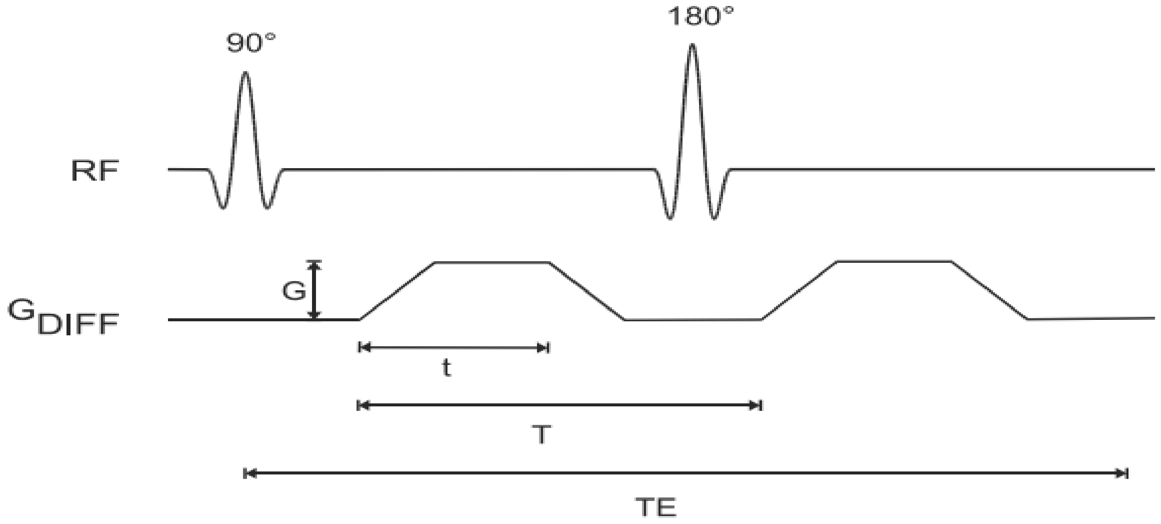

Figure 3.4.1: Stejskal-Tanner view of a spin-echo sequence with diffusion gradients (G_{Diff}), where "t" is the duration of the gradient pulse and "T" is the time between the 2 pulses. Diffusion weighting occurs when the diffusion gradient is applied. Adopted from [13].

Equation 3.4.2 defines the b-value or attenuation factor, which is the key aspect to determine the gradient strength and the diffusion coefficient by plotting $\ln\left(\frac{I}{I_0}\right)$ with b, which is defined in **equation 3.4.3**

$$b = \gamma^2 G^2 t^2 \left(T - \frac{t}{3}\right) \text{ (\textbf{Equation 3.4.2})}$$

$$\ln\left(\frac{I}{I_0}\right) = -b * D \text{ (\textbf{Equation 3.4.3})}$$

The b-value from **equation 3.4.2** can highlight the signal sensitivity to the motion. Larger b-values can be attained if the G-value is high, longer gradient pulse durations or longer times between the gradient pulses. Tissues or systems that have low D-values or diffusion have little motion, and it can experience signal loss when imaged. On the other hand, tissues with large D-values or diffusion move faster, thus create a very attenuated signal [13]. Moreover, the D-values of the desired solvent can be determined by inserting signal intensities into the Stejskal-Tanner equation in **equation 3.4.3**.

(3.5) Solvent(water) suppression

Whenever the intensity signals of the solvent are larger than the resonance of interest, it is important to consider solvent suppression. Recall how the signal intensity area in a ^{1}H NMR pulse spectrum is proportional to the number of ^{1}H nuclei that contributes to the signal. Water in metabolites have a concentration about 10 000 times larger than the metabolite of interest, which produces a large water peak that can potentially overshadow or ‘drown’ the peaks of interest from the metabolite above the background noise. A common approach to supress the water signal is to utilize a Chemical Shift Selective (CHESS) pulse as seen in PRESS and STEAM. CHESS is centered at the water resonant frequency in order to saturate the water protons. When the factor of water suppression is 100 or higher, then a single pulse is enough to supress the water signal, thus reducing signal contamination [4, 145-146] Another method to deal with the large water signal is to use deuterated solvents. However, there are several limitations. The first limitation is that some deuterated solvents cause some protons in chemical groups like -NH or -OH to exchange with deuterium ions, which will make it seem that these groups to disappear from the ^{1}H NMR spectrum. Not to mention, deuterium solvents are substantially more expensive than protonated ones, especially if the amount of solvent needed for sample preparation is large [4]. In a paper by D. I Hoult, it stated that saturating power should always be applied a long, but low power rf pulse in order to reduce the solvent signal [4, 147].

(4)Materials

All chemicals mentioned are obtained from Sigma-Aldrich. The following chemicals were used for the synthesis in the experiment:

- N-isopropylacrylamide (NIPAM,>99%)
- Ammounium persulfate(APS, BioXtra, 98%
- N,N,N,N-tetramethylethylenediamine (TEMED, 99%)
- (+)-N,N-diallytartramide (DAT, 99%),
- β-cyclodextrin (βCD,>97%) [9.5mM]
- Deuterium oxide (99.9 atom %D)
- Distilled water

(5)Methods and experiment protocols

(5.1) Synthesis of PNIPAM and βCD, and sample preparation

The synthesis of the P(NIPAM) and βCD was based on the description provided by Malgorzata Anna Wisniewska's PhD of "Characterizing mass transport in hydrogels using Nuclear Magnetic Resonance [4]." Some modifications were done as a way to directly synthesize the hydrogel in the 10mm NMR-tube.

βCD

A 25 mL 9.5 mM βCD solution was prepared. Around 0.2696 g of βCD was measured on a plastic weight plate. The βCD powder was funnelled in a 25 mL volumetric flask with an 80% D_2O and 20% distilled H_2O solvent carefully. The solution was mixed well, and the volumetric flask was exposed to hot water to assist in dissolving βCD to achieve full homogeneity.

P(NIPAM)

The hydrogel was synthesized via ***free radical polymerization.*** The monomer, NIPAM was mixed with the crosslinker, DAT, and a redox couple, APS/TEMED as the initiator. Approximately 0.3961 g of NIPAM, 0.0548 g of DAT, and 0.0182 g of APS were mixed in a glass vial together carefully. The powders were dissolved in 5mL of distilled water. Afterwards, the solution was placed in an ultrasonic bath for 10 minutes, which was followed up by a subsequent nitrogen bubbling to deoxygenate the solution. The deoxygenation was done for 5 minutes. After deoxygenation, a micropipette was used to pipette 1mL of the solution in a 10 mm NMR tube. To activate the gelation, 2.4 µL of TEMED was pipetted in the 10 mm NMR tube carefully, and let the reaction occur for 24 hours.

Note that it is important not to shake the tube vigorously, and when pipetting the TEMED, make sure that the drop of TEMED lands DIRECTLY on the solution to prevent inhomogeneity and precipitation, which was observed in some attempts. 24 hours after the hydrogel synthesis, the hydrogel was dialyzed for 7 days by removing the dialysis medium (distilled water). This was to remove the excess monomers that did not react. After 7 days of dialysis, the hydrogel was dried for 3 days at room temperature before incubating the dried hydrogel with excess 9.5 mM βCD solution as shown in **figure 5.1.1**. After the incubation, the sample was prepared for NMR analysis by pipetting an 80% D_2O and 20% distilled H_2O mixture in the 10 mm NMR tube. The moment the NMR tube was placed in the spectrometer, the starting point of the experiment($t_{initial}$) was recorded. Moreover, the sample was positioned in a way that assured that the interface between the hydrogel and release medium was at the center of the gradient and rf coils as precisely as possible.

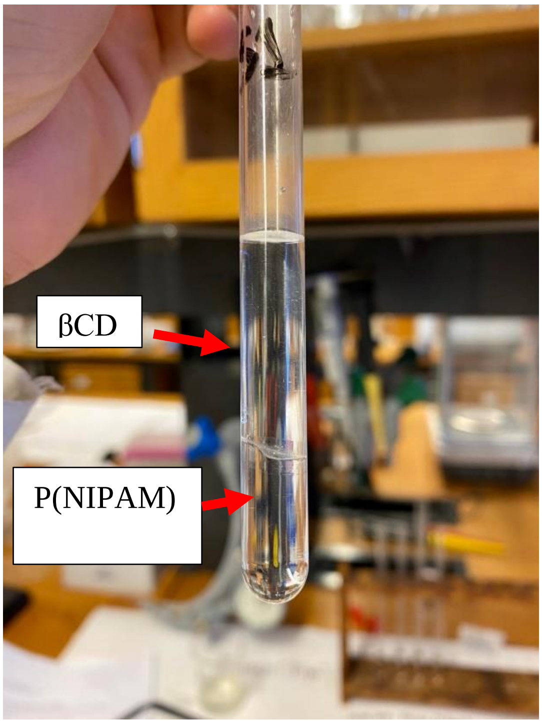

Figure 5.1.1: P(NIPAM) incubated with βCD. The interface of the gel is not perfectly flat.

(5.2) MRI and NMR temperature calibration protocols

Table 5.2.1: Overview of the temperature experiments with their respective protocols

Code	Temperature interval [°C]	Temperature nature	Duration [minutes]
40S	25-40	***Slow heating***: probe temperature increases by 1°C every 4 minutes from 25°C	210
31T	25-31	***Temperature jump***: probe temperature should begin around 31°C.	180
40T	25-40	***Temperature jump***: probe temperature should begin around 40°C.	180
40ST	25-40	***Mix of 40T and 40S**: T*he temperature starts at 25°C instead of 40°C prior to sample insertion. Once inserted, the temperature is jumped to 40°C immediately.	*240*

Identical to how the experiment was conducted in Malgorzata's PhD experiment, the experiments were done using Bruker Ascend 500 Wb MHz NMR spectrometer with a Bruker MicWB40 micro imaging probe head, and a Micro 2.5 gradient system. The temperature was controlled using the Bruker BCU20 cooling device [4]. There were 4 main experiment protocols, namely 40S(slow-heating), 31T and 40T (temperature jump), and 40ST (slow-heating and temperature jump hybrid). An overview is seen in **table 5.2.1**.

Temperature calibration to determine the probe temperature.

The temperature of the probe and the Bruker BCU20 unit's thermometer differs due to the thermocouple used by the cooling unit is positioned just below the sample tube. It is not positioned at the center of the RF-coil, where all the NMR measurements are done. Due to this, a temperature calibration curve must be made in order to account for this gap between the real temperature and the temperature shown by BCU20 device [6]. A general schematic diagram is portrayed in **figure 5.2.1** showing how the probe with the sample can have a different temperature than what the temperature control unit will say. The experiment utilized water cooling for the gradient system through a closed loop water circuit, which is operated using a water pump. This can be adjusted to increase or decrease the temperature of the flowing water.

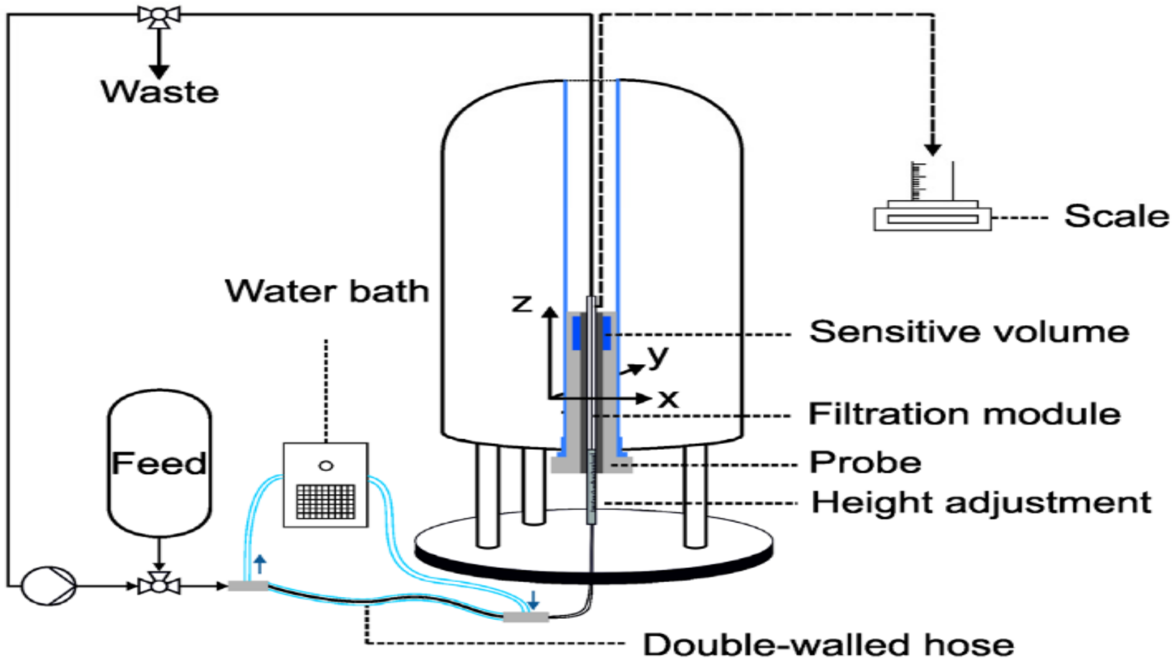

Figure 5.2.1: A schematic diagram showing how and where the thermocouple is positioned, whilst being attached to the cooling unit. The diagram shows a transfer of the cooling agents between the probe and the water cooler. Due to the travelling time between the cooler and the probe being present, the sample in the probe can have varying temperatures, and this can also be influenced by the position of the probe in the magnet [6]. This necessitates for determining the actual temperature of the probe using a standard sample. For this experiment, glycol (80 wt%) in DMSO-d_6 was used.

Glycol (80 wt%) in DMSO-d_6 was used as the nature of the experiment required a temperature higher than room temperature. The difference between the 2 chemical shifts provides the real temperature of the sample. However, the downside of such a method is that the resistance of the magnet shim coils changes slightly. When the temperature changes or increases in this case, this can affect the shimming currents, and influence the NMR line shapes of the resonances. To counteract this limitation, the reference sample can be reshimmed every time temperature was changed [179]. The protocol of temperature calibration was done as stated:

1. The temperature of the micro imaging probe was kept around 25°C for 1 hour before the sample was inserted.
2. Once the temperature was stabilized, a 5 mm NMR tube with the reference sample of glycol (80 wt%) in DMSO-d_6 was placed inside an empty 10 mm NMR tube without the cap.
3. The sample was inserted in the NMR machine and was tuned and matched accordingly using the wobble adjustment in the FLASH (Fast low angle shot) ortho protocol before running.

4. After running and dragging the FLASH ortho on the screen, the voxel (2.5mm voxel size) was placed at the center of the dragged picture to check the shimming.
5. The sample was locally shimmed before running using the STEAM protocol.
6. After running STEAM, the temperature on the Bruker BCU20 cooler was increased by 2°C. This was done for a total of 10 runs, including the 25°C basepoint reference.
7. The spectrum was loaded in Topspin, and the chemical shift difference between the CH_2 and OH singlets were determined.
8. The chemical shift difference was inserted in the NMR thermometer software and calculated the real temperature for the given run [2]. For parallel 2, every step was repeated, but the change in the temperature increased from 2°C→3°C between each run until 8 runs were obtained, including the 25°C basepoint.

Temperature-time calibration protocols for slow-heating experiments (40S)

This calibration followed the same protocol as '***temperature calibration to determine the probe temperature'*** with the exception that after obtaining the reference run, the temperature on the Bruker BCU20 cooler was increased by 1°C every 4 minutes until 40°C was reached. Two parallels were done for this calibration.

Temperature-time calibration protocols for temperature jump experiments (31T and 40T)

This calibration followed the same protocol as '***temperature calibration to determine the probe temperature'*** with the exception that the temperature of the micro imaging probe was kept around 31°C for 31T and 40°C for 40T for 1 hour before the sample was inserted. Once the sample was inserted, tuned and matched, it was locally shimmed once, and STEAM was used to record the spectra for 1 hour straight with no pause in between. Two parallels were done for this calibration. Note that one parallel for 40T was locally shimmed after every run.

Temperature-time calibration protocols for hybrid experiments (40ST)

This calibration followed the same protocol as '***temperature calibration to determine the probe temperature'*** with the exception that after obtaining the reference run, the temperature on the Bruker BCU20 cooler was increased from 25°C to 40°C directly. The 40ST protocol is referred to as the 'hybrid protocol' due to being a mix of the slow-heating experiment and the temperature jump experiment.

(5.3) MRI and NMR protocols used

The following MRI and NMR protocols were used in this specific order for:

1. Fast low angle shot (FLASH)
2. Multi-slice multi-echo (MSME)
3. Local shim cylindrical (B_0 mapping)

4. Stimulated Echo Acquisition Mode (STEAM) at various voxels (2 mm and 6 mm)
5. MEGA PRESS (0%-30%, and 50% z-gradients) [Diffusion experiment]

FLASH ortho

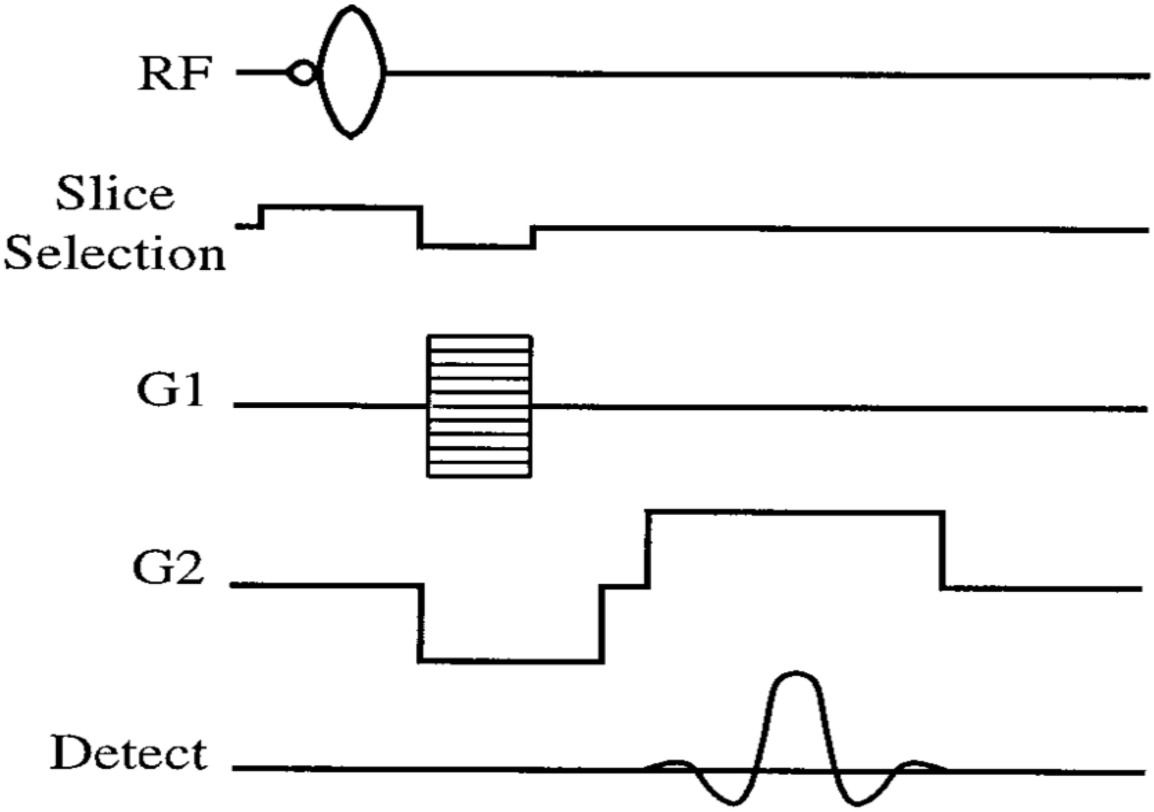

Figure 5.3.1: FLASH gradient-echo sequence [7].

FLASH uses a frequency excitation pulse with a low flip angle, which are angles lower than 90° [8]. This low angle creates an equilibrium of longitudinal magnetization. With that in mind, the FLASH sequence was used for the wobble adjustment as the sequence did not take long to run, and it removed the effects of the transverse coherence using a semi-random spoiler gradient subsequently after every echo; essentially spoiling the steady state and triggering a phase shift [9-10]. The echo sequence is shown in **figure 5.3.1**.

During the experiment, the echo time (TE) was 4 ms, whilst the repetition time (TR) was 60 ms. The average and repetition were both 1, and the sequence used an angle of 30°. The image pixel size was 128 x 128 with a field of view (FOV) of 20 x 20 mm^2. The areas of the sample with the highest concentration of hydrogen atoms were the areas of the brightest on image [10]. The sequence was only done once in each temperature experiment run to check the shimming of the sample.

MSME

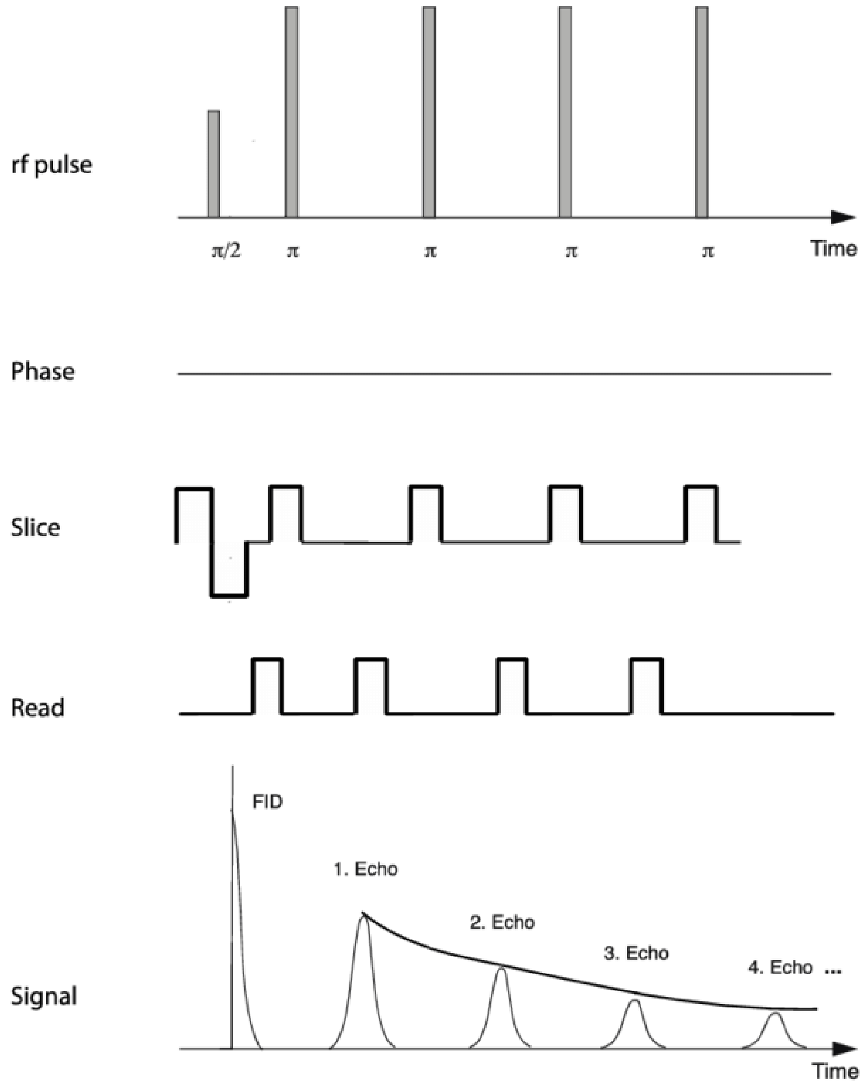

Figure 5.2.2: Pulse sequence of MSME. The read-out gradient, phase-encoding gradient, and the slice-selection gradient are superimposed on the main magnetic field(B_0) to achieve a spatial resolution. Each subsequent echo or refocusing pulse obtained after the FID are used to record the T2-relaxation times [11].

The MSME sequence was used to monitor the hydrogel's change with respect to the temperature increase. 5 sagittal slices were recorded for each run. The sequence used in the experiment had an echo time (TE) 4.50ms. The repetition time (TR) was 1000ms. The field of view (FOV) was 25 x 25 mm^2, and the slice thickness was 2 mm. In addition, the pixel size of the obtained images were 64 x 64. The echo was repeated once. The pulse sequence is shown in **figure 5.3.2**. These MSME pictures were mostly used to monitor the macroscopic change(shrinking) of the hydrogel during temperature change.

Localized shim(cylindrical) and B_0 mapping

B_0 mapping was used to calculate the B_0 variance inside the sample. The machine shimmed the desired voxel based on the B_0 mapping as the acquired phase (φ) at position "r" was proportional to the local field variation ΔB_0 and the TE. The mathematical definition for φ is provided in **equation 5.3.1** [12]:

$$\varphi\left(\underset{r}{\rightarrow}, TE\right) = \varphi_0 - \gamma \times \Delta B_0\left(\underset{r}{\rightarrow}\right) \times TE \ (\textbf{Equation 5.3.1})$$

Where:

- γ→ Gyromagnetic ratio
- φ_0→Initial phase
- ΔB_0→ Local field variation
- TE→ Echo time
- r→ Position

Any offset to φ_0 was eliminated with the multiple echo times, and the shimming followed a cylindrical pattern to match the 10 mm NMR tube.

STEAM in gel and outside the gel

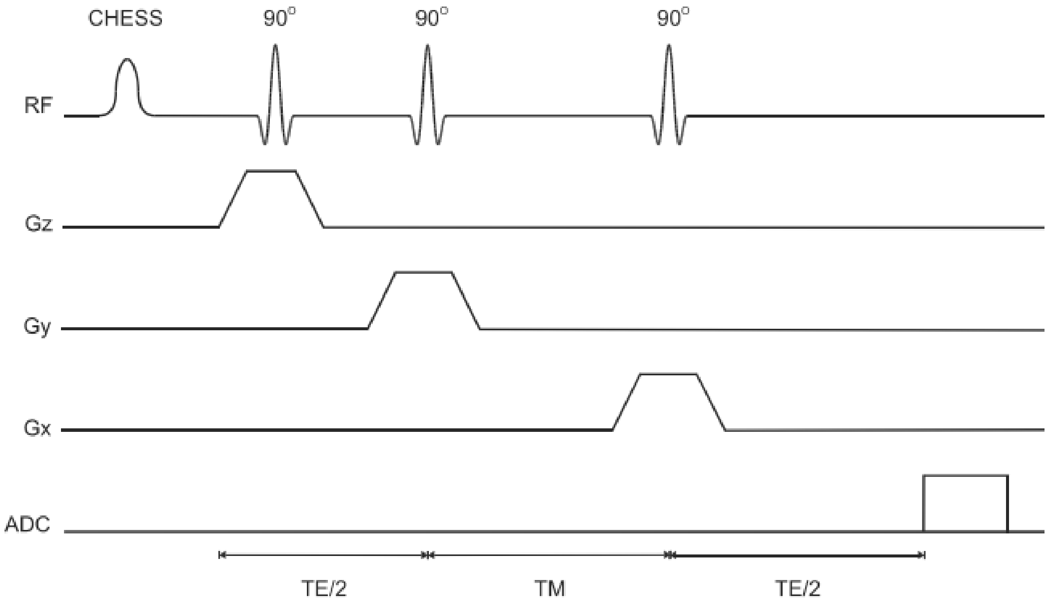

Figure 3.3.2: STEAM pulse sequence timing diagram. Similar to PRESS, and a CHESS rf pulse is used to supress the water signal [13].

The localized spectroscopy technique, STEAM was utilized to provide a spectrum of the ^{1}H chemical shifts in the middle of the hydrogel, and its description was described in **section 3.3: *MRI theory (localized spectroscopy)*** [4, 13]. During the experiment, the voxel size was 3x3x3. Subsequently, the 0mm voxel position varied due to the nature of the interface between the hydrogel and the release medium not being straight and flat all the time. At times, it had a convex interface, thus the 0mm voxel was defined at the point where the extreme points of the hydrogel met the release medium. The TE was 3ms, and the TR was 2500ms. The acquisition points were 2048, which had a bandwidth of 5498.53 Hz. The sequence was repeated once with an average of 16 scans. For water suppression, variable power and optimized relaxation delay (VAPOR) was combined with the sequence, which is a 7 CHESS pulse scheme [14]. The sequence is visualized in **figure 3.3.2**. The voxels that were positioned inside the hydrogel were always shimmed before running the STEAM sequence. However, the voxels positioned outside the gel were only shimmed once for a reference run, but the rest of the runs were not shimmed to preserve the time frame schedule of the experiment.

MEGA-PRESS [Diffusion]

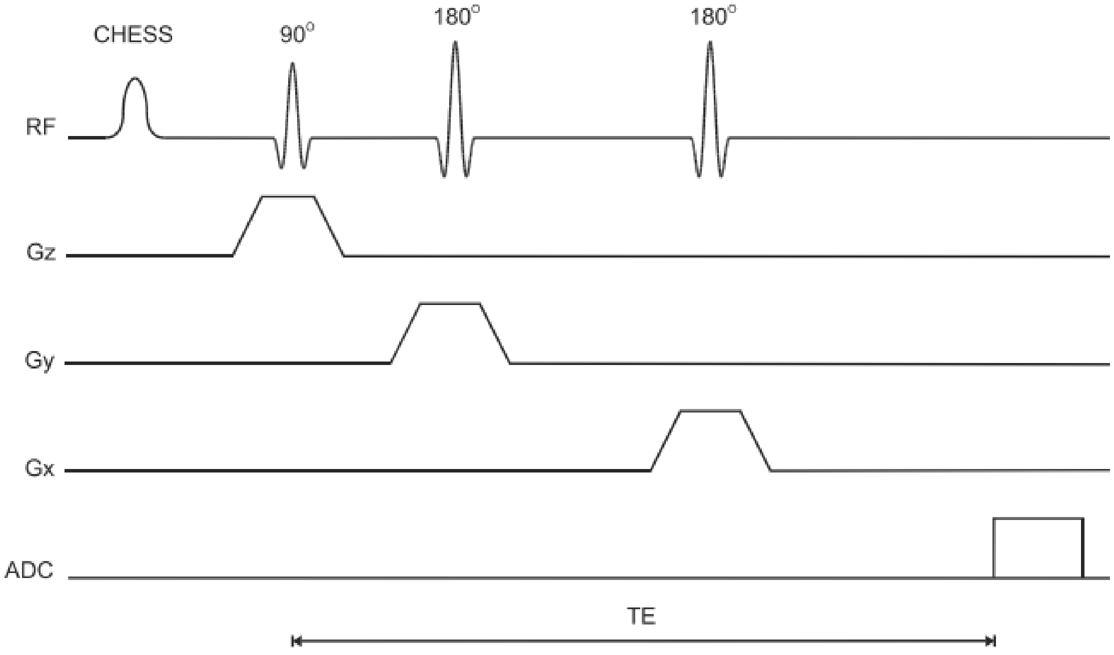

Figure 3.3.1: PRESS pulse-sequence diagram with a CHESS rf-pulse for water suppression [13].

Point resolved spectroscopy (PRESS) is similar to STEAM, and it was described in **section 3.3: *MRI theory (localized spectroscopy)***. For this experiment, PRESS was modified with MEshcher-Garwood Point RESolved SPectroscopy (MEGA), which revealed spectral peaks of interest and removed any spectral overlap. In this case, it was the βCD that was of interest [14]. MEGA-PRESS is a difference-edited technique, which uses 2 datasets. In the 1st dataset, an editing pulse was sent to selectively refocus the evolution of J-coupling, whilst in the 2nd dataset, the inversion pulse was applied somewhere else, so that the J-coupling evolved freely throughout the TE. The 2nd dataset was referred to as the non-refocused spectrum. The remaining peaks in the spectrum were not affected by the editing pulses, so the difference of the refocused spectrum from the non-refocused spectrum removed these “unwanted” peaks and kept the peaks that were affected by the editing pulses [15]. The acquisition scheme for MEGA-PRESS is shown in **figure 5.3.3**

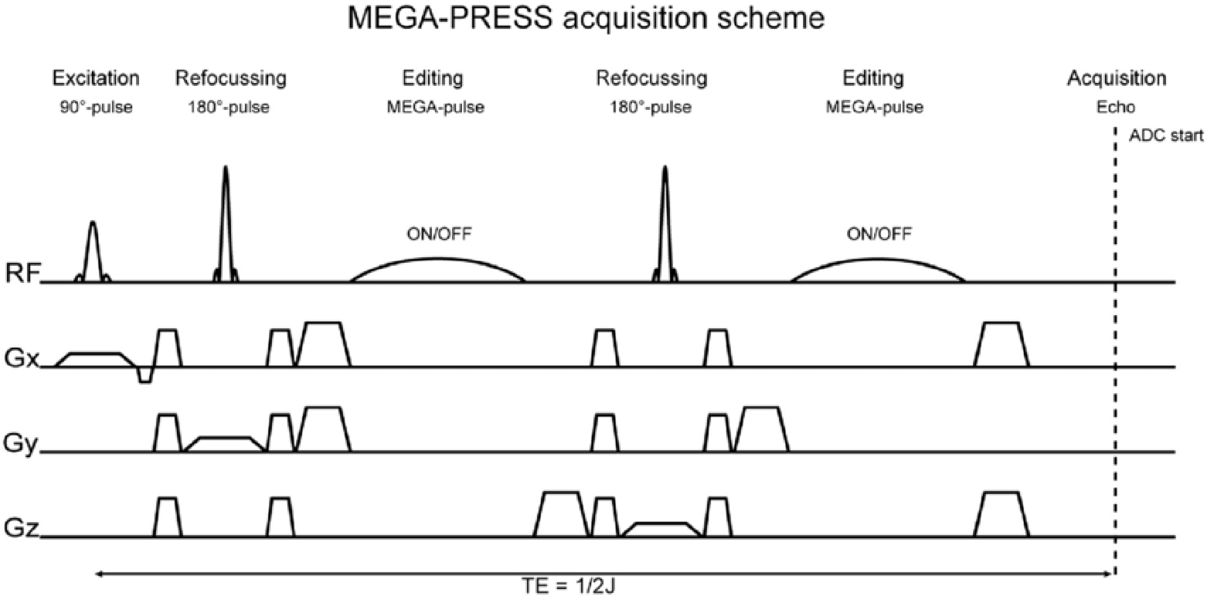

Figure 5.3.3: MEGA-PRESS sequence scheme. A PRESS localization module is extended using 2 MEGA pulses for editing water/lipid suppression at the 2nd refocusing pulse. The sequence is normally used for J-editing, but this experiment will use this sequence to determine the diffusion coefficients of the βCD in the hydrogel [16].

The TE was standardized around 68 ms with a TR of 2500 ms. The sequence averaged 16 scans with 1 repetition. The voxel size was 3 x 3 x 3 with 8192 as its acquisition point value. The acquisition bandwidth was 5498.53 Hz. The voxel that was positioned inside the hydrogel. MEGA PRESS was used 4 times each experiment run with varying gradient strengths at the z-axis, namely 0%, 20%, 30%, and 50% for the 40S, 40T, 31T, and 40ST temperature experiments. The MEGA PRESS with the 0% gradient strength was shimmed and duplicated 3 times with the last 3 aforementioned gradient strengths. This was done to observe the change of the signal intensity with respect to the b-value using MATLAB as temperature increased. The slope of the function provided the self-diffusion coefficient. The reference values for the self-diffusion coefficient of super distilled water, 80:20 D_2O/SDH_2O (super distilled H_2O) mixture, and βCD were obtained by doing the same procedure as the temperature experiments, but the difference being that instead of using 0, 20, 30, and 50 z-gradient strengths, the reference value will use 0,5,10,15,20,25, and 30 %z-gradient values. This is to make sure that there were more points for the slope calculation, as well as reducing the uncertainty and making sure the gradient strength choices for the z-axis was not too large.

(6)Data analysis

(6.1) Temperature calibration of the BCU20 unit and correlation with time

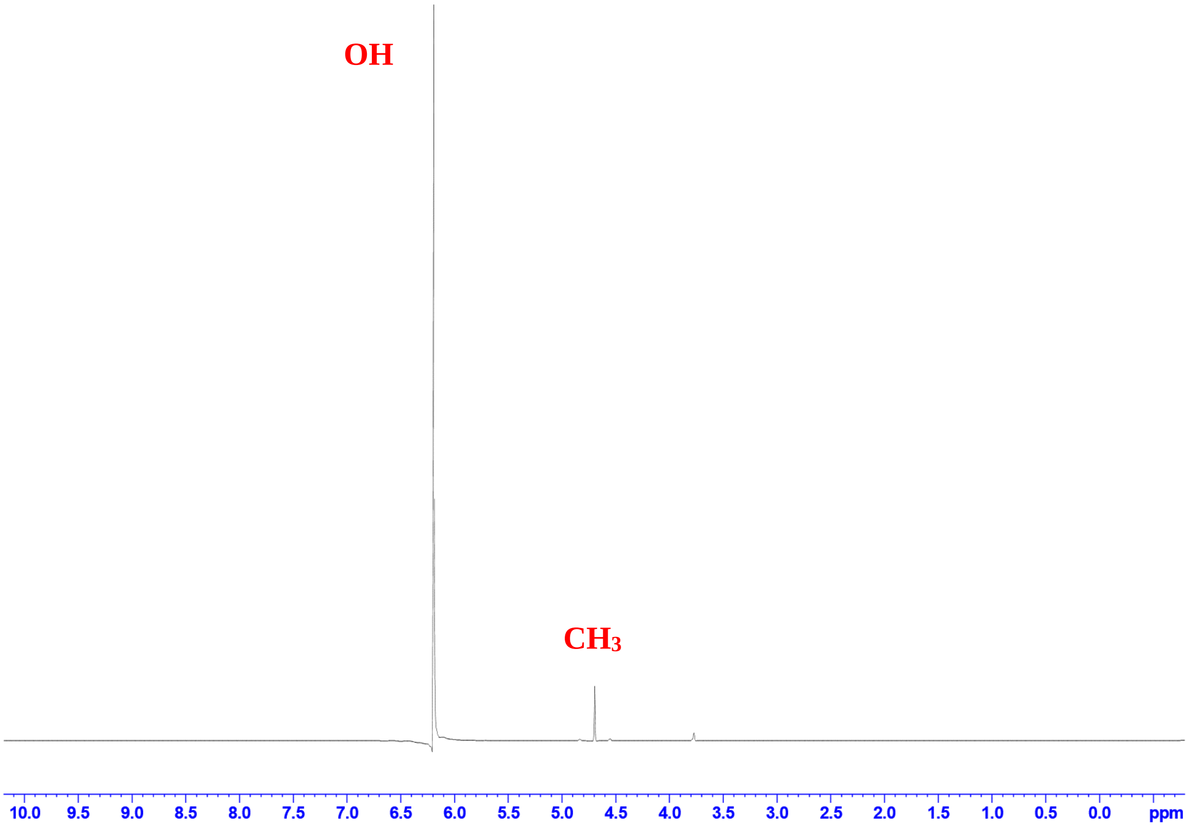

Figure 6.1.1: NMR spectrum of glycol (80 wt%) in DMSO-d_6. The OH and CH_3 peaks are highlighted in red

When calibrating the actual temperature of the probe, glycol (80 wt%) in DMSO-d_6 was used as it is able to calibrate temperatures as low as 300K and as high as 420K. This experiment's interval was between 25°C (298K) and 40°C (313K). In determining the actual temperature of the probe or "real temperature," an NMR thermometer software was used to measure the real temperature of the probe by taking the chemical shift difference between two peaks. The STEAM sequence was used for the temperature calibration, and the peaks of the glycol reference sample are visualized **figure 6.1.1,** and **figure 6.1.2** shows how the peaks were used to determine the chemical shift difference for the temperature calibration of the probe. The uncertainty for the acquired temperature from the NMR thermometer software was ±0.30K or ±0.30°C [1].

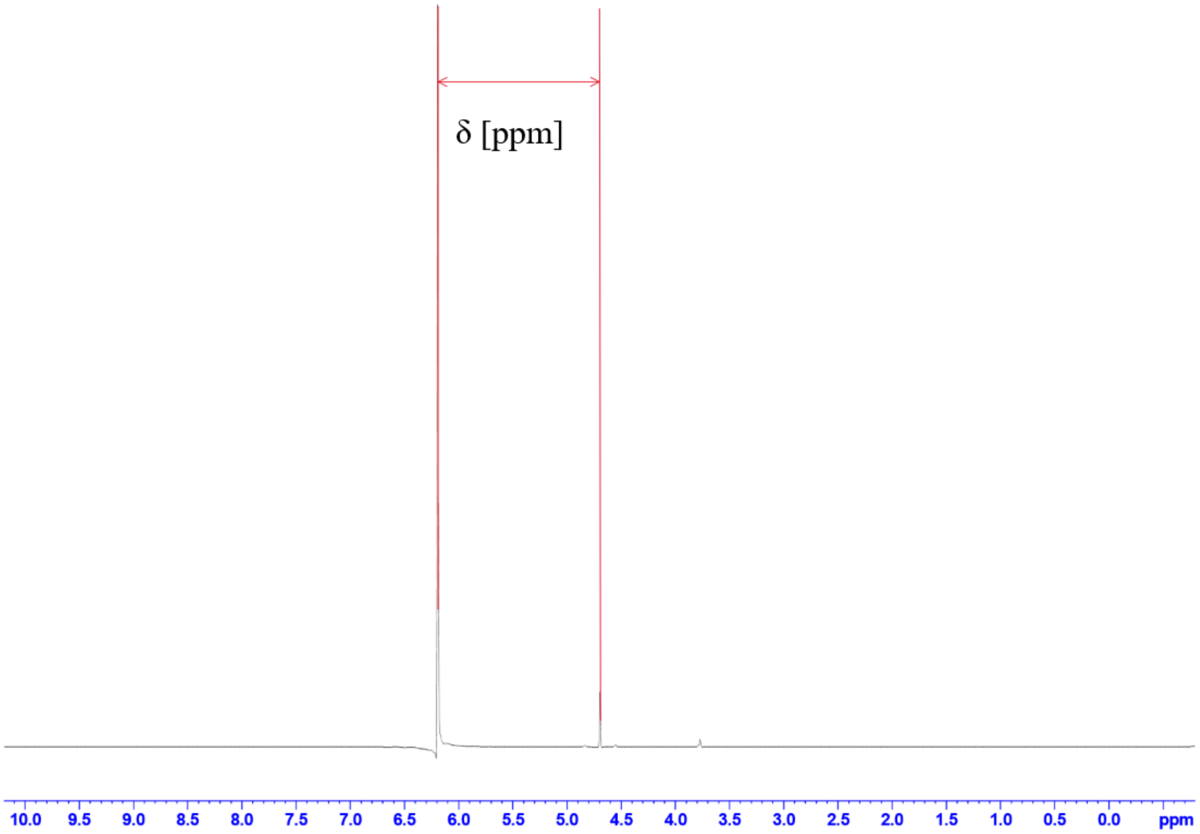

Figure 6.1.2: NMR spectrum of glycol (80 wt%) in DMSO-d₆. The chemical shift difference between the red marks is recorded and inserted in the NMR thermometer software to determine the real temperature of the sample in the probe. This value is correlated with a recorded time stamp for each run.

Moreover, the NMR thermometer software was based on the variable temperature calibration formula from BRUKER. It is represented in **equation 6.1.1**, but every calculated value using the NMR thermometer software deviated by 0.25% from **equation 6.1.1**.

$$T = \frac{(4.218 - \Delta\delta)}{0.009132} \quad \textbf{(Equation 6.1.1)}$$

Where:

- T→Real temperature of the sample [K]
- Δδ→Difference in ppm between the CH_2 and OH singlets.

This deviation was due to the calibration of the software being a compromise between that published by C. Ammann, P. Meier and A. E. Merbach "A simple multinuclear NMR thermometer" J. Magn. Reson., 46, 319-321 (1982) [3] and M. L. Kaplan, F. A. Bovey and H. N. Cheng "Simplified method of calibrating thermometric nuclear magnetic resonance standards" Anal. Chem., 47, 1703-1705 (1975) [2,5]. The deviation was not substantial, thus deemed acceptable. The recorded ‘real’ temperature points are plotted against time in minutes, and the temperature-time correlation curve was determined for 40S, 40T, 40ST and 31T. The 40S temperature-time correlation curve calibration ran for 90 minutes. On the other hand, the temperature-jump experiments (31T, 40ST, and 40T) ran for 60 minutes. 2 parallels were done for each temperature experiment, averaged, and the standard deviations were calculated for the common points from each temperature experiment. These standard deviations were placed on the average fit curve.

(6.2) Shrinking progress and voxel placement in and out of the hydrogel

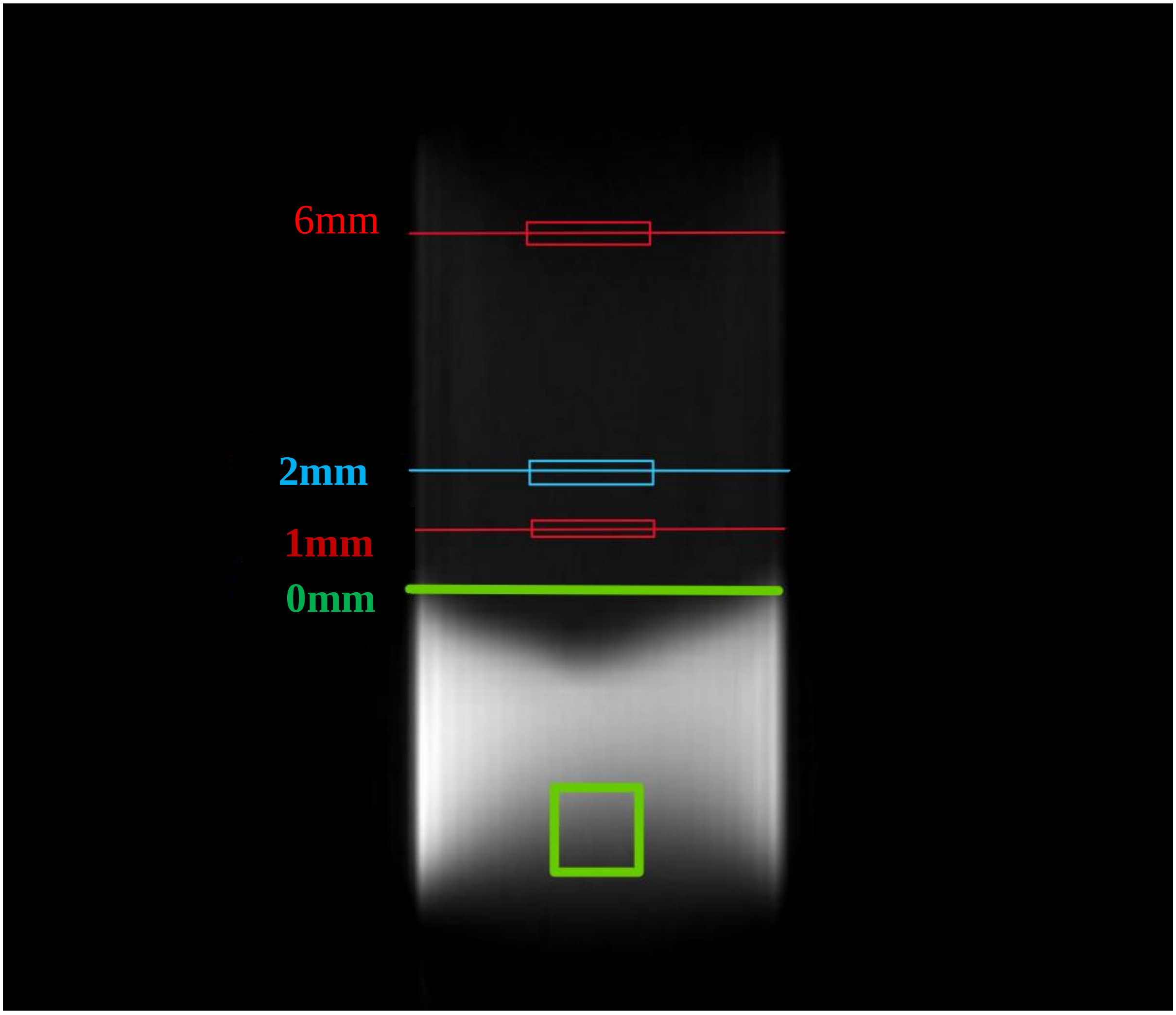

Figure 6.2.1: Visualization of the voxel placements of the gel using MSME using slice 3 from 31T's MSME as a reference. Note that the voxels are not precisely scaled in size. Their respective size parameters are mentioned in ***section 5.3(MRI and NMR protocols used)*** *as this is purely for a qualitative visualization purpose. The green square highlights the voxel inside the gel, and the green line shows where the 0 mm interface begins. The 0mm interface is placed at the center of the rf coil. The 1mm, 2mm and 6mm voxels were found by increasing the distance value with respect to the 0 mm interface. These are shaped as small rectangles, and the voxel positions are found at the center of the shape. This applies also to the voxel inside the gel (green square). For all the temperature experiments, only the 2mm and 6mm voxels were taken further for discussion, but the 0mm and 1mm voxel is shown here for visual reference.*

Figure 6.2.1 shows the placement of the voxels in the MSME picture of the hydrogel using 31T as the reference MSME. These voxel sizes were drawn on the MSME picture as a general visualization of the voxel placement and obtain a qualitative perspective on the shrinkage of the hydrogel to support the quantitative data for βCD diffusion and intensity change within and at the exterior of the gel. Their parameters were provided in **section 5.3 (MRI and NMR protocols used)**.

The green voxel in the hydrogel was placed down in the slice to account for the shrinkage that is expected to occur using STEAM and MEGA-PRESS respectively to analyze the βCD intensity change, as well as the diffusion coefficient as a function of time. The rectangular voxels outside the gel with their associated distance with respect to the 0mm interface of the hydrogel and the release medium were marked with red. For the 1mm and 6mm voxels, red was used. Blue was used to mark the 2mm voxel. When accounting for βCD diffusion onto the medium using STEAM, only the 2mm and 6mm voxels were taken further as the 1mm voxel was deemed to near the 0mm interface and 2mm voxel. None of these voxels were moved during the whole experiment to maintain the frame of reference, and their positioning from the 0mm reference is from the center of their voxel shape. For the voxel inside the hydrogel, the position of the gel voxel was uniform throughout the experiment, where it was kept at -6.5mm at its center point. This ensured that the voxel was deep at the center of the gel as much as possible to account for the expected collapse after VPTT.

(6.3) NMR spectra of P(NIPAM) and βCD in and out of the gel

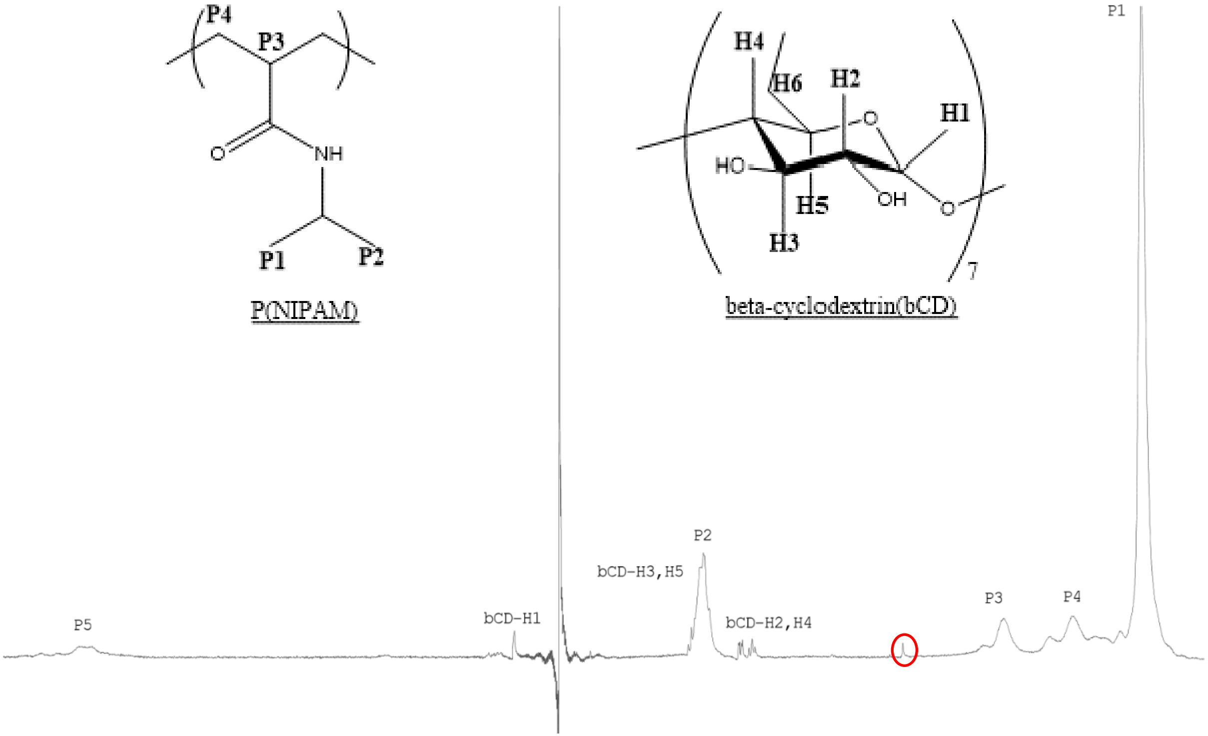

Figure 6.3.1: ^{1}H-NMR spectrum of P(NIPAM) with βCD with their respective structures. Each chemical structure has its hydrogen environments marked accordingly in the spectrum. VAPOR water suppression was used. The encircled signal is a potential monomer was not removed completely during dialysis.

For reference, the 40S STEAM experiment runs were used to show the NMR spectrum of the voxel in the hydrogel (green box) as shown in **figure 6.2.1**. The spectrum is visualized in **figure 6.3.1** at 25°C, 10 minutes after the reaction began and the sample was inserted into the NMR machine. Each STEAM run was marked with their designated peaks, particularly before and after the vital temperature points, such as LCST, VPTT and 40°C. Their time stamps after temperature change were also marked. If the peaks were difficult to distinguish, then the peaks were zoomed in. This was done to compare the signals of the βCD and P(NIPAM) molecules as it approaches and surpasses 40°C. The last spectrum for each temperature experiment was also compared to one another, as well as the first run of their respective temperature experiment. All of these were used to support the quantitative data of βCD change in and out of the gel, as well as diffusion of βCD and water inside the gel.

When it comes to the quantitative analysis, the spectra were analyzed using MATLAB by calculating the integrals of specific peaks, specifically for βCD. These peaks of interest are P_2, H_2, H_3, H_4, and H_5. The H_2 and H_4 signals' integrals from the βCD were measured in every run at various temperatures, and it was used to determine the βCD intensity or concentration within the gel. Outside the gel, the H_3 and H_5 signals were included along with H_2 and H_4 as P(NIPAM) was not present at the 2mm and 6mm voxels, so the P_2 signal cannot influence the integral calculation of the H_3 and H_5 βCD peaks. Their calculated integral values were normalized with the first initial integral value to obtain (I/I_0). This was then plotted against time(t) in minutes. This provided a visualization on a microscopic perspective to the collapse of P(NIPAM) and the diffusion of βCD onto the release medium.

(6.4)Self-diffusion of βCD in the gel and water

MATLAB was used to determine the self-diffusion coefficients of βCD and water inside the gel by measuring the intensity peaks of H_2 and H_4 and its signals' integrals using the MEGA-PRESS sequence at various temperatures. The voxel of the MEGA-PRESS sequence was positioned in the gel as shown by **figure 6.2.1**. The MEGA-PRESS sequences for 40S, 40ST, 40T, and 31T varied the z-gradient strengths percentage in the order of 0%, 20%, 30%, and 50%. The parameters set for the MATLAB analysis had a gradient variation of $1\text{x}10^{-3}$ and a max gradient value of 1.4T/m. The water interval that was analyzed was 4.6-4.8 ppm, whilst the βCD interval was 3.4-4.2. The βCD interval was at times shortened between 3.4-3.7 or 3.4-3.8 to avoid the H_3 and H_5 signals for βCD as it is positioned at the same shift as P(NIPAM)'s signal for P_2. Failure to do this led to a negative self-diffusion value and produce a significantly higher uncertainty. If the run had insufficient water suppression and if it was affecting the slope of the curve negatively to a high degree, then the run was discarded.

Loading the experiment runs with their respective gradient strengths produced a decreasing linear function of ln(I/I_0) against the attenuation factor(b) using 4 points as shown in **figure 6.4.1** and with 3 points as shown in **figure 6.4.2**. For reference, water's graph was shown. The slope was better in **figure 6.4.2**, so the last data points of every run for 40S, 40T, 40ST and 31T were not included. This function observed in both aforementioned figures is based around **equation 3.4.3**, where the b-value was mathematically defined in **equation 3.4.2**. The gyromagnetic ratio of the observed nucleus is $\gamma=267.522\times10^6$ rad $T^{-1}s^{-1}$. Both these equations were found **section 3.4** (**Diffusion in MRI and hydrogels**).

$$b = \gamma^2 G^2 t^2 \left(T - \frac{t}{3}\right) \text{ (\textbf{Equation 3.4.2})}$$

$$\ln\left(\frac{I}{I_0}\right) = -b \cdot D \text{ (\textbf{Equation 3.4.3})}$$

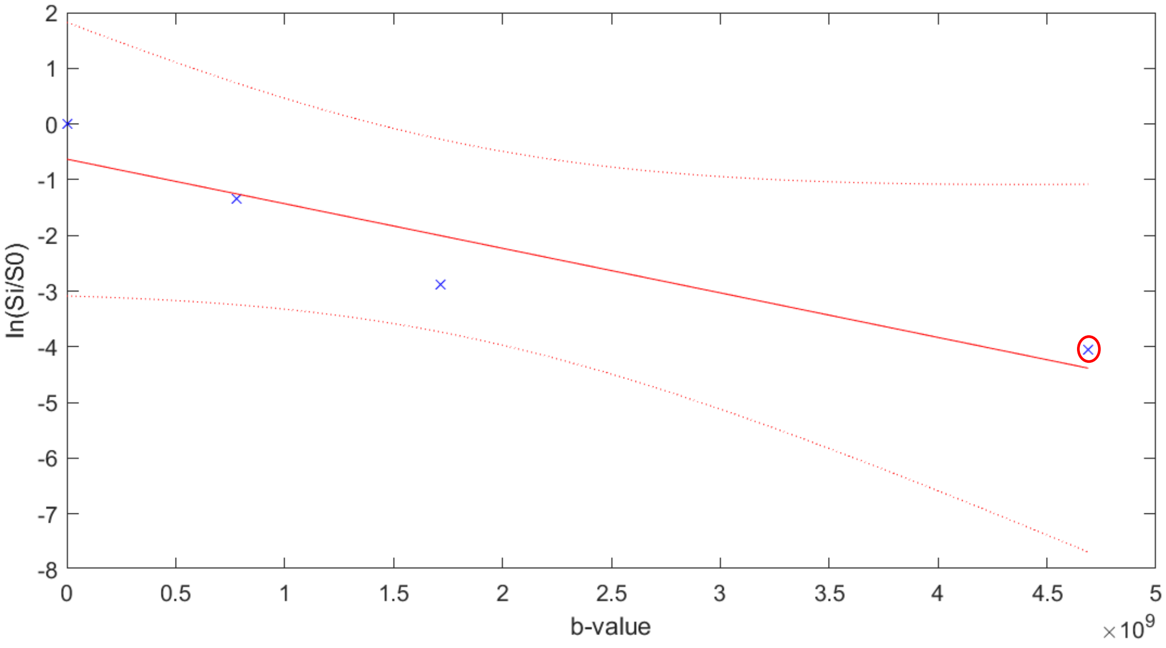

Figure 6.4.1: 31 °C diffusion of D_2O/H_2O with 4 data points. The intensities of the signals are correlated to the b-value. The slope was within the wide confidence interval, and one could observe that the points do not have a superb fit with respect to the slope, thus the last data point is removed (encircled in red).

The slope of the function was the self-diffusion coefficient. The self-diffusion coefficients of both βCD and D_2O/H_2O were normalized with a bulk βCD self-diffusion coefficient and a bulk 80:20 D_2O/SDH_2O (super-distilled H_2O) self-diffusion coefficient respectively.

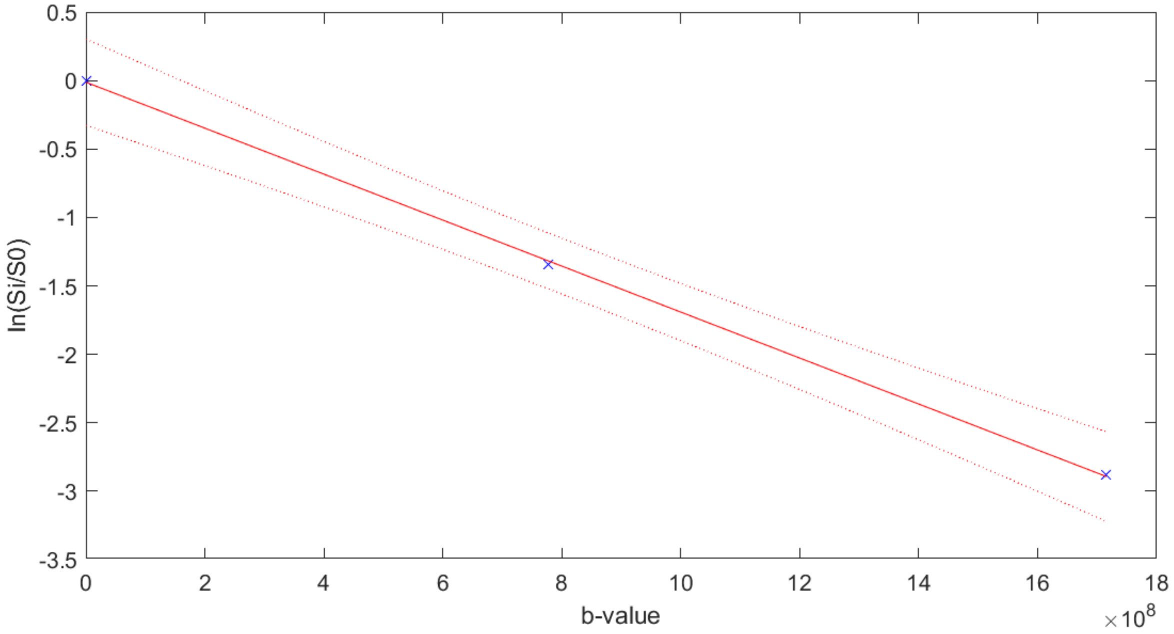

Figure 6.3.2: 31 °C diffusion of D_2O/H_2O with 3 data points. The intensities of the signals are correlated to the b-value, and one can see the improvement after removing the last data point. The change of intensities data points now has a good fit with the linear slope. This was the criteria for the slope when determining the self-diffusion coefficients.

A reference analysis was also done for pure super-distilled water and bulk βCD in an 80:20 D_2O/SDH_2O (super distilled H_2O) mixture using the same protocol for described for the temperature experiments using MEGA-PRESS. The super distilled water with D_2O and pure super distilled water were measured with the following z-gradient strength interval of 0%, 5%, 10%, 15%, 20%, 25%, and 30%. Any value deviating from the confidence interval and the linear curve extensively were removed. If a gradient strength setting for the z-gradient was too strong and created points that did not have a good fit with the slope, then the data point was removed from the analysis as well.

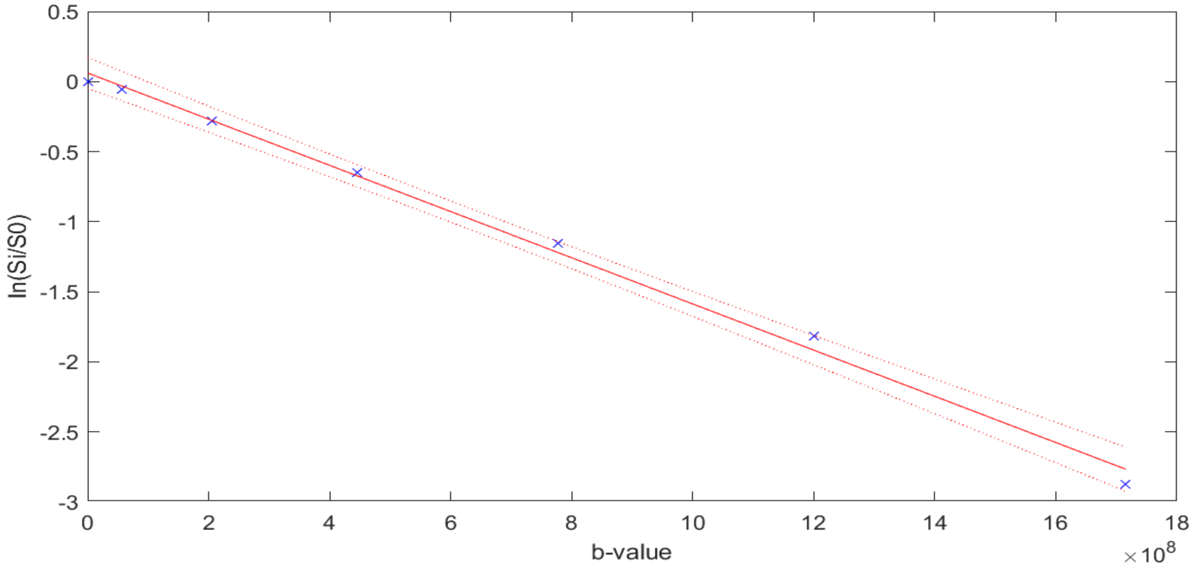

Figure 6.4.3: Determining the D_0 signals of the 80:20 D_2O/SDH_2O mixed with βCD by plotting $\ln\left(\frac{S_i}{S_0}\right)$*against the b-value. This was the first run at 25°C using the gradient interval: 0%,5%,10%,15%,20%,25%, and 30% z-gradient strengths. The slope shown fulfils the criteria for determining the D_0-value, in which the fit of the data points are good with respect to the slope, as well as being within the confidence interval.*

The bulk analysis makes it possible to create a linear function in determining the D_0 value at a given temperature, which were used to compare the self-diffusion or D-value of the βCD or water in P(NIPAM) for the 40S, 40ST, 40T, and 31T experiments. The results were compared to [4] and discussed in **section 7(results and discussion)**. The signal intensity change with the b-value and the spectra for D_2O/SDH_2O in bulk are shown in **figure 6.4.3** and **figure 6.4.4** respectively. **Figure 6.4.5** shows an example of a run that does not fulfil the criteria of determining a reliable D_0-value using a signal intensity change with the b-value of βCD as an example. The signal intensity change with the b-value and the spectra for βCD are shown in **figure 6.4.6** and **figure 6.4.7** respectively. The H_3 and H_5 signals were included in the integration calculation as there is no P(NIPAM present. The D_0 values of the water and βCD solution was done at 25°C, 31°C, 35°C, 38°C, and 40°C.

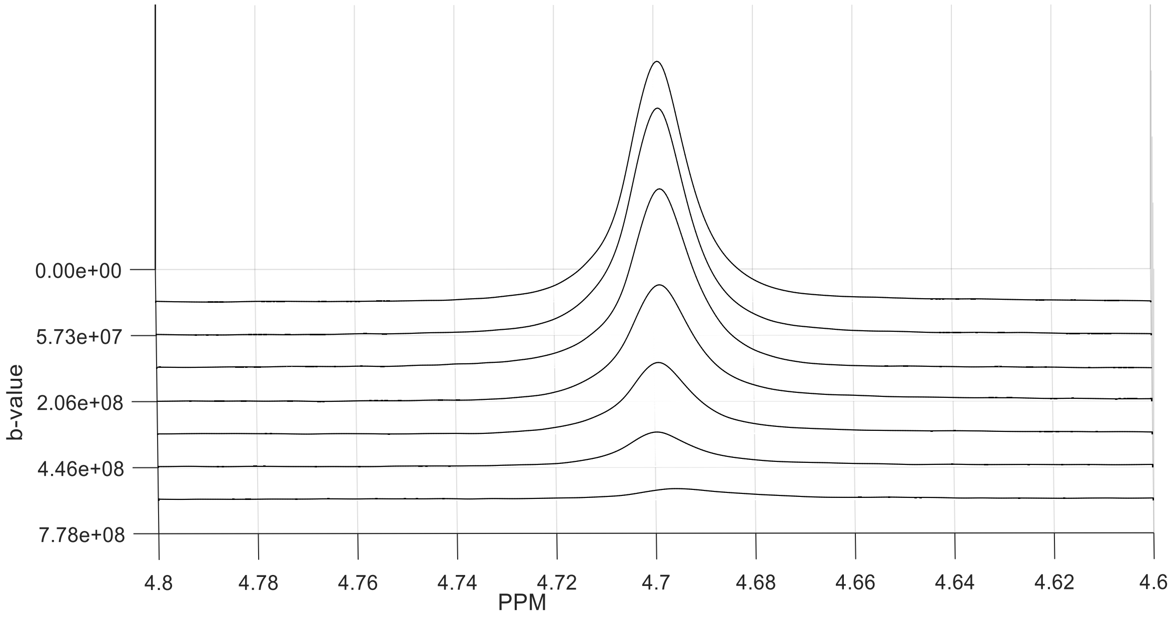

Figure 6.4.4: Spectrum of the bulk 80:20 D_2O/H_2O mixed with βCD, which was used to calculate the change of signals in ***figure 6.4.3***. *The interval focuses on the D_2O/H_2O mixture solvent from 4.6ppm-4.8ppm.*

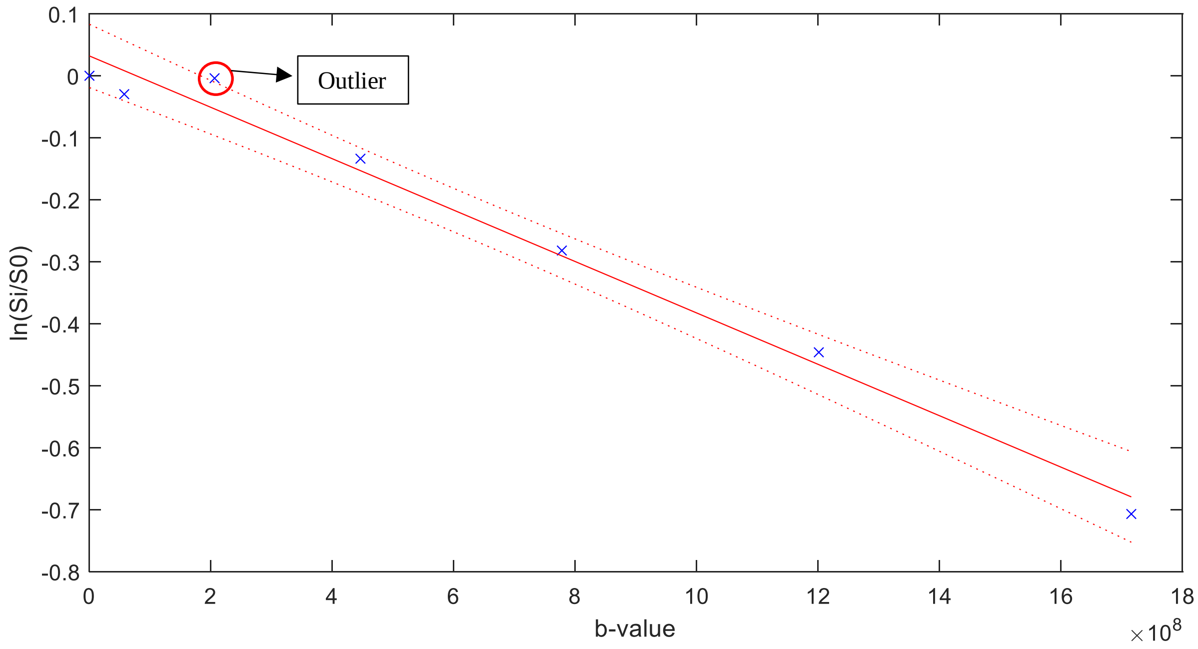

Figure 6.4.5: Determining the D_0 signals of βCD in 80:20 D_2O/H_2O mixed by plotting $\ln\left(\frac{I}{I_0}\right)$*against the b-value using the gradient interval: 0%,5%,10%,15%,20%,25%, and 30% z-gradient strengths . The 3rd datapoint is encircled in red and was marked as an outlier. To obtain a more accurate D_0-value by improving the linear slope, this outlier had to be removed.*

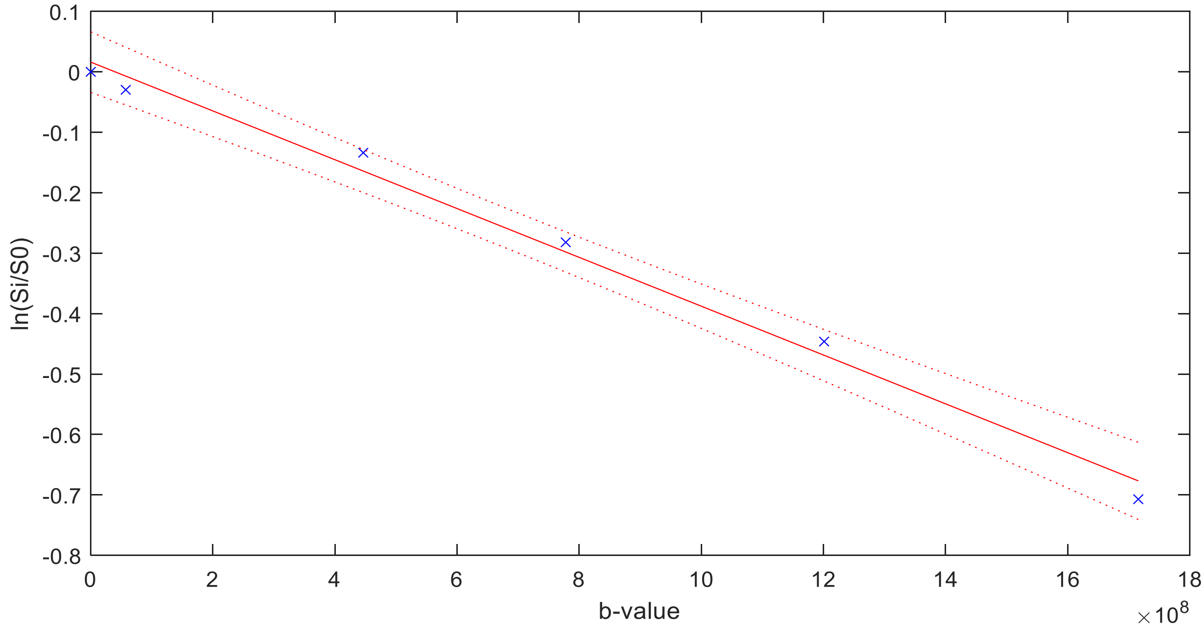

Figure 6.4.6: Determining the D_0 signals of βCD in 80:20 D_2O/H_2O mixed by plotting $\ln\left(\frac{I_i}{I_0}\right)$ against the b-value. This was the first run at 25°C using the gradient interval: 0%,5%,10%,15%,20%,25%, and 30% z-gradient strengths. The slope shown fulfils the criteria for determining the D_0-value, after removing the 10% z-gradient point.

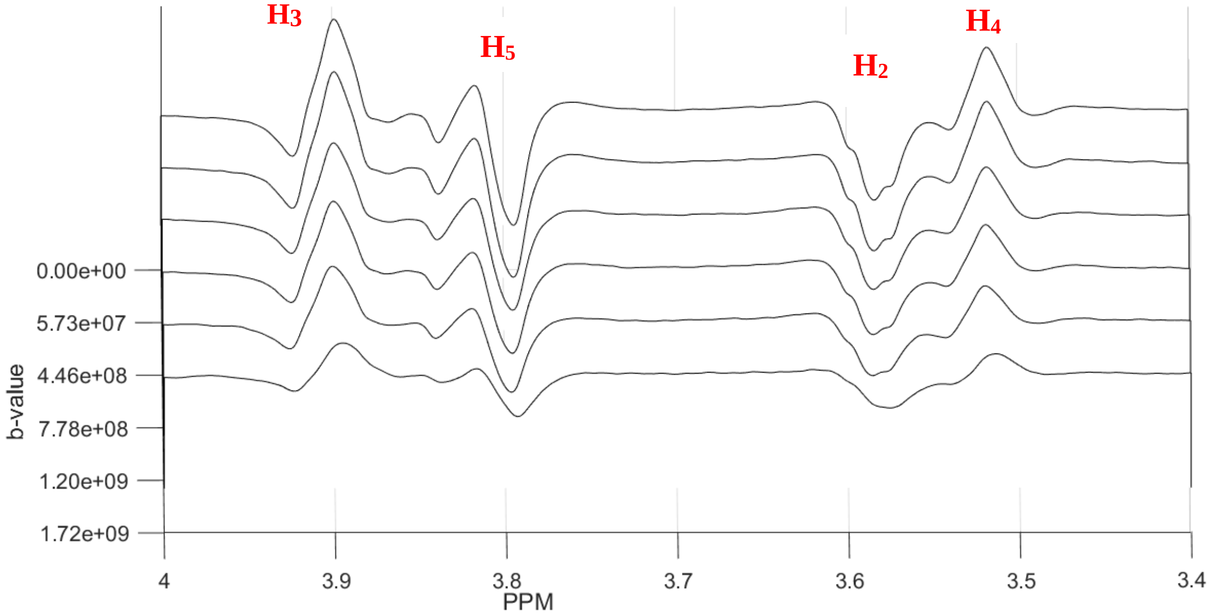

*Figure 6.4.7: Spectrum of the bulk βCD in 80:20 D_2O/SDH_2O, which is used to calculate the change of signals in **figure 6.4.6**. The interval focuses on the βCD signals H_2-H_5 from 3.4ppm-4.0ppm. H_3 and H_5 are included as there is an absence of P(NIPAM) in the bulk solution.*

It should be noted that even though the gradient strength was not calibrated for the diffusion experiments, the self-diffusion values(D) of 40S, 40ST, 40T, and 31T were compared against the reference self-diffusion coefficient(D_0) for normalization. This removes the factor of systematic error due to a lack of gradient strength calibration. The diffusion experiment aims to measure relative changes in diffusion, not absolute diffusion.

(7)Results and discussion

(7.1) NMR temperature calibration of the probe

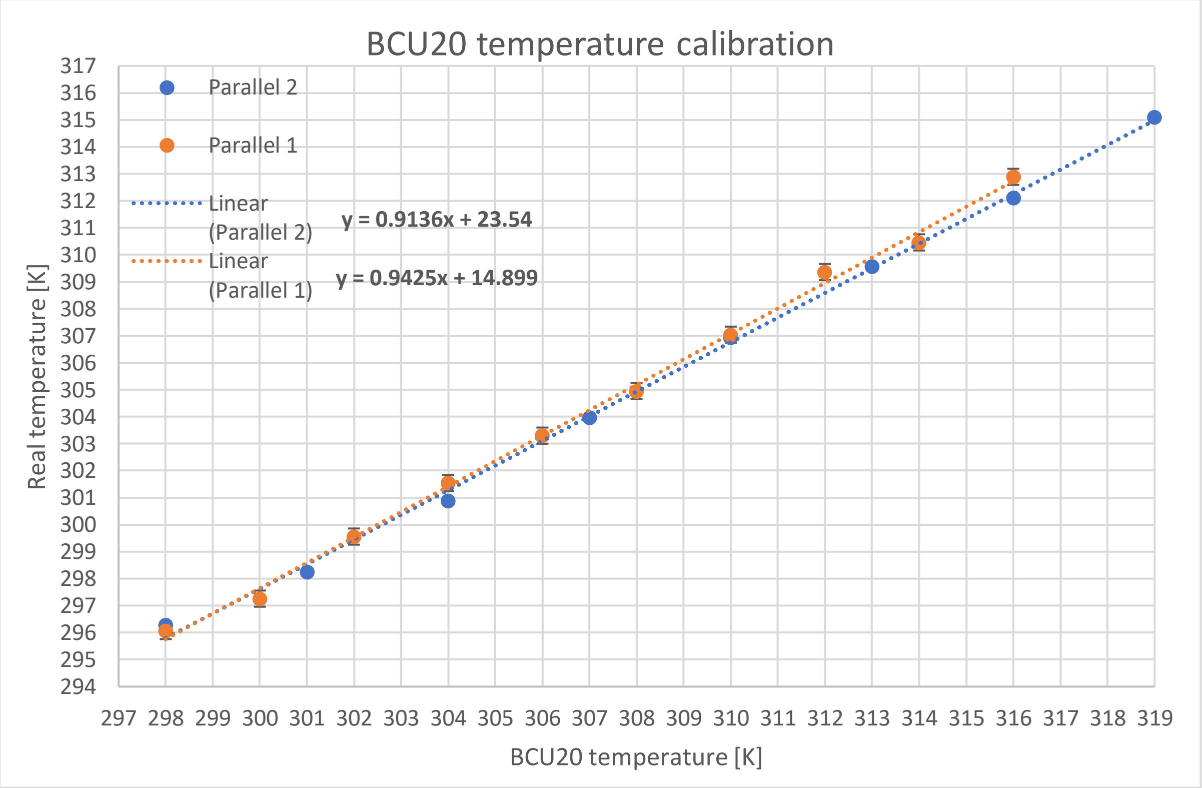

Figure 7.1.1: Temperature calibrations of parallel 1 and parallel 2 with their respective linear functions shown in the figure. Parallel 1 had fewer points than parallel 2. Both parallels appear to have good coherence, and the deviation between the parallel's points and trendlines start off low, but gradually increased with higher temperatures. Parallel 2 has the linear curve: y=0.9136(x)+23.54, whilst parallel 1 has a curve y=0.9425(x)+14.899. The uncertainty for both parallels are fixed at ±0.30K as stipulated by the NMR thermometer software used for the experiment [1].

Table 7.1.1: Identical calculated temperatures for parallel 1 and parallel 2

Temperature of BCU20 [K]	Parallel 1 [±0.30K]	Parallel 2 [±0.30K]
298	295.76	295.76
304	301.42	301.42
310	307.07	307.07
316	312.73	312.73

When combining the parallels for the temperature calibration curve together in **figure 7..11**, it can be noted that both trendlines appear to be almost identical, particularly when it comes to their slope pattern. **Table 7.1.1** noted the same temperature measurement points that ***parallel 1*** and ***parallel 2*** shared during the calibration. Inserting these values in their respective parallels' linear equations shown in **figure 7.1.1** yielded identical values.

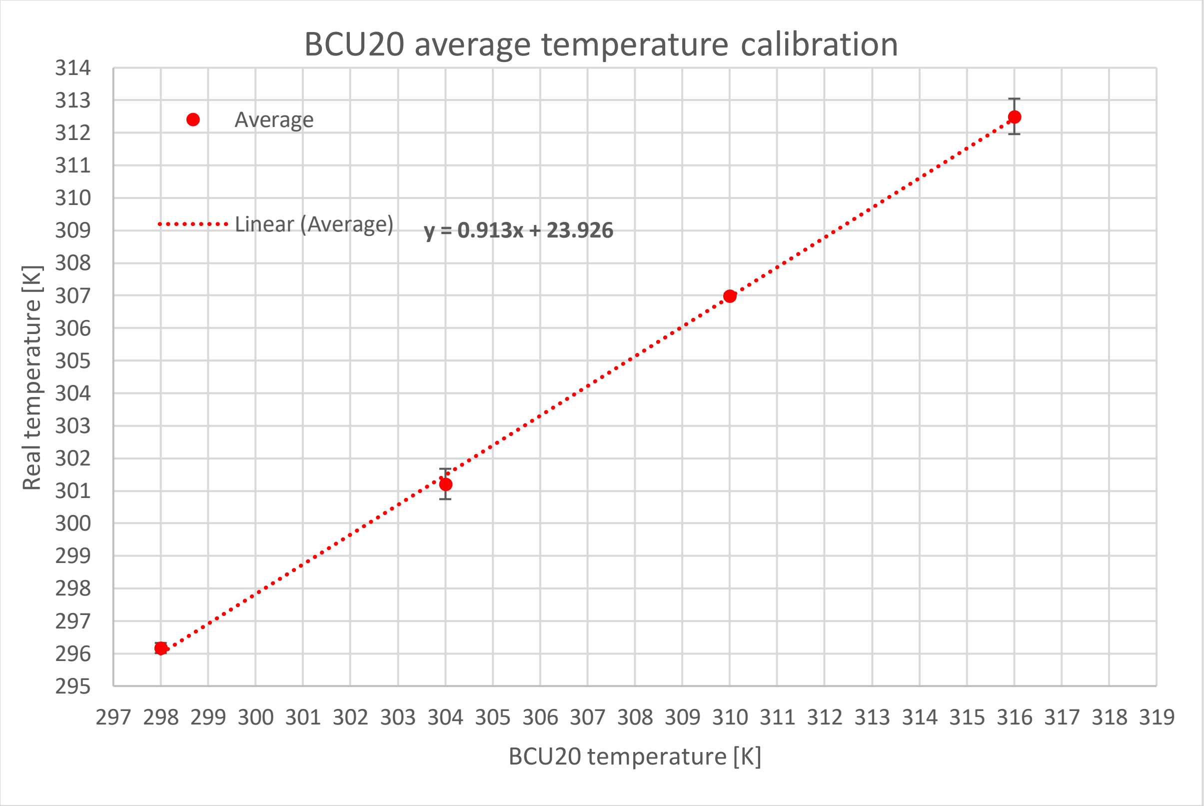

Figure 7.1.2: Average linear fit curve of parallel 1 and parallel 2 using their identical temperature measurements on the BCU20.The points have a good fit with the trend, and the standard deviations are low. The linear equation of the trend is y=0.913(x)+23.926.

To demonstrate the calculations done for **table 7.1.1**, the linear equations from **figure 7.1.1** were used. They are defined as **equation 7.1.1** and **equation 7.1.2**, and are used under with the reference (x)-value being 310K:

$$Y_{P1} = 0.9425(x) + 14.899 \text{ (\textbf{Equation 7.1.1})}$$

$$Y_{P1} = 0.9425(310K) + 14.899 = 307.074K$$

$$Y_{P2} = 0.9136(x) + 23.54 \text{ (\textbf{Equation 7.1.2})}$$

$$Y_{P2} = 0.9136(310K) + 23.54 = 307.074K$$

Despite the temperature jump gaps between each of the parallels' data points and slight deviation from the parallels' trendlines, both parallels still produce identical probe temperature values, hence both are acceptable to use in order to determine the probe temperature used for all the temperature experiments, namely the temperature calibrations for 31T, 40S, 40T and 40ST. ***Parallel 1's* linear function** was utilized further to calibrate the real temperature of the probe as it had the most points, and had a longer interval compared to parallel 2.

(7.2) Temperature and time correlation for experiment protocols

To account for the delay between the BCU20 unit and the sample probe, a temperature-time correlation curve was made for all the experiment protocols compiled in **table 5.2.1** using the temperature calibration of glycol (80 wt%) in DMSO-d_6 shown in **table 7.2.1**. This was to give an indication of the temperature with respect to time.

40S

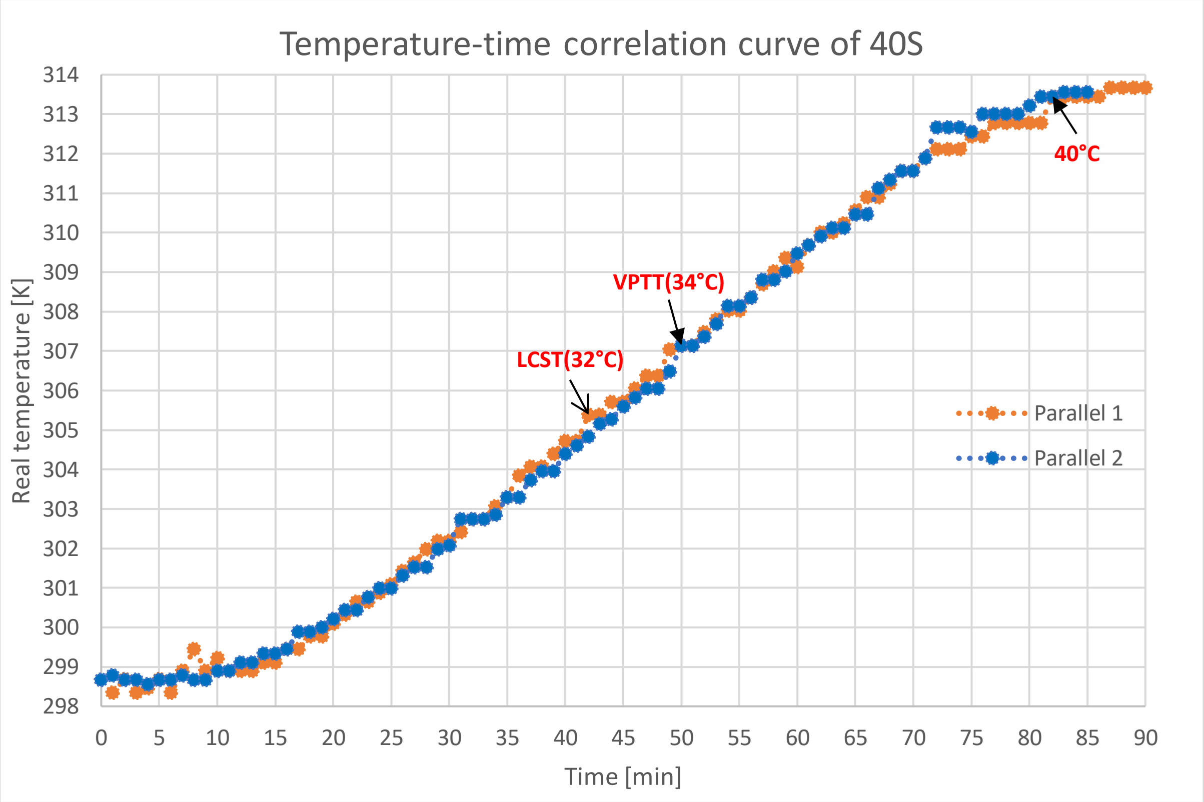

Figure 7.2.1: Combining both temperature-time correlation curves of parallel 1 (orange) and parallel 2 (blue) for 40S in one graph. The important transition temperatures, LCST, VPTT, and 40°C are also marked in red in the graph. Both parallels appear to be identical, have a good fit, and have minimal deviation from one another, except for parallel 1 between the 8–10-minute mark as it deviates to some extent from parallel 2. Some slight of deviation is also seen from the 70-85 minute-mark. Aside from that slight deviation, both parallels provide a good insight on how temperature will increase in the 40S experiment protocol.

Figure 7.2.1 shows the temperature-time correlation curve for 40S, where the y-axis describes the real temperature of the probe, and the x-axis describes the time after the first temperature change. According to the figure, it indicates that LCST was reached when t= 43 minutes and VPTT was reached when t= 50 minutes. 40°C was reached at t= 82 minutes after temperature change. The curve also appears almost linear in nature except at the beginning and at the end where it creates a small a slight plateau. The average correlation curve for 40S is shown in **figure 7.2.2** with error bars. The standard deviation between the 2 parallels is not large, but some noticeable deviations were observed at the beginning of the graph, and at higher temperatures.

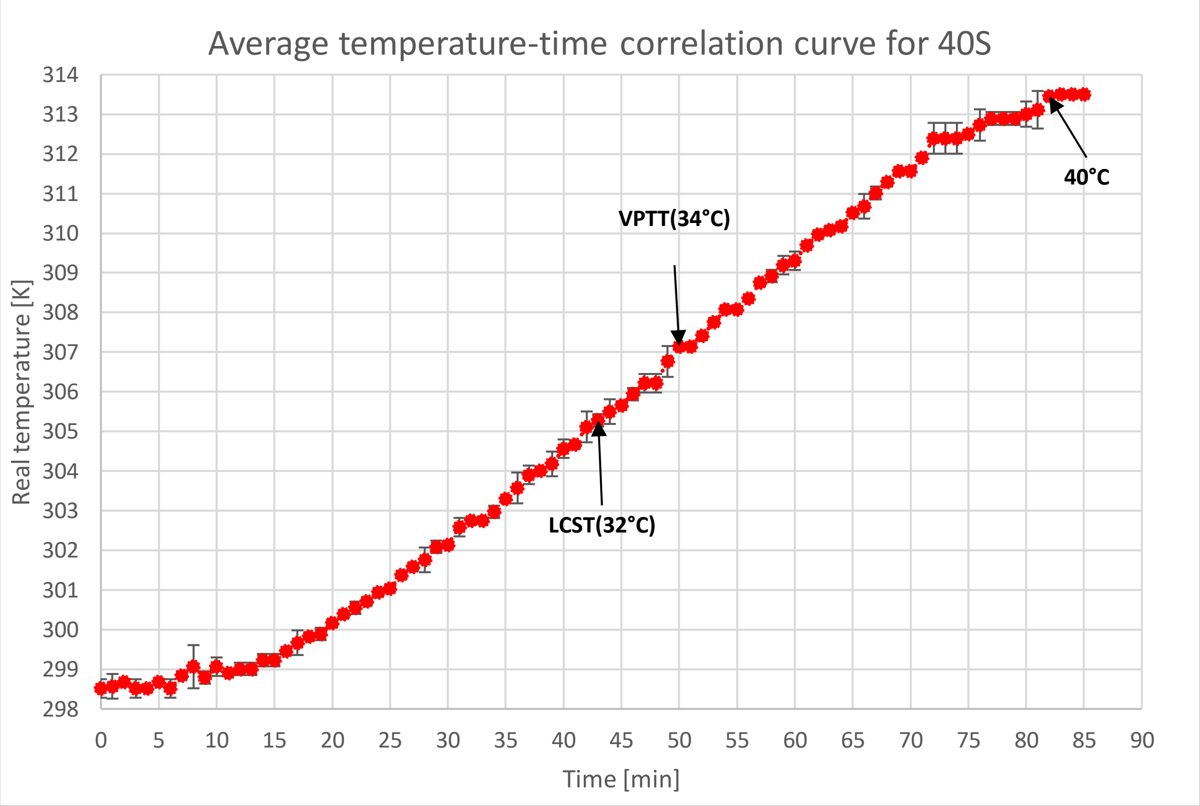

Figure 7.2.2: Average fit curve of 40S's temperature-time correlation curve from ***figure 7.2.1****. The standard deviation shown are minimal throughout the curve.*

This slight deviation observed in **figure 7.2.2** can be related to how the glycol peaks were measured and interpreted as the peaks were not optimally sharp or clear on where the center of the peak was. It is also noted that only two parallels were done for this experiment, and the sample was only shimmed once at the beginning, which could influence on the sharpness of the glycol peaks. An example of peak comparison can be visualized in **figure 7.2.3**, where it shows a red and blue peak with a green line cut through the middle vertically. The green line shows where the center of the peak is. As one might be able to observe, the blue peak has reduced sharpness compared to the red peak, thus making it slightly more difficult to obtain precise chemical shift measurements due to the slight curvature causing measurements to not be 100% centralized to the peak(distortion). Fortunately, average from **figure 7.2.2** does correspond with a similar pattern seen in **figure 7.2.1**, so uncertainty for this correlation curve is expected to be low and useable for the 40S temperature experiments later on. The VPTT, LCST and 40°C marks were achieved at the same time stamps as seen in **figure 7.2.1**.

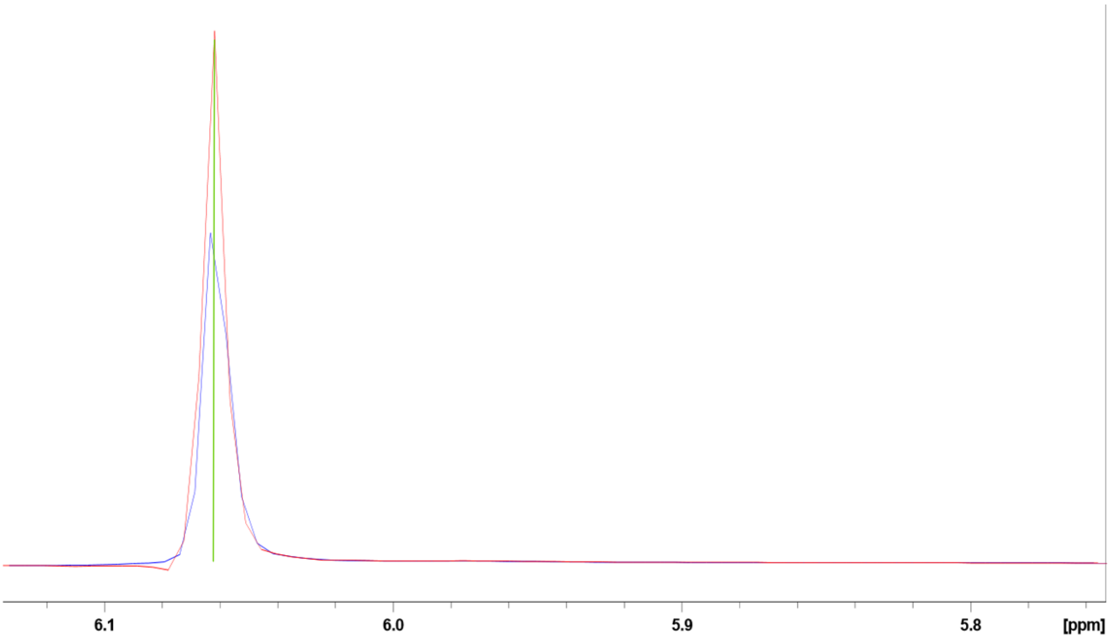

Figure 7.2.3: The reduction of sharpness of the peak can affect how the temperature at a specific time point is determined. The red peak represents a point with excellent sharpness, which makes it easy to determine the center of the peak and measure the separation value in ppm to be inputted to the NMR thermometer software. Both are normalized to one another, and the green line shows where the peak measurement starts for determining the real temperature of the probe. On the other hand, the blue peak represents the peak with the non-optimal sharpness. Its curvature has a distinct difference from the red peak, which could be influenced by shimming as the sample was only shimmed once before running nonstop for the entire duration. The peak distortion makes it more difficult to obtain very precise measurements of the peak separation for glycol.

40T

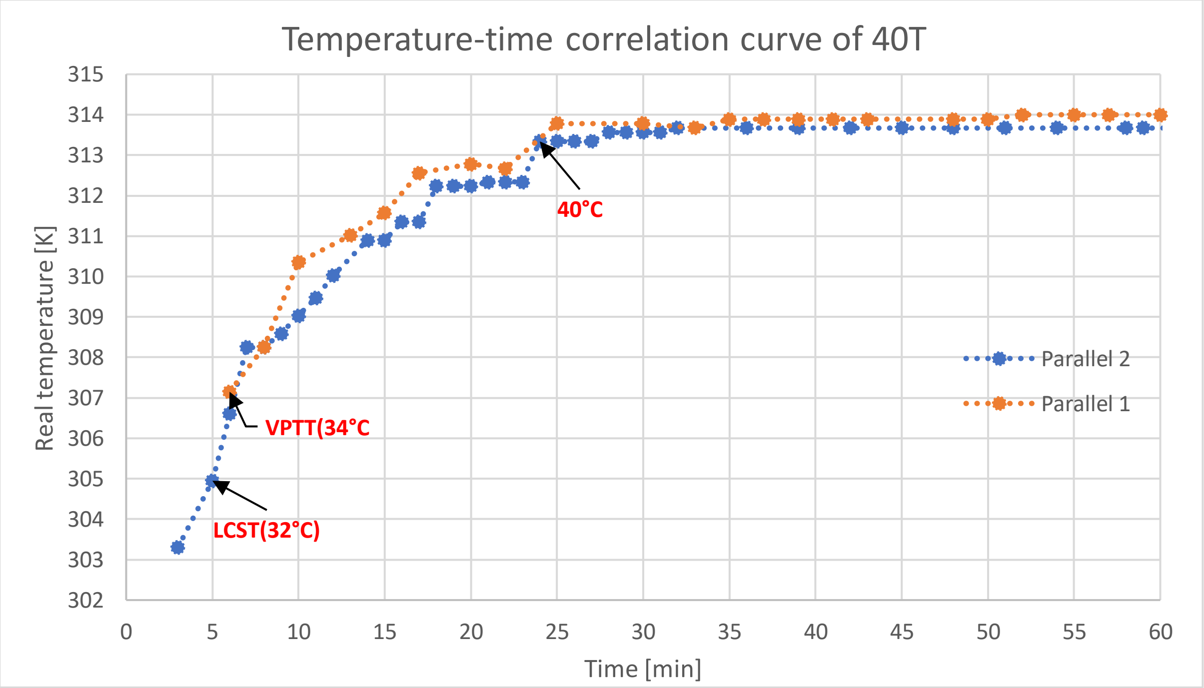

Figure 7.2.4: Combining both temperature-time correlation curves for parallel 1(orange curve) and parallel 2 (blue curve) for 40T in one graph. Both parallels appear to be identical in their progression trends. Parallel 1 has fewer points than parallel 2 due to the fact that every run was locally shimmed, whilst parallel 2 was only shimmed once at the beginning of the experiment. However, parallel 2's additional points at an earlier time frame made it possible to record the temperatures before LCST, but it does appear to have a slightly higher curve than parallel 2. Despite this variation, both parallels agree with each other when parallel 1 is extrapolated at lower t-values with respect to parallel 2's curve.

Figure 7.2.4 shows the temperature-time correlation curve for 40T. According to the figure, parallel 2 indicates that LCST is reached when t= 5 minutes, and VPTT is reached when t= 6 minutes. 40°C is reached at t= 24 minutes after temperature change. After reaching 40°C, a plateau is observed. The curve for 40T appears to steeply increase with time when the standard sample was exposed to 40°C, so the transition temperatures, namely the LCST and VPTT were reached in quick succession.

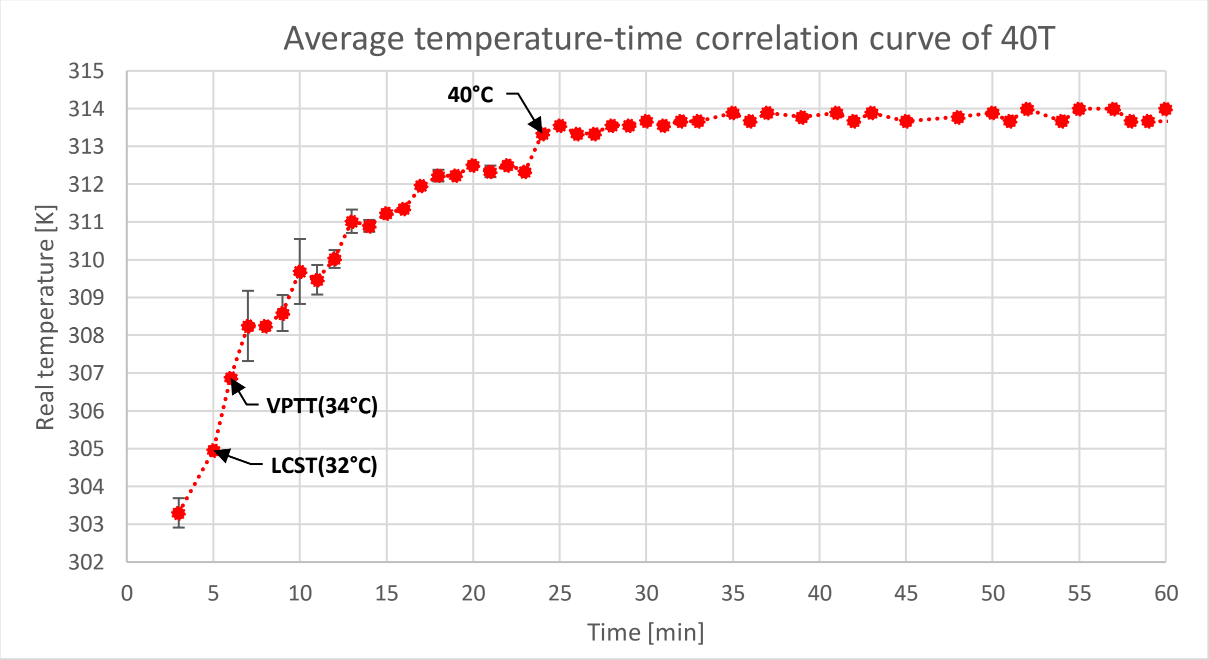

Figure 7.2.5: Average fit curve of 40T's temperature-time correlation curve from figure 7.2.4. Both parallels that shared the same time stamps were averaged during measurement, and their error bars are shown in the graph. LCST, VPTT and the 40°C are shown as well.

The average fit curve is seen in **figure 7.2.5**, and the trend is identical to both parallel 1 and 2 with the error bars shown for data points that were recorded at the same timestamp. Some slight variation is seen, particularly at the beginning of the time interval, but this is most likely due to the nature of the experiment being a temperature jump. Hence the errors bars observed here are slightly higher than what was seen in the 40S correlation curve in **figure 7.2.2** as it was a slow-heating experiment. The lack of shimming in parallel 2 could be a contributor to the variances observed similar to what was seen in 40S due to the reduced sharpness and curvature of the glycol peaks. However, this was necessary as it made it possible to record temperatures before LCST, even at a high temperature jump, so this was an acceptable compromise. The VPTT, LCST and 40°C marks were also achieved at the same time stamps as seen in **figure 7.2.4**.

40ST

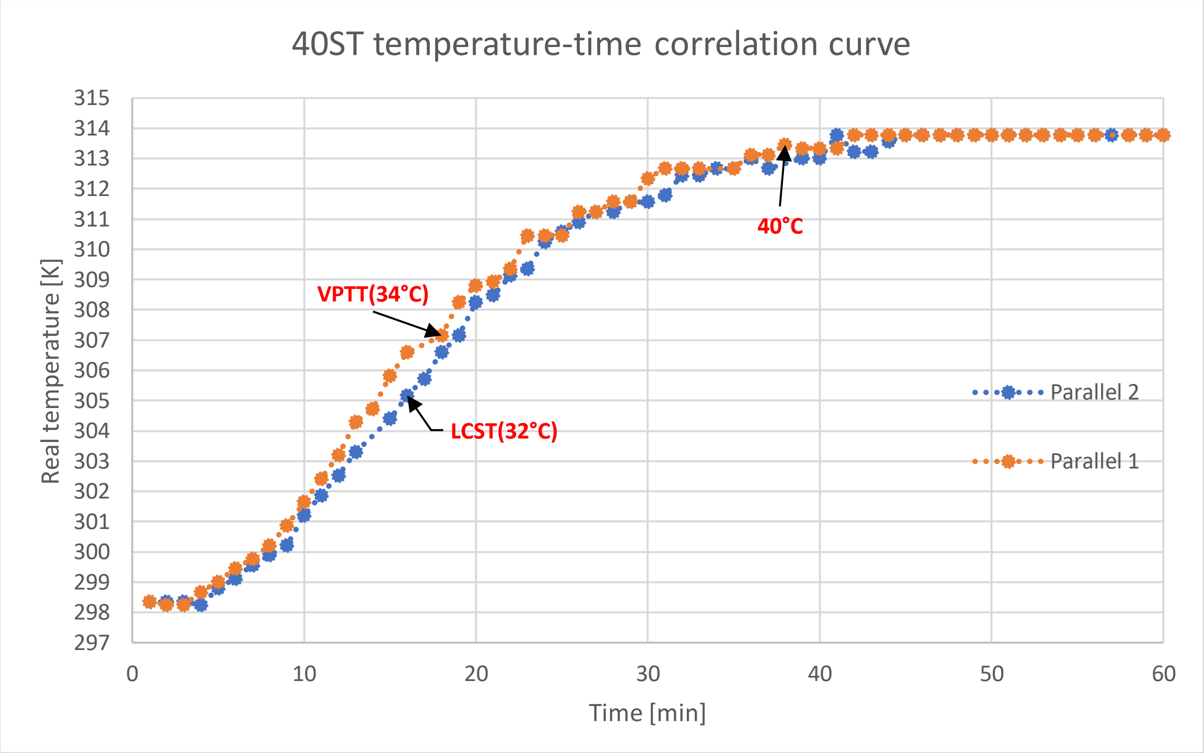

Figure 7.2.6: Combining both temperature-time correlation curves of parallel 1 and parallel 2 for 40ST in one graph. The important transition temperatures, LCST, VPTT, and 40°C are also marked in red in the graph. Both parallels appear to be identical, have a good fit, and have minimal deviation from one another, except for parallel 1 between the 10–20-minute mark as it deviates to some extent from parallel 2. Aside from that slight deviation, both parallels provide a good insight on how temperature will increase in the 40ST experiment protocol.

Figure 7.2.6 shows the temperature-time correlation curve for 40ST. According to the figure, it indicates that LCST is reached when t= 15-16 minutes after temperature change, and VPTT was reached when t=18-19 minutes after temperature change. 40°C was reached between t= 38-40 minutes after the temperature change. These intervals are due to varying values from the two parallels. To choose when exactly LCST, VPTT and 40°C are reached, the average fit curve would be needed. The curve appears to steeply increase with time similar to 40T's curve at **Figure 7.2.4**, but the increase is not as steep, and the curve appears to have some linear characteristics at the middle of the curve similar to 40S in **figure 7.2.2**. This is apparent between 10 minutes and 30 minutes, but quickly establishes a plateau when t=42 minutes. The characteristic of the slope is as the experiment name implies, a "hybrid" protocol that mixes the "slow-heating" protocol and "temperature jump" protocol of 40°C. Therefore, it makes sense that it shares the slow-heating protocol's linear characteristic and the temperature jump's steep increase as it approaches 40°C.

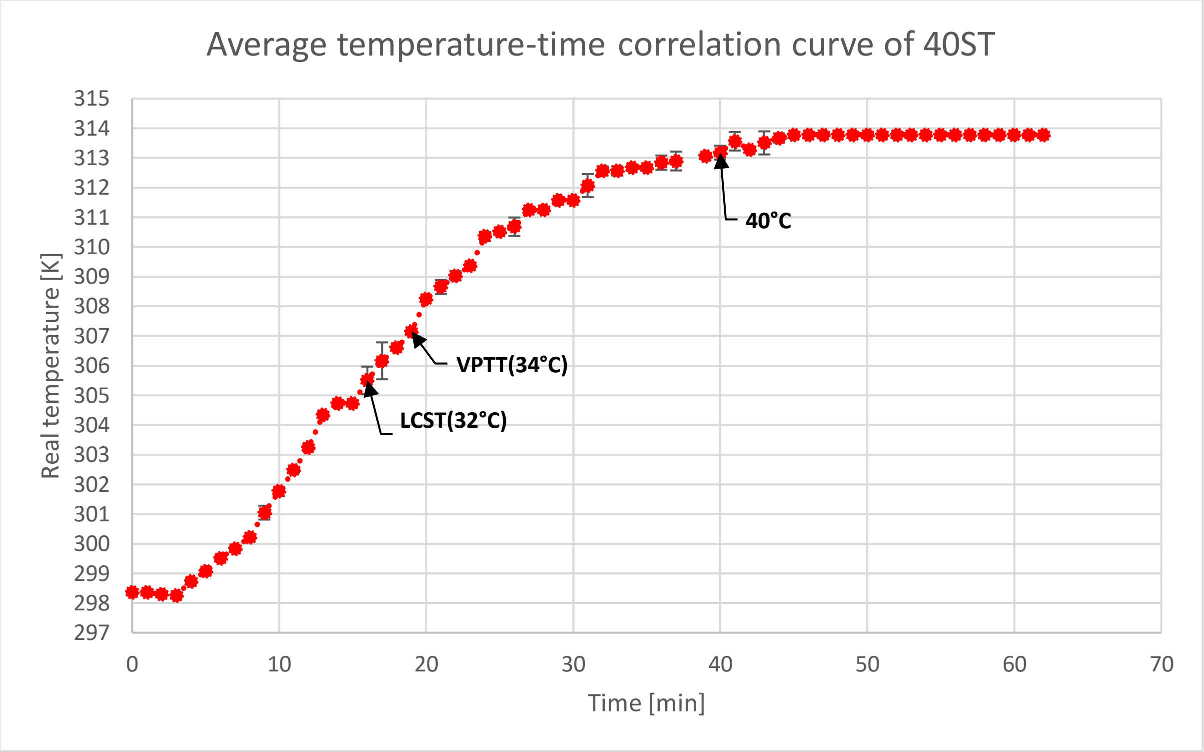

Figure 7.2.7: Average fit curve of 40ST's temperature-time correlation curve from figure 7.2.6. Both parallels that shared the same time stamps during measurement wee averaged, and their error bars are shown in the graph. LCST, VPTT and the 40°C are shown as well.

The average fit of the curve of both parallel 1 and 2 are shown in **figure 7.2.7**. In this figure, LCST is reached when t=16 minutes, whilst VPTT is reached when t=19 minutes. 40°C is reached when t=40 minutes. The uncertainties are also shown, and they can be seen to be minimal throughout the graph with some minor variation at the middle of the time interval and when temperature was approaching the plateau. Compared to the 40T curve, 40ST's correlation curve is not as sharp, and it took slightly longer to obtain the transition temperatures. This temperature experiment allows for more control and better monitoring of the temperature and time correlation compared to the 40T as it allows the experiment to begin at a controlled time, whereas the 40T had to be done rapidly as the sample is inserted in order to obtain a value below LCST, which required compromises, such as less shimming, skipping the FLASH ortho sequence, and rushing the sample preparation due to speed in which temperature increases. Overall, the average fit curve agrees with both parallel 1 and 2, and it can be used to correlate temperature and time for 40ST's experiment.

31T

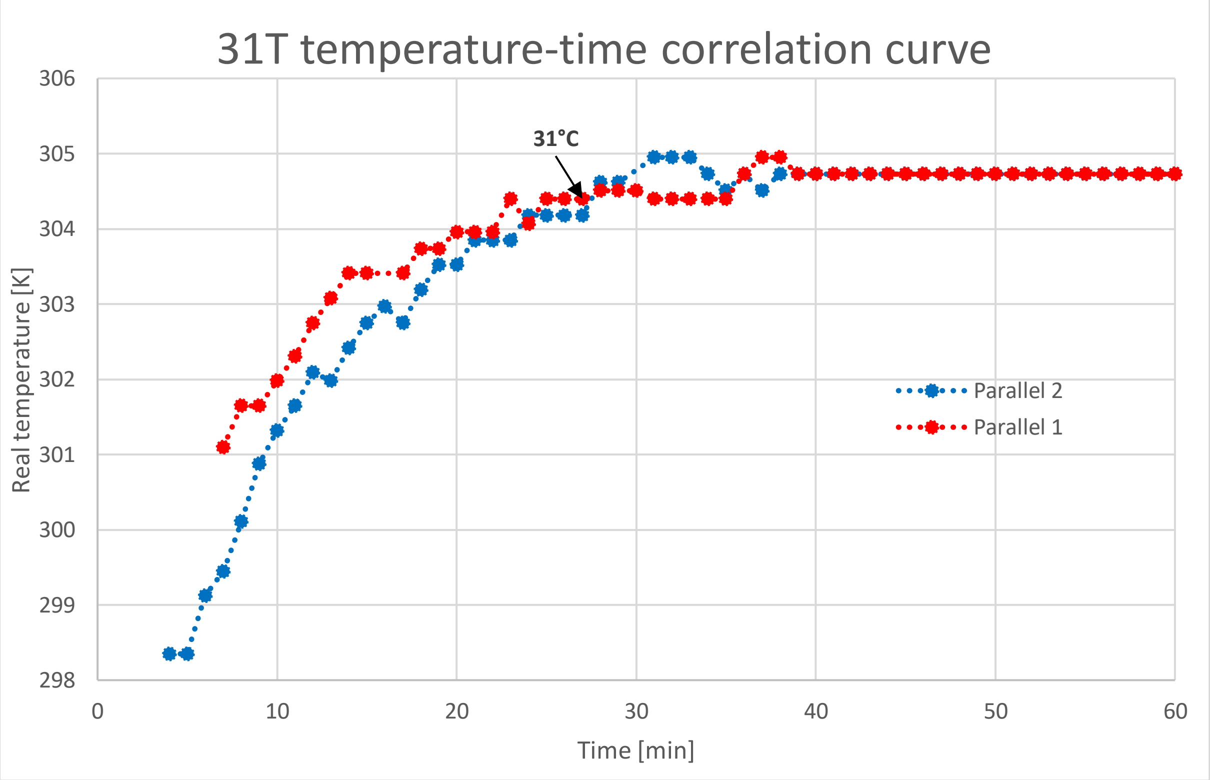

Figure 7.2.8: Combining both temperature-time correlation curves for parallel 1 and parallel 2 for 31T in one graph. Both parallels appear to be identical in their progression trends. Parallel 1 has fewer points from t=4-9 minutes than parallel 2 due to a slight delay due to human error during the experiment, which delayed the shimming of the first point by several minutes. Despite this setback, the trend has a good general trend, but there are more noticeable variations throughout the graph.

Figure 7.2.8 shows the temperature-time correlation curve for 31T. According to the figure, it indicates that LCST and VPTT were never achieved. The 31°C mark was reached at t= 24-25 minutes after temperature change. The curve appears to steeply increase with time when the standard sample was exposed to 31°C, so the curve is similar to 40T. A plateau is established for both parallels when t= 39 minutes. Similar to 40ST, the definite moment 31°C was reached is determined in the average curve in **figure 7.29**. From the figure, it can be observed that 31°C is reached specifically when t=25 minutes. The variation seen in **figure 7.2.8** is visualized through the error bars in **figure 7.2.9**, which shows very high variations at the beginning of the experiment. Several factors influenced this variation with the first being the lack of shimming at every run similar to what happened in 40T, where distortion can make it difficult to accurately measure the peak separation. The second influencing factor is the human error done during measurement as this affected the flow of the experiment and caused delays for the experiment. Although time stamps were marked and recorded for every run, it is still worth considering. All these factors can potentially explain the variation see between the two parallels. These uncertainties become reduced as temperature stabilizes towards 31°C.

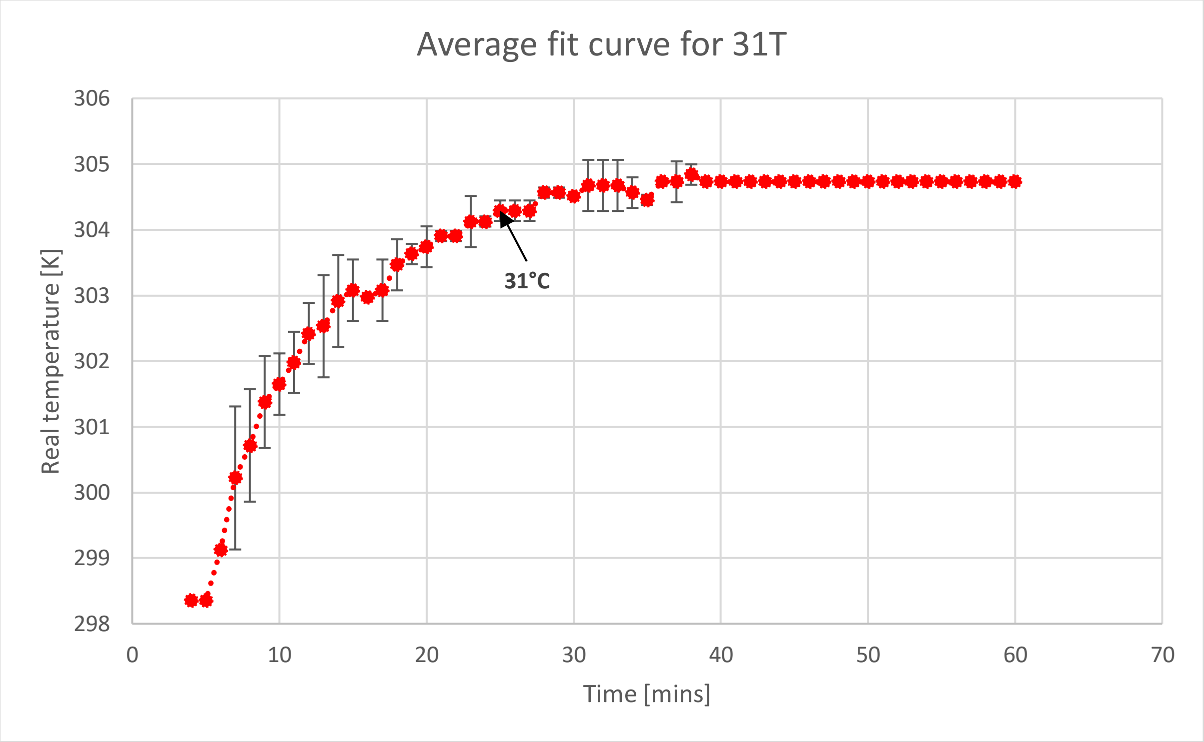

Figure 7.2.9: Average fit curve of 31T's temperature-time correlation curve from figure 7.2.8. Both parallels that shared the same time stamps during measurement wee averaged, and their error bars are shown in the graph. The errors bars appear larger than the ones compared in 40S, 40ST and 40T.

Overall, the temperature-time correlation curves for all the temperature experiments appears to have an excellent fit with their own respective parallels, except for 31T. These uncertainties for each correlation curve can be reduced if more parallels were done, particularly for the 31T. Another option would be to have an extra run, where each run is locally shimmed. This can reduce the distortions during temperature change, but will offer less points, thus should only be used to validate existing runs. It is imperative to maintain a quick procedure for the temperature-jump experiments as it would mean risking losing a data point measurement at the important transition temperatures. All in all, these correlation curves can be used to determine the temperature throughout the experiment for 40S, 40ST, 40T, and 31T. An overview of the important time stamps for each temperature experiment is shown in **table 7.2.1**, and it shows the fastest transitions are observed for 40T followed by 40ST and then 40S. 31T was the only temperature protocol that never achieved LCST or VPTT.

Table 7.2.1: Overview of transition temperatures for each temperature experiment with their respective timestamps

Transition temperatures [°C]	**Time [mins]**			
	40S	**40T**	**40ST**	**31T**
LCST (32°C)	43	5	16	-
VPTT (34°C)	50	6	19	-
40°C or 31°C (for 31T only)	82	24	40	25

(7.3) Qualitative visualization of shrinkage of P(NIPAM) using MSME

The MSME pictures of each experiment protocol summarized in **table 5.2.1** were compiled together with respect to time. Each MSME picture seen here shows the 3rd sagittal slice out of the 5 analyzed slices. Each temperature experiment will have two compilations, namely (1) progression of shrinkage before LCST→40°C and (2) progression of shrinkage after reaching 40°C. The lines outside the voxel show the position of the central horizontal line of the voxel.

40ST

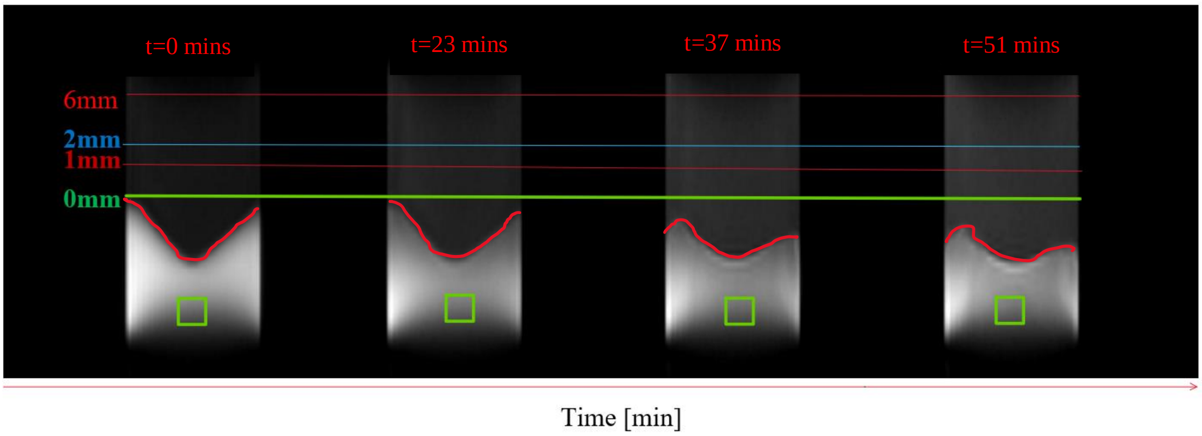

Figure 7.3.1: 40ST's MSME pictures at 4 different points during the experiment, where the red line on the gel highlights its borders. The categorization is identical to what was explained in ***figure 6.2.1****. Visually, the MSME progression shows how the pictures become gradually opaquer than the 1st initial picture. Each picture shows slice 3 at 0 mins, 23 mins, 37 mins, and 51 mins respectively from left to right. The categorization is identical to what was explained in* ***figure 6.1.1****. The voxel positions both in and out of the hydrogel are always maintained to preserve the frame of reference. The green line shows the 0 mm interface, which is positioned at the center of the rf coil. The voxel inside the gel was -6.500 mm from the center of the rf-coil, and the time frames here show the shrinkage progression(left→right) before LCST(1st), after VPTT(2nd), just before reaching 40°C(3rd), and finally going over 40°C(4th). The temperature markings converted from Kelvin to Celsius are as stipulated by the correlation curve in* ***figure 7.2.7****: (1st) 25.2°C, (2nd)36.21°C, (3rd)39.75°C, and (4th) 40.63°C.*

Figure 7.3.1 shows shrinkage progression of 40ST before LCST→40°C. The figure indicates that some shrinkage occurred at LCST and VPTT, but they were not as noticeable until nearing 40°C. For example, after reaching VPTT when t=23 minutes, slight shrinkage began to take fold inside P(NIPAM), but shrinkage does not appear to occur, or at the very least, not as substantial. The effects of the shrinkage become more apparent as it reaches 40°C. The MSME picture at t=37 minutes and 51 minutes appear shrunken, which coincides with the temperature values for this time mark as both have reached the max temperature for the experiment, 40°C. It is also observed that the pictures become opaquer as temperature increases. This is the same finding by Knorgen who characterized the reduction of brightness at higher temperatures as an indication of lower T_2-values(**figure 1.4.1**). This indicates the loss of mobility for the network chains as the hydrogel shrinks, which restricts movement of both water molecules and the βCD as steric hindrance becomes stronger.

As the sample incubates at 40°C, the degradation of the hydrogel progresses until it is almost indistinguishable at t=226 minutes in **figure 7.3.2**. By taking reference to the height difference from it started at **figure 7.3.1** and at the end of the experiment in **figure 7.3.2**, it is a significant change. According to **table 7.2.1**, the transition temperatures of 40ST were the second fastest to be achieved, lagging behind by 40T. Given how 40ST has a long incubation time at 40°C, it would explain the significant rapid degradation of the hydrogel. However, unlike the 40T, it was easier to monitor the change for this temperature experiment as temperature was only changed after doing 1 reference run from 25°C, so it was possible to obtain more details about the shrinkage prior to the phase transition in 40ST than 40T.

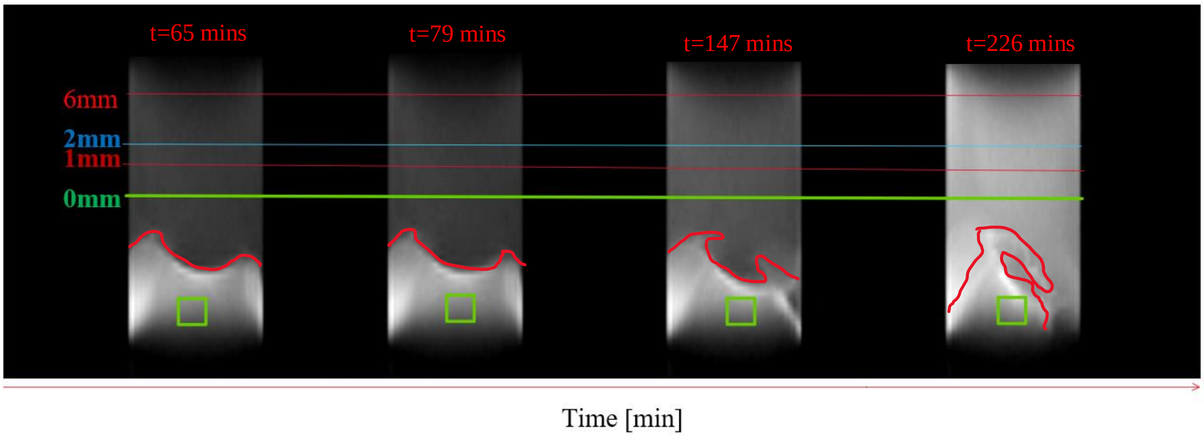

Figure 7.3.2: 40ST's MSME pictures(left→right) incubating at 40.6°C with their respective time stamps. The voxel positions were never moved from ***figure 7.3.1****. Overtime, it is noticeable that the gel continues to degrade and shrink as time passes by with the worst degradation and shrinkage occurring at the last image 226 minutes after changing temperature from 25°C directly to 40°C on the BCU20. It is even almost impossible to distinguish the borders of the gel at the last picture.*

31T

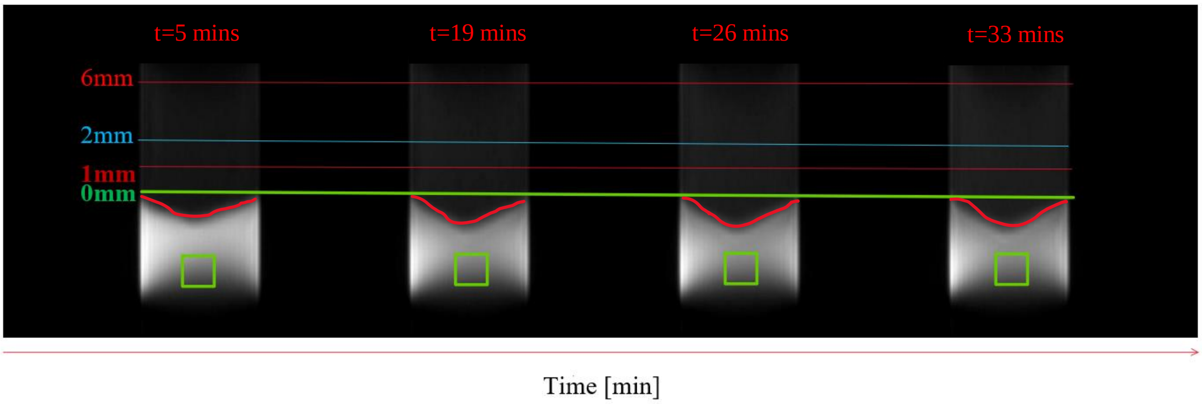

Figure 7.3.3: 31T's MSME pictures at 4 different points during the experiment, where the red line on the gel highlights its borders. Similar to 40ST, the pictures become opaquer with time. Each picture shows slice 3 at 5 mins, 19 mins, 26 mins, and 33 mins respectively from left to right. The categorization is identical to what was explained in ***figure 6.2.1****. The voxel positions both in and out of the hydrogel are always maintained to preserve the frame of reference. The green line shows the 0 mm interface, which is positioned at the center of the rf coil. The voxel inside the gel was -6.500 mm from the center of the rf-coil. The time frames here show progression towards 31°C, so no transition temperatures are reached. This can explain why there is minimal shrinkage from a glance, even when reaching 31°C at the last picture to the right. The temperature markings converted from Kelvin to Celsius are as stipulated by the correlation curve in* ***figure 7.2.9****: (1st) 25.2°C, (2nd)30.48°C, (3rd)31.14°C, and (4th) 31.53°C.*

Looking at the only temperature experiment that never reached beyond the transition temperatures of LCST or VPTT, the 31T sample reached 31°C between 25 minutes, and it achieved equilibrium at t= 39 minutes according to its temperature-time correlation curve in **figure 7.2.9**. Ergo, it never underwent volume phase transition or VPT. This explains why there is minimal change in shrinkage, and the MSME can show this as there is minimal height difference between the first run of 31T in **figure 7.3.3** compared to the last run-in **figure 7.3.4.** There is a clear disparity between the gel shrinkage between 40ST and 31T, which correlates with the hydrogel shrinking kinetics. One aspect that both 40ST and 31T shares is that both become opaquer as temperature increases. However, given how there is no substantial shrinkage for the entire duration of the experiment, it can be safe to assume that the crosslinkers for P(NIPAM) are still intact and remain in the swollen state.

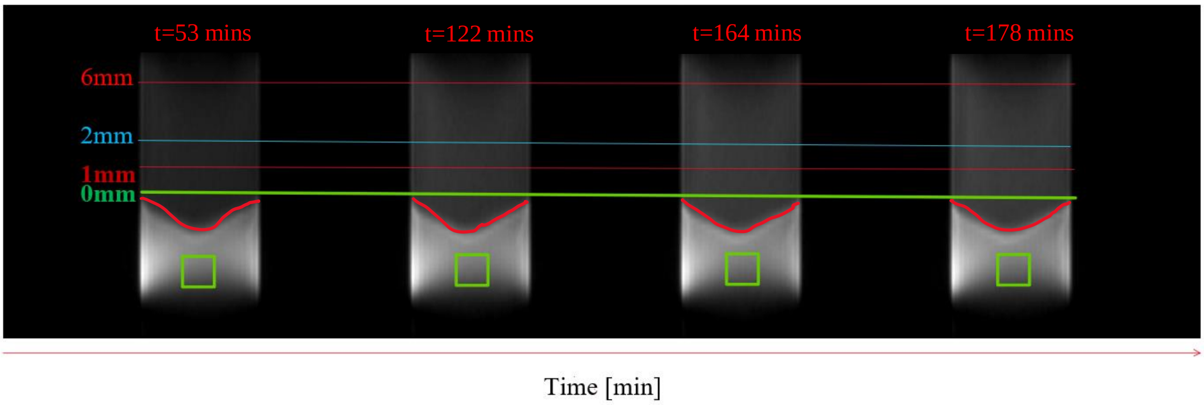

Figure 7.3.4: 31T's MSME pictures(left→right) incubated at 31.58°C with their respective time stamps. The voxel positions were never moved from ***figure 7.3.3****. Unlike 40ST, 31T's gel appears to have very minimal shrinkage, even being just 0.4°C away from LCST. The height difference is not noticeable from these MSME images.*

40S

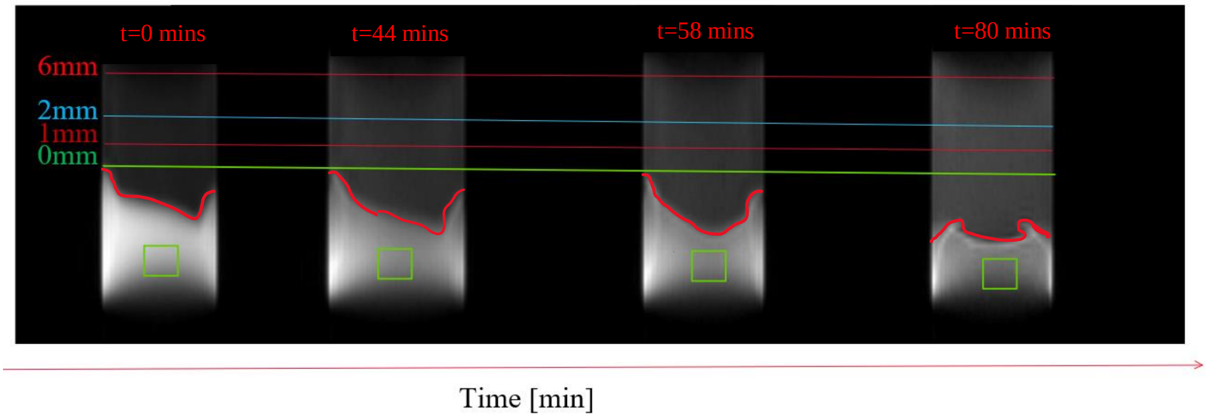

Figure 7.3.5: 40S's MSME pictures at 4 different points during the experiment, where the red line on the gel highlights its borders. The difference in opaqueness is similar to 40ST, where it increased with temperature. Each picture shows slice 3 at 0 mins, 44 mins, 58 mins, and 80 mins respectively from left to right. The categorization is identical to what was explained in ***figure 6.2.1****. The voxel positions both in and out of the hydrogel are always maintained to preserve the frame of reference. The green line shows the 0 mm interface, which is positioned at the center of the rf coil. The voxel inside the gel was -6.500 mm from the center of the rf-coil, and the time frames here show the shrinkage progression(left→right) before LCST(1st), right after LCST(2nd), after VPTT (3rd), and just before reaching 40°C(4th). The temperature markings converted from Kelvin to Celsius are as stipulated by the correlation curve in* ***figure 7.2.2****: (1st) 25.37°C, (2nd)32.35°C, (3rd)35.88°C, and (4th) 39.86°C.*

Figure 7.3.5 shows the progression of the gel's shrinkage from 0 minutes to 80 minutes, which covers the important transition temperatures up to 40°C. Similar to 40ST and 31T, the opaqueness increased with increasing temperature. Shrinkage is not very observable or apparent for the naked eye as the heigh difference does not differ until 80 minutes, where the temperature is close to 40°C. Even reaching LCST and going slightly over VPTT, the shrinkage is not as visible, which is a similar observation seen as well in 40ST. In the last picture in **figure 7.3.5** where t=80 minutes and the temperature is at 39.86°C, the shrinkage is more obvious. This shrinkage pattern is similar to 40ST's progression as seen in **figure 7.3.1**, but the keynote here is that 40S's hydrogel does not appear to aggressively deform like what happened to 40ST as 40S is a slow-heating experiment, so reaching the transition temperatures takes a longer time than in 40ST. The sample for 40S is also incubated for less time than the 40ST. As of now, 31T's hydrogel is the only temperature experiment that did not exhibit any significant shrinkage. 40ST's and 40S's hydrogel samples showed shrinkage, but 40ST's was more rapid and aggressive compared to 40S's sample due to the hybrid nature of 40ST's temperature protocol.

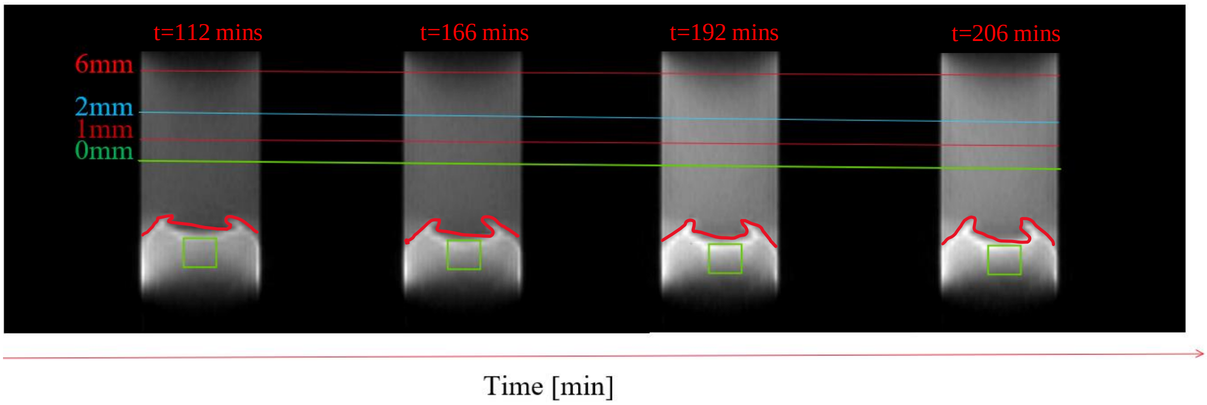

Figure 7.3.6: 40S's MSME pictures(left→right) incubating at 40.52°C with their respective time stamps. The voxel positions were never moved from ***figure 7.3.5****. Overtime, it is not as noticeable that the gel continues to degrade and shrink as time passes by, especially compared to 40ST, where the last MSME pictures have the most extensive shrinkage from all the runs. However, there is a significant shrinkage compared to the 1st run at 25.37°C just like 40ST as one can see the height difference from the original position of the 0mm interface.*

Comparing **figure 7.3.6** and **figure 7.3.2**, both hydrogels show shrinkage as time passes by. The distinguishable factor here is that 40S's degradation is more subtle, whereas the 40ST's degradation was more aggressive as shown by its last MSME picture in **figure 7.3.2** where the borders are very difficult to see. In 40S's MSME pictures in **figure 7.3.6**, shrinking can be noticed as the border of the of hydrogel gets closer with the green voxel inside the gel, which indicates shrinkage is still occurring, but not as rapid. This behavior correlates well with the nature of a slow-heating experiment, thus it spent less time in 40°C than 40ST and achieved the transition temperatures at a later time mark.

40T

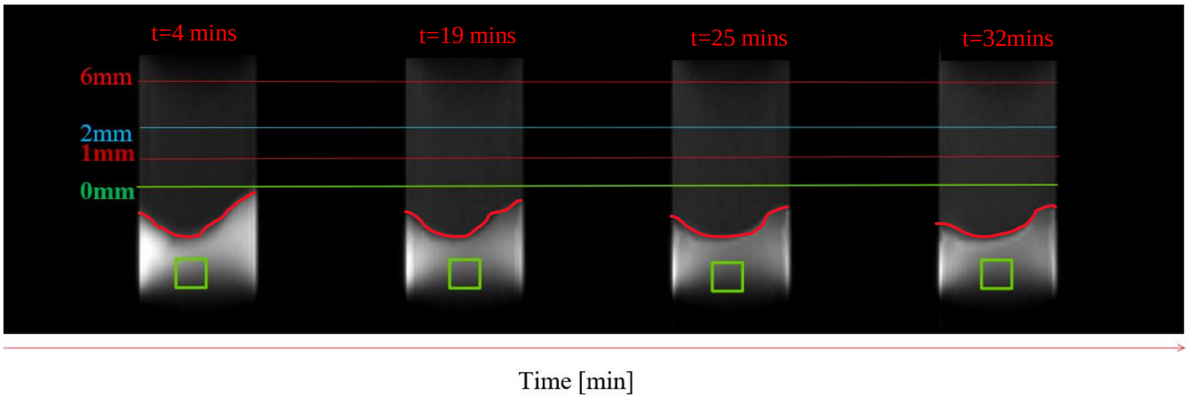

Figure 7.3.7: 40T's MSME pictures at 4 different points during the experiment, where the red line on the gel highlights its borders. Similar to 40ST, 31T, and 40S, the MSME pictures show how the opaqueness of the pictures become more extensive with time and temperature. Each picture shows slice 3 at 4 mins, 19 mins, 25 mins, and 32 mins respectively from left to right. The categorization is identical to what was explained in ***figure 6.2.1****. The voxel positions both in and out of the hydrogel are always maintained to preserve the frame of reference. The green line shows the 0 mm interface, which is positioned at the center of the rf coil. The voxel inside the gel was -6.500 mm from the center of the rf-coil. The time frames here show progression towards 40°C in a temperature jump setting from left to right. The 1st picture is 1°C before LCST, the 2nd picture is after VPTT and 1°C from 40°C, and the 3rd and 4th picture are at 40°C. The temperature markings converted from Kelvin to Celsius are as stipulated by the correlation curve in* ***figure 7.2.5****: (1st) 31°C, (2nd)39°C, (3rd)40.41°C, and (4th) 40.52°C. As one can see, this has the most rapid shrinkage compared to the rest of the experiments, even compared to 40ST.*

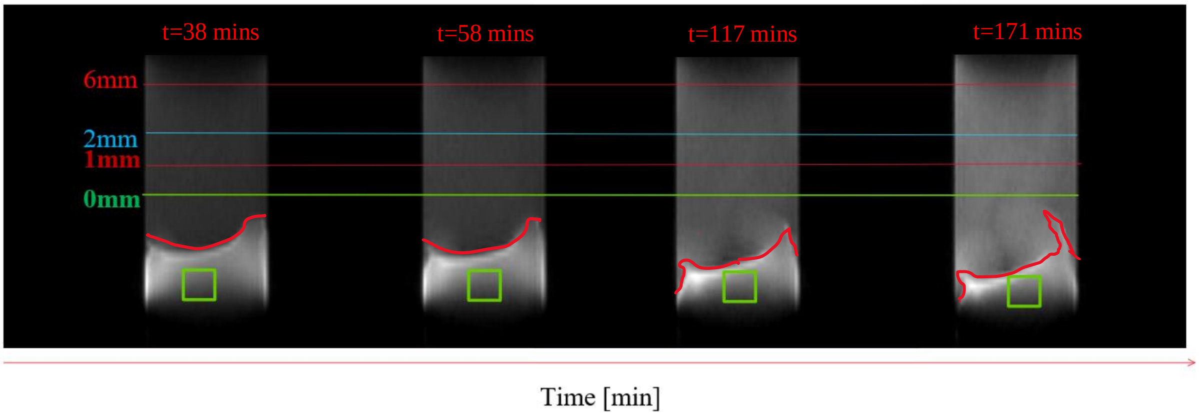

*Figure 7.3.8: 40T's MSME pictures(left→right) incubating at 40°C with their respective time stamps. The voxel positions were never moved from **figure 7.3.7**. Unlike 40S and 31T, it is very noticeable that the gel continues to degrade and shrink as time passes by. Even compared to 40ST, the shrinkage is more extensive and aggressive as 40T was incubated at 40°C the longest. The last MSME image here shows substantial degradation of P(NIPAM) at the highest temperature value used in the experiment.*

For the final temperature experiment, 40T, the MSME pictures shown in **figure 7.3.7** visualize a very rapid shrinkage, even similar to 40ST. The first MSME picture shows that after 5 minutes, the temperature is already 1°C away from LCST. At the second picture when t=19 minutes, the gel has already shrunken to some degree as it is only 1°C away from 40°C, which is also the temperature mark where the gel's become apparent in 40ST and 40S. Compared to 40ST and 40S, 40T achieved the transition temperatures the fastest, which correlates well with the observed rapid shrinkage in **figure 7.3.7**.

The incubation of the sample at 40°C in **figure 7.3.8** shows a mirroring effect seen in 40ST's hydrogel. Both 40ST's and 40T's hydrogels degraded rapidly and showed more drastic change to its physical appearance on the 3rd slice compared to 40S in **figure 7.3.6**. However, one could even argue that between 40ST and 40T, the hydrogel in 40T appeared to have a smaller gel, almost disappearing completely from the MSME. Comparing the last MSME images of both 40ST and 40T in **figure 7.3.2** and **figure 7.3.8**, the 40T sample has a shorter experiment time of 180 minutes, whereas 40ST had 240 minutes and already it can be seen that the 40T sample has almost disappeared from the MSME due to the degradation of the P(NIPAM). This can be supported by the fact that 40T was exposed to 40°C at the start of the experiment compared to 40ST and 40T that had to be incubated at 25°C for some time before their respective temperatures. Hence, it is expected to see a rapid shrinkage for 40T, which is followed by 40ST and then 40S.

From a purely qualitative perspective, these MSME results correlates well with the hydrogel shrinking kinetics as temperature increases. Shrinkage occurred for all the temperature experiments except for 31T, but overall, they significantly shrunk at 40°C; not at the VPTT or LCST, so there is a delay before actual shrinkage happens. The pictures also show that as sample approaches 40°C, the hydrogel becomes opaquer. The observations from the experiments mentioned previously was a similar finding according to Kaneko et al's paper. Kaneko observed that the gels gradually became opaquer as temperature was increased from 10°C→40°C [20]. It also correlates with Knorgen's findings [113] and Wisniewska's paper , which showed the P(NIPAM) significantly shrinking as temperature went beyond VPTT, particularly near 40°C (see **attachment 4**) [4]. In particular, her 40S experiment showed significant drops in A/A_0 only at 38°C, which is also the same temperature where the most change is seen in the MSME pictures.

(7.4) NMR spectrum of P(NIPAM) with βCD before and after VPTT and LCST using STEAM

In **figure 6.3.1**, it showed that the synthesis of the hydrogel was successful and βCD was successfully infused in the hydrogel. The peaks of both the P(NIPAM) and βCD peaks are visible enough. The 80:20 D_2O/H_2O mixture used for the experiment it made possible to forego manual water suppression during the experiment run, thus making βCD visible as compared to the previous attempts where pure distilled water was used at first. However, there was a small, but sharp peak observed between P_3, and H_2 and H_4. This was encircled in red. This could potentially be unreacted monomers that were not removed completely during the dialysis in the synthesis stage. This is taken into consideration when evaluating the diffusion data of βCD in the coming sub-sections. Aside from that, the peaks of both P(NIPAM) and βCD were compared before and after the vital transition temperatures and at 40°C. The temperatures were characterized according to the correlation curve for 40S in **figure 7.2.2**

Before and after LCST (32°C)

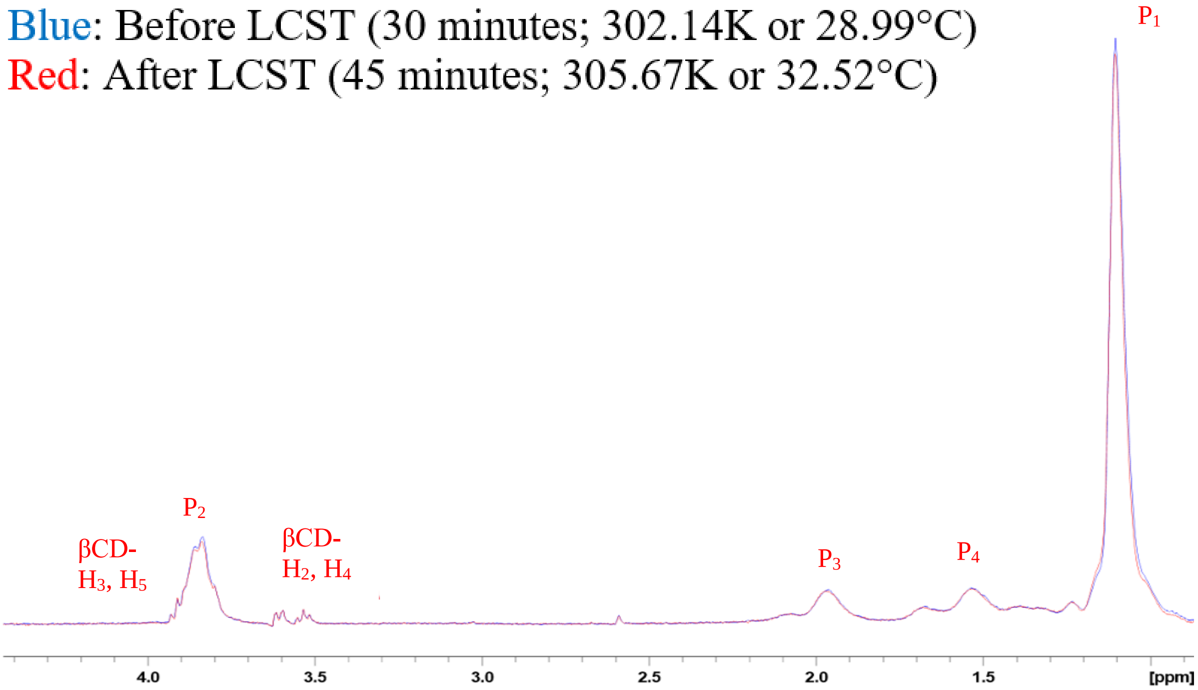

Figure 7.4.1: Spectrum of 40S before and after LCST. The blue peaks represents the hydrogel and βCD before LCST, whilst the red is after LCST. LCST is 32°C. The difference between the peak intensities are minimal, so the hydrogel network is still intact and βCD is still inside the hydrogel.

Looking at the changes of the βCD and P(NIPAM) intensities during a temperature increase, the 40S sample is used as a reference example. **Figure 7.4.1** shows the spectrum of the P(NIPAM) and βCD before and after LCST with the time stamps and supposed temperature values according to the glycol reference in **table 7.2.1**. **Figure 7.4.2** focuses on some of the points of interest, and it can be observed that the βCD peaks: H_2-H_5 barely changed, whilst the peaks for the P(NIPAM): P_2 and P_3 has a small difference in intensity. When the temperature is around LCST, the peaks for the red spectrum are smaller than the blue peaks, which indicates that the hydrogel is shrinking, albeit feeble in its extent. This coincides with the MSME pictures for all temperature experiments that indicated that temperatures at LCST showed minimal shrinkage. By just looking at MSME pictures alone, it would be easy to be deceived that no shrinkage happened at all, but the STEAM sequence allows for visualization on a microscopic scale via NMR spectra.

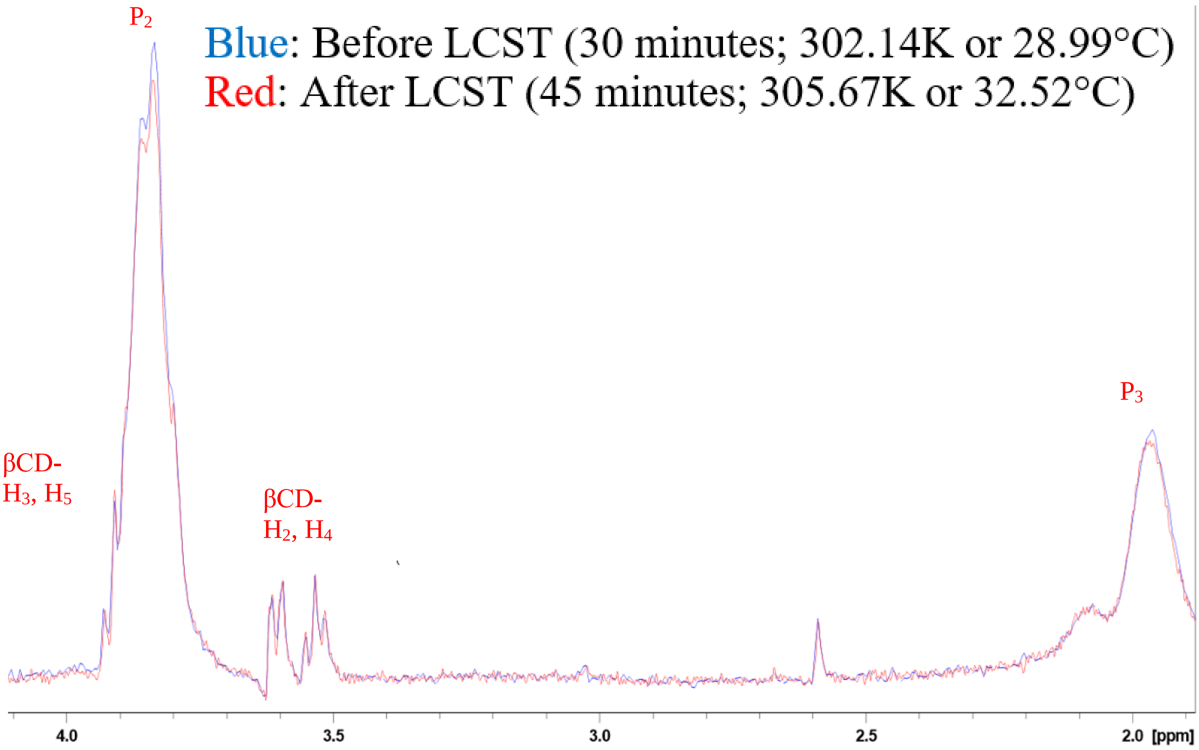

Figure 7.4.2: Zoomed in view of ***figure 7.4.1****. There is a slight decrease of intensity for P(NIPAM), but not for βCD. This indicates the beginning of the phase separation and shrinking is starting to take shape. The shrinkage becomes more substantial when the temperature>LCST.*

Before and after VPTT (34°C)

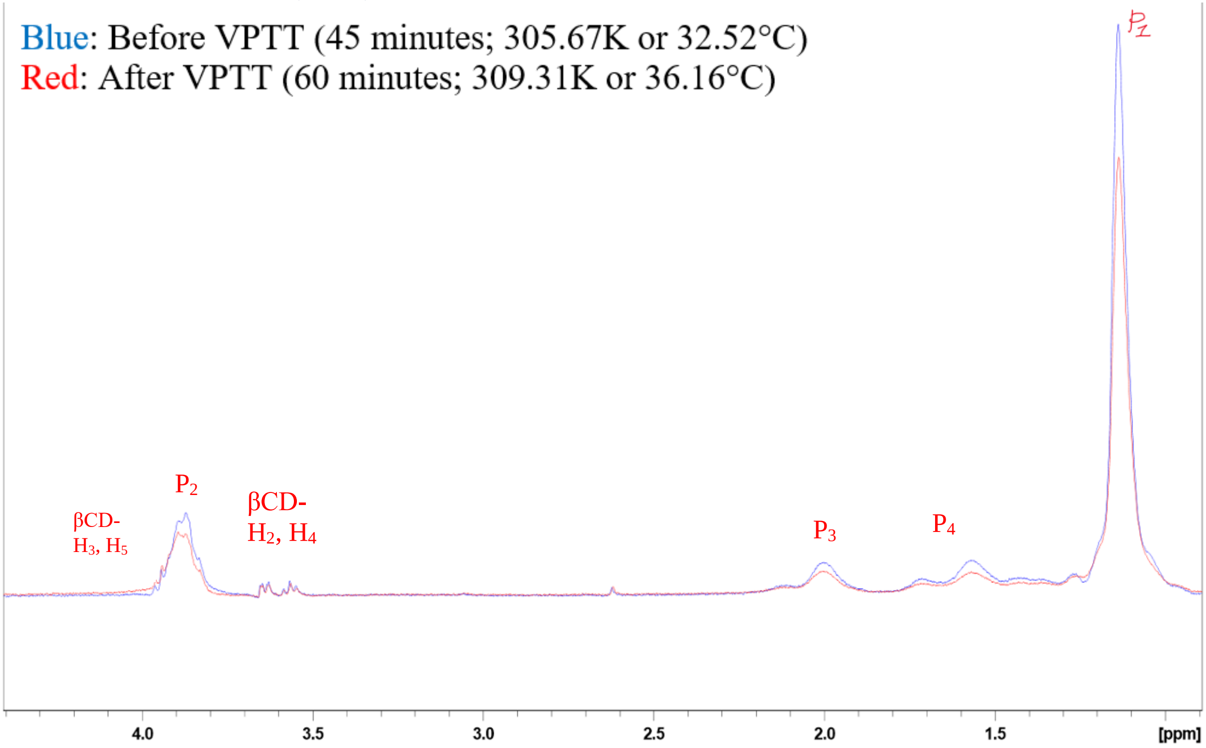

Figure 7.4.3: Spectrum of 40S before and after VPTT. The blue peaks represent the hydrogel and βCD at LCST, whilst the red is after VPTT, where VPTT is 34°C. The difference between the peak intensities are more apparent in contrast to what was observed in ***figure 7.4.1****. This indicates that the shrinkage is becoming more significant as the temperature>LCST and VPTT. The βCD intensity is still almost identical and have minimal change as observed for the* H_2 *and* H_4 *signals.*

Between the time interval of 30-45 minutes, **figure 7.4.3** shows the spectrum of the P(NIPAM) and βCD before and after VPTT with the time stamps and supposed temperature values according to the glycol reference in **Table 7.2.1**. **Figure 7.4.4** focuses on the βCD peaks: H_2-H_5 and the peaks for the P(NIPAM): P_2- P_4. The βCD peaks, H_2-H_5 barely changed, similar to what was observed in **Figure 7.4.2** before and after LCST. However, the P_2-P_4 peaks showed a substantial difference between intensities when the temperature approached and surpassed VPTT as seen by the height difference between the red and blue spectrum. This continuous, but gradual shrinkage was foreshadowed by the slight decrease of the P(NIPAM) intensities for P_2-P_4 before and around LCST observed in **Figure 7.4.2**. Further increase above LCST and VPTT would lead to a more accelerated phase separation and shrinking as a result of the degrading polymer network, but it will take time

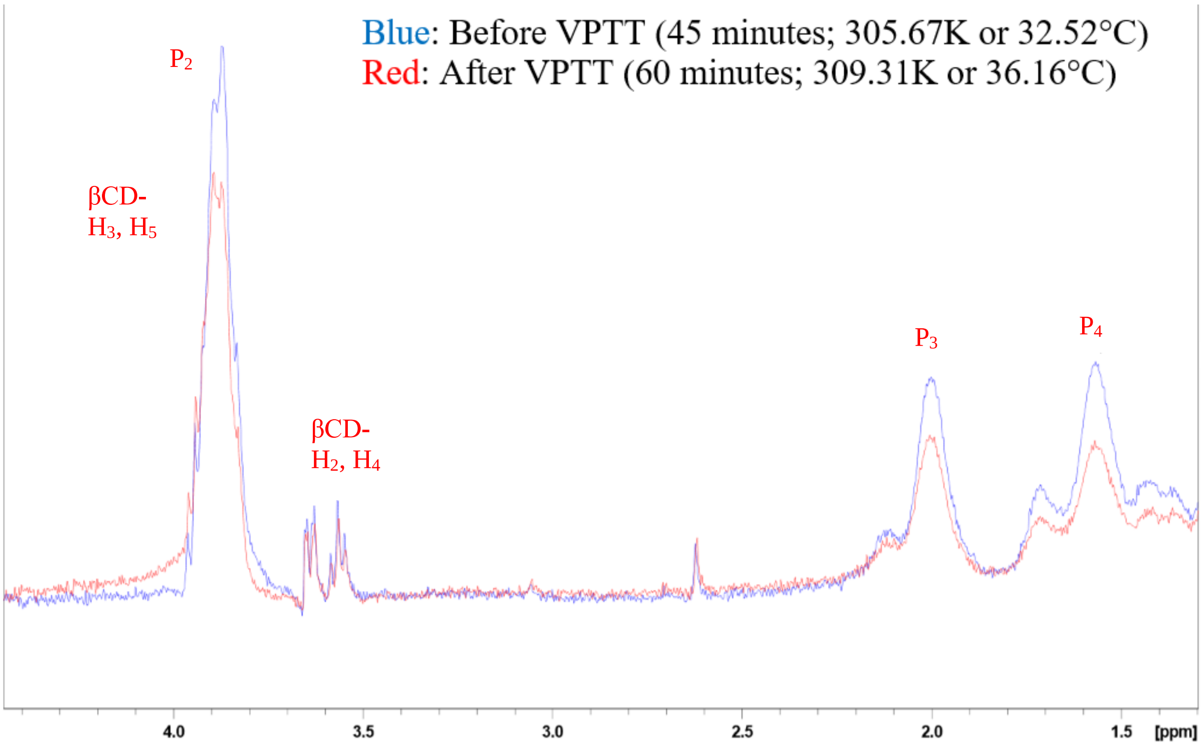

*Figure 7.4.4: Zoomed in view of **figure 7.4.3**. There is a more substantial decrease of intensity for P(NIPAM) as seen on the red spectrum. However, this was not the same case for βCD. The intensity of βCD peak, specifically for the H_2 and H_4 peaks have minimal deviation from one another. The phase separation and shrinking has become more substantial than what was seen in **figure 7.4.2** as the temperature>LCST and VPTT.*

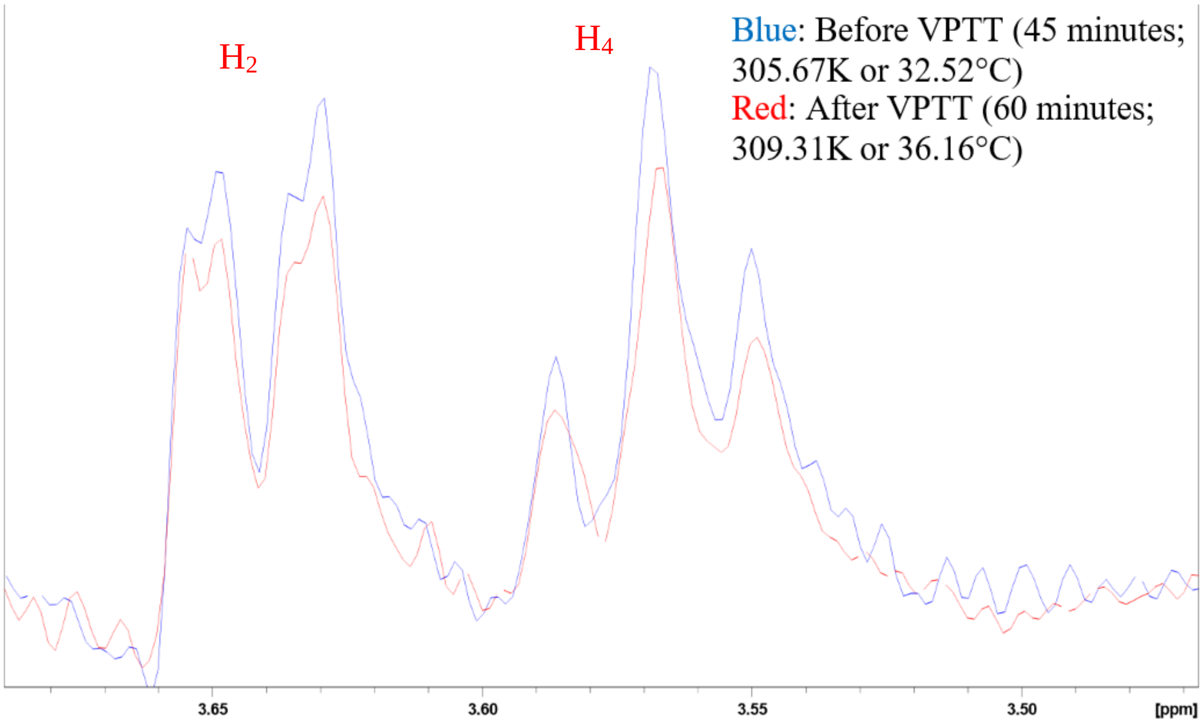

Figure 7.4.5: Zoomed in view of the H_2 and H_4 signals of βCD shows that surpassing VPTT led to a loss of intensity for βCD.

Figure 7.4.5 visualizes a magnified perspective of the signal intensities for a closer look into the H_2 and H_4 signals for βCD around the same time frame. A closer look shows that the βCD is actually beginning to gradually diffuse out of the hydrogel voxel onto the release medium as the signals for the red spectrum have a relatively weaker intensity than the blue spectrum. This ties in with the finding from **figure 7.4.3** and **figure 7.4.4**, where the hydrogel undergoes phase separation and, according to [20], the bubble formation on the surface will cause the entrapped βCD solution to be released outside and the hydrogel eventually achieves a stable and shrunken state.

Comparing 25°C and 40 °C

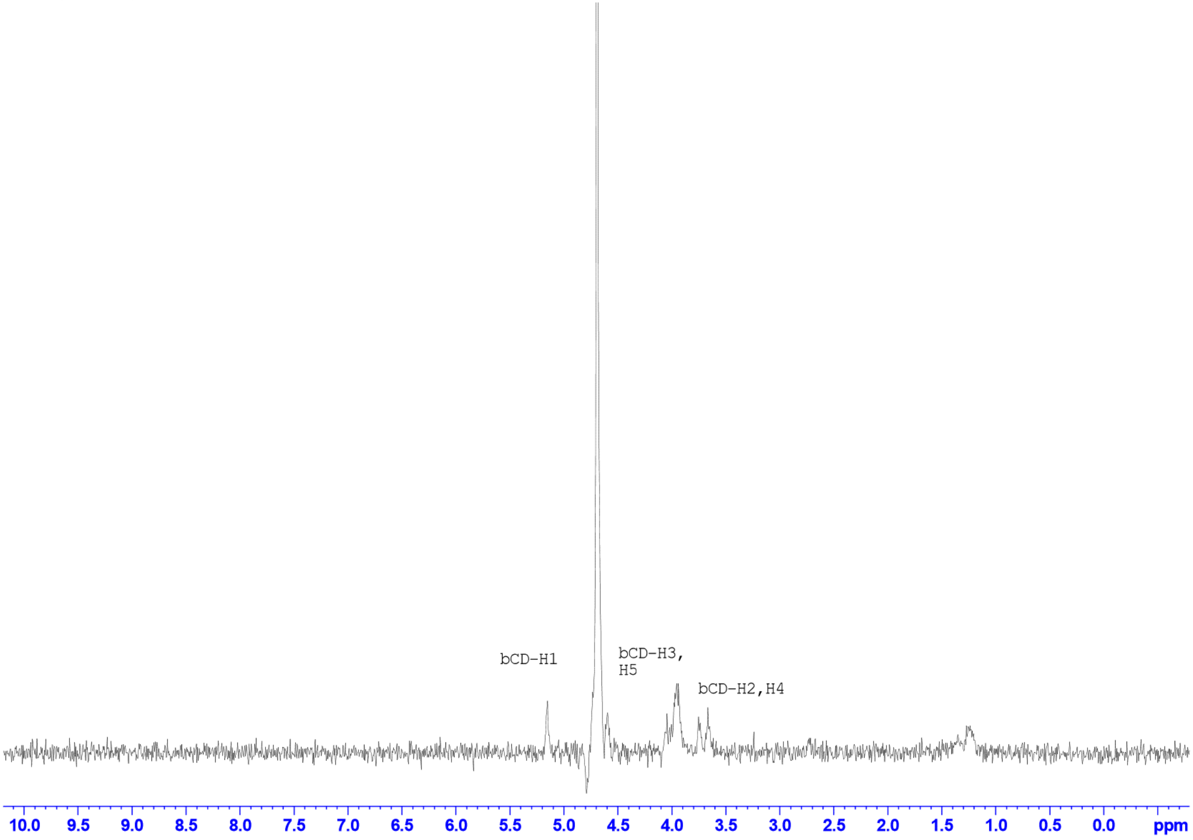

Figure 7.4.6: Last NMR spectrum at 40°C inside the gel. The P(NIPAM) signals have disappeared, and only the βCD is left. The spectrum was zoomed in to highlight the βCD signals clearly. However, this is deceptive as the degradation of the hydrogel network should lead to the release of significant portions of βCD onto the release medium.

Figure 7.4.6 shows the last run for 40S (210 minutes after temperature change), and it clearly shows that the signals for P(NIPAM) are now missing at 40°C. Only the βCD signals remain, but this is a magnified view of the peaks, and thus the βCD signals are actually weak, especially when compared to the first initial run at 25°C.

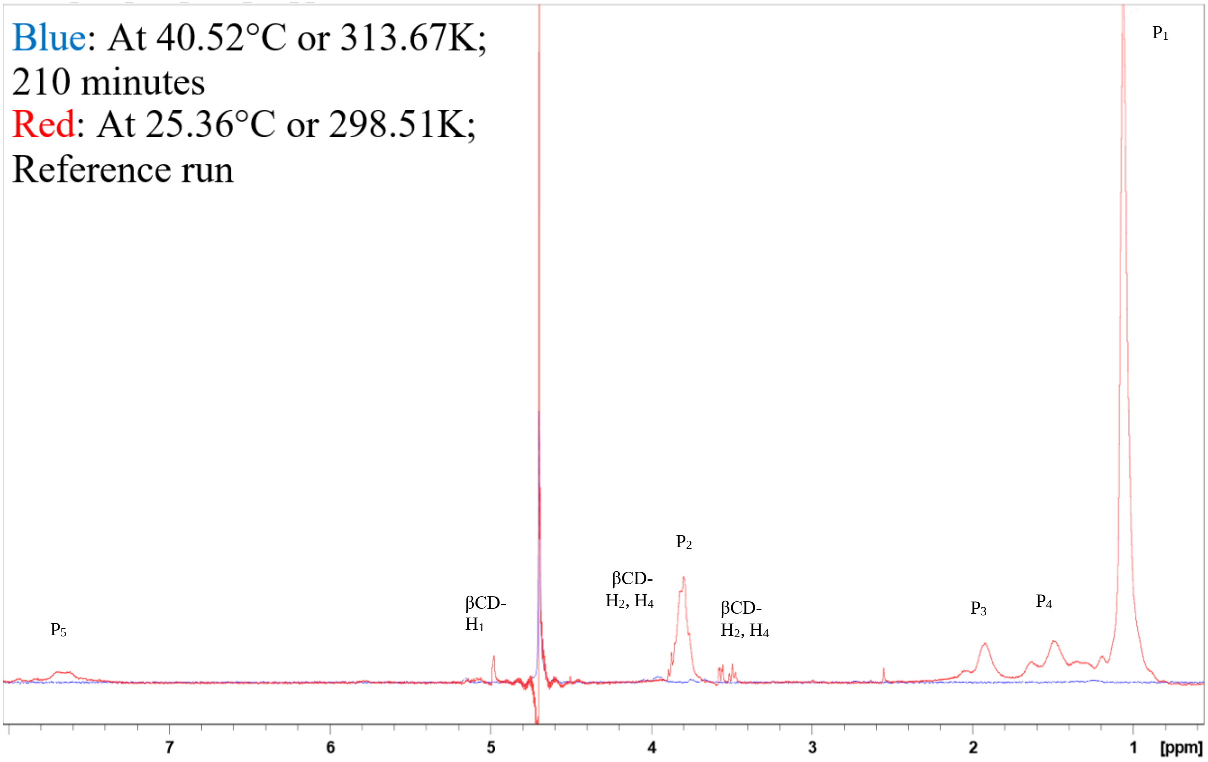

Figure 7.4.7: Comparison of NMR spectrums at 25°C (blue) and 40°C (red). The signals for βCD and the P(NIPAM) for the blue peaks are not visible, which indicates that the polymer network has degraded, and hydrophobicity has been achieved. In addition, a significant portion of the βCD has been diffused out to the release medium.

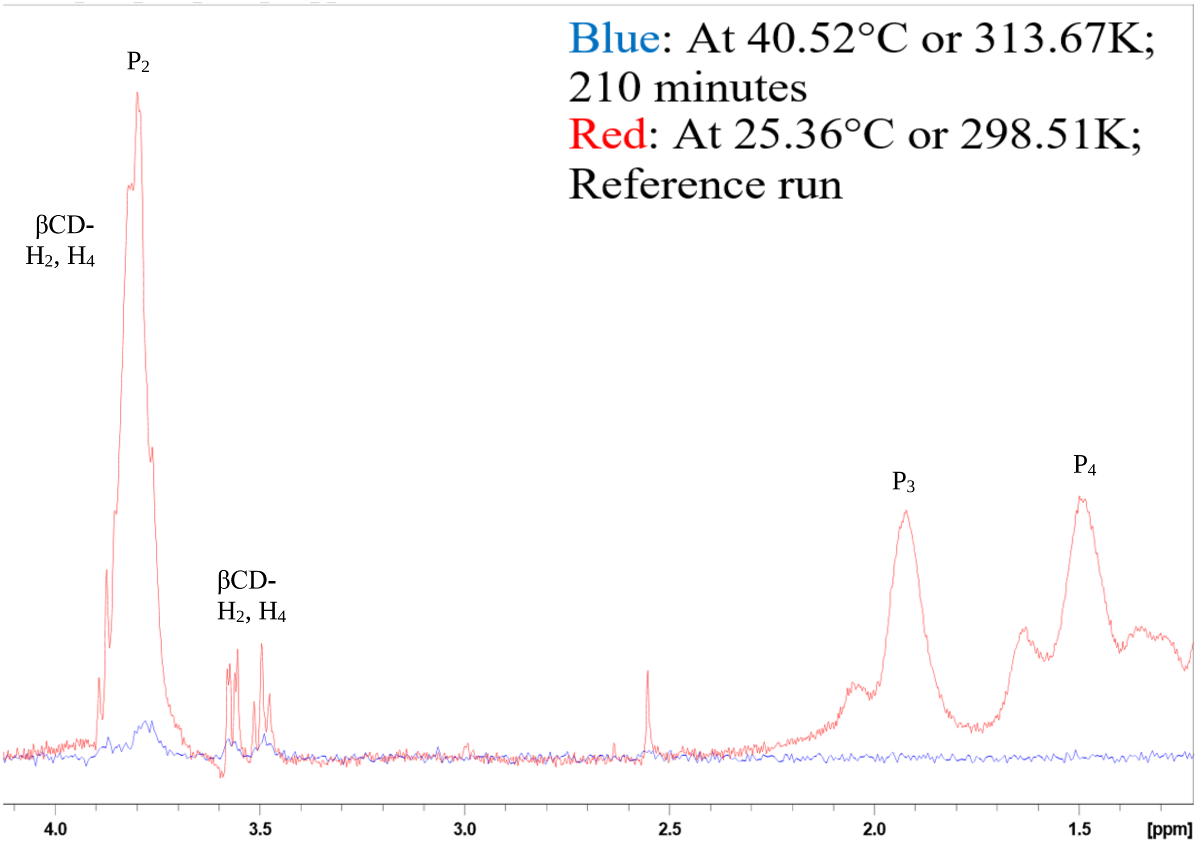

Figure 7.4.8: Zoomed in view of ***figure 7.4.7*** *for H_2-H_5 and P_2-P_4 signals. This confirms that the signals for βCD and P(NIPAM) have disappeared or at the very least have minimal presence in the voxel at the last run for the blue spectra after 210 minutes.*

With that in mind, the signal intensities, when scaled with respect to the first run at 25°C, are shown in **figure 7.4.7** and **figure 7.4.8**. The βCD signals and the P(NIPAM) signals for the blue spectrum are not visible at the end of the experiment when the temperature was 40°C. This consequently confirms that the hydrogel network has underwent coil-globule transition and the βCD solution was extruded into the release medium as supported also by the MSME pictures of 40S, 40ST, and 40T. **Figure 7.3.2, 7.3.6, and 7.3.8** shows how much has the P(NIPAM) degraded at the last experiment run. If some βCD signals were seen to be strong enough in the spectra, this could be explained by the substantial shrinkage of the gel that could occur. A significant shrinkage of the gel can lead to the voxel inside the gel to eventually border or protrude outside the 0mm interface of the collapsed gel. This was apparent for 40T in **figure 7.3.8** where the voxel inside the gel is very close to the 0mm interface now due to the rapid degradation of the gel structure. Given some time, it will most likely protrude outside eventually, thus record in the spectra that a significant βCD signal is observed, even though the previous runs showed that βCD was found at a very low concentration. Steps were taken to reduce this possibility as by placing the voxel deep within the hydrogel to account for the shrinkage, and as such, avoided this scenario for all temperature experiments.

Last experiment runs for 31T, 40S, 40ST, and 40T

Figure 7.4.9 shows an overview of the last runs for each temperature experiment. 31T never reached LCST or VPTT, so the signals for both P(NIPAM) and βCD are still present, and the intensity of the peaks are stronger here than in 40S, 40ST, and 40T. On the other hand, the 40ST, 40T and 40S temperature experiments showed no signals for the P(NIPAM) and very feint signals for βCD. These weak signals are made visible through magnification in **figure 7.4.10**. Even at the end of the experiments, βCD is present in all experiments, but only in small concentrations. Given how 40ST, 40T, and 40S eventually surpasses VPTT, the decrease in signal intensities for both βCD and P(NIPAM) were expected as a result of the coil-to-globule transition.

In addition, this transition gives an indication that the mobility of the P(NIPAM) chains become more restricted and slowed as hydrogel undergoes the coil-to-globule phase transition, which leads to the water and βCD to be diffused out of the polymer network. The transition's consequence is that the gel become solid-like as a result of the strengthening of hydrophobic interactions. A paper done by Anders Larsson mentioned that there is a clear distinction of liquid and solid spins. Solid compounds exhibit more restriction when it comes to mobility as a result of dipolar interactions on a molecular scale because it leads to rapid relaxation and broadening of the resonance signals of the collapsed P(NIPAM). This broadening makes it impossible to be detected in a liquid-state NMR technique, which was the same technique used for this experiment. Moreover, it was also observed in Ander's paper that the loss of the 1H signal of the P(NIPAM) meant that the T_2-relaxation was decreasing as well [24]. This was observed as well in Wisniewska's paper, particularly for her 40°C temperature jump, and to a lesser extent, her 40°C slow-heating experiment (see **attachment 5**) [4]. The literature work point to the direction higher temperature=lower T_2, which means lower mobility of the molecules inside the polymer network. The spectras have shown the disappearance of the P(NIPAM) after incubating for several hours in 40°C, and it is impossible to see the peaks du to the usage of a liquid-state NMR technique.

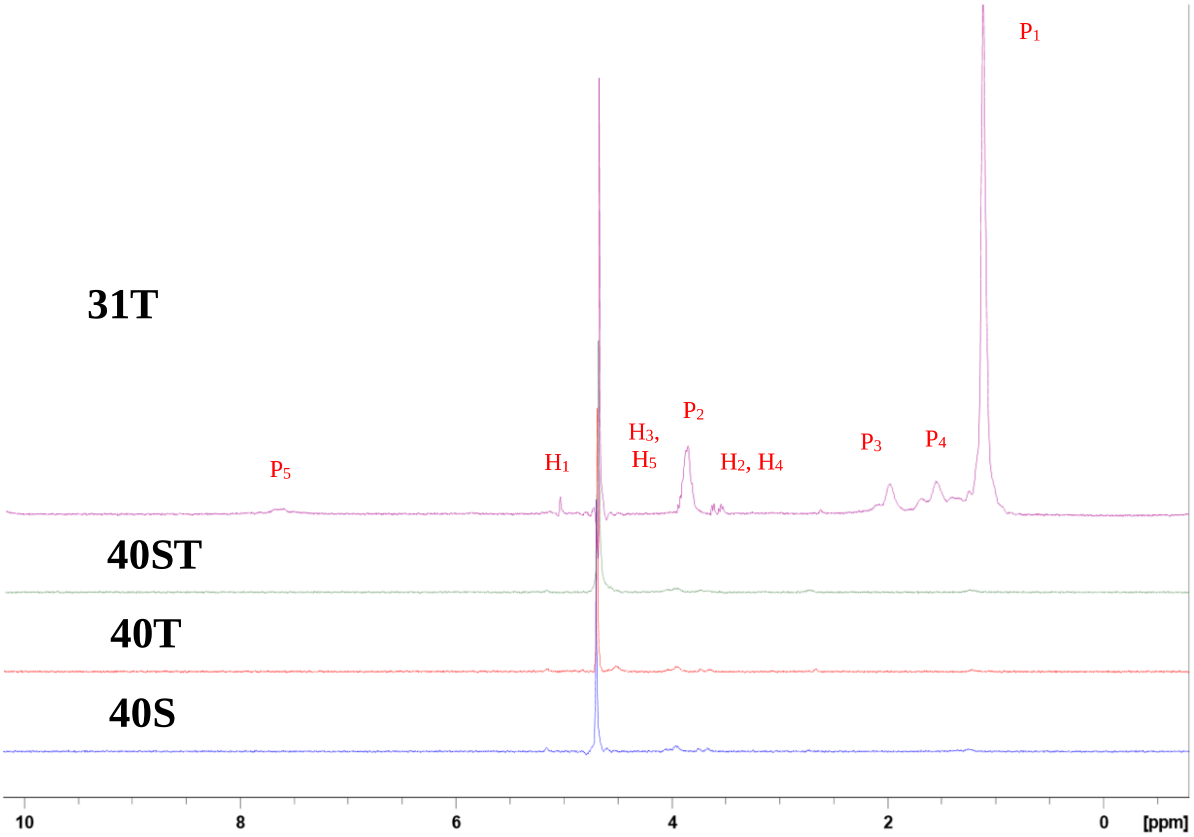

Figure 7.4.9: Overview of the last run for each temperature experiment. The peaks are labelled on the 31T as a reference point. 31T's spectrum is represented by the red violet color, followed by 40ST's green representation, 40T's red representation, and the final experiment, 40S is represented by the blue color. The peaks for the P(NIPAM), the $P_{(x)}$ signals are not seen clearly for 40ST, 40T, and 40S, but in the 31T, the peaks are present. The βCD signals, $H_{(x)}$ are significantly visible for 31T, but not for the rest of the temperature experiment as they are too weak to be seen. This overview coincides with the MSME of all the temperature experiments.

The broadening effect was also observed in a paper by Tokuhiro et al. His paper reported a broad peek centered around 8 ppm at 34°C and a gradual disappearance of all the hydrogel's signals below LCST as temperature was increased. Tokuhiro described the transformation of the CH_3, CH_2 and CH peaks in the swollen state into a part of the new broad peak as temperature increased, even during the hydrogel's collapsed state. Kinetically, the process was slow, so the time the band took to equilibrate was lengthy. This broadening effect was influenced by the dipole-dipole interactions between the protons that dominated during the collapsed state(after VPTT), which overpowered the motional narrowing effect. The motional narrowing effect was the effect in which the molecules moved around more vigorously as temperature increased, which allowed for peaks to be more discernible. In the case of P(NIPAM), this was apparent for P_3 and P_4(see **attachment 6**). Tokuhiro also mentioned that in the collapsed state, the spectral width of the broad peak was around 3.1 kHz when it was 35.6°C. The experiment conducted for this dissertation used the same spectral width value as [4], which was 5.5 kHz. Both spectral values are relatively comparable to one another [25].

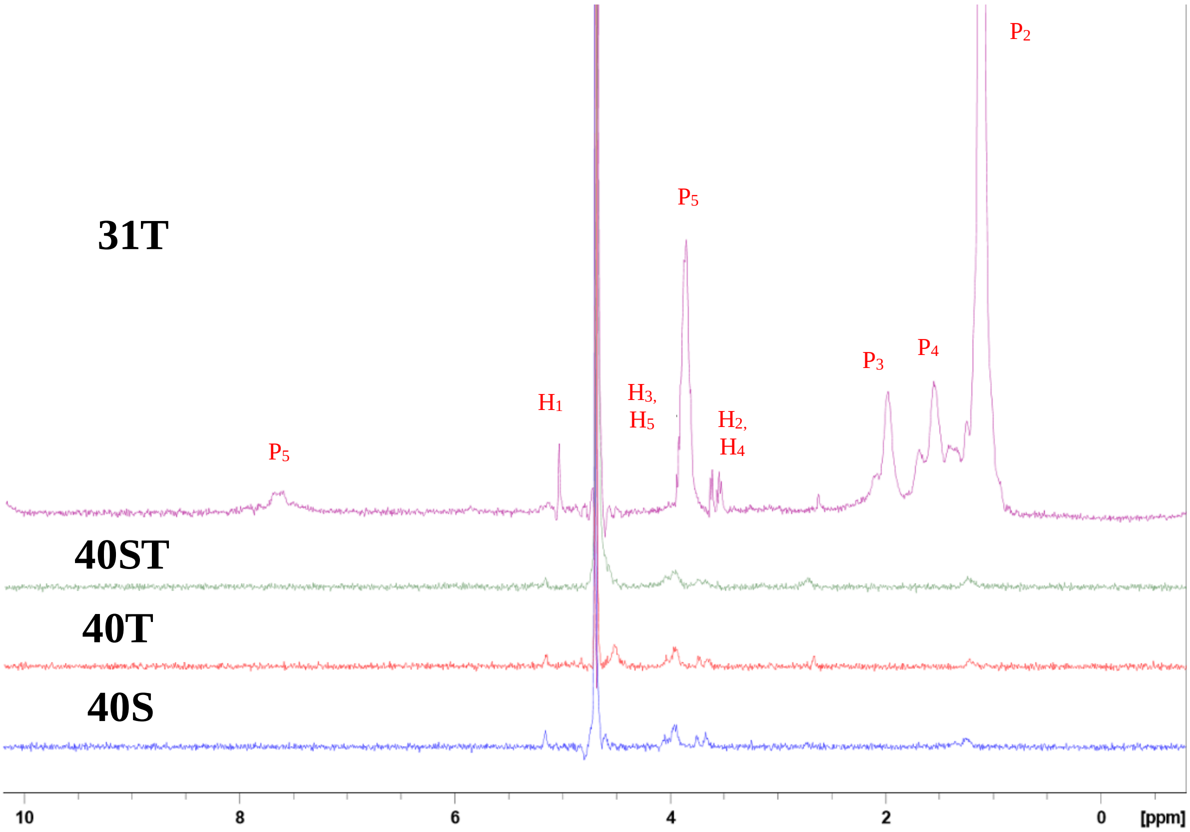

*Figure 7.4.10: Closer view of **figure 7.4.9**. The $H_{(x)}$ signals for βCD are more visible for all the temperature experiments. Focusing on 40ST, 40T, and 40S, it can be confirmed that some βCD still remains in the gel, albeit in a very small concentration, especially compared to the 31T experiment.*

The sample right before 40°C

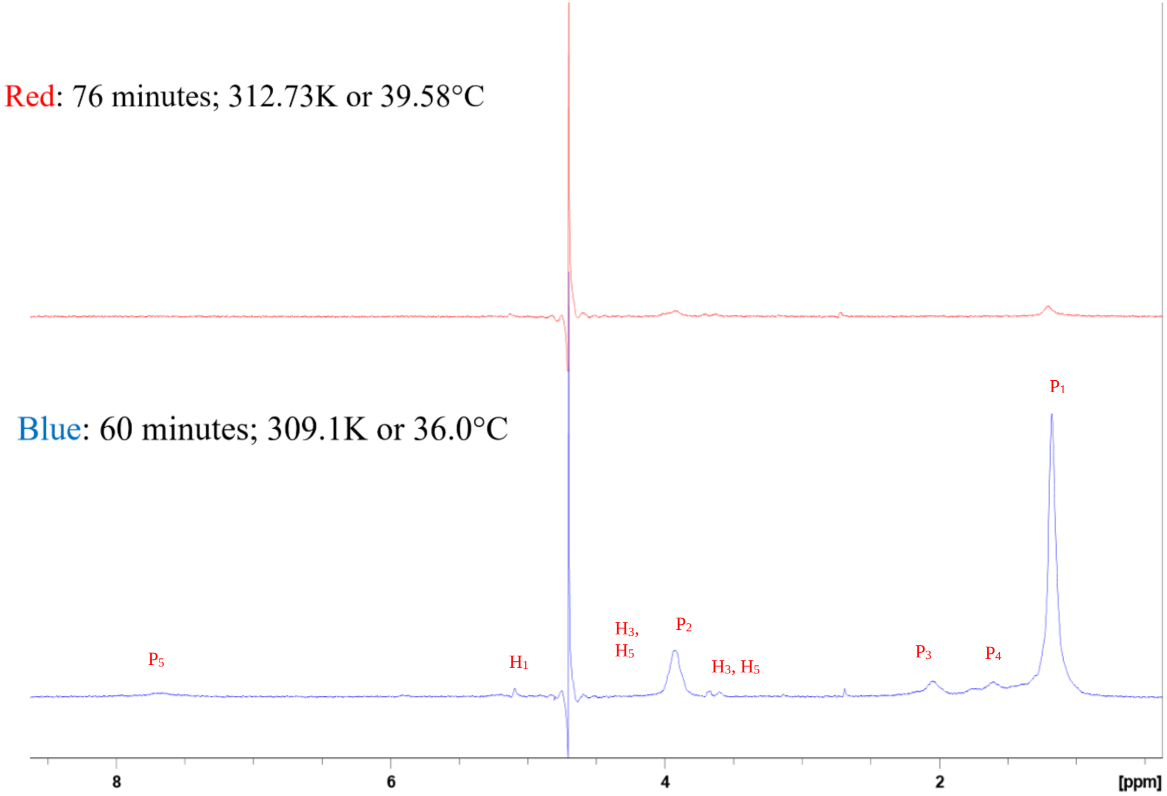

Figure 7.4.11: P(NIPAM) and βCD signals transitioning from 36°C to 39.58°C as the sample approaches to 40°C. The 16 minute gap between the two spectra shows a majority of the signals for both P(NIPAM) and βCD have disappeared significantly. Some weak intensities are still observed, but these will most probably degrade and weaken overtime as the sample incubates at 40°C as shown by the MSME pictures in the previous subsection (7.3).

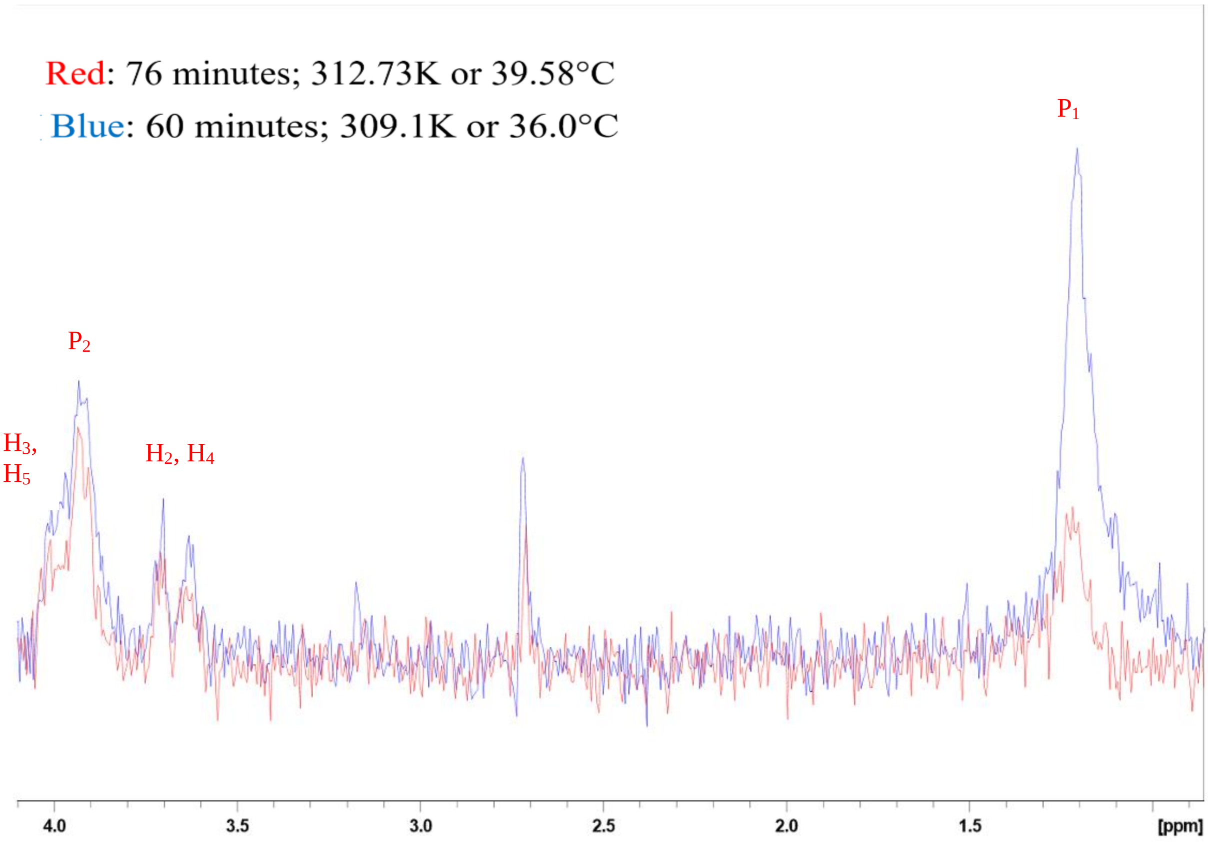

Figure 7.4.12: A closer look of the hydrogel sample between 1.0ppm-4.0ppm when t=60minutes(blue) and t=76 minutes(red). The blue spectrum is at 36.0°C, just 4°C shy from 40°C. The red spectrum is at 39.58°C, which is approximately 0.4°C away from the final temperature for the interval. This zoomed in visualize supports the description of ***figure 7.4.11****, particularly for the* P_1 *signal. Although VPTT was surpassed, the most apparent changes occur as temperatures is increased further from VPTT. In this case, the closer the sample is to 40°C, the more dramatic the changes become in a short space of time.*

The signals for both βCD and P(NIPAM) decrease overtime as shown in **figure 7.4.11**, where the signal change gap between the two spectra become larger from the 60th minute mark transitioning to the 76th minute mark as the sample approaches 40°C. Looking at **figure 7.4.12** afterwards, one can observe a closer look of the details seen in **figure 7.4.11**, where signal intensity gap between the two spectra are highlighted. However, this also indicates that P(NIPAM) signals even after VPTT, will require time before the complete collapse is fully realized. Although βCD is still present, the changes in intensity will gradually become lower as the diffusion equilibrates inside the collapsed polymer network and in the release medium. To know whether the βCD concentration will drop at the expected transition temperatures inside the hydrogel, A βCD intensity analysis using MATLAB would be needed and discussed further in the next sub-section.

(7.5) Quantitative analysis of βCD release inside of the gel using STEAM 40S

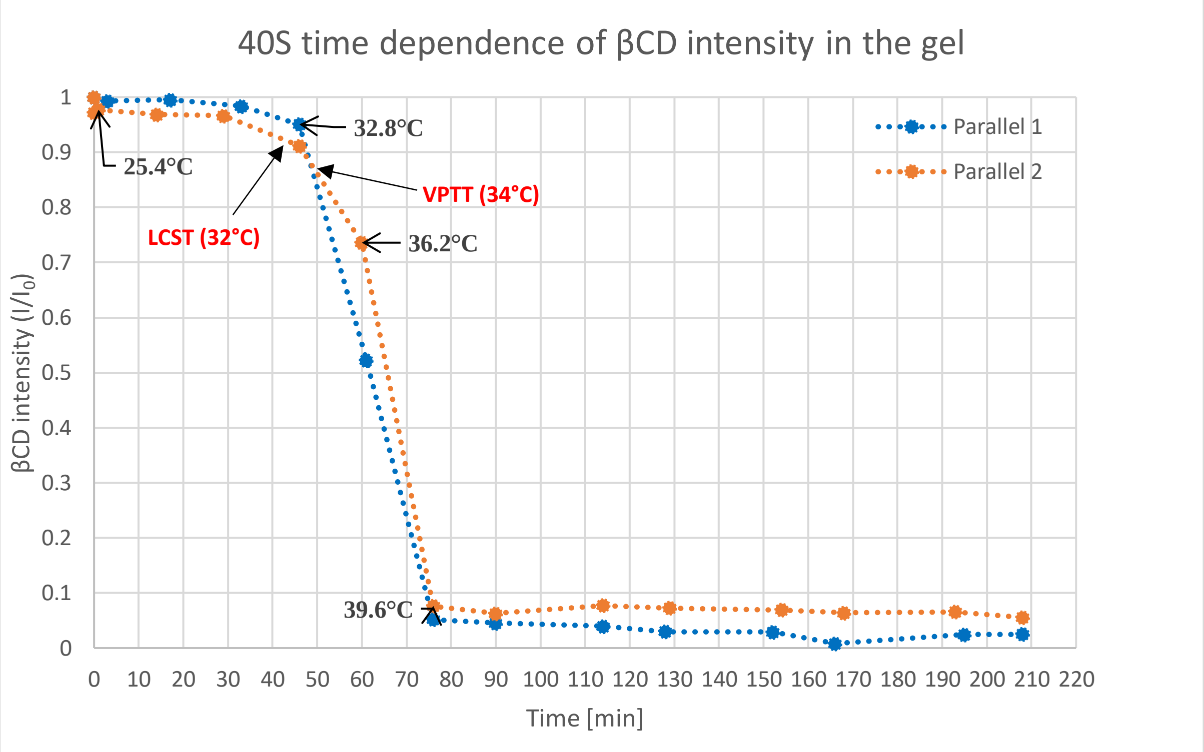

*Figure 7.5.1: Time dependence of the normalized βCD intensity with respect to their initial reference value for 40S. 2 parallels were done, and temperature marks are labelled with respect to temperature-time correlation curve in **figure 7.2.2** to observe the trend right before VPTT and after VPTT. VPTT for 40S is achieved when t= 50 minutes after the temperature change, and LCST is achieved when t= 43 minutes after the temperature change. The graph shows how the decrease of βCD gradually begins before the 40 minute mark(LCST), and the steep decrease in βCD intensity happens after the 50 minute mark(VPTT). The transition between 32.8°C and 36.2°C(before and after VPTT) highlights the phase transition of the P(NIPAM) and extrusion of βCD from the polymer network as temperature>VPTT. Once 40 °C was achieved, both parallels showcased a low plateau that approached 0 on the y-axis, thus signaling that a majority of the βCD has been expelled.*

The βCD intensity before LCST and shortly after LCST only decreased to 98%-90% of the initial βCD intensity between the 2 parallels. Compare this to the steep decrease of βCD intensity seen after LCST as temperature approaches and goes over VPTT at t= 50 minutes in **Figure 7.5.1**. For parallel 1, the βCD intensity goes from 95% → 53% → 5% between t= 46-76 minutes. For parallel 2, the βCD intensity goes from 91% → 74% → 8% in the same time interval described for parallel 1. Both parallels, although not mirroring the exact values for βCD intensity during the phase separation, still showcase a high degree of similarity, particularly before VPTT and at the end of the hydrophobic transition of P(NIPAM) after VPTT. **Figure 7.4.13** takes both parallel 1 and 2 to create the average fit curve. The curve follows the general pattern seen from both parallels and have minimal variation except at t=60 minutes, where the standard deviation is relatively high. This variation happens during the significant drop in βCD intensity after VPTT as a result of diffusion of βCD out of the degrading polymer network.

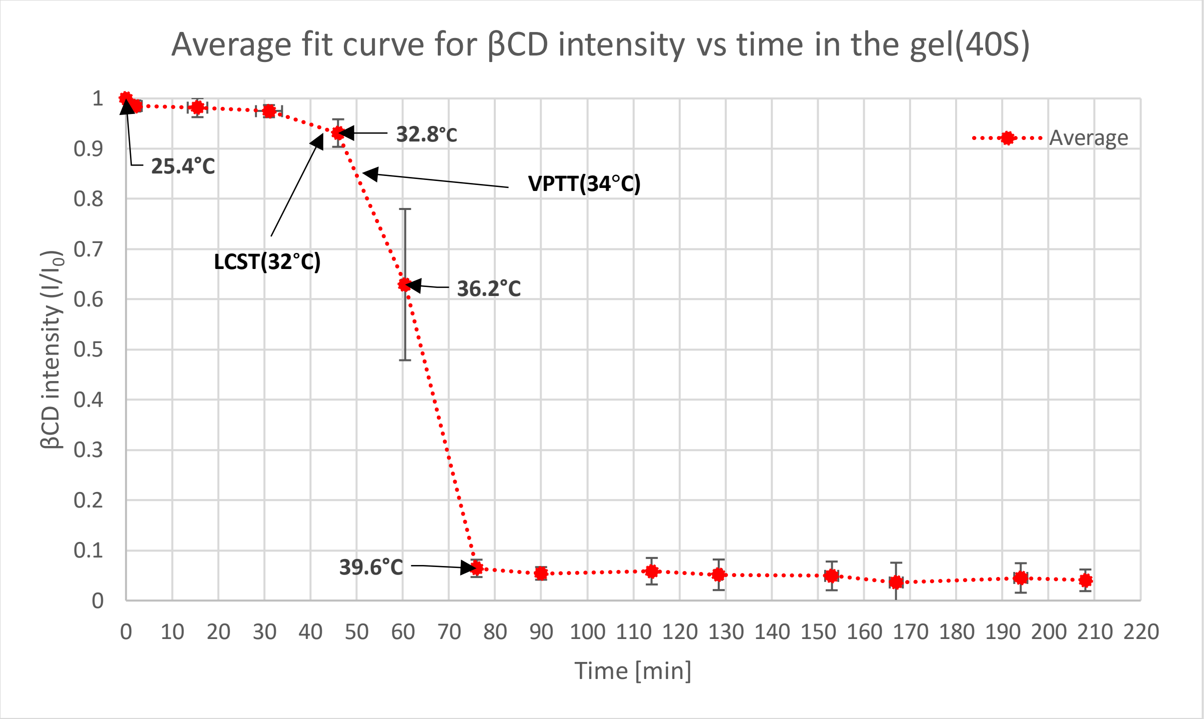

*Figure 7.5.2: Average fit curve of **figure 7.5.1** with error bars and temperature markings. The variation was at the highest during the steep decrease in βCD intensity when t=60 minutes. Here the temperature has already surpassed VPTT by 2°C and the intensity has dropped to 60.5% of the initial intensity. Around LCST, the βCD intensity never went lower than 90% of the initial intensity. The plateau is established after VPTT when t=76 minutes, where the temperature is 39.6°C, and the intensity ratios are only close to zero, signalling that some βCD still remains in the gel voxel.*

The trend seen in **figure 7.5.2** agrees with both the MSME pictures of 40S in **figure 7.3.5** and the spectra comparison before and after LCST in **figure 7.4.1**, where it showed minimal change both on the surface level and on the microscopic scale in the NMR spectra for βCD and P(NIPAM). Although the change is not as observable on the MSME pictures before and after VPTT besides the increase in opaqueness, the phase separation that occurs at VPT is clear in **figure 7.4.3** and **7.4.4**. It is after VPTT where the substantial decrease in both P(NIPAM) at βCD signals begin to take place. Interestingly, the MSME images show minimal changes when t=58 minutes compared to its 1st run in **figure 7.3.5**. It wasn't until 40°C was reached t=80 minutes before any significant changes appeared on the MSME. Although some correlation can be seen with the gradual opaqueness being associated with the deswelling of P(NIPAM) as it approaches LCST and VPTT, the STEAM sequence ultimately illuminates the hidden reaction inside the polymer network on what could have been missed if only the MSME images were taken. By t=80 minutes, there is no more βCD left inside the voxel in the hydrogel, thus signaling that it has been squeezed out of the system most likely due to VPT.

With this in mind, The decrease of signal intensity for both βCD and P(NIPAM) continues on as the sample approaches 40°C as seen in **figure 7.4.11** and **figure 7.4.12**. These support the sharp decrease seen in **figure 7.5.2** after VPTT as the point where βCD begins to diffuse substantially as a result of the coil-to-globule transition. The low plateau observed at the end after 40°C indicates that there is still some βCD left, but the concentration here is very low. This is supported by **figure 7.4.11** and **7.4.12**, where it showed that even being very near 40°C, some βCD and P(NIPAM) signals were still present, but the intensities are feeble. Eventually the P(NIPAM) signals disappear completely as shown in **figure 7.4.6**, except for βCD.

40ST

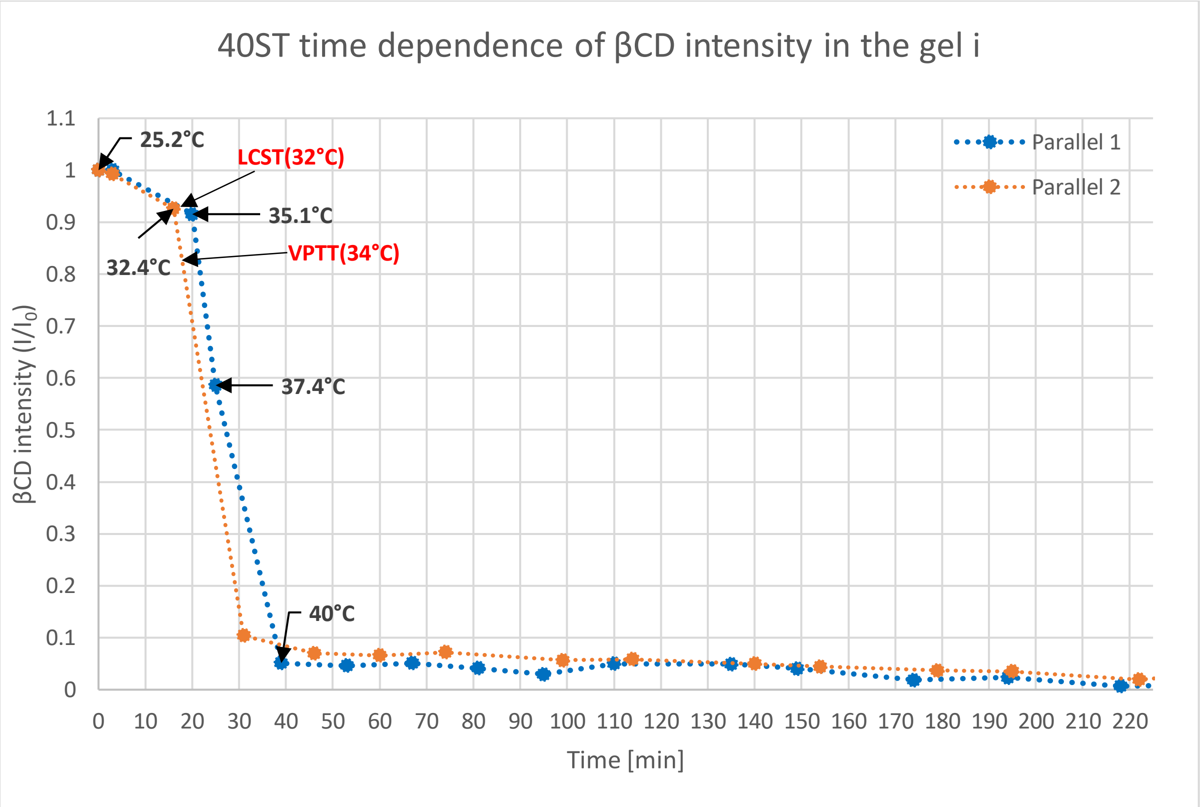

*Figure 7.5.3: Time dependence of the normalized βCD intensity with respect to their initial reference value for 40ST. 2 parallels were done, and temperature marks are labelled with respect to temperature-time correlation curve in **figure 7.2.7** to observe the trend right before VPTT and after VPTT. VPTT for 40ST is achieved when t=19 minutes after the temperature change, and LCST is achieved when t=16 minutes after the temperature change.*

Looking at **figure 7.5.3**, the time dependence of the normalized βCD intensity is visualized in a graph for 40ST for parallel 1 and 2. The transition temperature marks are present along with the recorded temperatures before and after LCST, and VPTT. It should be noted that the gap between LCST and VPTT for 40ST, similar to what is expected for all the temperature jump experiments, is very short, especially compared to the slow-heating experiment, 40S. Parallel 1 and parallel 2 in **figure 7.5.3** shows some similarities to what was observed in **figure 7.5.1** for 40S, namely having the steep decrease of the βCD intensity after VPTT and having a low plateau after reaching 40°C at t=39 minutes according to **figure 7.2.7**. The βCD intensity from the steep decline to the low plateau for parallel 2 goes from 93% → 10% for parallel 2 when t= 16 minutes and t=31 minutes respectively after temperature change. For parallel 1, it goes from 92% →59% → 5% when t=20, 25, and 39 minutes after temperature change in that specific order. With this in mind, the general patterns seen for parallel 1 and 2 from the gradual decrease seen around LCST, to the steep decline after VPTT and the lower plateau at 40 °C shares similarities with 40S. The key difference here however is that the vital transition events for **figure 7.5.3** occurred sooner due to the temperature-jump setting in 40ST as stated in **table 5.2.1**. It is noted that in parallel 1, the βCD intensity at t=20 minutes is 92%, which is higher than one might think after reaching VPTT. However, it is only a minute since VPTT was achieved, and it should be recalled in the spectra comparisons at **figure 7.4.4** and **figure 7.4.5,** the βCD intensity peaks decreased overtime. The decrease in concentration becomes more substantial the higher the temperature.

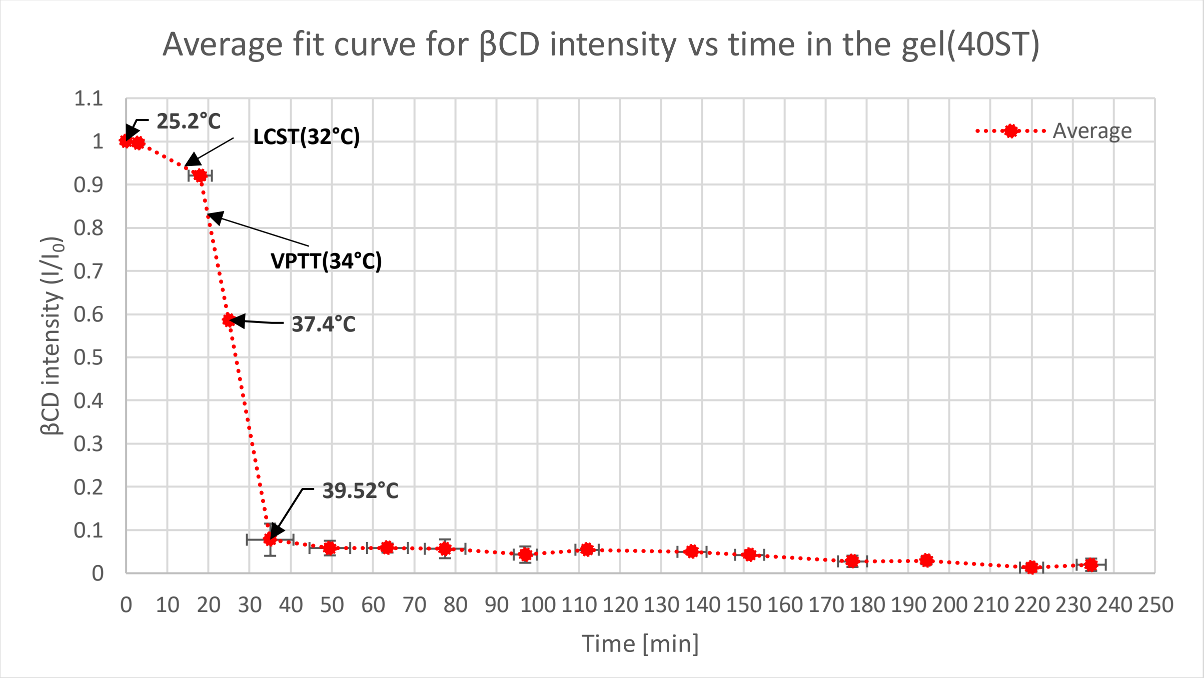

Figure 7.5.4: Average fit curve of ***figure 7.5.3*** *with error bars and temperature markings. The variation was low overall on the βCD intensity. The variation for time varied to some extent due to different measurements done at a slightly later or earlier time stamp than the other parallel. The point after VPTT has a temperature value of 37.4°C when t=25 minutes, and it shows that the average βCD intensity here is 59% of the initial intensity. Like the 40S trend for the βCD intensity, the βCD intensity never went lower than 90% of the initial intensity near LCST, and a plateau is established when the temperature is near 40°C when t=35 minutes.*

Similar to the 40S trend and observations in **figure 7.5.2**, **figure 7.5.4** is coherent with the MSME pictures and hydrogel transition kinetics at LCST, VPTT and 40°C. The low plateau at t=35 minutes shows that the hydrogel has collapsed as shown in the MSME picture at **figure 7.3.1**, where the pictures at the 37th minute mark shows the distinct shrinkage as the 0mm interface of the hydrogel becomes displaced as a result of the temperature jump. In addition, the significant drop in βCD occurs after VPTT, gradually increasing in magnitude with higher temperatures as shown in the spectra comparison before and after VPTT at **figure 7.4.3-7.4.5.** It can also be visualized in the spectra comparison, where the temperature is close to obtaining 40°C in **figure 7.4.11** and **figure 7.4.12**. The decrease in intensity becomes more extensive. As mentioned earlier, the transition temperatures for 40ST are achieved faster, thus the changes of the βCD intensity with time are more rapid. For reference, the steep decline for 40ST in **figure 7.5.4** does not occur until t=18 minutes after temperature change, whilst 40S in **figure 7.5.2** starts its steep decline when t=45 minutes after the first temperature change.

40T

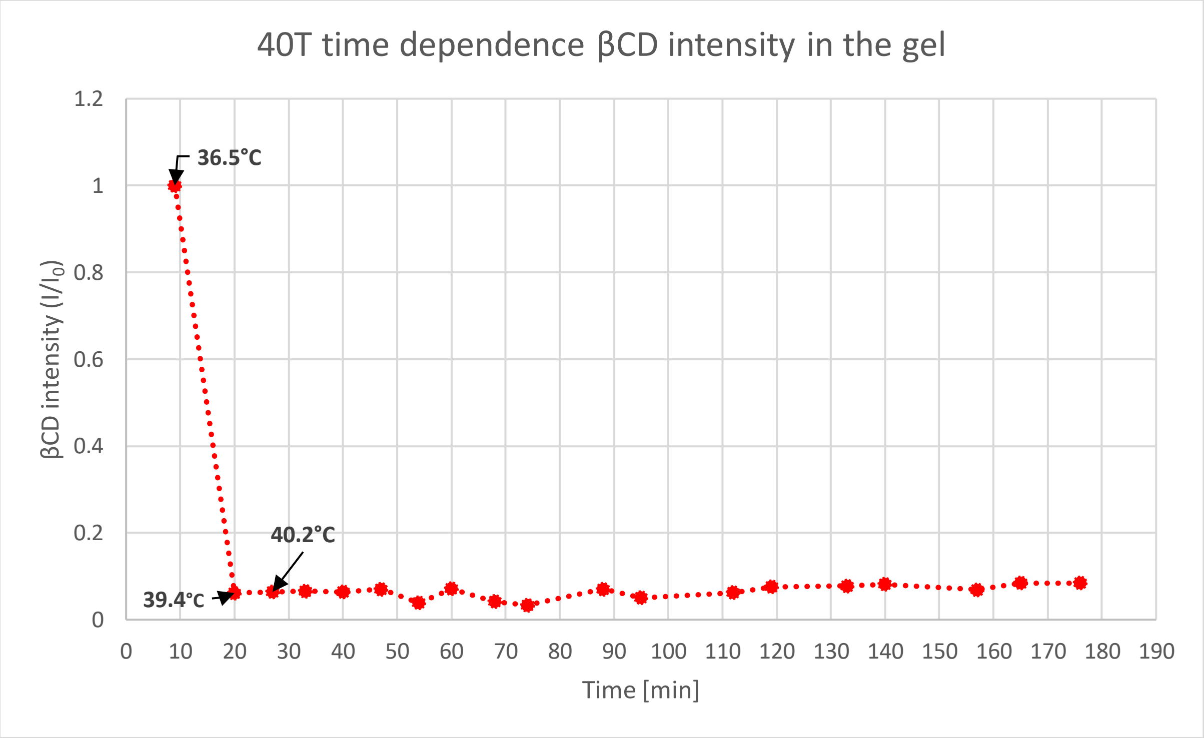

Figure 7.5.5: Time dependence of the normalized βCD intensity with respect to their initial reference value for 40T. 1 parallel was done, and temperature marks are labelled with respect to temperature-time correlation curve in ***figure 7.2.5*** *to observe the trend right before VPTT and after VPTT. VPTT for 40T is achieved when t= 6 minutes and LCST is when t= 5 minutes, thus this experiment's 1st run was already too late to record the data points prior to LCST and VPTT. Due to the nature of this temperature jump experiment, this was difficult to avoid, and was the reason the 40ST temperature protocol experiment was created to get a better visualization of the activity inside the hydrogel at a more controllable pace.*

Figure 7.5.5 visualizes the time dependence of the normalized βCD intensity for 40T. The first recorded data point was recorded at t=9 minutes(36.5°C), which is already above VPTT and LCST. Similar to 40ST, the LCST and VPTT gap is small, and because of the time it took before the 1st STEAM sequence was run, the experiment started already surpassing both LCST and VPTT at t=9 minutes after the sample was inserted. This means that phase separation and substantial portions of βCD was being diffused out of the polymer network. This can be observed as the 2nd point already shows the steep decline and low plateau in βCD intensity when t= 20 minutes after the sample was inserted. The temperature at the 2nd point is at 39.4°C already, and the shrinkage is noticeable in **figure 7.3.7** as one can observe the heigh difference from t=4 minutes(31°C) and t=19 minutes (39°C). The intensity of βCD at the plateau varied between 6-8% from its original βCD intensity from the 10 minute-mark. The observations support the characteristic rapid shrinkage and transition for this temperature experiment protocol, which was mentioned in the qualitative description of the hydrogel in 40T.

31T

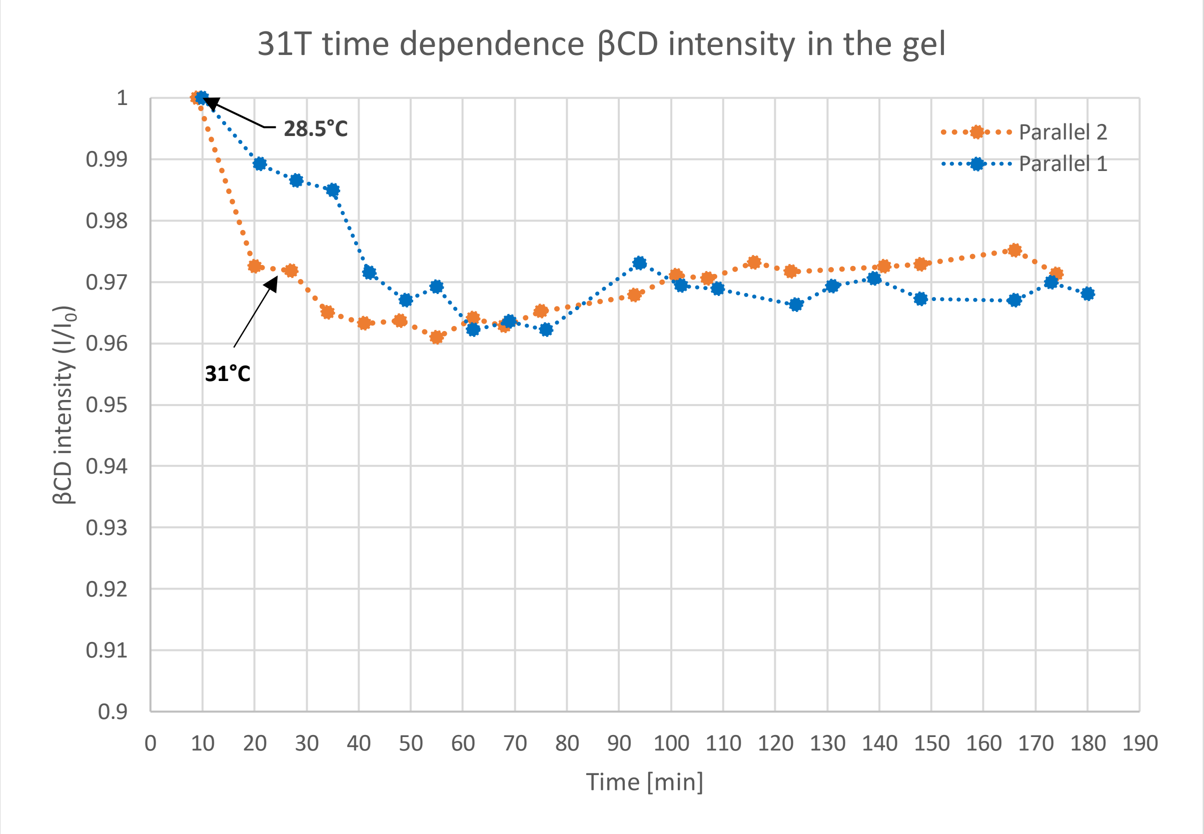

*Figure 7.5.6: Time dependence of the normalized βCD intensity with respect to their initial reference value for 31T. 2 parallels were done, and temperature marks are labelled with respect to temperature-time correlation curve in **Figure 7.2.9** to observe the trend. For this temperature experiment, both LCST and VPTT were not reached, and 31°C was reached when t=25 minutes after inserting the sample.*

Figure 7.5.6 visualizes the time dependence of the normalized βCD intensity, and **figure 7.5.7** shows its average fit curve. The first recorded data point was recorded at t= 9 minutes for parallel 2 and t=10 minutes for parallel 1. Both parallels shows some variations with their I/I_0, but their values only varied between 96%-99% of the initial βCD intensity value. Both still show a similar good general trend of decreasing slightly at the beginning up to 60th minute before increasing slightly and fluctuating in between values. Their low I/I_0 values, especially compared to the previous temperature experiments reflect the experimental conditions for 31T, in which it never reached beyond LCST or VPTT. Consequently, phase transition never occurred and βCD is still trapped inside the hydrogel network. The average fit curve of **figure 7.5.7** shows that both parallels only varied at the beginning of the experiment before eventually reducing its uncertainty. In the grand-scale, these variations are not as significant compared to 40S, 40T, and 40ST as this temperature experiment only decrease up to 96% of the initial βCD intensity at best.

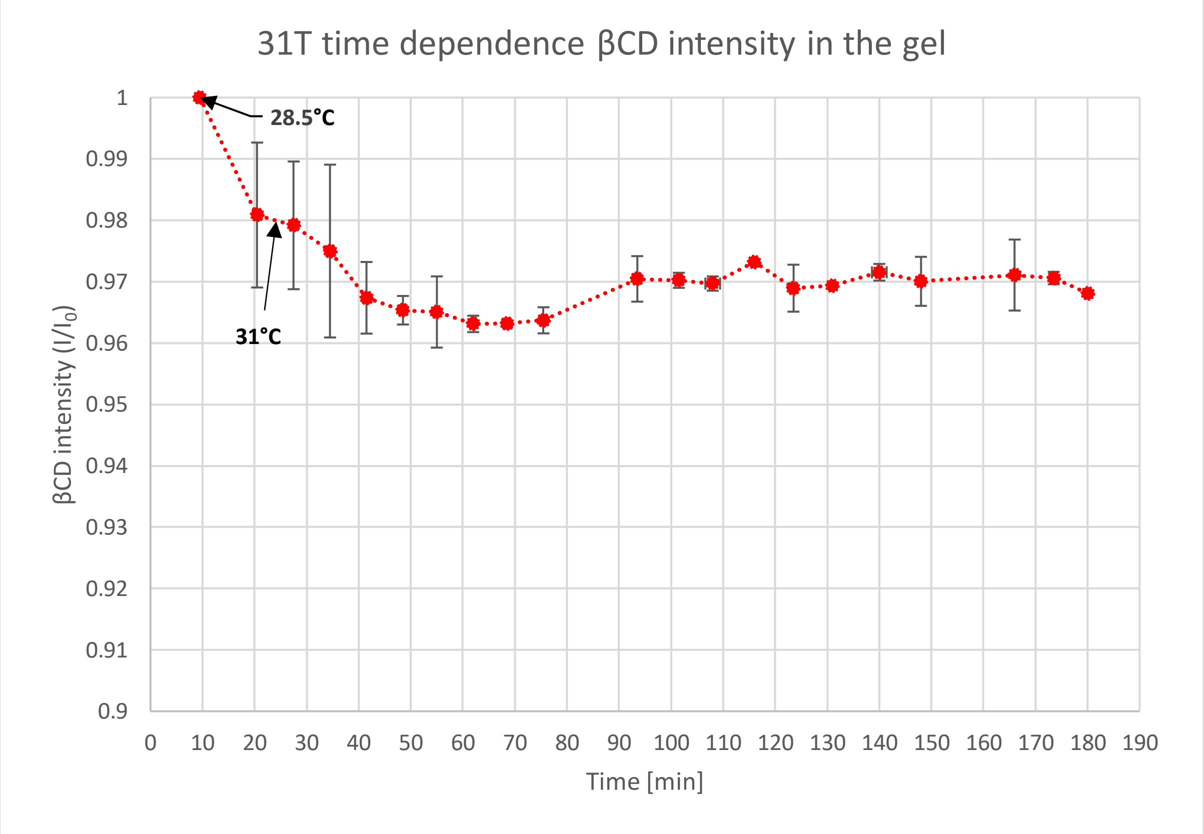

*Figure 7.5.7: Average fit curve for 31T of **figure 7.5.6** with error bars and temperature markings. The error variation appears the largest at the beginning of the graph before stabilizing at the end of th experiment. However, this variation is low overall, especially when considering that intensity only varied around the 90%-values when comparing the intensity value of βCD with its initial value.*

Due to the absence of the hydrogel hydrophobicity, it means that the βCD inside the P(NIPAM) was never able to significantly diffuse out of the polymer network. This ties up with the observation on the NMR spectra before and after LCST in **figure 7.4.3-7.4.5** and the MSME pictures in **figure 7.3.3**, which showed very minimal change in βCD intensity, P(NIPAM) intensity, and shrinkage. No significant changes were even observed at the end of the experiment as shown in the MSME pictures in **figure 7.3.4** and the spectra comparison of all the temperature experiments in **figure 7.4.9**. These observations indicates that even if the LCST and VPTT were never reached, the βCD is still being diffused, but the scale of which is nothing substantial, especially compared to the 40T, 40ST, and 40S experiments. The temperature has to surpass both LCST and VPTT for any significant change in βCD intensity inside to happen. If the polymer structure were to collapse completely to diffuse 99% of the βCD, the temperature would have to be close to 40°C as previously seen in **figure 7.5.2**, **figure 7.5.4**, and **figure 7.5.5** in 40S, 40ST, and 40T respectively.

Overview of the combined temperature experiments

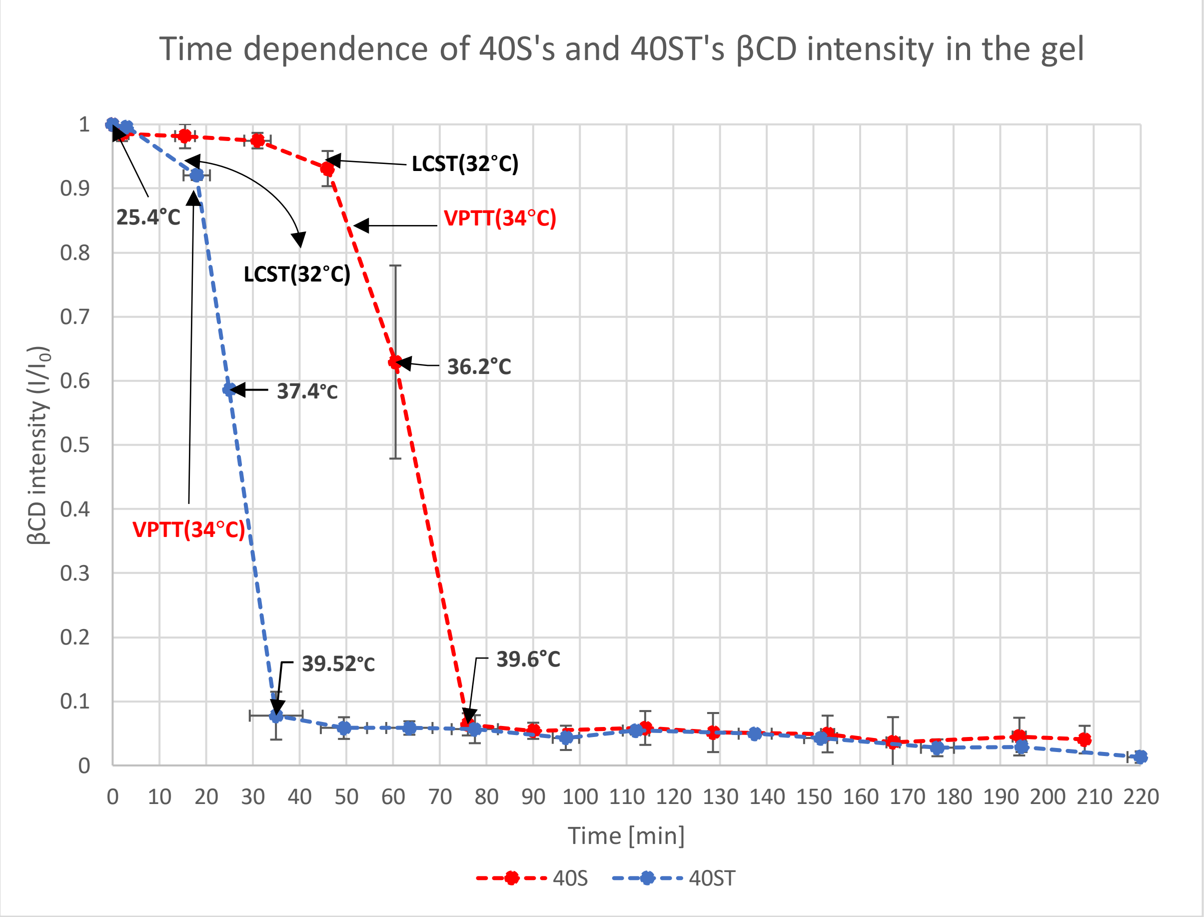

Table 7.5.8: Overview of the time dependence of 40S and 40ST with respect to the normalized βCD intensity. The 40S experiment is represented by the red curve, whilst the blue shows the curve for 40ST, which was the slow-heating and temperature-jump hybrid experiment. Each of the temperature experiments' temperature markings and error bars are also placed in the figure.

Figure 7.5.8 shows the overview comparison between the average fit curves of 40S(red) and 40ST (blue). Their LCST, VPTT and temperature stamps were marked in the figure above. Due to the temperature jump nature of 40ST after incubating the sample at 25°C, it does end up reaching the LCST and VPTT temperatures first before 40S as described also by **table 7.2.1**, thus the hydrogel at 40ST experience a steep decrease of the βCD intensity earlier than 40S. For comparison, refer to the point with the 37.4°C marking in 40ST and the 36.2°C marking for 40S. Both are found around the same βCD intensity value with the 40S data point having a slightly higher I/I_0 value than 40ST. However, the 40ST data point is obtained after 25 minutes, whilst the 40S data point obtained it after 60 minutes. Notice also how 40S had more data recordings prior to the steep decline in intensity, where the βCD intensities decreased up to 96% of the initial βCD intensity before LCST. Overall, both 40S and 40ST shows similar gradual decrease pattern, becoming slightly larger as it approaches the LCST of 32°C and eventually steeply decreasing the amount of βCD inside the hydrogel voxel after VPTT of 34°C.

At the end of the stark decline of βCD intensity, a low and gradual decreasing plateau is established for both temperature experiments, where βCD intensities started at 8% for 40ST and 6% for 40S. At this point, the temperature is already very close to 40°C w for both temperature experiments, and the intensities gradually decrease further. These findings were supported by the spectral comparisons before and after the vital transition temperatures, as well as the MSME findings from each of their respective temperature experiments. All observations support showing substantial shrinkage near 40°C and the phase transition of P(NIPAM) coinciding with the transition temperatures as shown by both the spectral comparisons described in the previous section and the βCD graphs in this current section. When reaching VPTT, the concentration of βCD begin to decrease sharply as it approaches 40°C.

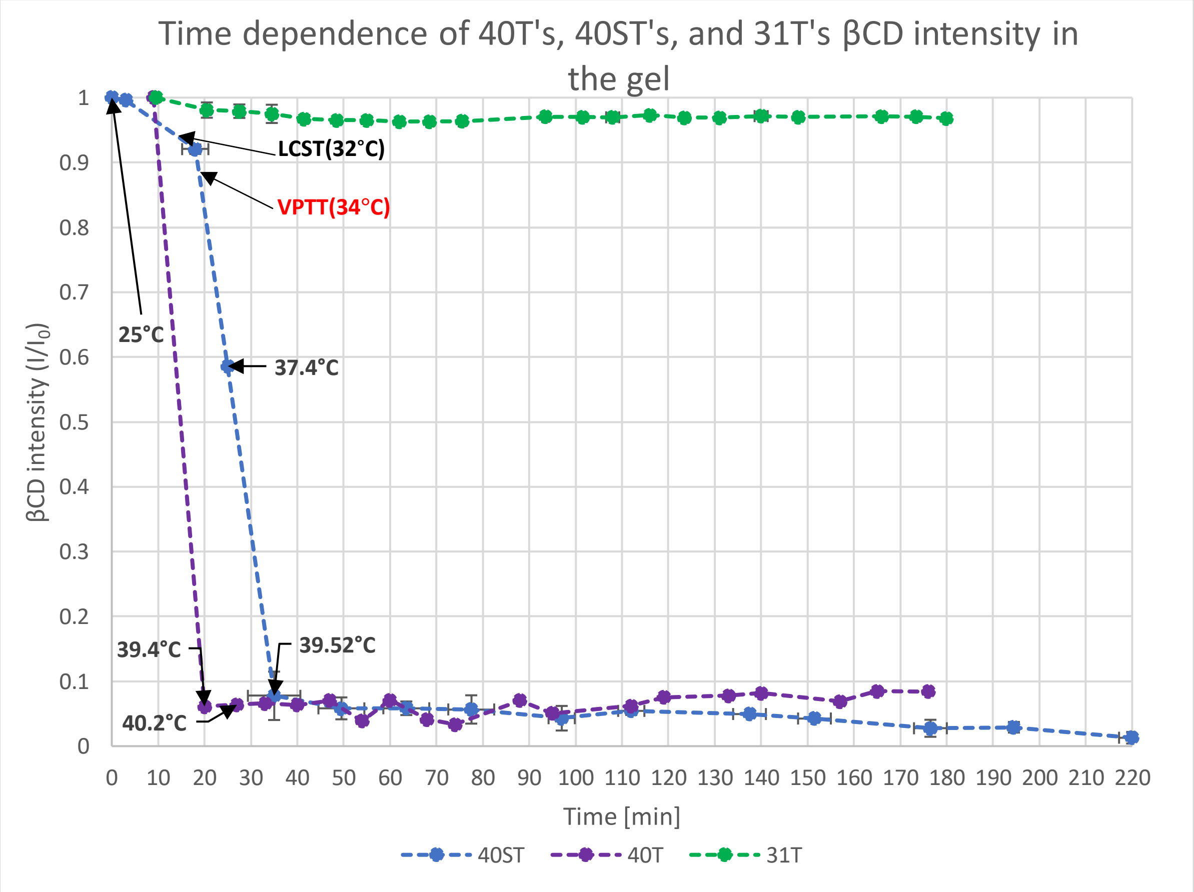

Figure 7.5.9: Overview of the time dependence of 40ST, 40T, and 31T with respect to the normalized βCD intensity. The 40T experiment is represented by the violet curve, whilst the blue shows the curve for 40ST, which was the slow-heating and temperature-jump hybrid example. The 31T temperature experiment is marked with the green curve. The temperature markings for 40ST and 40T are shown. The error bars for 40T and 40ST are also shown.

Figure 7.5.9 shows the overview comparison between the samples from 40T (purple), 31T (green) and 40ST (blue). The LCST, VPTT and temperature stamps are marked and described for 40ST and 40T. The 31T's temperature marks were left out as it never went beyond the transition temperatures. As stated in **table 7.2.1**, 31T reaches 31°C when t=25 minutes. When compared to the other temperature-jump experiments, the change in βCD intensity overtime never goes lower than 96%. Instead, it fluctuates around the 90's. This reflects well with its MSME pictures and the spectra comparison and before and after VPTT as no significant changed occurred, regardless of the duration. The extreme opposite of 31T is the 40T experiment, and that temperature experiment shows the most rapid shrinkage for the P(NIPAM) as shown its MSME pictures in **figure 7.3.8**. As mentioned previously, the hydrogel in the 40T experiment has already surpassed VPTT by the 1st recording, thus the trend shows an immediate sharp decrease after 10 minutes. The second fastest shrinkage occurred for the 40ST hydrogel as it does attain the transition temperatures faster than 40S, but not as fast as 40T. Consequently, its sharp decline only began right after the 18-minute mark. All the temperature experiments adhered to the spectra comparisons of P(NIPAM) and βCD, as well as with their MSME pictures. It also adheres well with the A/A_0 analysis against time done **attachment 4** [4], sharing almost the same pattern of decrease, where it showed that the hydrogels with the most rapid shrinkage were those that were exposed 40°C longer. With this in mind, this coincides with the observed pattern discussed here as 40S had latest shrinkage and release of βCD, followed by 40ST, and finally by 40T.

(7.6) Quantitative analysis of βCD release outside of the gel using STEAM

When analyzing the reaction inside the gel after VPTT, it is pertinent to monitor the outside part of the hydrogel to see if the concentration of βCD indeed increases. **Figure 7.6.1** shows a spectra comparison for the 1st experiment run at 40S (blue) and the last experiment run(red) at the 6mm voxel above the hydrogel interface. Clearly, the spectra shows a relatively strong peak increase for the βCD signals. Couple this observation with the findings for the quantitative analysis inside the hydrogel, where the βCD intensity decrease after VPTT, the increase of βCD at the 2mm and 6mm voxels can be expected to increase or correlate with similar timings as the voxels inside the hydrogel.

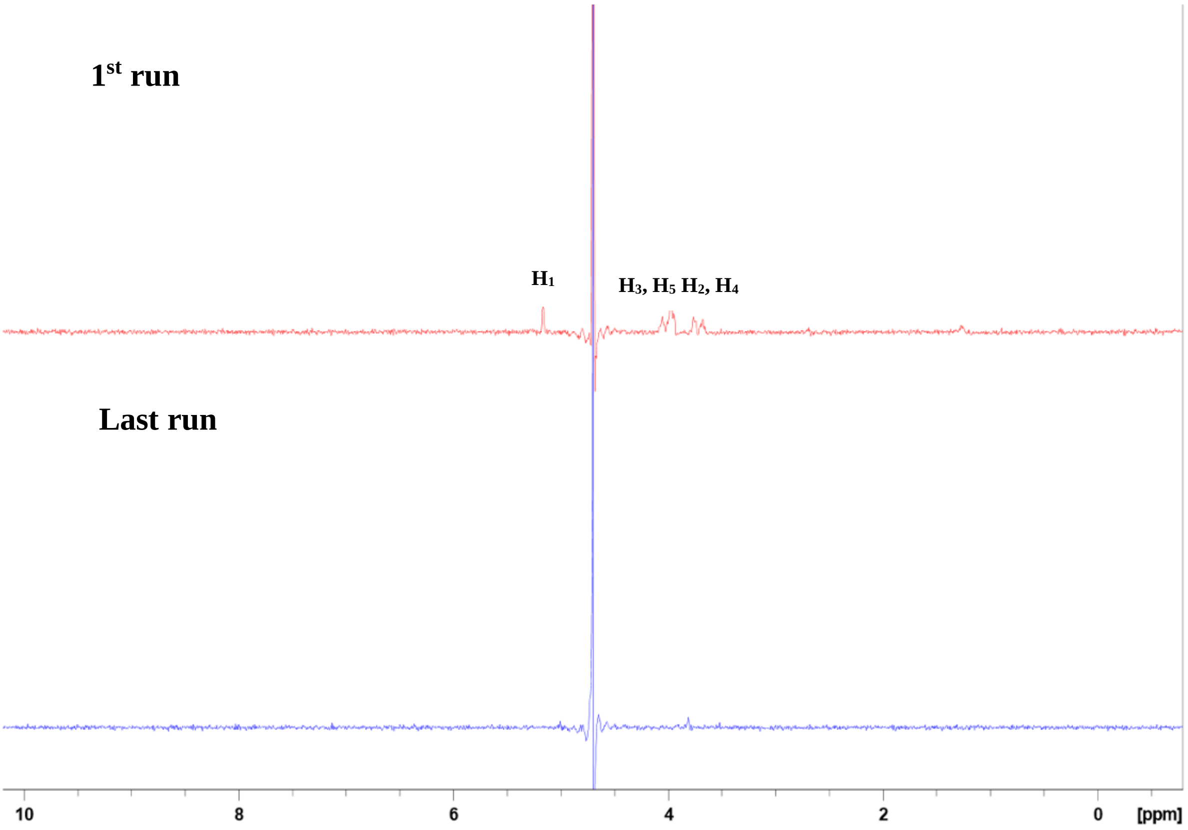

Figure 7.6.1: Spectra comparison of the 1st 6mm voxel experiment and the last 6mm voxel experiment for 40S, where the red spectrum represents the last experiment whilst the blue spectrum represents the very first experiment. There is an increase of βCD signals overtime as a result of diffusion.

40S

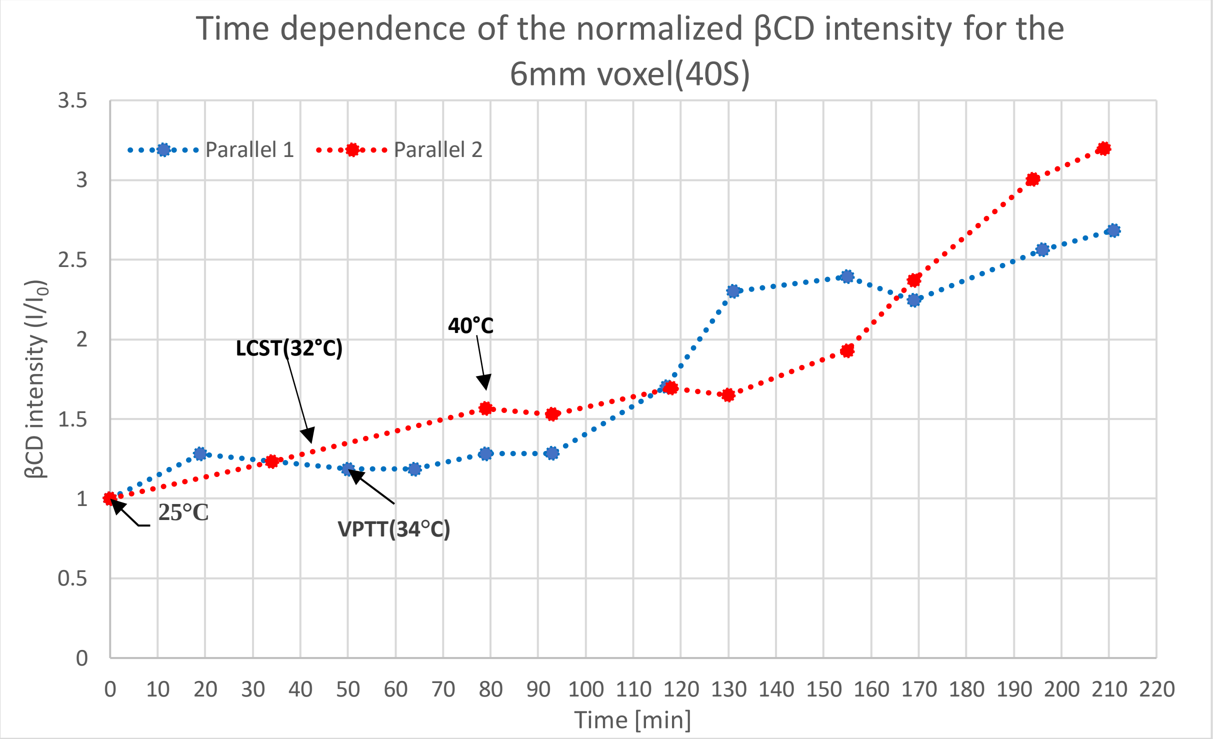

*Figure 7.6.2: Time dependence of the normalized βCD intensity at the 6mm outside the gel. Parallel 1's curve is blue and parallel 2's curve is red. The temperature markings are shown in the graph, which were obtained from 40S's temperature-time correlation curve in **figure 7.2.2**.*

Figure 7.6.2 and **figure 7.6.3** shows the 1st parallel (blue) and 2nd parallel(red) for 40S's release of βCD at the 6mm voxel and 2mm voxel above the 0mm hydrogel interface. Both parallels from each of the voxels show similarities in their curve patterns, but there is some variance on the timing of some of these points at the 6mm voxel in **figure 7.6.2**. Despite this variance, both figures do show a general increase of βCD, particularly after VPTT. The increase becomes sharper after reaching 40°C, especially for the 2mm voxel. Combining the parallels from both the 2mm voxel graph and the 6mm voxel graphs yields **figure 7.6.4**.

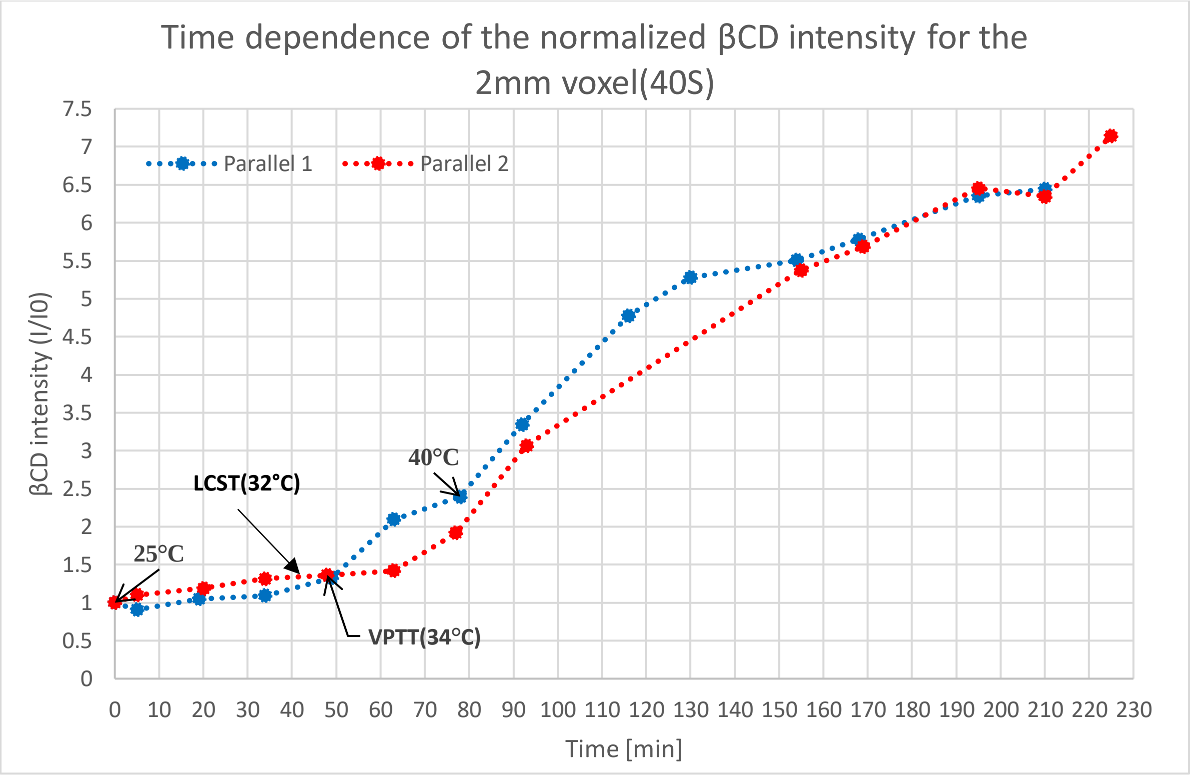

Table 7.6.3: Time dependence of the normalized βCD intensity at the 2mm voxel outside the gel. Parallel 1's curve is blue and parallel 2's curve is red. The temperature markings are shown in the graph that were from 40S temperature-time correlation curve in ***figure 7.2.2***

Before LCST, both voxels show minimal change in βCD intensity increase as what was previously seen in the βCD intensity graphs inside the gel(**figure 7.5.2**), as well as the spectra comparison before and after LCST in **figure 7.4.1** and **figure 7.4.2**. The last data points before reaching LCST show that the 2mm voxel has 122% of the initial βCD intensity whilst the 6mm voxel has 142%. Both values are close to one another, but this changes gradually after LCST and VPTT. After VPTT, both βCD intensities for the 6mm and 2mm voxels begin to show disparity with the 2mm voxel showing a stronger intensity trend. After reaching 40°C, the βCD intensity for the 2mm voxel is 212% of the initial βCD intensity, whilst the 6mm voxel has 144% of the initial βCD intensity. So far, changes are more apparent to the 2mm voxel, which is no surprise since it is closer to the 0mm interface of the hydrogel.

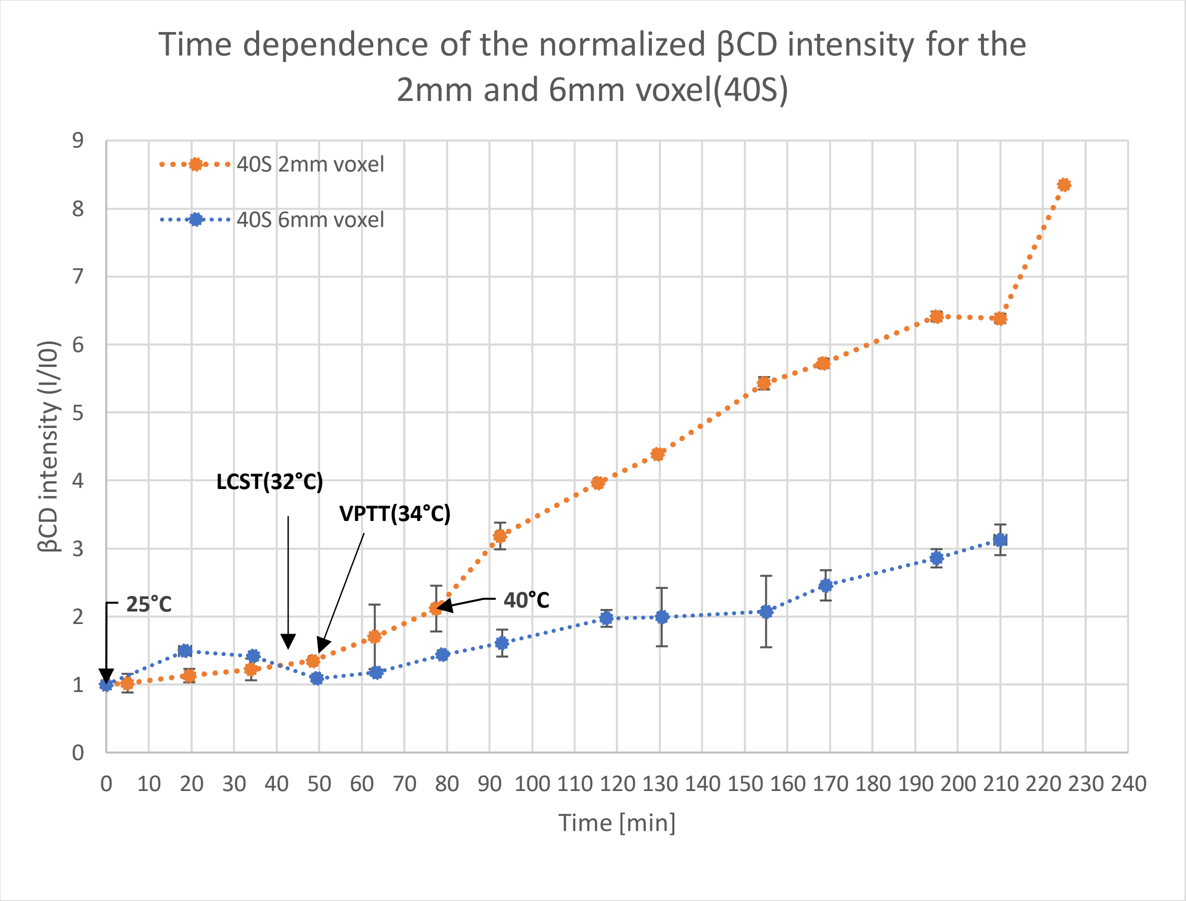

*Figure 7.6.4: Average fit curves for the 2mm and 6mm voxels of both parallel 1 and 2. The averages fits are based on **figure 7.6.2** and **figure 7.6.3**. The orange curve represents the 2mm voxel, whilst the 6mm voxel is represented by the blue curve. Their temperature markings are included based from the temperature-time correlation curve. There is also minimal variation overall in the graph, but it is noted that variance is a relatively higher for the 6mm voxel, especially at the later stages of the experiment. Both curves a general increase in βCD with the 2mm voxel showing a higher increase, especially after 40°C.This correlate well with the previous observations for the MSME pictures, spectra comparison at the transition temperatures, as well as the graphs analyzing βCD inside the hydrogel.*

Consequently, this disparity in βCD intensity becomes more extensive as time progresses after 40°C is achieved. By this point, the MSME pictures for 40S showed that the hydrogel has completely collapsed at this point when t=80 minutes. The same observation was seen in **figure 7.4.11**, where the NMR spectra comparison between t=76 minutes and t=60 minutes showed that the signals for both P(NIPAM) and the βCD have reduced to a magnanimous degree that it is almost not seen in the spectra. **Figure 7.5.2** also shows that the βCD inside the hydrogel by the 75-minute mark, has already left as indicated by its low plateau. These together coincide and indicate that the diffused βCD has exited the polymer network and into the release medium, where the voxels are positioned. As a result, βCD will continue to diffuse onto the voxels until the end of the experiment, with the 2mm voxel receiving a higher βCD intensity than the 6mm voxel. At the end of the experiment, the 2mm voxel has 835% of the initial βCD intensity and the 6mm voxel has 313% of the initial βCD intensity. Both adhere to the shrinking kinetics expected for P(NIPAM) at the transition temperatures.

40ST

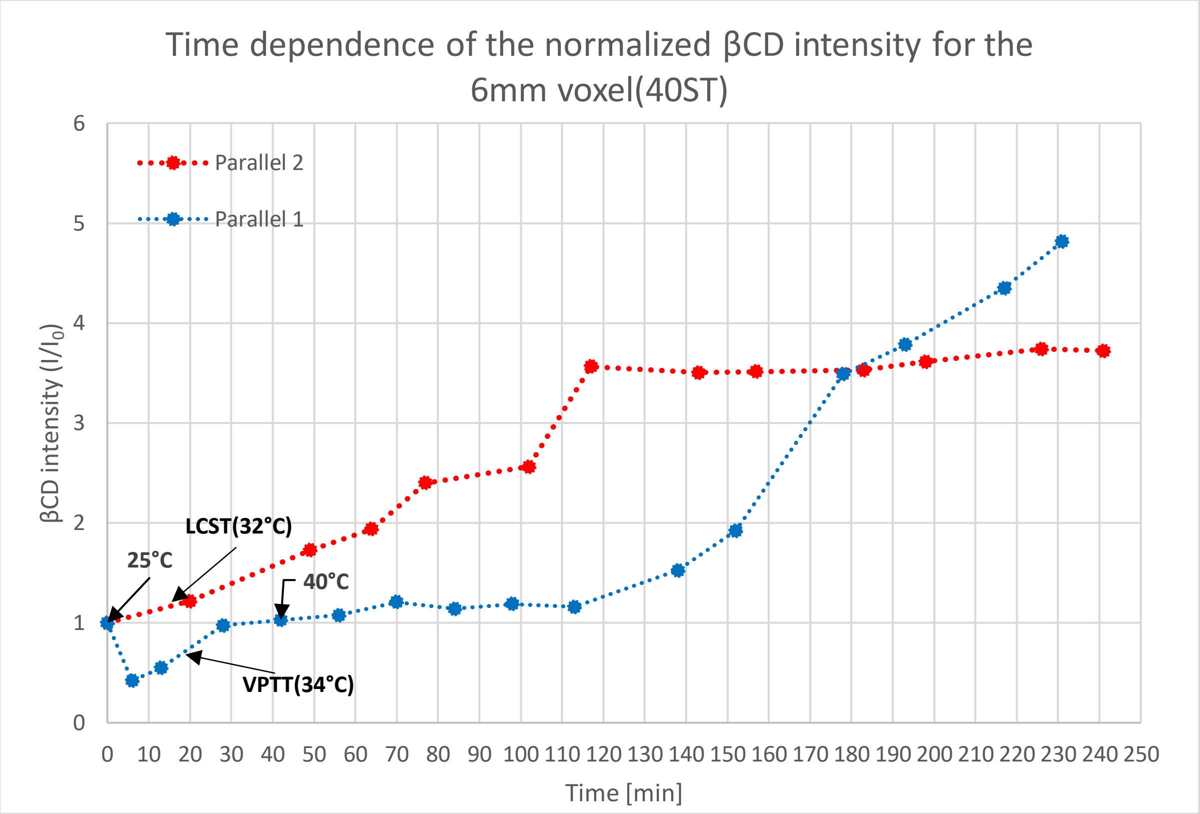

Figure 7.6.5: Time dependence of the normalized βCD intensity at the 6mm outside the gel. Parallel 1's curve is blue and parallel 2's curve is red. The temperature markings are shown in the graph that were from 40ST temperature-time correlation curve shown in ***figure 7.2.7****.*

Looking at **figure 7.6.5** and **figure 7.6.6**, the change of βCD intensity with time is visualized for the 6mm and 2mm voxels with two different parallels for each figure. Recalling **table 7.2.1**, the LCST and VPTT for 40ST is quickly obtained one right after the other in quick succession. Both voxels show the same trend seen in 40S, where minimal changes occur before VPTT. As soon as VPTT is reached, the increase of the βCD intensity can be observed, and it becomes more significant and sharper in increase as it approaches closer to 40°C. However, the variation between the two parallels in each voxel is more substantial than the 40S experiment. Similar to the 40S experiment, the timing of which the sharp increases in βCD intensity happens is different. For the 6mm voxel in **figure 7.6.5**, it occurs at t=102 minutes for parallel 2 and t=152 minutes for parallel 1. Moreover, a plateau is seen for parallel 2 at t=117 minute with some minor fluctuations until the end of the experiment. This is in contrast with the continuous increase of parallel 1 that occurs until the end of the experiment. However, both parallels eventually intersect around t=180 minutes. It can also be observed in **figure 7.6.5** for parallel 2 established a plateau at t=115 minutes, which is also the same time mark where a very similar pattern is seen for the 6mm voxel in **figure 7.6.6**. The exception here is that the 2mm voxel is still gradually increasing from 413% of the initial intensity of βCD to 529% when t=240 minutes.

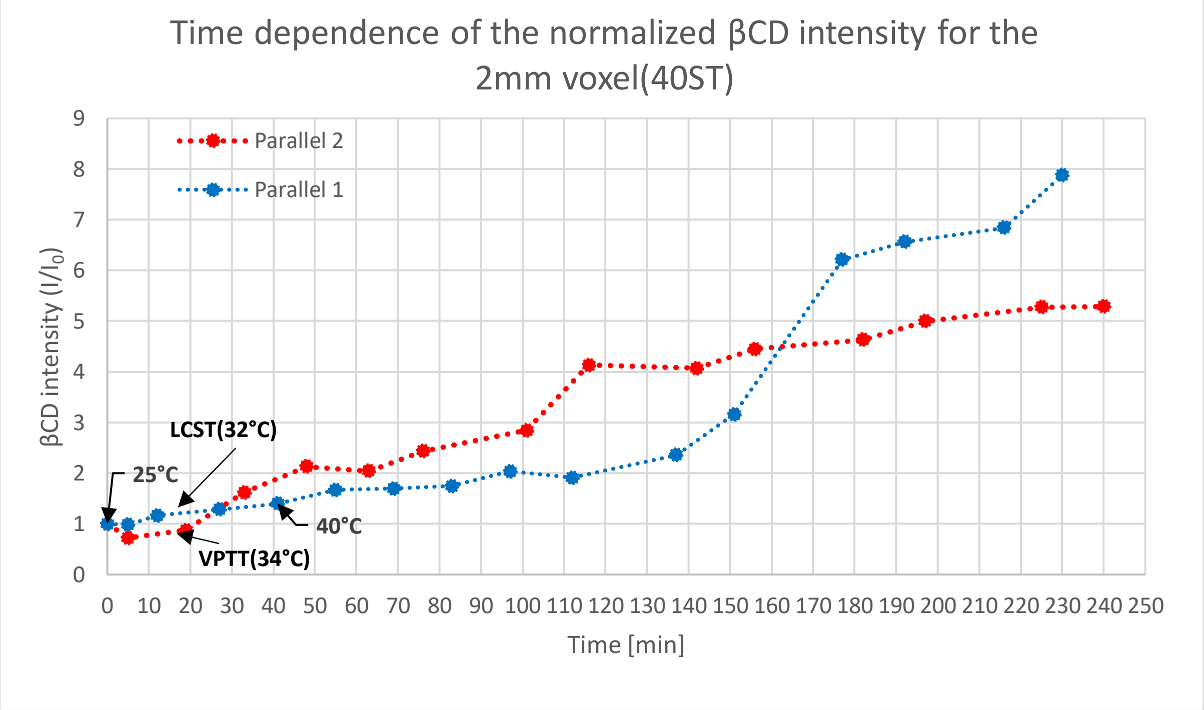

Figure 7.6.6: Time dependence of the normalized βCD intensity at the 2mm outside the gel. Parallel 1's curve is blue and parallel 2's curve is red. The temperature markings are shown in the graph that were from 40ST temperature-time correlation curve shown in ***figure 7.2.7****.*

This extensive variation between the two parallels for the 2mm and the 6mm voxel will create large error bars for the average fit curve in **figure 7.6.6**. At the end of the experiment, 2mm voxel curve have a βCD intensity 659% of the initial βCD intensity, whilst the 6mm voxel has 443% of the initial βCD intensity. Generally, the 2mm voxel curve, like the 40S trend in **figure 7.6.4**, shows a higher curve than the 6mm voxel curve. Regardless of the variation, both parallels of the 2mm and 6mm voxels still adhere to the expected shrinking kinetics at the transition temperatures for P(NIPAM), achieving the sharp increases after 40°C. The trends are similar to 40S, but 40T's voxels saw the sharp increase sooner at t=73 minutes whilst 40S saw this increase at t=79 minutes. Recalling from the MSME pictures of 40ST in **figure 7.3.1**, the gel has already shrunk on the 3rd picture, where the temperature is 39.75°C at t=37 minutes. This is also around the same time when βCD was at its low plateau in **figure 7.5.4** inside the hydrogel. This means that βCD is no longer in the voxel in the gel, and thus is expected to be outside of the gel at a large concentration. However, there is a delay before the sharp increases happen for both 40ST and 40S.

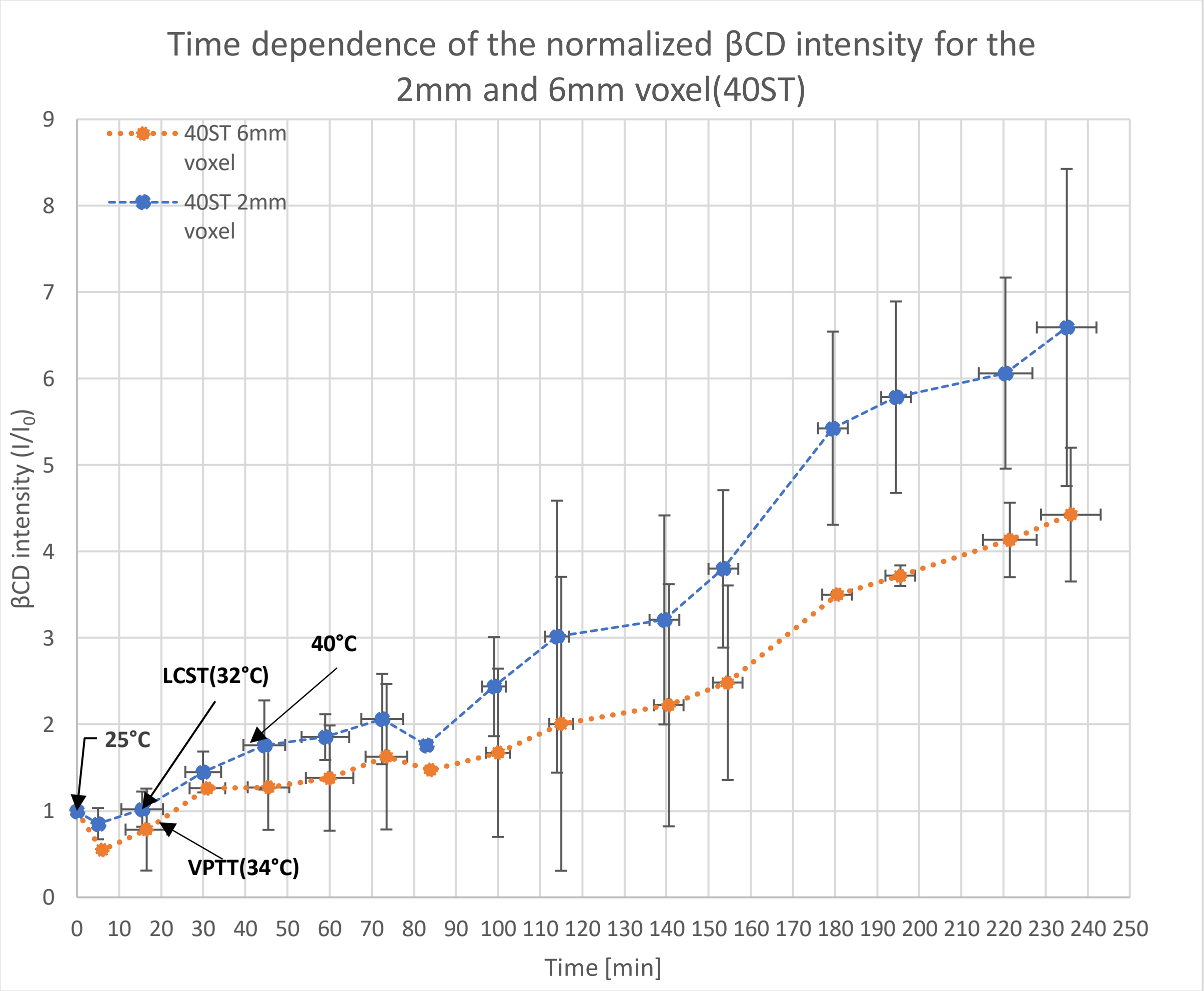

Figure 7.6.7: Time dependence of 40ST's normalized βCD intensity at the 2mm and 6mm voxels based from ***figure 7.6.5*** *and* ***figure 7.6.6****. The orange curve represents the 6mm voxel, whilst the blue curve represents the 2mm voxel. Their temperature markings are included based from the temperature-time correlation curve for 40ST, as well its errors bars. Similar to 40S, both voxel curves show a general increase, particularly after 40°C. This correlate well with the previous observations for the MSME pictures, spectra comparison at the transition temperatures, as well as the graphs analyzing βCD inside the hydrogel.*

In a paper done by Kaneko, he mentioned that the gradual increase of opaqueness on the gel indicates that polymers are experiencing a phase separation from the water molecules at the molecular level. These polymers layers were dense as to prevent the permeation of the encased water in the hydrogel interior being released outside of the polymer network. As a result of this, the diffusion rate becomes limited. In addition, the formation of such a dense layer is associated with an increase in hydrostatic internal pressure as to balance the deswelling forces. This increase of hydrostatic internal pressure from the aggregation of the P(NIPAM) can be alleviated if the entrapped water is squeezed out from the hydrogel network via bubble formation on the surface. These bubbles will swell overtime on the surface of the hydrogel and release the water through the bubble via convection. Consequently, the internal pressure becomes reduced, and the hydrogel reaches a shrunken, but stable state [19-23].

With that in mind, this means that even if the βCD reached its plateau inside the hydrogel voxel as shown in all the temperature experiments previously (except for 31T), this doesn't necessarily mean that the βCD inside will be directly transported outside. There will be an expected delay for the release of the water and βCD. For this case, it was not until t=73 minutes before the increase in βCD intensity outside the hydrogel began for both the 2mm and 6mm voxels. For 40S in **figure 7.6.4,** it was not until t=79 minutes before the steep increase in βCD intensity occurred.

40T

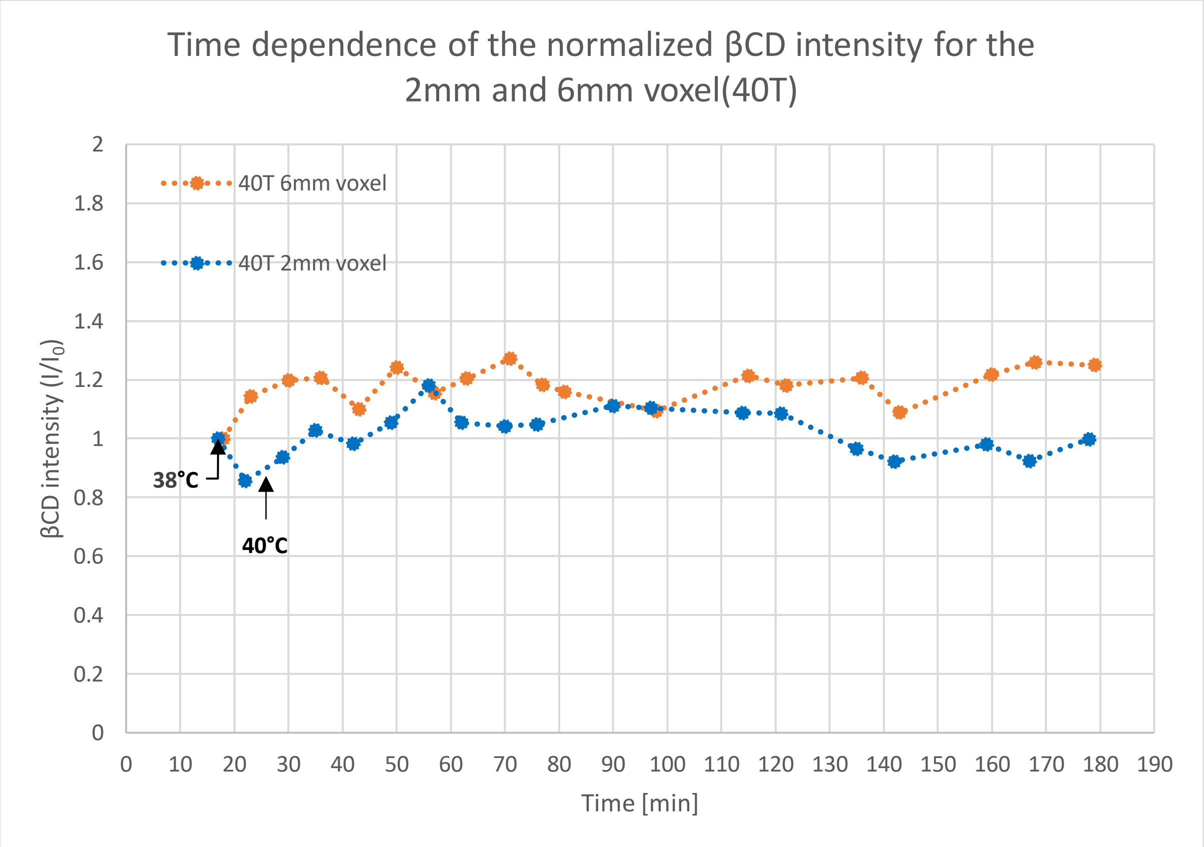

Figure 7.6.8: Time dependence of 40T's normalized βCD intensity at the 2mm and 6mm voxels using parallel 1's runs. The 2mm voxel is marked with the blue curve, whilst the 6mm voxel is marked with the orange curve. The temperature marks were obtained from ***figure 7.2.5****.*

Both the 2mm and 6mm voxels in **figure 7.6.8** appear to have very similar patterns, where the 6mm voxel consistently has the higher βCD intensity throughout the entire experiment in comparison to the 2mm voxel. The 1st recording outside the voxel was recorded when t=17 minutes. In addition, overall, the trend appears for the 2mm and 6mm voxels are only varying between 80%-130% of the initial βCD intensity, which is contrasting of what was seen in 40S (**figure 7.6.4**) and 40ST(**figure 7.6.7**), where the βCD intensities for the 2mm and 6 mm voxels increased beyond the percentage interval given for 40T. Looking at the 1st point in **figure 7.6.8**, the temperature is at 38°C already, so VPTT has already been surpassed, and the sample is just

2°C away from 40°C. LCST and VPTT were obtained at t=4 minutes and t=5 minutes according to **table 7.2.1**. 40°C is also reached in 24 minutes.

Consequently, phase transition was already in progress. The MSME pictures in **figure 7.3.7** shows that at t=19 minutes, the gel already has noticeable shrinkage and opaqueness. Referring to the spectra comparisons as the sample approaches close to 40°C in **figure 7.4.11**, the signals for both βCD and P(NIPAM) quickly disappear, even more so for a temperature-jump experiment. As a result of this rapid temperature experiment, reaching these transition temperatures will rapidly lead to the degradation of the polymer network, as well as the release of βCD inside the hydrogel. **Figure 7.5.5** coheres well with **figure 7.6.8** where data recordings after VPTT already shows significant βCD loss inside the hydrogel. At t=20 minutes, only 6% of the initial βCD concentration remained and a plateau was established at this point. These together can explain why the variation in βCD intensity for 40T is low, especially compared to 40ST, which is also a temperature-jump hybrid experiment. For reference, the last βCD intensities for the 2mm voxel and 6mm voxel for 40T is 125% and 100% of the initial βCD intensity.

31T

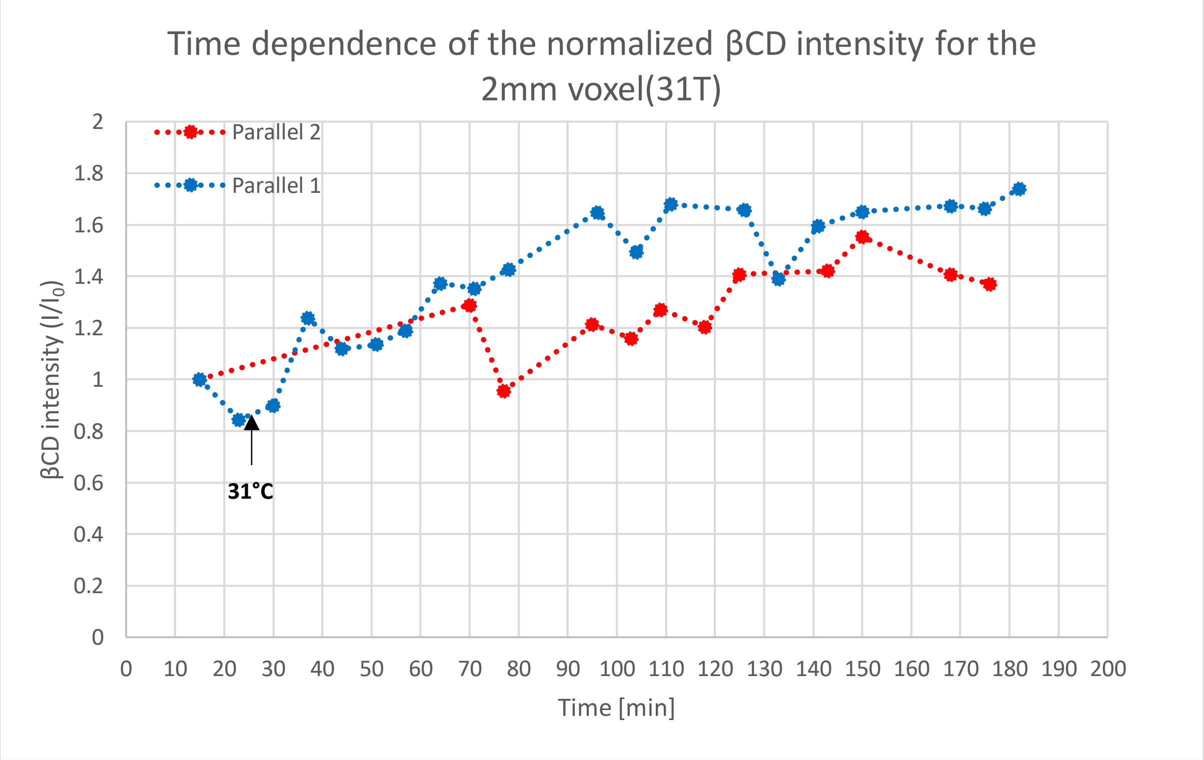

Figure 7.6.9: Time dependence of the normalized βCD intensity at the 2mm outside the gel for 31T. Parallel 1's curve is blue and parallel 2's curve is red. The temperature markings are shown in the graph that were from 40ST temperature-time correlation curve shown in ***figure 7.2.9****.*

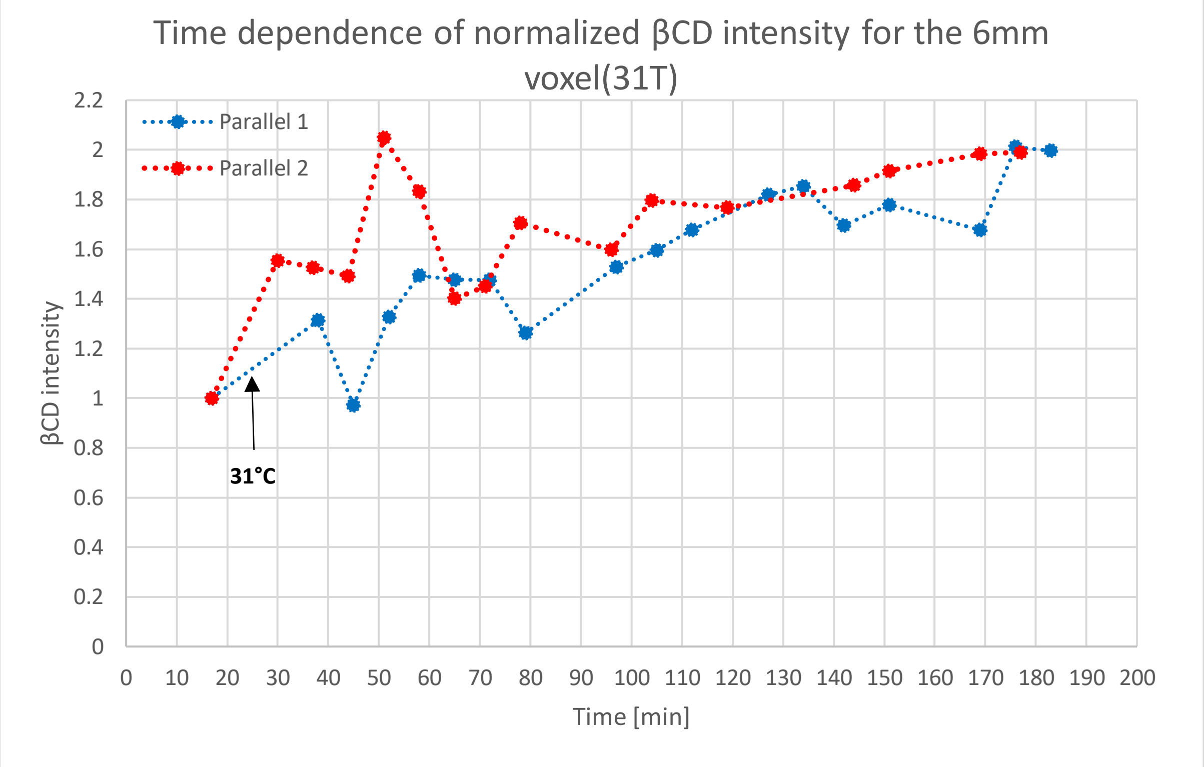

Figure 7.6.10: Time dependence of the normalized βCD intensity at the 6mm outside the gel for 31T. Parallel 1's curve is blue and parallel 2's curve is red. The temperature markings are shown in the graph that were from 40ST temperature-time correlation curve shown in ***figure 7.2.9****.*

Figure 7.6.9 and **figure 7.6.10** shows the 2mm and 6mm voxel parallels respectively. Both show some variation. For the 2mm voxels, the variation is the highest in the middle of the graph. Moreover, parallel 2 for the 2mm has less points than parallel 1 due to poor water suppression during the 1st hour of the experiment. Regardless of the optimization, the βCD intensity values were always negative. They had to be excluded in **figure 7.6.9.** With regards to the 6mm voxel, water suppression was sufficient enough to obtain positive βCD intensity values, and it showed the same general trend as the 2mm voxel, where the βCD intensity values were increase with time, even though the temperature never surpassed LCST or VPTT. The increase, however, is not large. Combining the parallels together yields the average fit curve for 31T's 2mm and 6mm voxels for better visualization.

The curves for the 2mm and 6mm voxels in **figure 7.6.11** appear to have a relatively similar pattern. After reaching 31°C, both curves show an increasing pattern for the βCD intensity with some occasional decrease along the way. A majority of the time in the experiment, the 6mm voxel had a relatively higher βCD concentration than the 2mm voxel. At the end of the experiment, the 6mm voxel attained 189% of the initial βCD intensity, whilst the 2mm voxel had 176% of the initial βCD concentration. This temperature experiment showcases a similar observation seen in 40T, in which the interval of increase for βCD outside the gel is low. However, the reason for 31T's low βCD intensity change compared to 40ST and 40S is that the hydrogel never went pass the transition temperatures, so a significant portion of the βCD is still within the interior of the hydrogel. This is the opposite of what happened in the 40T experiment where the 1st data recorded was already beyond LCST and VPTT due to the rapid nature of the temperature jump.

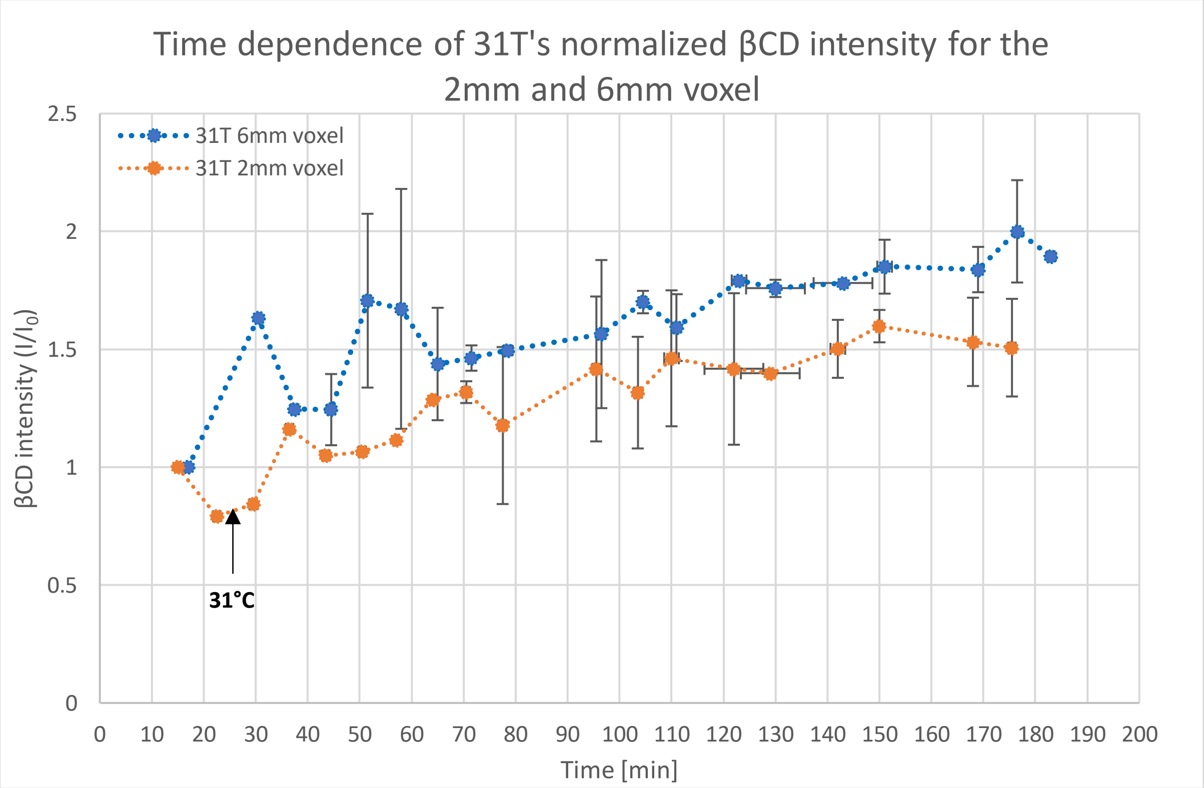

Figure 7.6.11: Time dependence of 31T's normalized βCD intensity at the 2mm and 6mm voxels outside the hydrogel. The 6mm voxel is represented by the blue curve, whilst the 2mm curve is represented by the 2mm voxel. Their temperature markings are included based on the temperature-time correlation curve for 31T, as well its errors bars. This correlate well with the previous observations for the MSME pictures, spectra comparison at the transition temperatures, as well as the graphs analyzing βCD inside the hydrogel.

To support the findings of **figure 7.6.11**, the MSME pictures of 31T in **figure 7.3.3** and **figure 7.3.4** showed very minimal change. Significant changes in the peak intensity for P(NIPAM) and βCD are only seen above VPTT and LCST as shown in the spectra comparison in **figure 7.4.3**. **Figure 7.5.7** also shows that the change in βCD is minimal inside the hydrogel voxel, never going beyond 96% of the initial βCD intensity. All in all, the observations made for **figure 7.6.11** coincides with the mentioned observations, which all indicated minimal change both inside the hydrogel and outside the hydrogel, especially when compared to 40T, 40ST, and 40S.

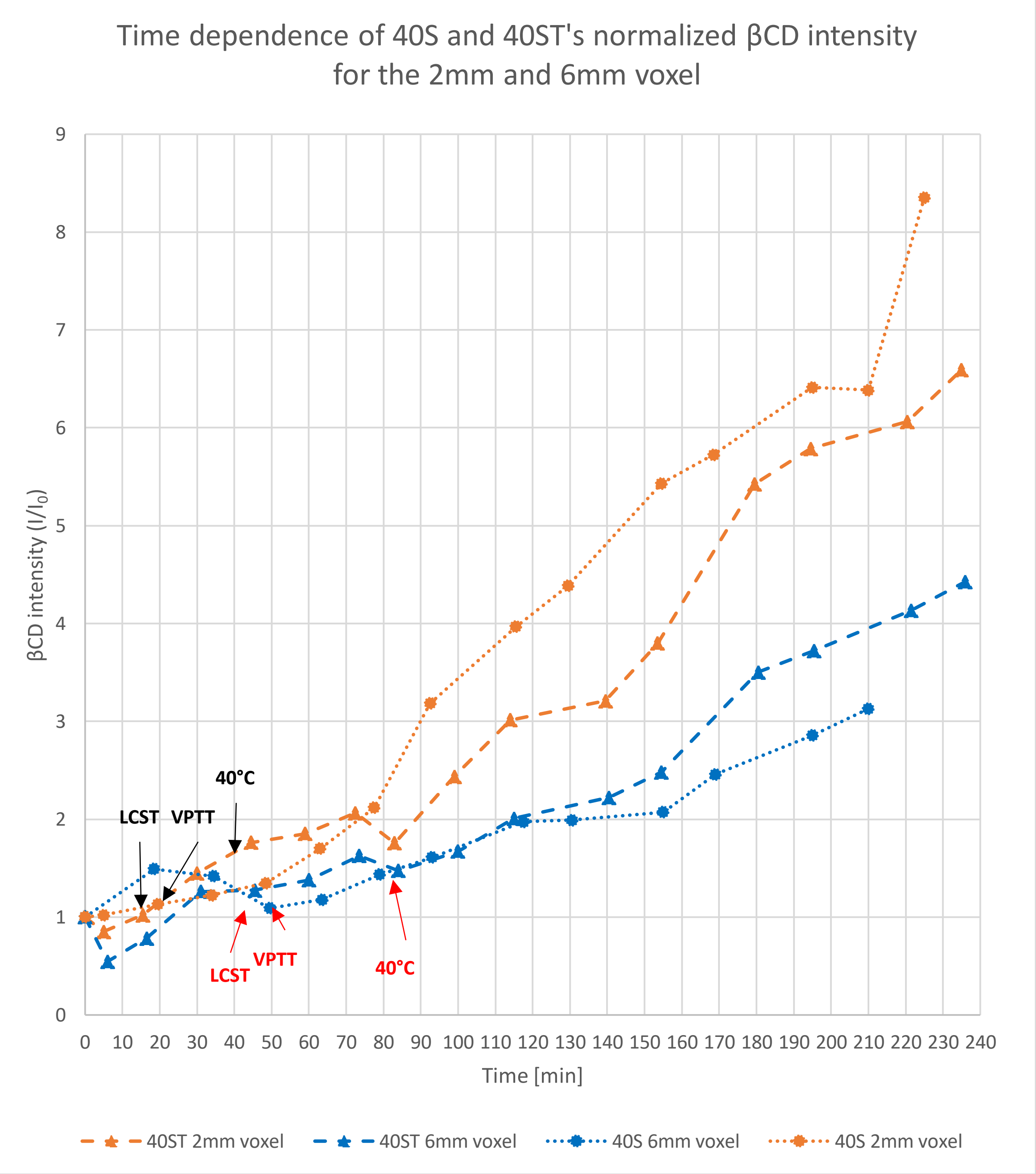

Figure 7.6.12: Comparison between the 2mm and 6mm voxels of 40ST and 40S. The orange curves represents the 2mm voxels, whilst the blue represents the 6mm voxels. The triangle data points and dashed lines represents the 40ST sample. The circle data points with the dotted curve represents the 40S sample. The red temperature markings are for 40S, whilst the black markings are for 40ST

Figure 7.6.12 shows an overview of the 2mm and 6mm voxels for both 40S and 40ST. The 2mm voxels are consistently showcase a higher βCD intensity after their designated VPTT mentioned in **table 7.2.1**. Both temperature experiments show a high degree of similarity with their increase trend, but the increase in the βCD intensity happened sooner for 40ST, which reflects its temperature-jump nature. Eventually the 40S curve catches up begins to have a higher βCD change than 40ST for the 2mm voxels. When looking at the 6mm voxels, both experiments appeared to have an identical pattern before the 40S experiment overtakes the 40ST curve. At the end of the experiment, the 40ST 6mm voxel achieved 443% of the initial βCD intensity, and the 40S 6mm voxel achieved 313% of the initial βCD intensity. For the 2mm voxels, the 40S experiment ended up with 835% of the initial βCD intensity. Both temperature experiments adhering to their respective observations from the previous sections and shrinking kinetics.

Combining all the temperature jump experiments in **figure 7.6.13** shows how the 40ST curves dominate the graph, showing a significant increase in βCD up to 659% and 443% of the initial βCD intensity by the end of the experiment for both the 2mm voxel and 6mm voxel. The 31T sample showed higher βCD increase with time compared to 40T, but only because 31T approaches 1°C before LCST, so some diffusion of βCD does occur, but only minimal diffusion as shown in its hydrogel voxel. Compare this to the 40T hydrogel where it has surpassed VPTT at the 1st point, and it is just a few degrees away from 40°C, thus a significant portion of the βCD has already left. This explains why its change is minimal, where both the 2mm and 6mm never even reached 200% of the initial βCD intensity, even though 31T managed to reach that increase, despite never increasing beyond LCST.

Overall, the temperature experiments provide a good visualization of the βCD increase with time and temperature. They all agree with the MSME pictures, spectral comparisons, as well as the βCD graphs inside the hydrogel. However, improvements must be made to counteract the large standard deviations observed in some of the experiments, particularly for the 40ST and 31T temperature. More parallels could be done for all the experiments, and the time stamps could be made more uniform to reduce the uncertainty on the time gap and the fluctuations of the βCD intensity at a given time. For 40T, the experiment protocol would have to be optimized to able to record at a quicker time mark, but this can be difficult to achieve as the LCST and VPTT are achieved in short succession at t=5-6 minutes.

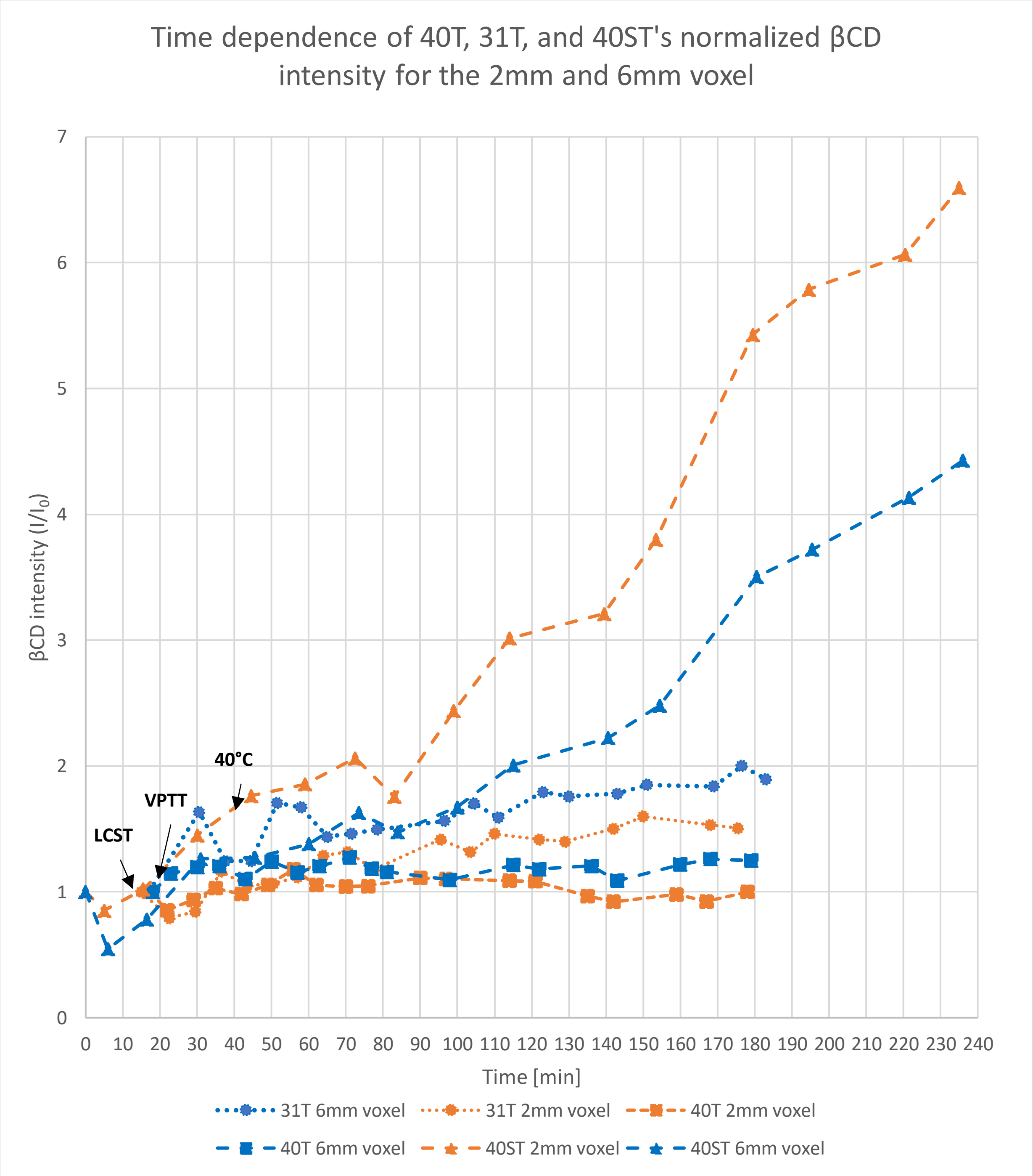

Figure 7.6.13: Comparison between the 2mm and 6mm voxels of 40ST, 40T, and 31T. The orange curves represent the 2mm voxels, whilst the blue represents the 6mm voxels. The triangle data points and dashed lines represents the 40ST sample. The circle data points with the dotted curve represents the 31T sample. The curve with dashed lines and square data points represents the 40T experiment. The temperature markings for 40ST is shown. For the 31T and the 40T temperature experiments, their temperature marks are left out as their first point is already close to their max temperature, 31°C and 40°C respectively.

(7.7) Diffusion of BCD and water references

Pure bulk water self-diffusion references(D_0)

Table 7.7.1: D_0 values of pure distilled water measured at different temperatures from [4]

Temperature [°C]	**Diffusion coefficient of pure distilled water [$m^{2-}s^1$]**
25	$2.29 \pm 0.07\times10^{-9}$
31	$2.70 \pm 0.02\times10^{-9}$
38	$2.84 \pm 0.04\times10^{-9}$
40	$3.27 \pm 0.04\times10^{-9}$

Table 7.7.2: Measured D_0 reference values of pure super-distilled water at different temperatures with deviation calculations from [4]

Temperature [°C]	**Diffusion coefficient of pure super-distilled water [$m^{2-}s^1$]**	**Deviation from the [4] D_0 values [%]**
25	$1.81 \pm 0.06\times10^{-9}$	21.17
31	$2.14 \pm 0.09\times10^{-9}$	20.62
35	$2.34 \pm 0.1\times10^{-9}$	-
38	$2.66 \pm 0.1\times10^{-9}$	17.67
40	$2.61 \pm 0.1\times10^{-9}$	20.13

Table 7.7.1 was obtained from [4]. The D_0 values seen in **table 7.7.1** increased with temperature, and their uncertainties were minimal. A similar pattern was observed for **table 7.7.2** right until the last data point at 40°C, where it decreased. Moreover, the uncertainties at **table 7.7.2** increased slightly. The largest value of the D_0 was found at 40°C in **table 7.7.1**, but it was found at 38°C for **table 7.7.2**. This is peculiar as the self-diffusion coefficient is expected to increase with higher temperatures due to the higher mobility of molecules. Ergo 38°C was marked in red in **table 7.7.2** as it can be a potential outlier. Looking pass the potential outlier at 38°C in **table 7.7.2**, it can also be observed that there are variations between the respective temperatures their D_0 values, and this can be due to the usage of different types of water. For this experiment, pure super-distilled water was used, but in [4], the experiment used pure distilled water. The values obtained in **table 7.7.1** were generally higher. Their deviations from the D_0 values compared to this experiment are listed in **table 7.7.2** except for 35°C. The 38°C row is marked in red to signal a potential deviation seen in **figure 7.7.1**. This can be potentially

due to the gradient strength for the diffusion experiment was not calibrated. Diffusion MRI is sensitive to poorly calibrated gradients as diffusion is heavily influenced by temperature, so this must be taken into consideration later in this subsection [25].

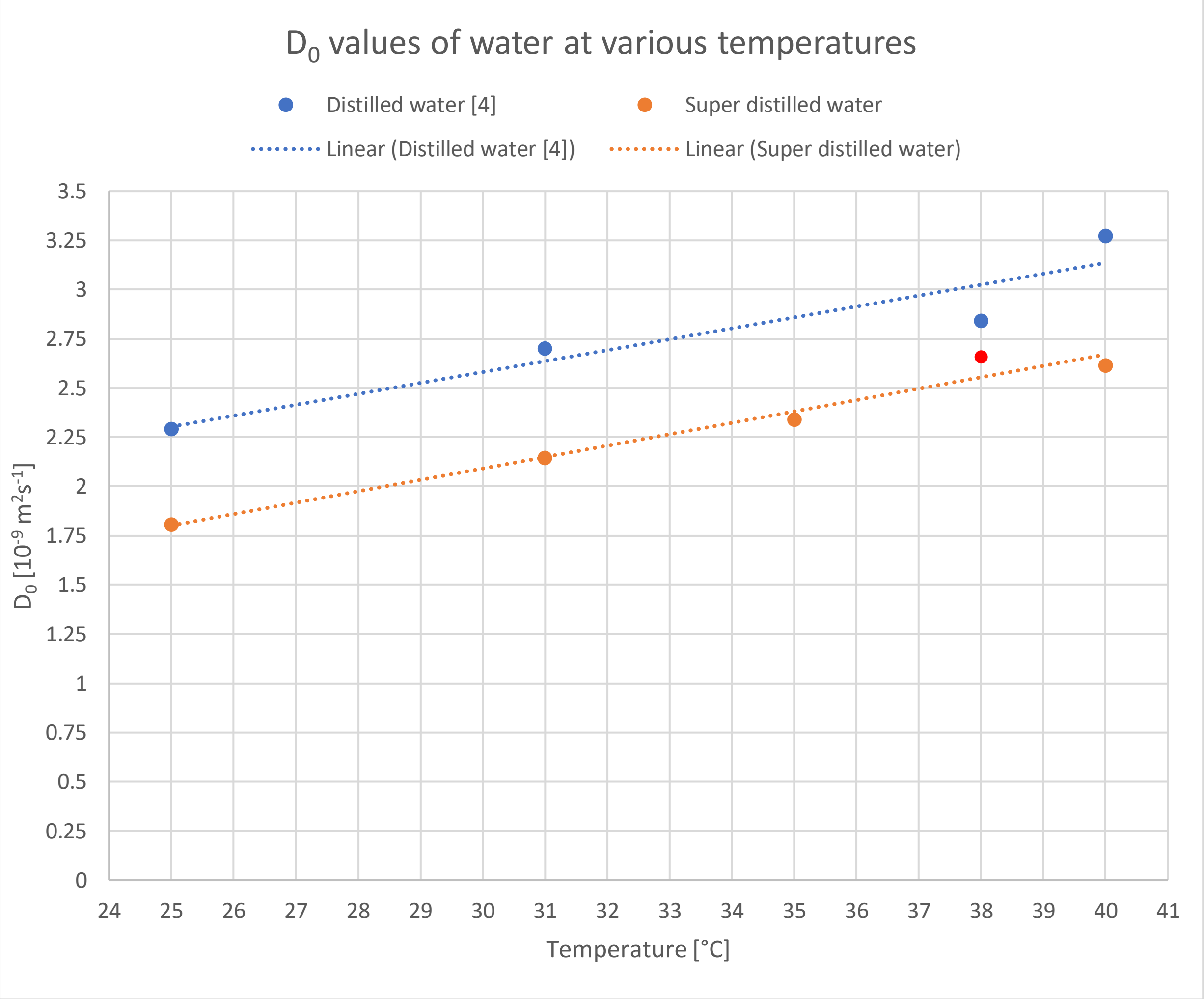

Figure 7.7.1: Comparison of pure distilled water used in [4] and the measured D_0 values of super distilled water with their respective linear trends. The D_0 value of both types of waters at 38°C deviated slightly from their trendlines along with the 40°C measurement for distilled water on the blue curve. The red dot represents the slightly deviating value from this experiment at 38°C. On the other hand, both show an increasing trend in D_0 as temperature increases, which is what is expected as more molecules are given more energy.

Figure 7.7.1 shows the graphical representation of the D_0 increase with temperature for both distilled and super-distilled water. Most of the points had a very good fit with respect to their linear trends, but some points like the 38°C and 40°C temperature marks from the blue curve ,and the 38°C temperature mark for the orange curve deviated slightly from their linear trends. These are considered further when looking at the D_0 values of βCD in the gel. Despite these slight deviations, both trends show an increasing pattern for D_0 with higher temperatures. This coincides with the temperature factor that can affect the diffusion kinetics. Higher temperatures lead to more molecules having more kinetic energy, thus have a higher diffusivity.

D_0 of 80:20 D_2O/super-distilled water (SDH_2O) with βCD reference values

Table 7.7.3: Bulk 80:20 D_2O/SDH_2O and βCD D_0 values measured at different temperatures

Temperature [°C]	**D_0 of water [m^2s^{-1}]**	**D_0 of βCD [m^2s^{-1}] [7 points]**
25	$1.6482 \pm 0.05\times10^{-9}$	$4.0384 \pm 0.2\times10^{-10}$
31	$1.7634 \pm 0.05\times10^{-9}$	$5.2858 \pm 0.5\times 10^{-10}$
35	$1.8164 \pm 0.06\times10^{-9}$	$5.5618 \pm 0.6\times10^{-10}$
38	$1.9044 \pm 0.06\times10^{-9}$	$7.7113 \pm 1.5\times10^{-10}$
40	$2.0496 \pm 0.06\times10^{-9}$	$7.9395\pm1.2\times10^{-10}$

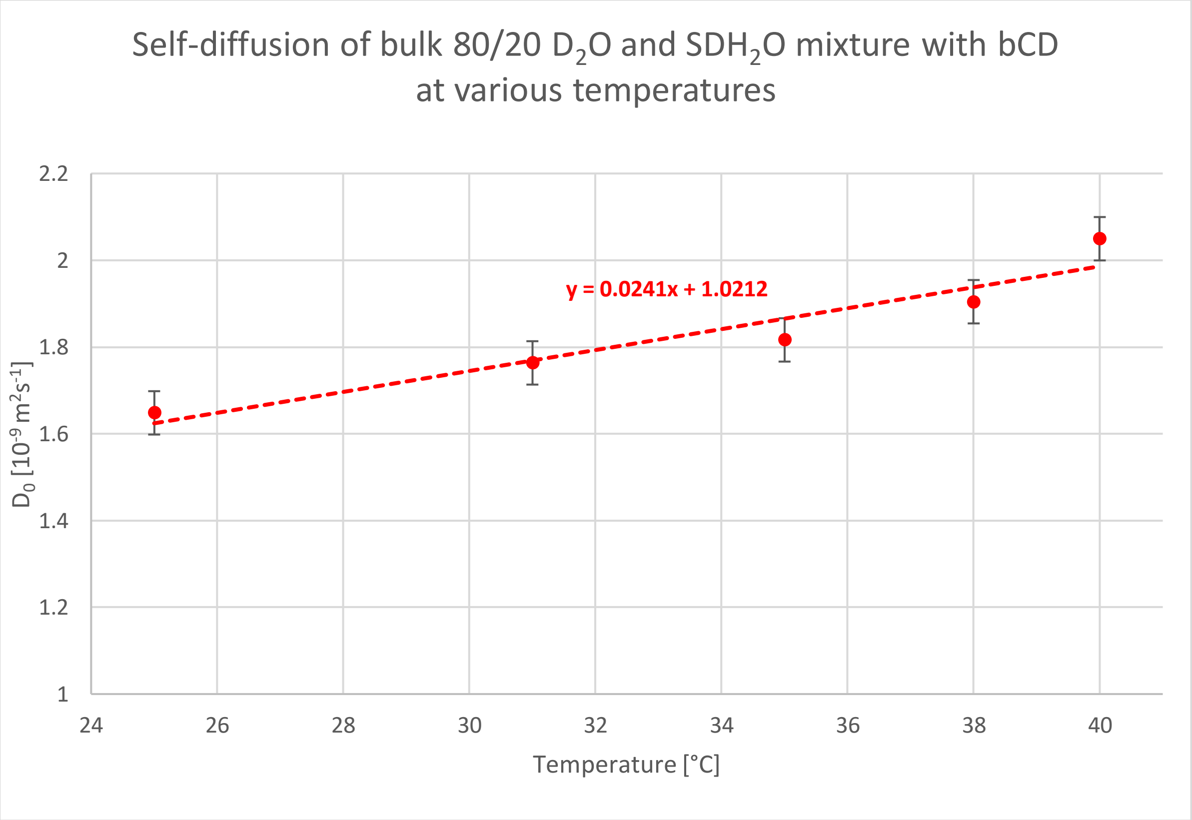

*Figure 7.7.2: The 80:20 D_2O and SDH_2O D_0 values are plotted against temperature. The standard deviation is shown on the y-axis values, which are based on **table 7.7.3**'s values. The linear function for the water mixture is y=0.0241(x)+1.0212.*

The D_0 values for the 80:20 D_2O/SDH_2O mixture with βCD is shown in **table 7.7.3**. The uncertainties for the water mixture are around 0.05×10^{-9} – 0.06×10^{-9}. The trend corresponds well with diffusion kinetics, showing an increase in D_0 as temperature increases similar with the other water references in **figure 7.7.3**.

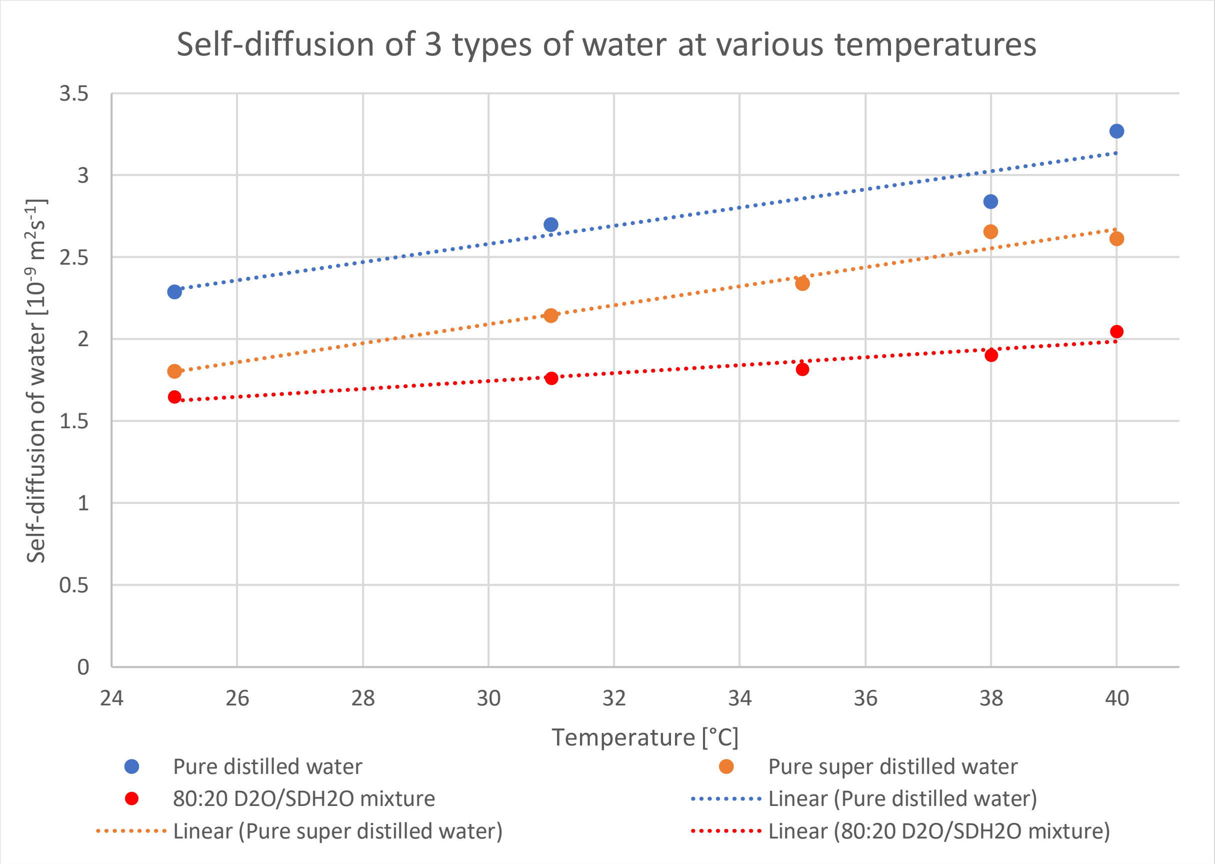

Figure 7.7.3: Overview of the self-diffusion of different types of water. All the curves show an increasing self-diffusion coefficient with temperature, with the pure distilled water showing the highest trend, whilst the 80:20 D_2O/SDH_2O shows the lowest curve.

When comparing the water D_0 values with temperature as shown in **figure 7.7.3**, it can be seen that the 80:20 D_2O/SDH_2O have the lowest curve compared to the distilled water reference from [4], as well as the pure super distilled water. All the curves are increasing with temperature. The same behavior can be seen for the βCD, but uncertainty is higher, particularly at the higher temperatures like 38°C and 40°C.The diffusion of the βCD is also lower compared to water, which is expected as βCD is a large molecule compared to water. Its large size makes it so that the movement of these βCD molecules will be slow. It is also noted that the values of the D_2O/SDH_2O mixture have the lowest D_0-value at every temperature mark compared to the distilled water reference from [4] and the pure distilled water. This can most like be due to D_2O being heavier and have stronger intermolecular forces compared to distilled and super distilled water. Stronger intermolecular forces make the liquid more viscous, thus making it so that the self-diffusion of the 80:20 D_2O/SDH_2O mixture being the lowest. This is supported by a paper done by Hardy et al, which shows the distilled water having lower absolute viscosity compared to pure deuterium oxide from 20°C→120°C (see **attachment 7**). The units Hardy used were in centipoises, so 1 centipois=0.001 Pa×s. It can also be due to the lack of gradient strength calibration, which can lead to lower diffusion as it can leave the b-factor in **equation 3.4.2** higher than one would like, thus making the gradient strength weaker. However, it was mentioned earlier that the experiment did not see the need of calibration as the project aims to measure relative changes in diffusion (D/D_0).

The D_0 values of βCD were increasing with temperature as shown **figure 7.7.4**. This trend is a similar finding in Erdos et al's paper (see **attachment 8**) [32], which found the βCD diffusion to be increasing with temperature. Erdos' Paper also found that the average number of hydrogen bonds for βCD decreased with increasing temperature (see **attachment 9**). Recalling the structure of P(NIPAM) and βCD, the structure of βCD, particularly its cavity can host water molecules through the small and large rims that act as entrance into the cavity. Due to this structural design, water can form hydrogen bonds with the cyclodextrin, but the average amount of hydrogen bonds decrease with increasing temperature as more hydrogen bonds are being broken down [26]. This can explain why diffusion for βCD increases with temperature.

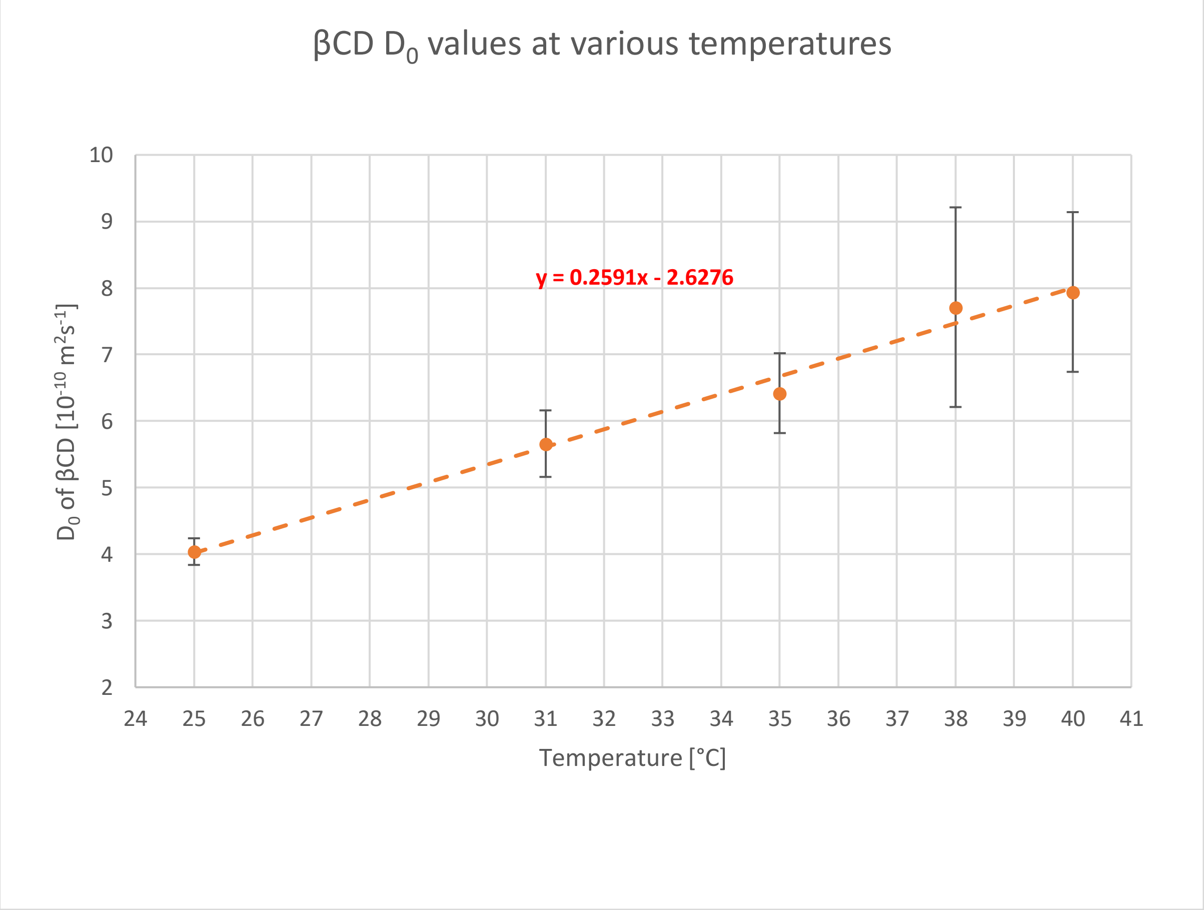

*Figure 7.7.4: The βCD D_0 values are plotted against temperature. The curve has the linear function y=0.2591(x)-2.6276. The data points have a good fit with the trendline, and uncertainties are given based on **table 7.7.3**. Uncertainty is at its highest at 38°C and 40°C.*

With that in mind, the explanation for the D_0 trend is supported by [26,27-29], which showed that solute-solvent interactions with hydrogen bonding affected diffusion of the solute in a solvent by slowing the diffusion process. Tominga et al found the polar cyclohexanol diffusing slower in alcohol than it did in cyclohexane due to the formation of a solute hydrogen bond with the solvent [28]. Chen and Chan also found that solutes that were able to form hydrogen bonds diffused slower than non-associated solutes. Moreover, they concluded that the retardation of diffusion was equivalent to an increase in the equivalent van der Waals volume of a hydrogen bonding solute. Chen also stated that solutes large than the solvent molecules can effectively pick up the smaller solvent molecules and diffuse as a complex [29]. Simulations from Lu et al supports these findings as it predicted slower diffusion coefficients for a solute that interacts in an attractive manner with the solvent but becomes faster if the forces are repulsive in nature between the solvent and solute [27]. In this case, the higher temperatures will break down more hydrogen bonds between the βCD cavity and the water solvent, which will allow the βCD to increase its movement, thus the D_0 values increase. Recalling the trend for water in **figure 7.7.2** and the βCD in **figure 7.7.4**, the D_0 values consistently increased with higher temperatures.

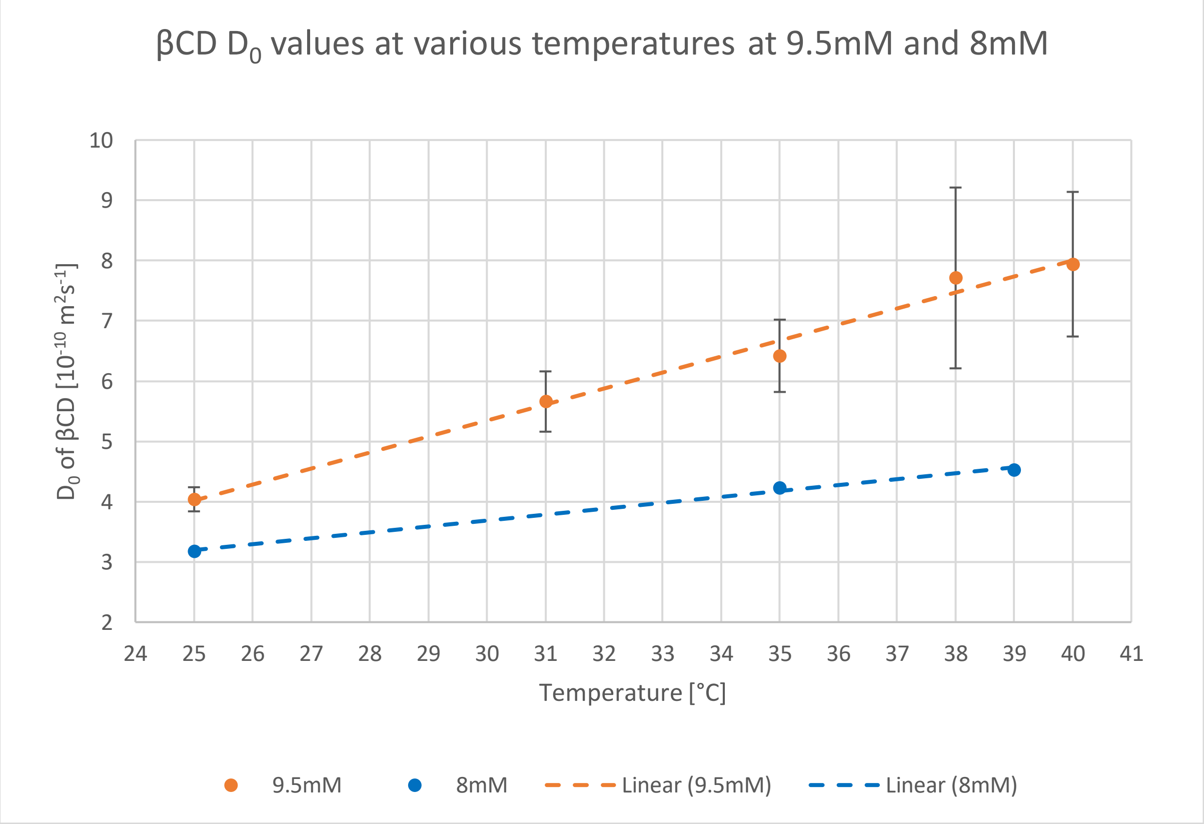

Figure 7.7.5: Comparison of 9.5mM βCD with 8mM βCD. The 9.5mM βCD was the concentration used for this experiment, whilst the 8mM βCD is from [31]. There is a clear disparity between the two curves. Higher concentrations of βCD are expected to have lower self-diffusion coefficients, but this is the opposite pattern seen here.

Taking reference from Paduano et al's paper [30] and Shrot et al's paper [31], their experimental values are used to compare this project's results at the 25°C, 35°C, and 40°C approximately. The solvents used for their βCDs were bi-distilled. Focusing on the concentration near this project's concentration of 9.5mM, we can extrapolate the trend observed in both [30] and [31]. In [30], the table shows $\bar{C}$ or concentration, particularly at 0.00994M(9.94mM), the diffusion is 0.3125×10^{-9} cm^2s^{-1} at 25°C (3.125×10^{-10} m^2s^{-1})(see **attachment 10**). From [31], the $\bar{c}$ or concentration around 0.008M(8mM), which was the closest concentration this project's βCD concentration, showed diffusion coefficients at 298.15K(25°C), 308.15K(35°C), and 312.15K(39°C). The paper from [31] showed that increasing concentration of the βCD led to the slight decrease of βCD. With that in mind, the self-diffusion coefficients were 3.18×10^{-10} m^2s^{-1},$4.23\times10^{-10}m^2s^{-1}$, and 4.53×10^{-10} m^2s^{-1} respectively. Erdos et al's paper also shows that free βCD in water at 298.15K is 3.50×10^{10} m^2s^{-1}[32]. Comparing these reference diffusion coefficients with the experiment's data in **table 7.7.3,** there is a clear disparity, especially around the higher temperatures of 35°C and 40°C, where the experiments D_0 values jumped substantially. This is shown in **figure 7.7.5**. It is worth just noting, but it is also pertinent that both [30] and [31] did not use MRI to measure diffusion, so comparisons must be taken with caution.

At 35°C for example, the experiment's D_0 value is $5.56\times10^{-10}m^2s^{-1}$, whilst the reference value from [31] obtained 4.53×10-10m2s-1. The D0 value at 25°C for [31] was $3.125\times10^{-10}m^2s^{-1}$, but the value obtained for this experiment is 4.04×10^{-10} m^2s^{-1}, so it is higher than expected. Despite this project's experiment using a slightly lower βCD concentration than the concentration used in [30], **attachment 10** does show that a lower $\bar{C}$ should lead to a higher βCD, thus the obtained D_0 values seen in **table 7.7.3** are higher than actually expected when compared to other reference values. This indicates that the references for this experiment were not correct according to previous literature, thus indicating a potential systematic error for the diffusion experiment. The cross referencing of this experiment's data with literature studies supports the consequence of lacking to calibrate the gradient strength for diffusion as the main factor to the value disparity between the experiment's data and the literature's data. This will be discussed further in the next sub-section (improvements and considerations). Despite this, the linear functions for both βCD and water in **figure 7.7.4** and **figure 7.7.2** respectively are used moving on in determining the D_0 to be compared with the D-values of 40S, 40ST, 40T, and 31T.

(7.8) Qualitative analysis of βCD diffusion inside the hydrogel

40S

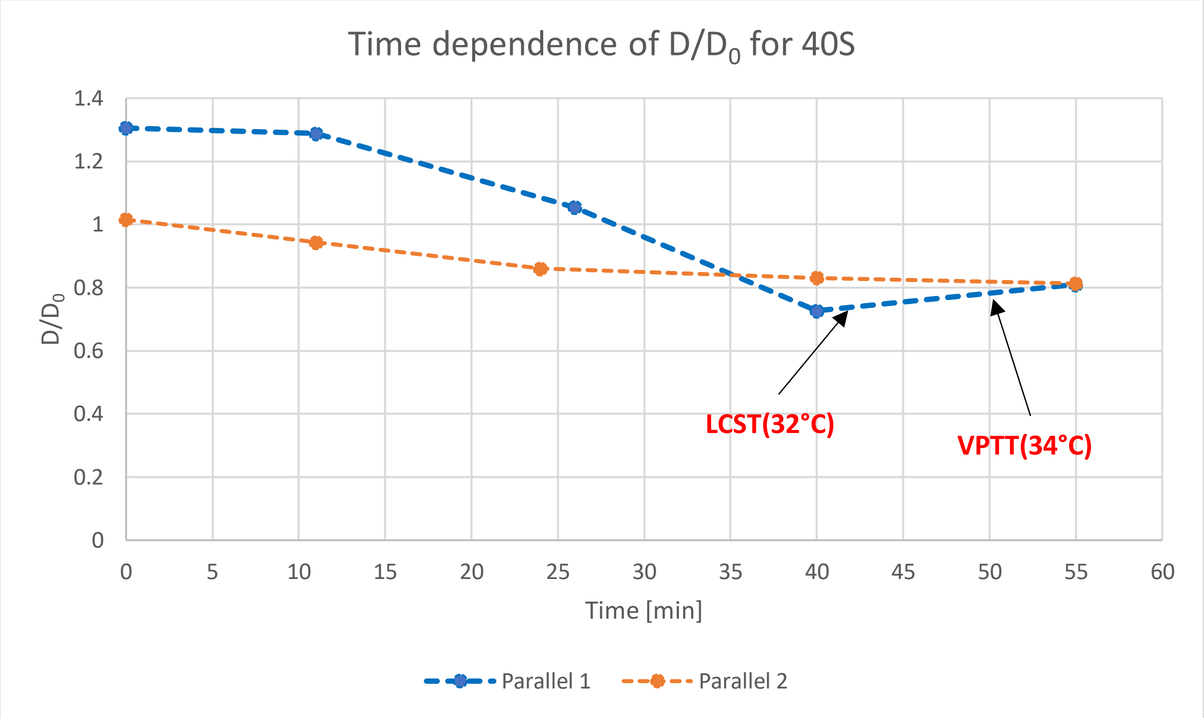

Figure 7.8.1: Time dependence of the normalized βCD self-diffusion coefficient of 40S parallel 1 and parallel 2, where the blue curve represents the 1st parallel, whilst the orange curve represents the 2nd parallel. LCST and VPTT markings are also presented.

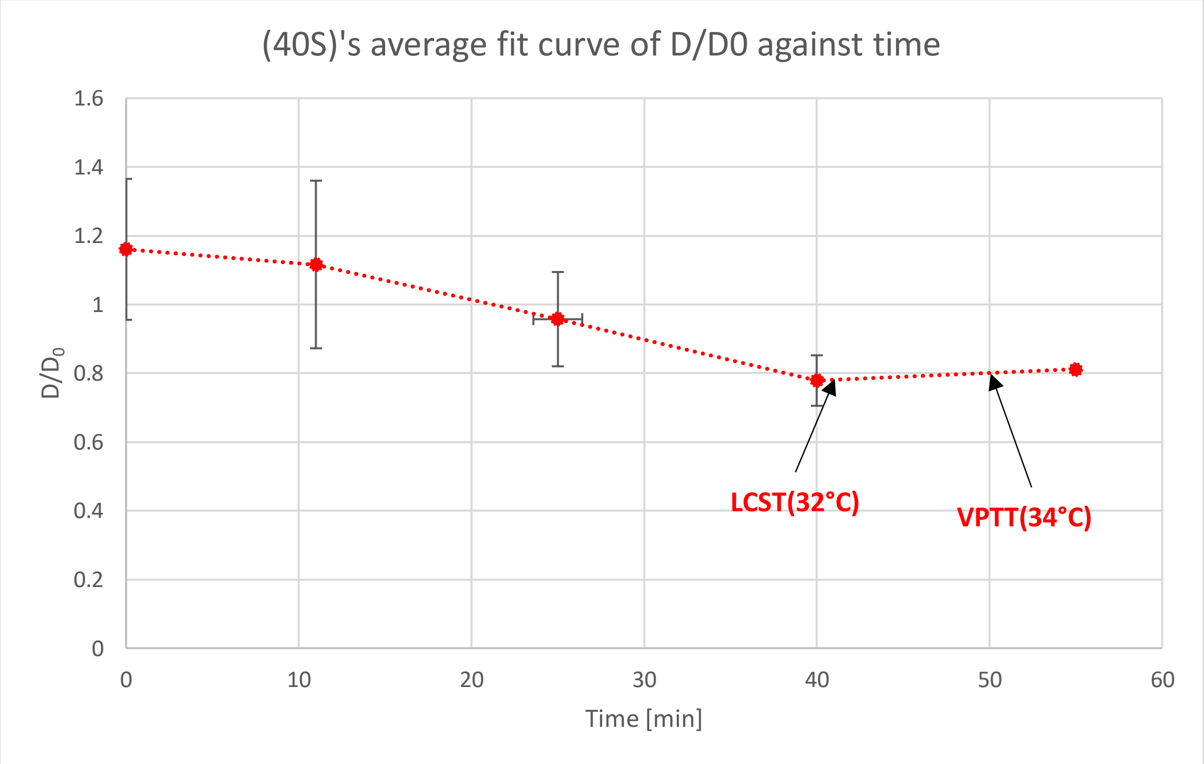

*Figure 7.8.2: The average fit curve of **figure 7.8.1** with the time. The temperature markings are labelled, and the curve has their error bars. The error bars for the 1st two data points appear large on the y-axis of the experiment, but it decreased substantially after some time. This gives rise of concern on whether the diffusion data at the beginning of the graph are stable.*

Figure 7.8.1 showcases the D/D_0 trend with time for the 40S or slow-heating experiment. It can be seen that both trends are relatively identical with parallel 1 being slightly higher at the beginning until switching with parallel 2 right before LCST. Parallel 2's curve begins at D/D_0, indicates that movement of the βCD molecules inside the hydrogel is equal to the supposed free βCD D_0 value. On the other hand, parallel 1 starts off at $D/D_0=1.3$, so the self-diffusion is higher inside the hydrogel than the free βCD. There is clear variation for both parallels, but they minimize the gap at the higher temperatures. At the end of the experiment when t= 55 minutes, both end up at 0.8 after VPTT. After this point, there is no more detected βCD signals for the MEGA PRESS to analyze. Combining both parallels gives the average fit curve for 40S in **figure 7.8.2**.

Looking at the average fit curve in **figure 7.8.2**, the variations seen between parallel 1 and parallel 2 are apparent, especially at the beginning of the experiment. The high initial D/D_0 indicates that βCD is not being restricted in its movement inside the polymer network. It is passively diffusing its molecules out to the medium gradually. This was observed in **figure 7.5.2,** where some βCD was seen to be decreasing in concentration little by little. The 2mm and 6mm voxels of the 40S experiment in **figure 7.6.4** shows a similar behavior, but it shows a small gradual increase of βCD outside the gel as it approaches LCST. Increasing the temperature decreases the D/D_0 to 0.78 when t=40 minutes. Even after reaching VPTT at t=55 minutes, the D/D_0 remains relatively unchanged, being around 0.80. This transition from a high D/D_0 to a low D/D_0 indicates a reduction of the βCD mobility inside the hydrogel as a result of shrinkage. The reduction of the polymer network size can cause it to reduce its mesh size and further restrict the diffusion of the βCD.

The lack of mobility is due to the degree of swelling in the gel decreasing correspondingly with temperature (see **attachment 11**). According to Tanaka et al's paper, the degree of swelling for P(NIPAM) decrease when temperature was increased from 20°C→30°C, and a transitional decrease was observed when the temperature was between 33-34°C. While the swelling decreased for the P(NIPAM), the diffusion of the water (HDO) increased (see **attachment 12**). However, this increase for the HDO(see **attachment 13**) only increased up to 34°C (via heating) before transitionally decreasing beyond VPTT. This decrease in diffusion led to broader signals being observed as a result of water molecules being caught up by the polymer networks, which are formed by the physical crosslinking at VPTT [33]. These results by Tanaka et al coincides with the results from Kaneko et al's paper, where he observed broadened peaks at higher temperatures and characterized dense layers that limited diffusion when temperature was increased [22]. A paper done by Griffith et al found a similar pattern, but he described the increase as being consistent, where the water self-diffusion coefficient increased from 24°C →56°C in the P(NIPAM) microgel system [4,35-37].

With these in mind, the decrease in D/D_0 for βCD can be associated with the shrinkage of the P(NIPAM) as it reduces the mesh size, which also slows the down the movement of βCD inside the hydrogel. A smaller mesh size coupled with a large molecule like βCD will lead to restricted movement as the small mesh sizes of the polymer network will act as physical obstructions. It shows the opposite trend seen Tanaka et al's paper for water due to the sheer size of βCD being not able to move as freely as the smaller water molecule, thus an increase in temperature up to VPTT will mean βCD will have limited movement inside the hydrogel network. However, given the lack of data points after VPTT, the experiment is inconclusive after this point. It is possible to speculate that degradation of these polymer networks sometime after the VPTT will lead to a continuatual decrease in D/D_0 as the physical crosslinkers present in the polymer network will collapse due to the coil-to-globule transition.

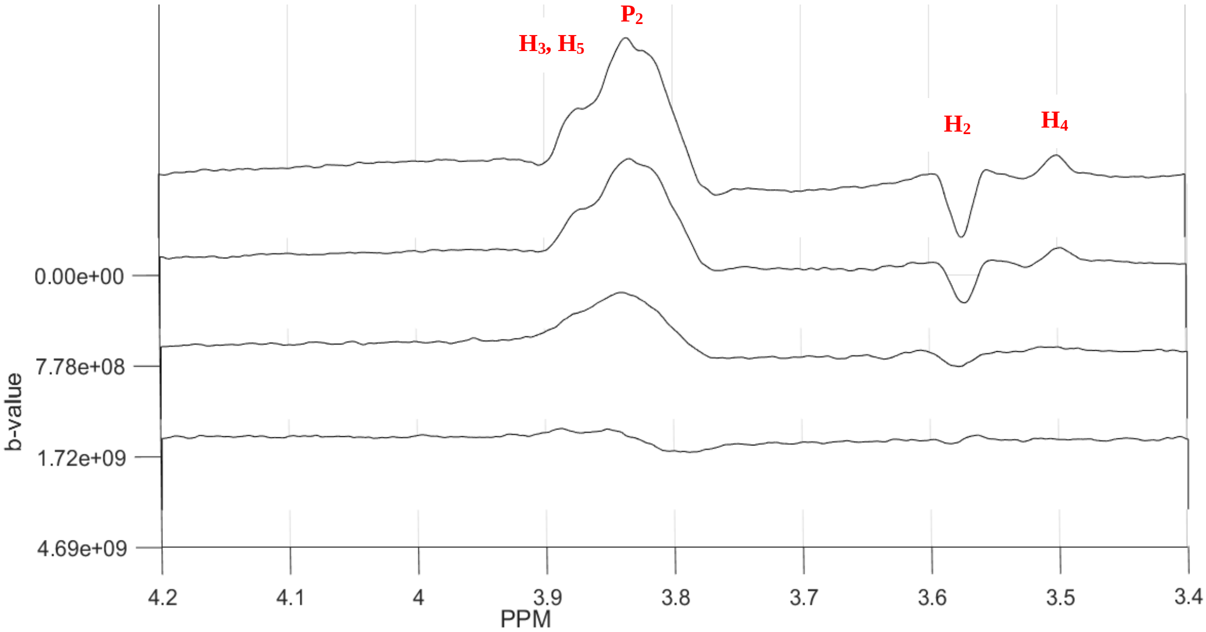

Figure 7.8.3: Signal graph of βCD at 25°C between 3.4ppm and 4.2ppm during the MEGA-PRESS sequence. This was taken as a reference run before temperature change. The signals of βCD, H_2-H_5 were all detected, and the b-values for each signal could be compared. The curve at the very bottom shows almost no signal due to the strong z-gradient as the strength here was 50%. It was excluded during the analysis as there is almost no signal detected. J-modulation is also present as some signals are inverted.

The lack of data points after t=55 minutes is associated with the technique itself to measure the D/D_0 of βCD and water. Coincidentally, this is also around the same time stamp in **figure 7.5.1** where the sharp decrease of βCD in the hydrogel happened. In **figure 7.6.4**, the increase in βCD can be seen to be increasing in magnitude before sharply increasing when t=79 minutes. With the delay of the sharp increase accounted for outside the gel, these observations support the significant decrease of βCD inside the hydrogel as a result of the phase transition. The loss of βCD inside the voxel means that the MEGA PRESS is unable to detect any signals of βCD after VPTT, thus no conclusion can be drawn after achieving VPTT and onward. The data points after the 55-minute mark were not usable as the background noise of the sequence was drowning out any signal for the βCD between 3.4ppm and 4.2ppm. Couple this with the low concentration of the βCD that was decreasing at an increasing pace due to VPT and the long TE times of the MEGA-PRESS sequence, which was 68ms, the signals were virtually impossible to detect after VPTT. As seen in the NMR spectra comparison in **figure 7.4.11**, the significant drop in βCD intensity and P(NIPAM) happened at 76 minutes, 16 minutes after surpassing a VPTT at t=60 minutes. For more visualization, compare **figure 7.8.3**, which shows the signals processed in MATLAB using MEGA PRESS at the first run at 25°C, and **figure 7.8.4**, which shows the signals at 38.4°C at the 70-minute mark. **Figure 7.8.4** shows only noise, whilst **figure 7.8.3** shows the clear signals for βCD.

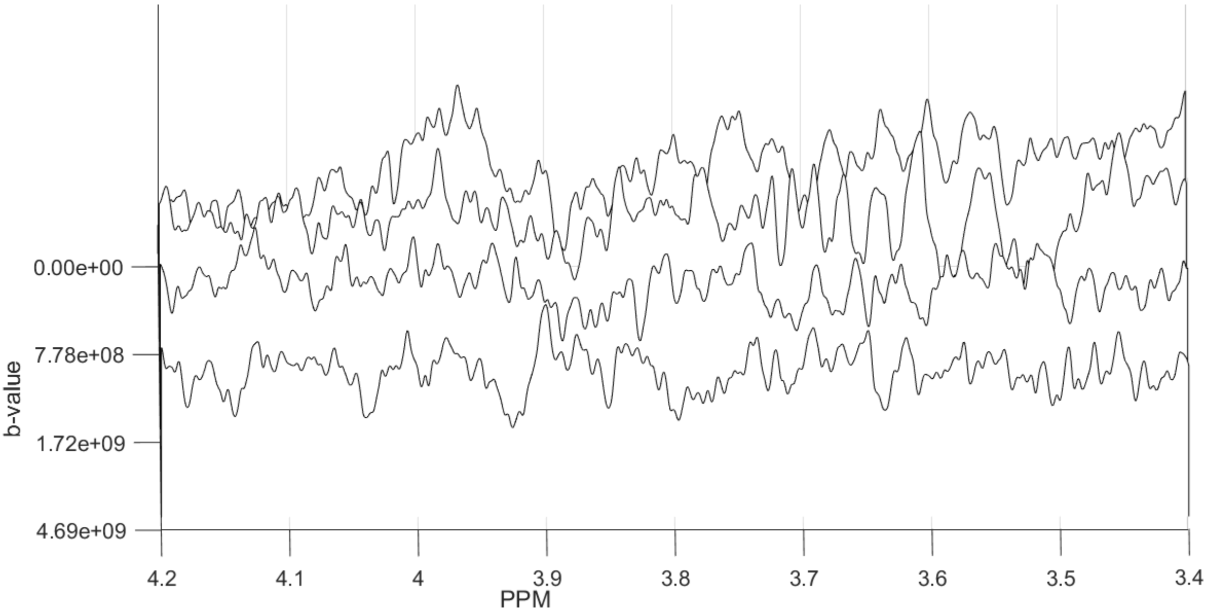

Figure 7.8.4: 6th data point analysis using MEGA-PRESS at 38.4°C. This was recorded 70 minutes after temperature change. Comparing it to ***figure 7.8.3****, the signals of βCD are no longer clear, and only noise remained. If there is βCD left, the noise level is too strong for the βCD signals to detected as the TE is long, which leads to strong J-modulation effects. As a result, the signal sensitivity is reduced.*

Both figures have chemical shift interval from 3.4-4.2ppm. The signals of H_3 and H_5 were not included during analysis as it integrated together with P_2 from the hydrogel, since the βCD is inside the hydrogel. It was also taken into consideration that the signals of the βCD was expected to have a higher chemical shift due to the increasing temperature. For the sake of visualizing the loss of signal, the H_3 and H_5 signals were included regardless of this mix integration. Given these circumstances and observations, this makes MEGA-PRESS not the best option to measure diffusion as it suffers from J-modulation from the J-couplings due to the high TE-value and the usage of the strong magnetic gradients, particularly for the z-gradient. Consequently, these factors reduce the intrinsic sensitivity, signal-to-noise ratio, spectral width, and resolution [33-34]. The weakening of the βCD signal intensities overtime due to diffusion and the effect of J-modulation is enough to prevent further recordings of data. This supports the notion that the diffusion graph presented is not conclusive, and it must be reevaluated to be attempted again with a different method, preferably with more repetitions to reduce the errors bars seen in **figure 7.8.2**. A factor that could also affect these diffusion data, specifically creating large variance between parallels is the water suppression. Although water suppression rarely did cause a problem during the experiment, it is pertinent to maintain good solvent suppression. If the water suppression during the run is not sufficient, this could create phasing problems for the water signal, thus affect the slope and the integral calculation when the peaks for βCD are processed in MATLAB can reduce uncertainty during integral calculation of the peak intensities.

40ST and 40T

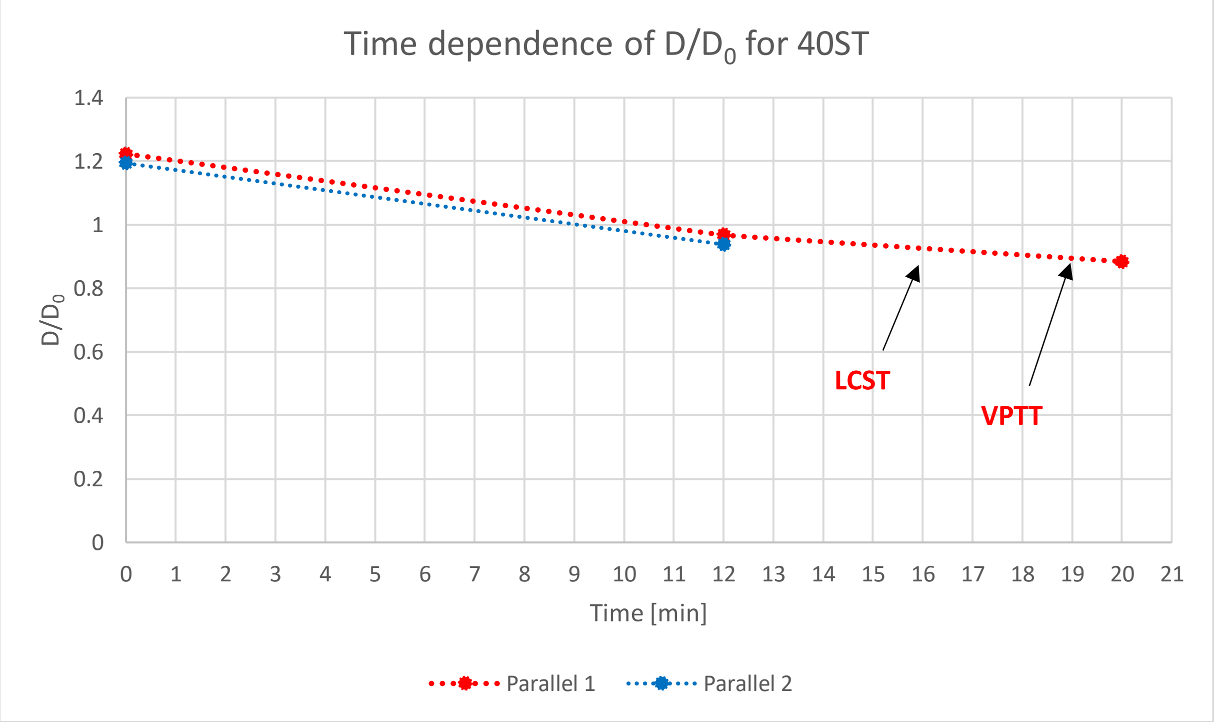

Figure 7.8.5: Time dependence of the normalized βCD self-diffusion coefficient of 40ST parallel 1 and parallel 2, where the red curve represents the 1st parallel, whilst the blue curve represents the 2nd parallel. The LCST and VPTT markings are also presented.

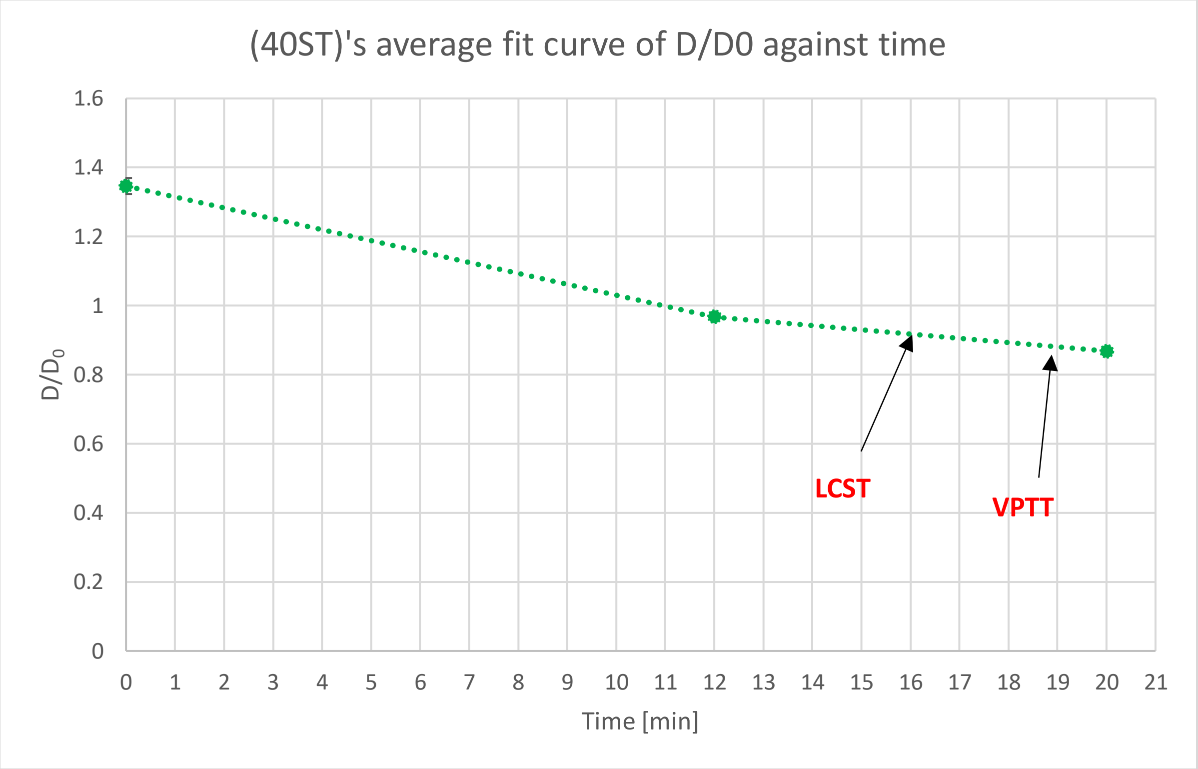

*Figure 7.8.6: The average fit curve of **figure 7.8.8** with the time. The temperature markings are labelled, and the curve has their error bars. There is no error bar for the last data point as **parallel 2** in **figure 7.8.7** did not have any recording at the 20 minute mark as it was recorded at the 25 minute mark. At that point, the βCD signals were no longer detected. The error bars at the first 2 points are minimal, especially compared to the curve in **figure 7.8.2**, which showed greater variance in the data points. However, like the 40S experiment, there are too few data points to get a good overview of the diffusion of βCD for the whole experiment.*

Looking at the diffusion data for 40ST in **figure 7.8.5**, both curves appears to have a similar trend of a decrease D/D_0 with time and have minimal deviation. However, parallel 2 lacks a 3rd point due to poor water suppression. The best fit curve in **figure 7.8.6** starts around $D/D_0=1.35$, which is a similar observation seen in 40S as well. A higher $D/D_0>1$ means that the βCD inside the hydrogel has more movement. From the few points available, it can be observed that the D/D_0 decreased in a sharper manner for 40ST than 40S as it reached LCST and VPTT quicker than 40S. As the temperature for 40ST approaches LCST, the βCD passively diffuses βCD into the medium, but the amount its diffusing is gradual and low. These findings are supported by **figure 7.5.4**, which does show a decrease in βCD as LCST is approached in the hydrogel. The sharp increase occurs around t=20 minutes. The events of **figure 7.5.4** is coherent with what is observed in **figure 7.8.6**. Similar to 40S, the βCD mobility is limited at VPTT due to the shrinkage of P(NIPAM).

This shrinkage reducing the mesh size makes it more difficult for the βCD to freely move due to the physical crosslinkers of the hydrogel. **Figure 7.6.7** does show the gradual increase of βCD around t=20 minutes, increasing its concentration sharply after a delay as it takes time to completely degrade the P(NIPAM). For reference, **figure 7.5.3** shows that at t=25 minutes, the voxel inside the hydrogel shows that only 59% of the initial βCD intensity remained; a significant drop in a short space of time, where the temperature is 37.4°C. Although **figure 7.8.6** is not conclusive, it does provide information about the reduction of mobility as temperature approaches VPTT. Unfortunately, there was no more available data after the 3rd recording as the signal for βCD was lost during the MEGA PRESS sequence, similar to what happened in 40S. For reference, look at **figure 7.5.4** as it shows 59% of the initial βCD intensity at the 25th minute mark, which is 9 minutes from the next MEGA-PRESS run at the 34th minute mark. At this point, the βCD intensity was already around 10% of the initial βCD intensity value thus it makes sense that no signals were no longer detected due to the rapid nature of the temperature experiment.

Similar to the 40S, both 40ST and 40T were not able to cover the diffusion progress of their experiment duration. 40ST recorded a maximum of 3 points accounting for both parallels, but 40T had no recorded data. By the time the MEGA sequence ran for 40T, it was 17 minutes already in due to the long shimming time of the MEGA PRESS sequence, and the previous sequences before it, namely FLASH, MSME, Local shim and B_0 mapping, and STEAM, were running before MEGA PRESS. According to **figure 7.2.5**, LCST was reached at 5 minutes and VPTT was reached between 6 minutes after inserting the sample. This is the most rapid temperature change, even compared to 40ST.

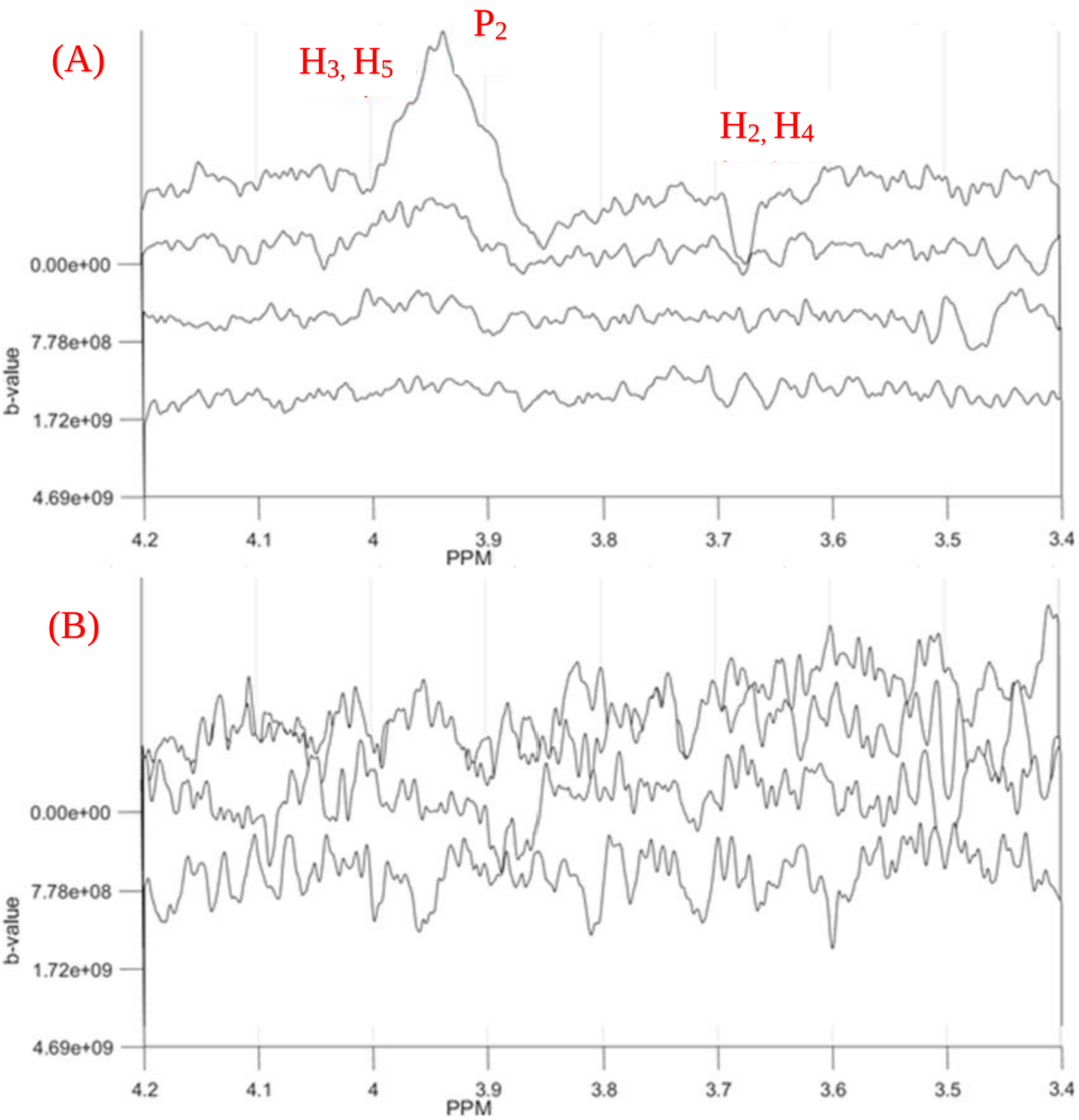

Figure 7.8.9:40T's graph, where the b-value is plotted against the chemical shift(ppm) interval of 3.4ppm-4.2ppm. The first run(A) was recorded 17 minutes after sample insertion, whilst (B) was recorded after 28 minutes. The βCD signals (H_2-H_5) and the P(NIPAM) signal, P_2 is shown at the top graph in (A) to show the absence of signals and the excess noise at (B).

At the 17-minute mark, the temperature of the sample is expected to be between 38.4-39°C, so the phase transition has already progressed substantially for 40T, and the concentrations of both P(NIPAM) and βCD are expected to be short. This can be seen in **figure 7.8.9(A)**, especially if one compares it to **figure 7.8.3** of 40S as the signals are severely weakened that it is almost difficult to distinguish the βCD signals, particularly for H_2-H_4. The signals for H_3 and H_5 are shown here for pure visualization as it is not included during data processing because P_2 is found at the same chemical shift as H_3 and H_5. A closer look at the H_2 and H_4 signals in **figure 7.8.10** shows the signals have very weak intensities, which indicates that VPT has already occurred for a while. The subsequent run in **figure 7.8.9(B)** after the 17 minute mark is not usable due to the noise level overpowering the βCD signals, making it virtually impossible to measure an accurate diffusion coefficient value from the H_3 and H_5 signals.

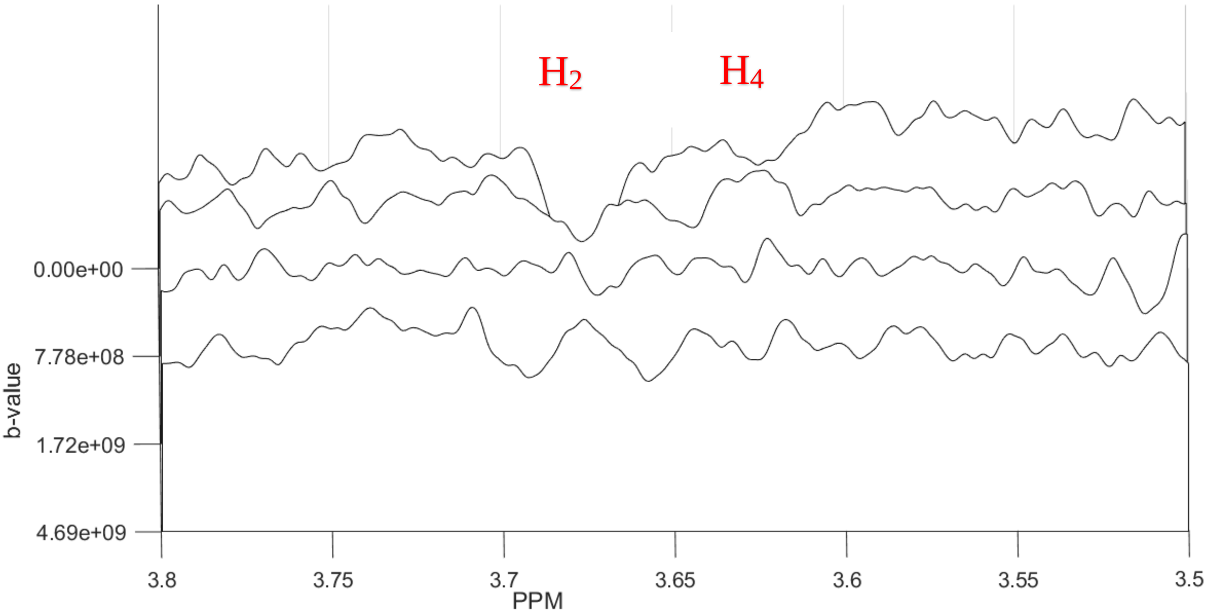

Figure 7.8.10: A closer look into βCD's H_2 and H_4 signals between 3.5ppm and 3.8ppm. The signals for βCD are almost drowning in noise, even at the first run, which strongly indicates that βCD concentration must be dwindling rapidly.

It wasn't until the last two runs at the 157th and 178th minute in which the noise level reduced enough for the βCD signals to be seen to some extent, but this is deemed still unacceptable as the H_2 and H_4 signals were still not as clear, and the uncertainty of the D-values were larger than the actual D-value itself. This can be due to the noise as it can still affect how the integration calculation will be processed for the βCD signals. These last two runs are shown in **figure 7.8.11(A)** and **7.8.11(B)** respectively. In addition, due to the absence of majority of the measurements prior to the last 2 runs, no graph was made as it would be futile as it cannot provide any information on how diffusion occurred for the βCD over the course of 3 hours in a temperature jump to 40°C. This absence of signals is unavoidable in MEGA-PRESS, worsened by the fact that the βCD concentration is low to begin with, and as more βCD diffuses out, the less there is inside the hydrogel. The low sensitivity and signal detection of MEGA PRESS makes it inevitable that no more βCD signals can be detected after surpassing VPTT and the polymer network collapses, so it had the worst effect on the 40T experiment, followed by 40ST and 40S in that order. Therefore, the method should be revaluated or replaced in the future as to obtain reliable D-values of βCD with minimal uncertainty, as well as utilize a method that has great sensitivity or signal detection.

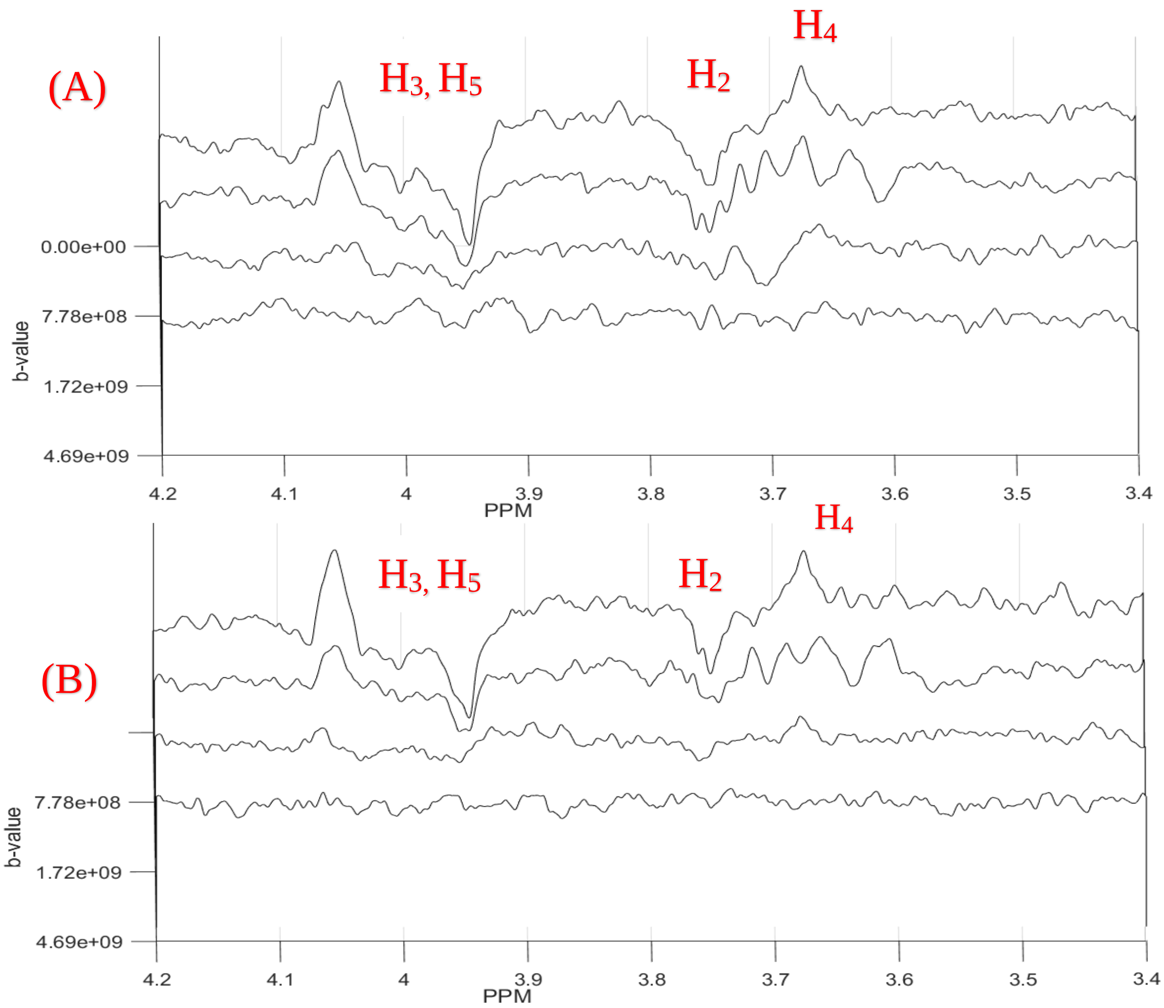

Figure 7.8.11: 40T's graph, where the b-value is plotted against the chemical shift(ppm) interval of 3.4ppm-4.2ppm. The first run(A) was recorded 157 minutes after sample insertion, whilst (B) was recorded after 179 minutes. The βCD signals (H2-H5) are highlighted above to show the presence of the weak signals. Noise is still present.

31T

Both parallel 1 and parallel 2 from **figure 7.8.12** appear to have a resembling pattern with regards to how D/D_0 varies with time. Both parallels begin when t=16 minutes at $D/D_0=0.8$, which indicates that the mobility of βCD is being limited inside the P(NIPAM). At this point, the temperature of the sample is expected to be 29.8°C for both parallels according to **figure 7.2.9**, so the temperature is already close to the final temperature just right before LCST. Initially, both curves increase, but at the 3rd point, they begin to fluctuate with parallel 2 decreasing sharper than parallel 1 at the 4th data point. At this moment, parallel 1 fluctuates up, whilst parallel 2 fluctuates down; lower than parallel 1. They both interchange until the end of the experiment, where parallel 1 achieved a D-value 68% of the D_0, whilst parallel 2 have 77% of the initial D_0. Throughout the entire duration, both parallels show a fluctuating pattern, increasing and decreasing at different intervals, but remaining between $D/D_0=0.85$ at the highest and $D/D_0=0.6$ at the lowest after t=60 minutes.

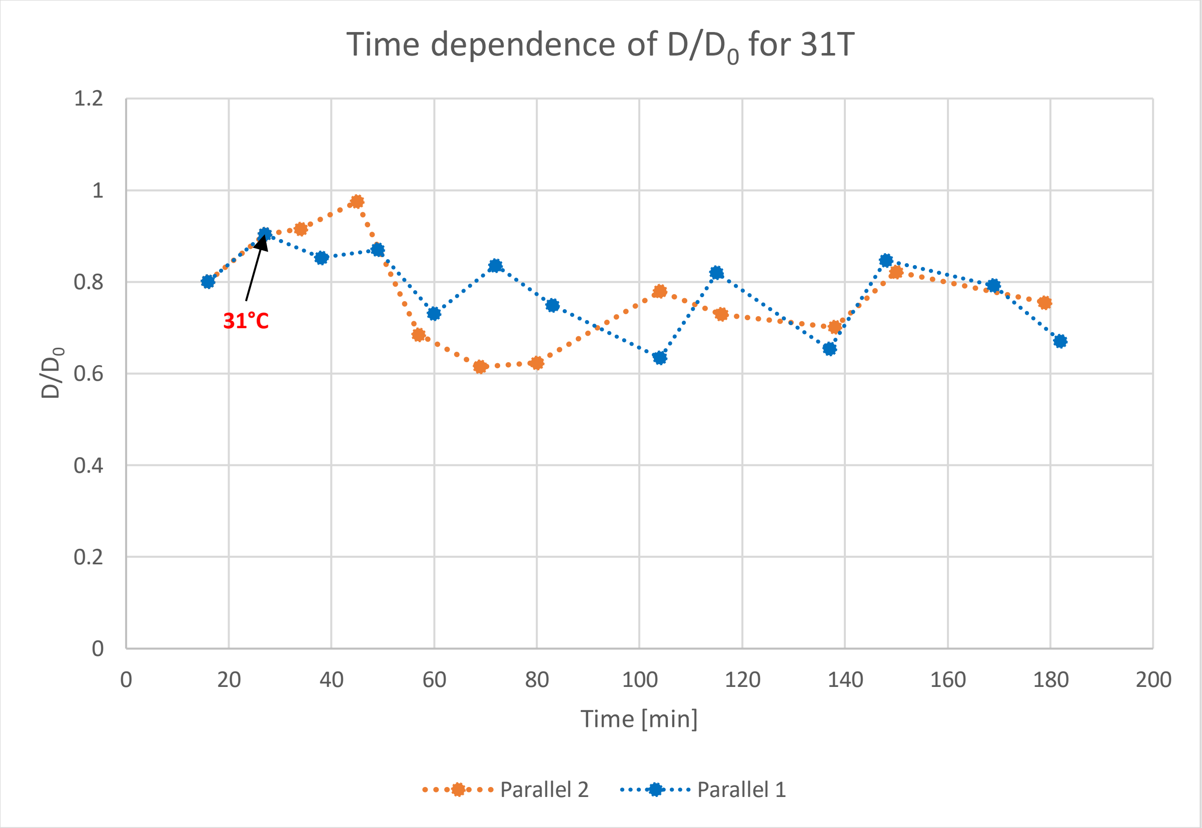

Figure 7.8.12: Time dependence of the normalized βCD self-diffusion coefficient of 31T's parallel 1 and parallel 2, where the blue curve represents the 1st parallel, whilst the orange curve represents the 2nd parallel.

The best fit curve for 31T is shown in **figure 7.8.13**, and the error bars show minimal deviation except in the middle of the graph, specifically at the 70-minute mark up to the 140-minute mark. On the other hand, variation is minimal when t=0-60 mins and t=140-180 mins. In addition, the best fit curve follows the pattern from both parallel 1 and 2, but it appears slightly stagnant and flat from the 60-minute mark up to the 120-minute mark. The pattern in **figure 7.8.13** almost follows the pattern seen in [4] starting at the 50-minute mark for 31T. The only difference being that **figure 7.8.13** shows a slight gradual increase in D/D_0 before sharply decreasing when t=47 minutes to D/D_0=0.7

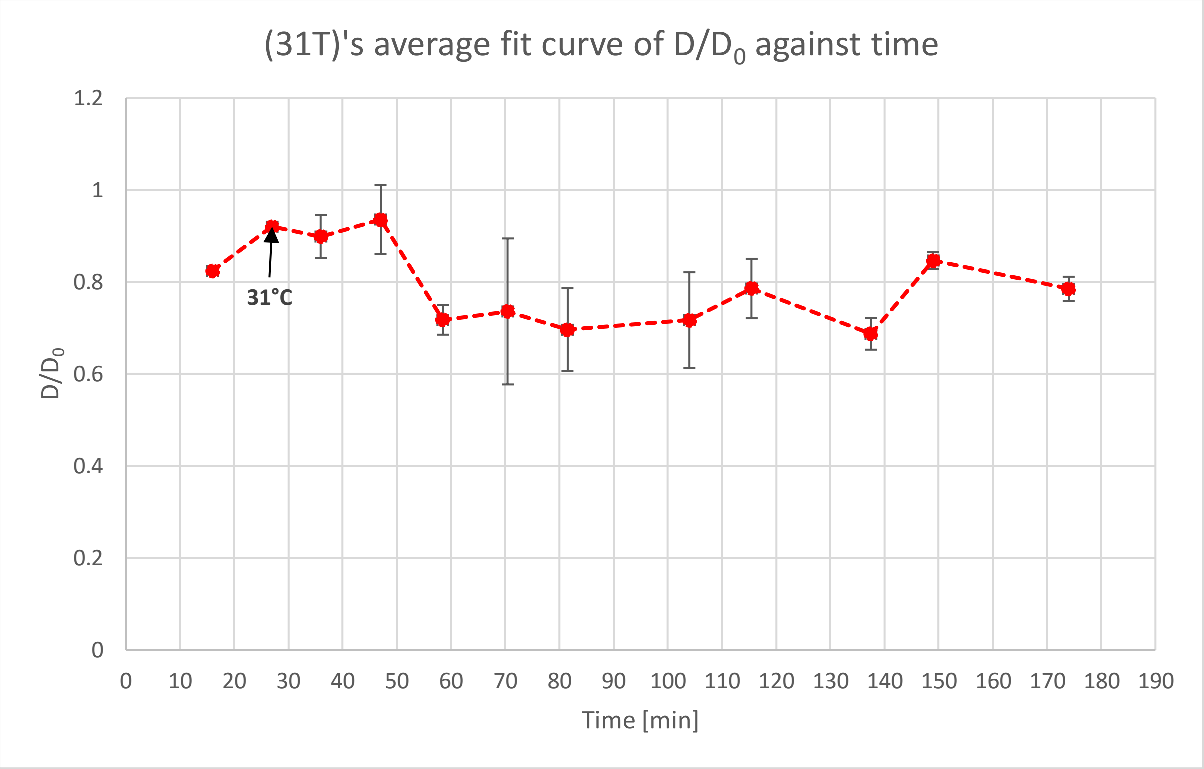

Figure 7.8.13: The average fit curve of ***figure 7.8.12*** *with the time. The temperature markings are labelled, and the curve has their error bars for each run. The error bars show a degree of variation, where the points from t=70 mins → t=120 mins showed the largest variation in the graph, with the 70-minute mark showing the largest variation out of all of them. Unlike 40S, 40ST and 40T, 31T managed to record the diffusion data for the entire duration of the experiment. This is most likely being attributed to the fact that the βCD concentration remained sufficient in the hydrogel as temperature never went over LCST or VPTT, in which was the points where the signals of βCD were not strong enough to be detected using MEGA-PRESS.*

This slight increase in D/D_0 and sharp decrease after the t=47 mins can be attributed to a slight gradual release of βCD from the hydrogel (**figure 7.5.7**) out into the 6mm and 2mm voxels from t=30 mins to 65 mins as shown in **figure 7.6.11**. Inside the hydrogel, although the βCD intensity remained above 96% of the initial βCD intensity, the gradual decrease up to t=60 minutes can be observed before eventually fluctuating around 97% until the end of the experiment. This diffused βCD most likely diffused out into the medium as it can be seen in both the 2mm and 6mm voxel in **figure 7.6.11**, where both voxels show a general increasing pattern. The βCD release, however, is not significant compared to the other temperature experiments, and similar to what was seen for the diffusion of the hydrogel at 40S and 40ST, the mobility of the βCD is limited as the hydrogel is 1°C away from LCST, so some shrinking has occurred, but enough for the βCD to be squeezed out via coil-to-globule transition.

Overview of the combined temperature experiments

An overview of temperature experiments' diffusion curve with respect to time is shown in **figure 7.8.14**. Only 40ST and 40S start at a higher D/D_0, but they decrease with time as temperature increases. Eventually all 3 temperature experiments stabilize around $D/D_0=0.8$, which indicates limited mobility for the βCD as a result of shrinkage of P(NIPAM). When the temperatures go beyond VPTT, the concentration of βCD becomes too low for MEGAPRESS to record any signal after for 40ST and 40S. This was not a problem for 31T as it never beyond LCST. The trends seen all correlate to previous observations, and the reference papers support the notion that due to βCD's size in the shrinking polymer network, it will have a decreasing self-diffusion as the mesh size decreases. The disappearance of the signals for 40S and 40ST are due to the expulsion of the βCD from the hydrogel after VPTT, so these observations support the βCD analysis of concentration change

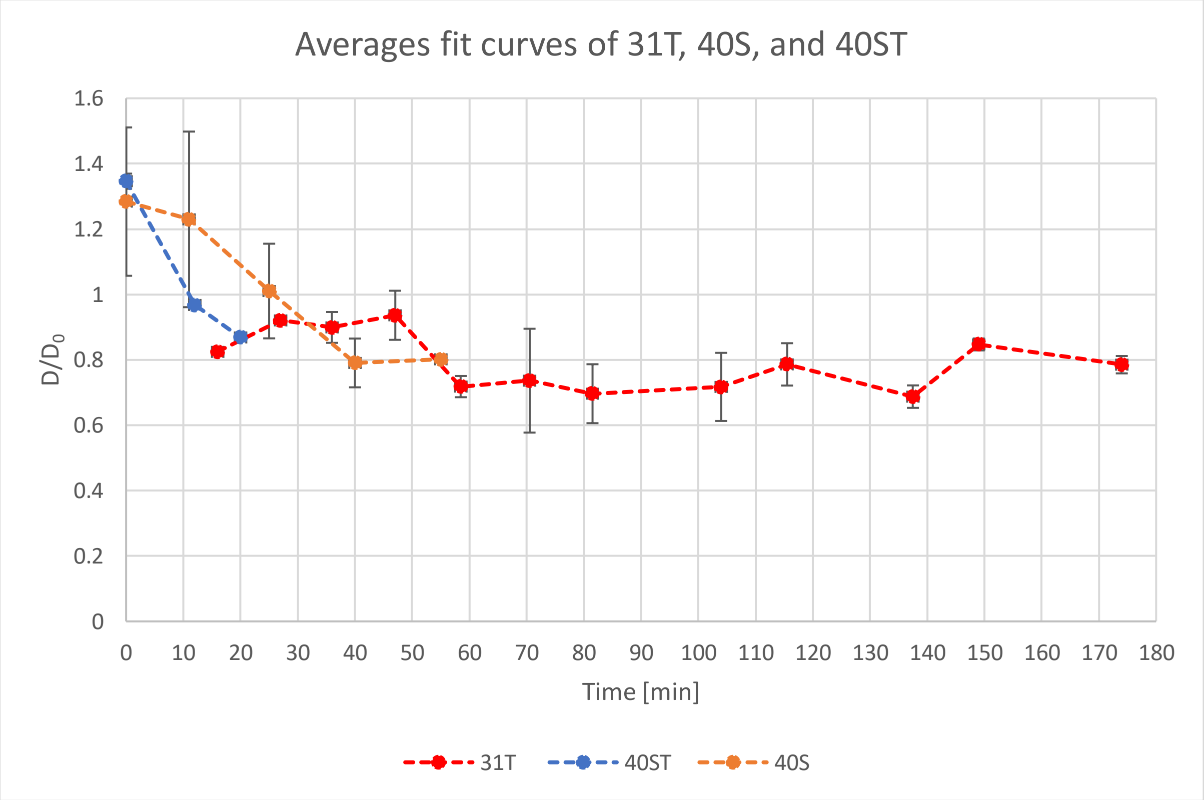

Figure 7.8.14: Overview of the average fit curves for 31T, 40ST, and 40S. The 31T experiment is represented by the red curve, the 40ST is represented by the blue, and the orange curve represents 40S.

Moreover, it is also worth noting that this was the only temperature experiment that was able to record diffusion data for the entire experiment's duration. The decrease of βCD concentration inside the gel voxel was not substantial, so the signal intensities were strong enough to be detected by the MEGA PRESS. This indicates that 31T never experienced any significant decrease in βCD concentration, which corresponds well to its findings in the βCD concentration change graph, as well its MSME and spectra comparisons before and after LCST. Noise was also minimal, so the calculations of the βCD diffusion using their peak integrals were acceptable. Consequently, this makes this MEGA PRESS sequence only sufficient for monitoring βCD before VPT. However, for future considerations to improve the method, it could be suggested that a higher concentration of βCD can be used. It can also be suggested that a larger variety of z-gradient strengths can be used. For this experiment, the pattern was 0,20,30, and 50% z-gradient strengths, with the last point being excluded due to the signal being drowned in noise as an overpowering gradient strength. Perhaps an interval of 0,5,10,15,20,25, and 30% z-gradient strengths can be suggested as more points would reduce the uncertainty of the integral calculations of the βCD peaks. This was the same gradient strength pattern used to obtain the D_0 values of βCD. However, the drawback for this would be then longer experiment times, so compromises will have to be made, especially for the temperature jump experiments.

Furthermore, a STEAM sequence could be used without the MEGA modification instead to remove the factor J-modulation due to J-couplings and the long TE-values. The inconclusive nature of 40S, 40ST and 40T after VPTT due to the usage of the MEGA-PRESS has left this experiment much to be desired when visualizing the diffusion of βCD itself for temperatures higher than VPTT. Water suppression was at times a problem, which can have negative consequences when calculating the peak intensities of βCD. Measured were taken to minimize the chances of solvent suppression influencing the integration calculation, but further optimization with the VP attenuation can done to further improve the accuracy of the MEGA PRESS calculations of self-diffusion as using D_2O on a mass scale can be costly.

Although the trends seen so far correspond to the data obtained in and out of the gel using STEAM, where they all adhered to the shrinking kinetics of P(NIPAM), it would be important to reduce the uncertainty of the D_0 values for βCD. The choice of solvent could also influence the results as every other literature paper used mostly distilled water, whilst this experiment used predominately a deuterium mixture with water (80:20 ratio). The reference values used the same water mixture, but with super distilled water. For better reflection, the same solvent should have been used, but water suppression would become a significant hurdle to overcome, particularly as it can potentially overshadow the signals of the βCD. Despite of these shortcomings, the diffusion data did partially provide information about βCD movement in the gel to some degree. The hydrogel and shrinking kinetics are followed in all observations as of now both in a quantitative and qualitative perspective, but clearly, improvements for the future are needed to obtain better and more extensive data coverage.

(7.9) Qualitative analysis of water diffusion inside the hydrogel

40S

Unlike the βCD signals during the MEGA PRESS run, the water signals (80:20 D_2O/H_2O) were present. **Figure 7.9.1** shows the dependence of D/D_0 against time. Both have minimal deviations from one another right until the 80th minute, where parallel 1 decreased and parallel 2 increased. Both started around $D/D_0=0.95$ and both end around $D/D_0=0.65\text{-}0.70$. The graph indicates that diffusion for water decreases for parallel 1 but increase generally for parallel 2. These two curves are combined in **figure 7.9.2** to yield the average fit curve.

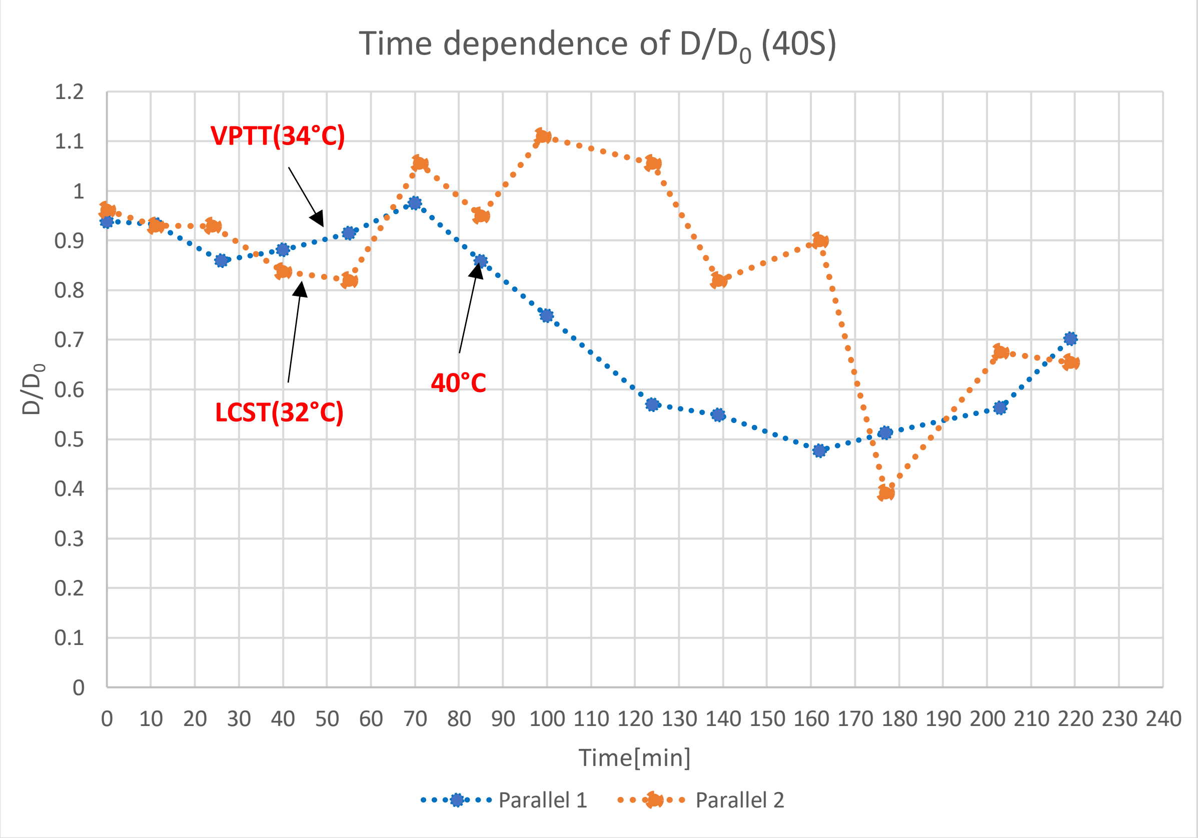

Figure 7.9.1: Time dependence of D/D_0 for 40S. Parallel 1 is represented by the blue curve, whilst parallel 2 is represented by the orange curve. The transition temperatures are marked on the graph.

Looking at the average fit curve in **figure 7.9.1**, some deviations can already be seen. The error bars are its largest from t=85-180 minutes. The curve also deviates from what other literature papers characterized for the diffusion of water inside the hydrogel. Tanaka et al and Griffith et al described the self-diffusion coefficients of water inside the hydrogel to increase with temperature. Tanaka specifically stated this increase should be expected until at VPTT, but this was not observed. Instead, it showed the opposite trend, where the D/D_0 decreased before increasing after VPTT. Just before 40°C at t=70 minutes, the curve shows a decrease in D/D_0, signalling a reduction of water mobility inside the transitioning hydrogel. This decrease continues until t=180 minutes before increasing to $D/D_0=0.7$. Overall, the curve does not appear similar to any reference papers, particularly to [4] since the 40S experiment is based off there. In [4], the trend showed an increase up to 38°C before decreasing once and stabilizing around 1.1 for D/D_0. **Figure 7.9.2** shows an extreme opposite, thus is deemed unreliable until more tests can be done to isolate the significant factor causing the deviation. However, it is also pertinent to consider that the general decrease seen here, especially after 40°C actually indicates that the water inside the gel is being restricted, most likely due to the collapsing polymer as mentioned by Tanaka et al in her paper [33]. Similar to the βCD, water is also being restricted due to the steric hindrance caused by the breakage of the polymer crosslinkers.

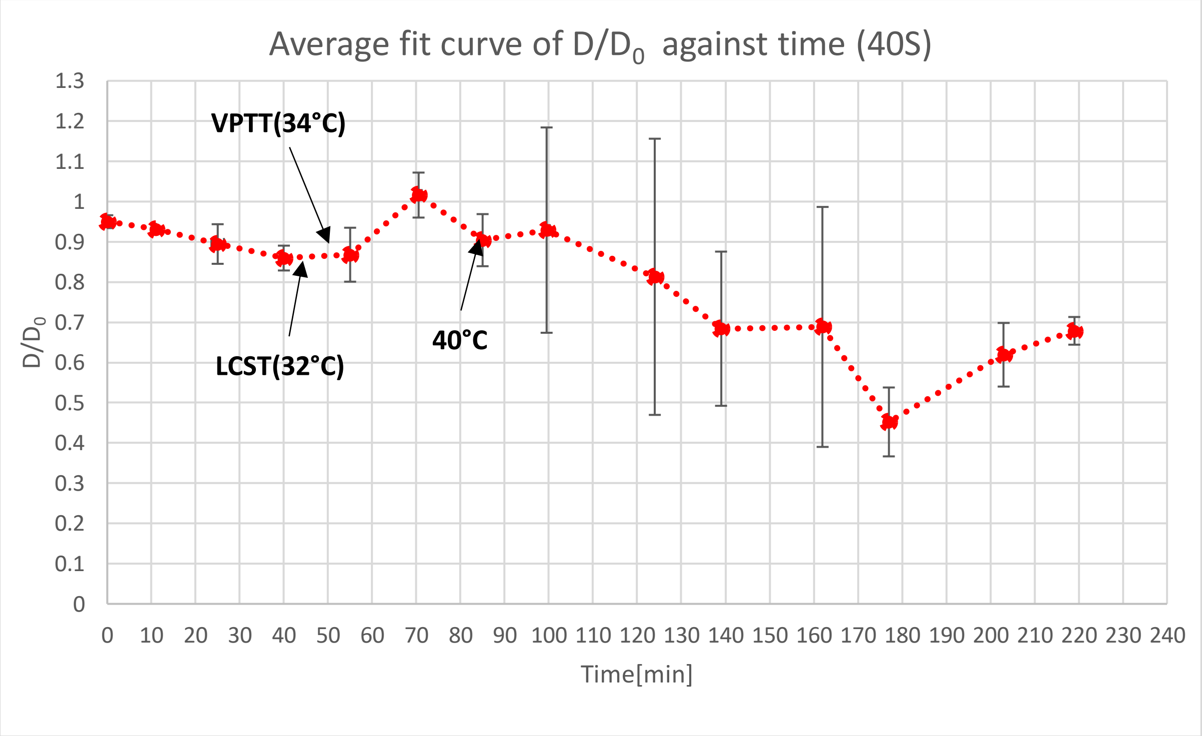

*Figure 7.9.2: Average fit curve of D/D_0 against time for 40S's water. The error bars seen in the middle of the graph is significant, and it is due to the large variation in D/D_0 between the two parallels in **figure 7.9.1**. The curve shows the opposite curve shown in [4], which makes this figure uncertain on whether it reflects the behavior of water inside the hydrogel for 40S.*

40ST

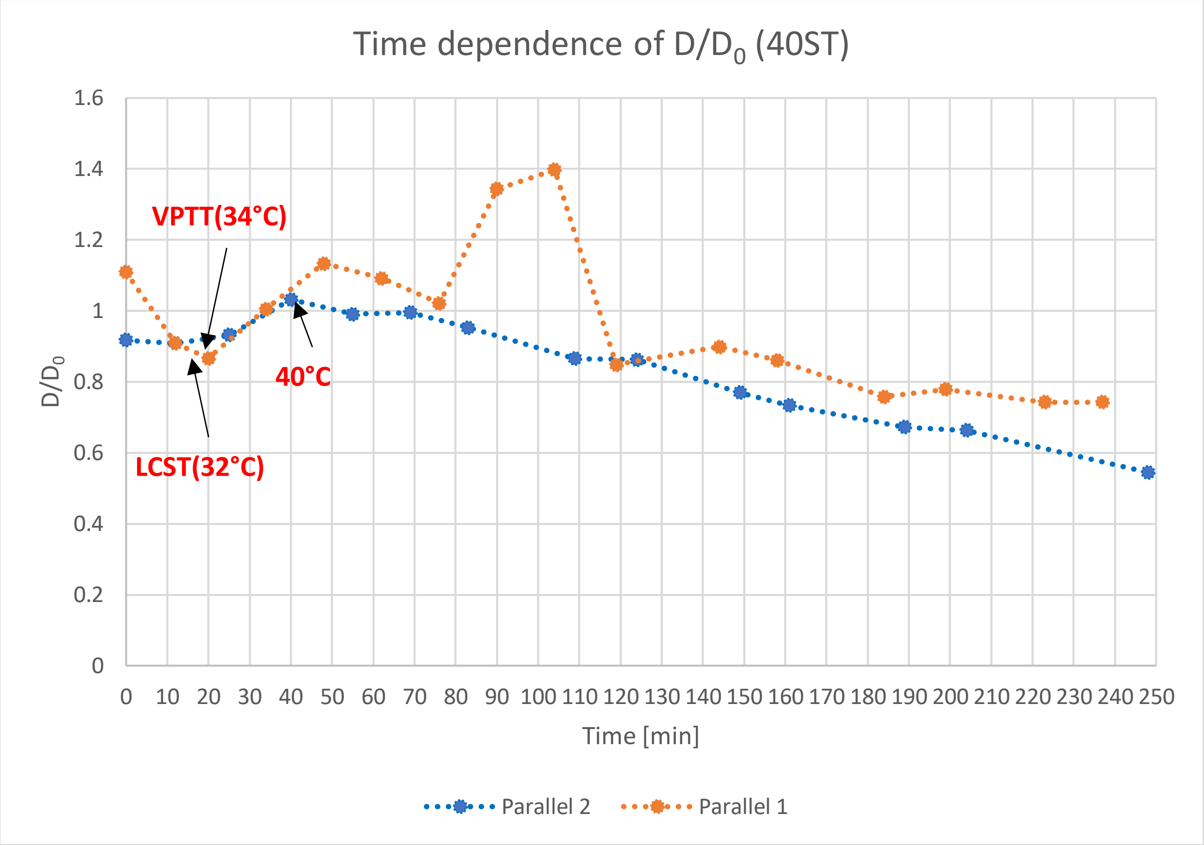

Figure 7.9.3: Time dependence of D/D_0 for 40ST. Parallel 1 is represented by the orange curve, whilst parallel 2 is represented by the blue curve. The transition temperatures are marked on the graph.

In **figure 7.9.3**, parallel 1 starts at a higher D/D_0 value of 1.1, whilst parallel 2 starts just under D/D_0=0.92. Both increase in their trend from t=20 minutes after VPTT. After reaching 40°C both decrease until reaching D/D_0=0.74 and 0.54 for parallel 1 and parallel 2 respectively. However, there are two potential outliers here in the curve for parallel. The two points found t=90 minutes and t=104 minutes are near D/D_0=1.4, despite the other parallel decreasing in trend. Moreover, parallel 1's curve predominantly shows its decreasing after 40°C, so these two can be the odd ones out of the curve. Plotting parallel 1 and parallel 2 together in **figure 7.9.4** shows the average fit curve with error bars. The largest deviations are found in the middle. Looking pass those two potential outliers in parallel 1, the curves for both parallel 1 and 2 are coherent with one another. Again, similar to what was seen in 40S, the pattern is decreasing only after t=107 minutes. The pattern seen here goes against the literature papers mentioned through out the experiment. D/D_0 is expected to increase before VPTT according to Tanaka's and Griffith's findings, but here it decreases similar to 40S. Tanaka mentioned that the self-diffusion of water should decrease only after VPTT due to the collapsing polymer network. However, the results in **figure 7.9.3** shows that the decreased happened at a very delayed time mark after VPTT. Instead, the curve showed an increase even after 40°C, which is already the point in which the gel has collapsed as shown in **figure 7.3.1** and **figure 7.3.2**. However, after t=105 minutes, it does proceed to decrease again. Unlike βCD, water is a smaller molecule, so it is able to traverse the collapsed network easier than βCD for example. This could explain some of its fluctuations. However, more tests should be done to verify the results, as well as reduce uncertainty.

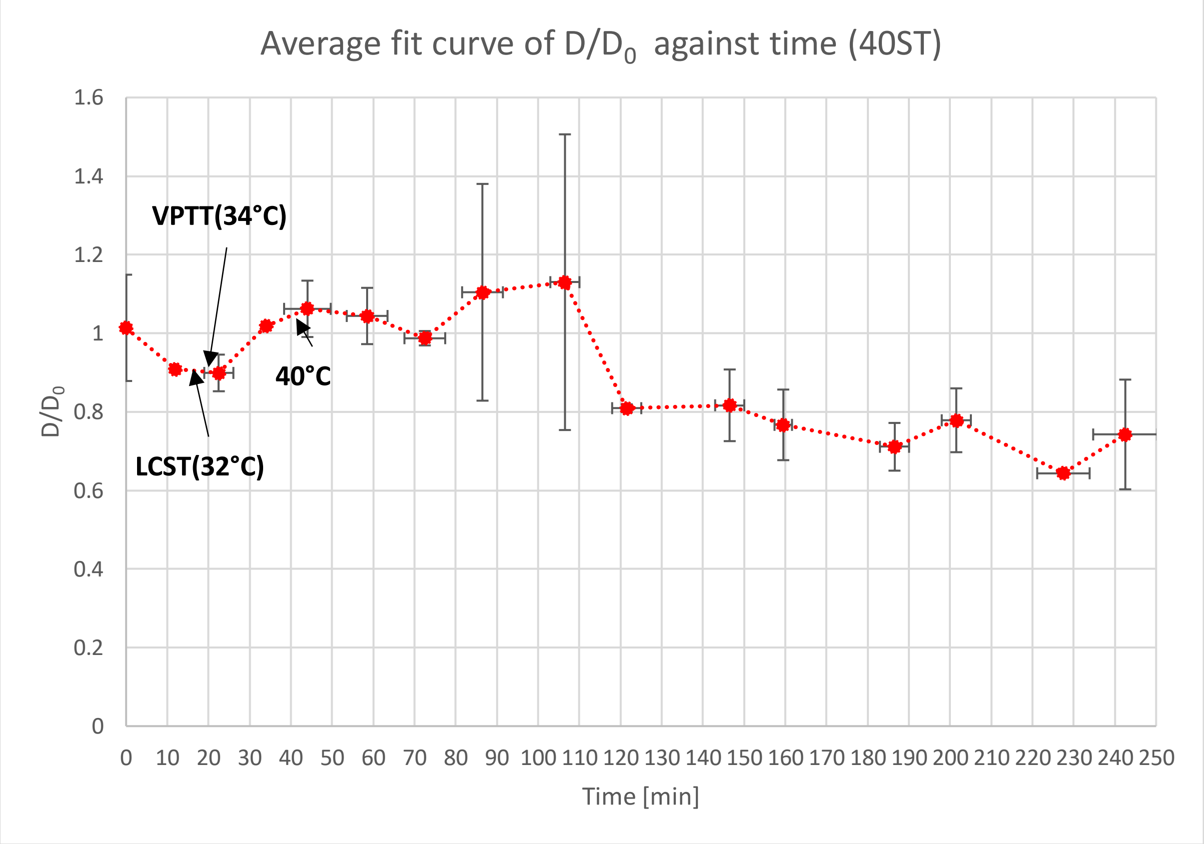

Figure 7.9.4: Average fit curve of D/D_0 against time for 40ST's water. The error bars seen are generally low, except in the middle when t=87 minutes and t=107 minutes.

40T

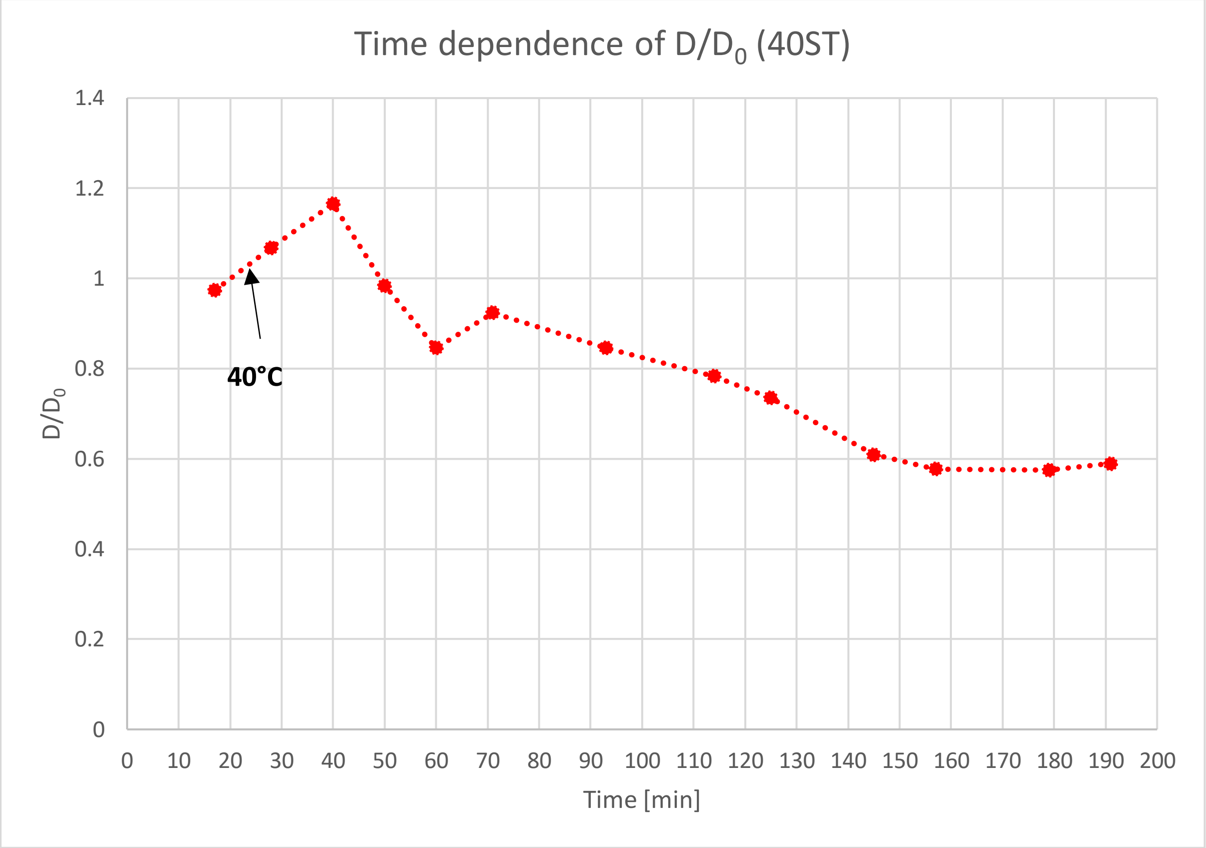

Figure 7.9.5: Time dependence of D/D₀ for 40T. Only 1 parallel was done for 40T. The temperature marking for 40°C is placed in the graph.

According to **figure 7.9.5**, it shows that there is an increase for D/D_0 for the 40T experiment right up until t=40 minutes. Afterwards, the D/D_0 decreases continuously until D/D_0=0.6 when t=190 minutes. This implies that the mobility of the water is restricted already. The pattern for the D/D_0 against time for 40T here is relatively similar to what was seen in Wisniewska's paper (see **attachment 13**) [4], but the difference here is that the decrease seen in **attachment 13** is that there is an increasing and decreasing fluctuation after the strong decline from D/D_0=1.4 to 0.7. In **figure 7.9.5**, there is no fluctuation. Instead, there is a steady decline from t=71 minutes at D/D_0=0.9 to 0.6 when t=190 minutes. To reference the observations for 40Sand 40ST, the trends seen here do not correlate with previous literature papers. VPTT and LCST were already surpassed for 40T. According to Tanaka et al's paper, it should be expected to see the self-diffusion of water to increase until VPTT before it decreases. Instead, the 40T curve in **figure 7.9.5** shows that the D/D_0 is increasing even after VPTT until it eventually decreased t=40 minutes. These indicate that 40T, 40ST, and 40S are all experiencing minor increases in D/D_0 probably due to increasing temperature, but quickly drop once the hydrogel collapses. Recalling the MSME pictures, spectral comparisons around 40°C, and the voxel analysis outside the gel, they all indicated a delay in the breakage of the polymer network, which could explain why there is a delay in the D/D_0 decrease for the water inside the gel. This is the limiting factor for water, and due to their small molecule size, the hydrogel would have to be very shrunken to be able to restrict water to the same degree it would to βCD. Hence it explains why it takes a long before the gradual and consistent decrease occurs for the water inside the collapsed hydrogel.

31T

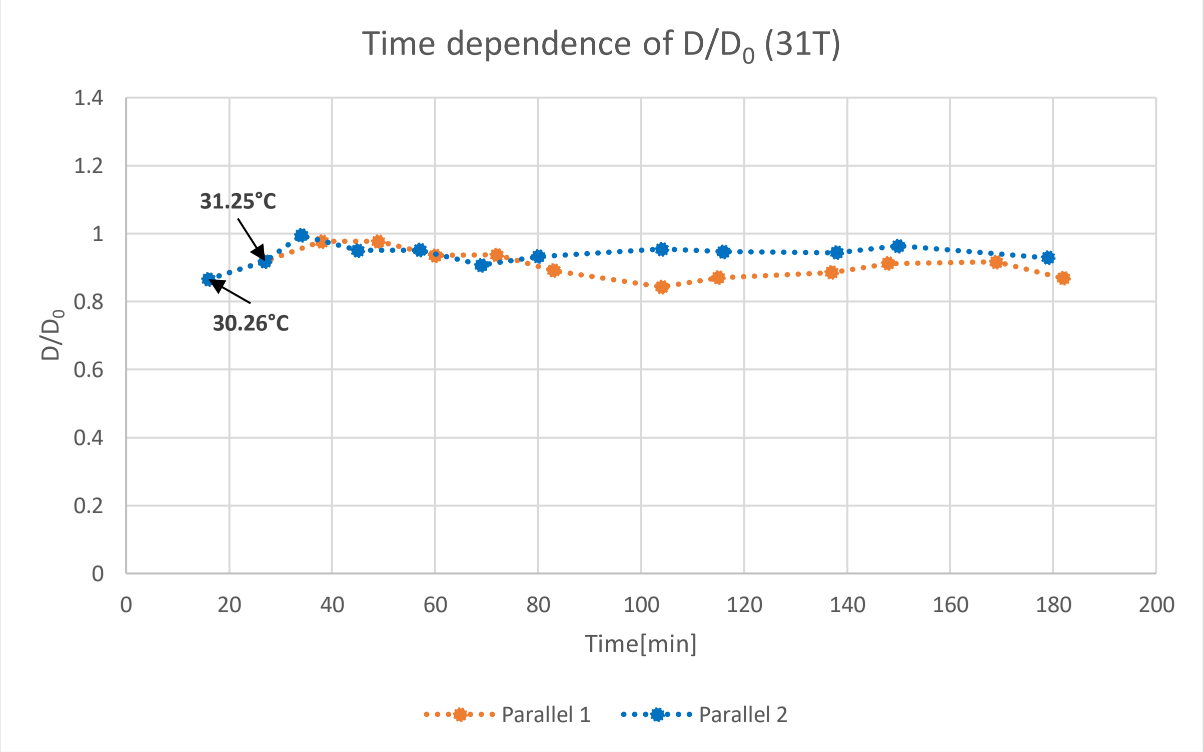

Figure 7.9.6: Time dependence of D/D_0 for 31T. Parallel 1 is represented by the orange curve, whilst parallel 2 is represented by the blue curve. The transition temperatures are marked on the graph.

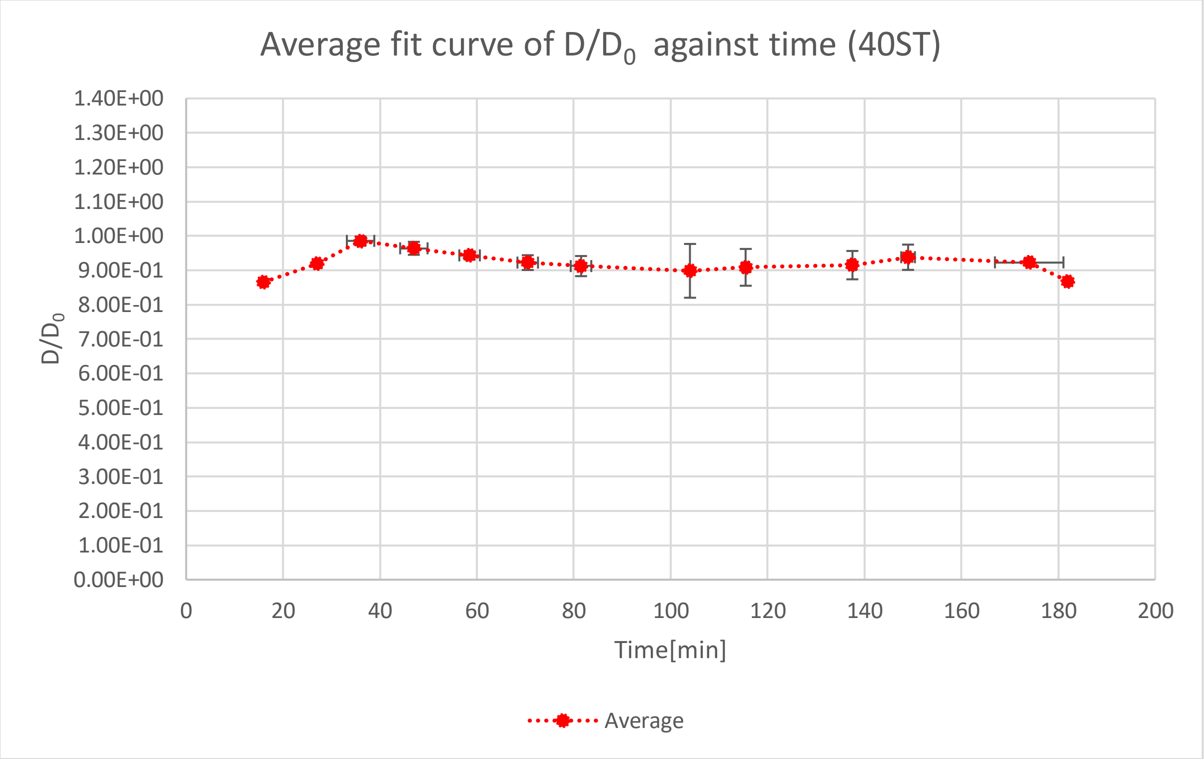

Figure 7.9.7: Average fit curve of 31T based on ***figure 7.9.6*** *with temperature marks and error bars. Deviation between the parallels appear minimal. The curve also shows a general stabilization around* $D/D_0=0.9$ *after t=40 minutes.*

31T's trend for water in **figure 7.9.6** shows minimal change and variation between the two parallels. The average fit curve in **figure 7.9.7** highlights this lack of significant diffusion of water inside the gel. For reference, the D/D_0 value starts at 0.87, which then increases up to 1 just before t=40 minutes. Afterwards, the trend shows a low gradual decrease towards 0.9 before stabilizing around this D/D_0 value. This implies that the water movement is restricted inside, which is the same finding mentioned in Wisniewska's paper [4]. This mimics the observations seen for MSME in **figure 7.3.3** and **figure 7.3.4**, where the gel interface barely moved or shrunk. Moreover, this lack substantial self-diffusion change mirrors what was seen in **figure 7.5.7**, where there is no sharp dip in βCD inside the hydrogel. Although some increase of βCD was seen outside the hydrogel in **figure 7.6.11**, it was not significant, especially when comparing it to the 40S and 40ST curves in **figure 7.6.4** and **figure 7.6.7**. These all correlate with the fact that the transition temperatures were never reached, so there are no expected significant changes to occur for both βCD and the water inside the hydrogel.

Overview of the combined temperature experiments

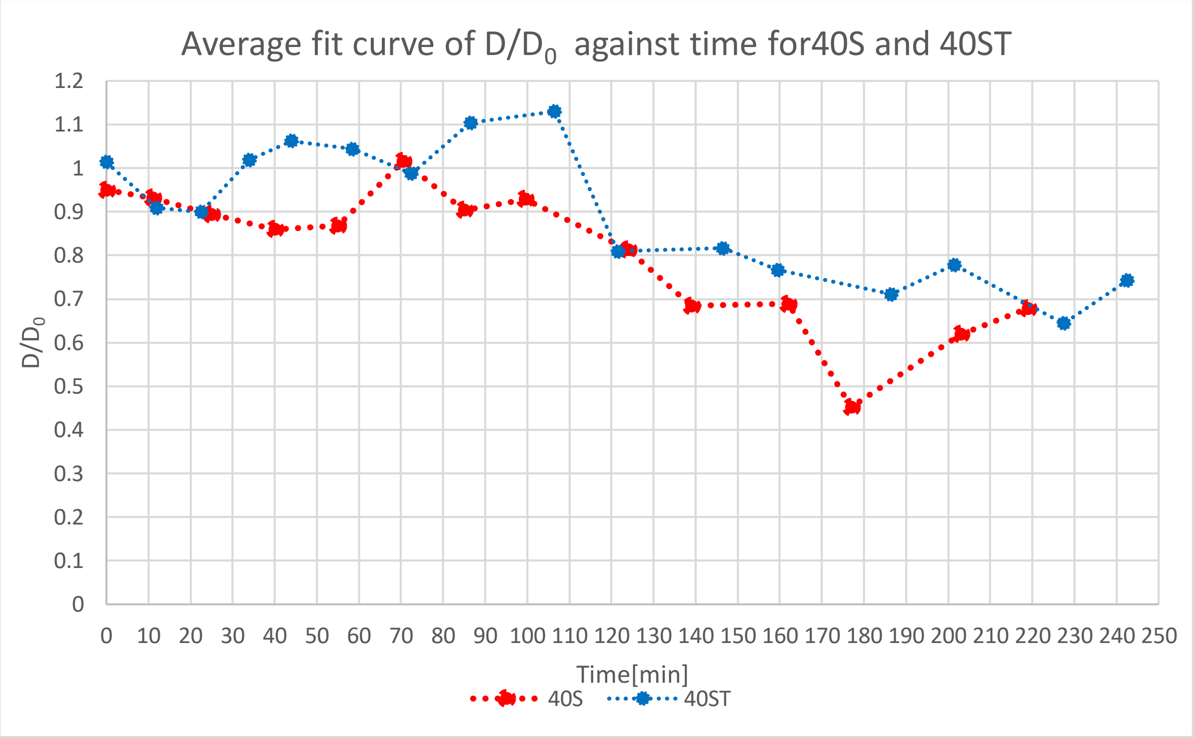

Figure 7.9.8: The combined average fit curves for D/D_0 vs time for 40S and 40ST. The red curve represents 40S, whilst 40ST is represented by the blue curve.

When comparing the slow heating experiment(40S) and the hybrid slow-heating and temperature jump experiment (40ST), the 40S curve increases generally up until t=105 minutes. Its increase also happens sooner than the 40S as it took t=70 minutes for the 40S curve to match one of the data points in 40ST. After this point, both show a decreasing pattern, with 40S showing lower D/D_0 values compared to 40ST. 40ST’s curve ends up with 0.74 at t=243 minutes, whilst 40S’s curve ends up with 0.64 at t=219 minutes, which is also near the same D/D_0 value with 40ST at t=228 minutes. Both curves show a declining D/D_0 for a majority of the experiment, which implies the movement of the water molecules are being restricted, but there is a delay due to the time it takes to fully destroy the polymer network, enough to restrict the movement of small water molecules. Tanaka et al’s paper supports this with her findings where a decrease in diffusion occurred due to a collapsing polymer network. The timing is different. In particular, the 40S experiment in Wisniewska’s paper showed a different pattern, thus supporting the notion that the diffusion experiment must be evaluated again to validate the results [33].

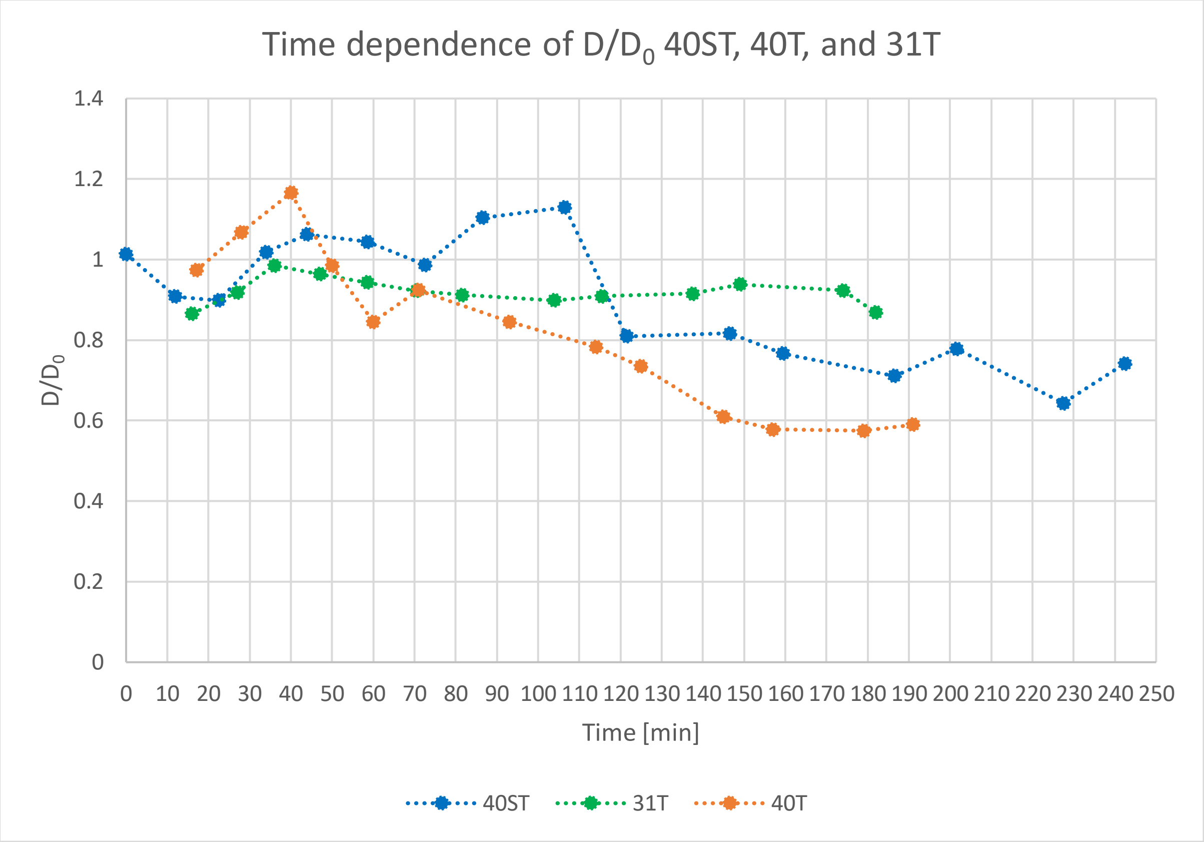

Figure 7.9.9: The combined average fit curves for D/D₀ vs time for 40ST, 40S, and 31T. The orange curve represents 40t, whilst 40ST is represented by the blue curve. 31T is represent by the green curve.

Both the 40ST and 40T temperature experiments shows a similar pattern with one another, with 40T achieving a higher D/D_0 at t=40 minutes compared to 40ST at the same time mark. This shows that the higher temperatures are increasing the water mobility. After this point, both decreases, particularly 40T. This sharp decrease can be similarly seen at t=107 minutes for 40ST, so there is a delay until this happens compared to 40T. Identical to 40S, both 40ST and 40T have low D/D_0 values at the end of their experiment run. On the other hand, 31T shows minor changes in D/D_0-value as it stabilizes around 0.9 until the end of its experiment run, showcasing slightly more mobility than both 40ST and 40T. 40S and 40T only showed higher D/D_0 values than 31T until their respective sharp decreases. 31T did show a slight increase up to D/D_0=1 around t=36 minutes before it began to gradually decrease to 0.9. This shows that the water molecules inside the gel are moving more freely as temperature increases, but due to the slight shrinkage that occurs with higher temperatures for the gel, this begins to gradually decrease.

(7.9) Further considerations and improvements for future experiments

Considering all observations seen as of now, both inside and out of the hydrogel at a microscopic and macroscopic scale, some improvements and considerations should be brought up to further improve the validity and accuracy of the results. In particular, the results of the diffusion data have to be made more extensive and tested again as the results do not correlate with some of the literature work. Although some rationalizing has been made to explain the behavior, more tests and parallels would help validate the results. Alternative methods could also be considered to replace MEGA-PRESS in determining the diffusion of βCD and water inside the hydrogel as it suffers from long TE-values, J-modulation, and thus low sensitivity for signal detection. It is not an ideal method to analyze the diffusion of βCD after VPTT as it can no longer detect any signal after that point. The use of STEAM would potentially circumvent the problems by MEGA PRESS as STEAM would have not have large TE-values, so J-modulation is avoided. This would potentially allow the visualization of the diffusion of βCD even after VPTT. Aside from the diffusion data of βCD, the results obtained for βCD both inside and outside the hydrogel have been successful in providing a good and new insight to the βCD activity as P(NIPAM) transitions through LCST, VPTT, and 40°C.

When it comes to water, there was not a paper that used an 80:20 D_2O/H_2O solvent, so this makes it difficult to compare and contrast. The choice of using an 80:20 D_2O/H_2O mixture is avoid water signals during the experiment. This saved time and effort from manually calibrating during the run. Although it is expensive to do this on a mass scale, the use of a D_2O/H_2O mixture reduced the noise and allowed for more points to be recorded with clarity. When it comes to the D/D_0 values of water, it followed a similar pattern to βCD, where the trends were consistently decrease. The only exception here is that water showed delays in its descent in D/D_0 compared to βCD. This is most likely due to its small molecule size compared to βCD, and the degree of degradation of the P(NIPAM) had to be high to be able to restrict such a small molecule. Although some parallels suffered from high standard deviations, the results for water are interesting, and the experiments should be repeated to validate the results.

(8)Conclusion

To conclude, this project has managed to provide new insight to the behavior of βCD both inside and outside P(NIPAM) as temperature is increased from 25°C. The MSME pictures of all the temperature experiments correlate and agree with the shrinking kinetics that characterize P(NIPAM). The pictures are supported by the spectra comparisons before and after the LCST, VPTT, and 40°C marking, showing what is happening inside the hydrogel while the shrinkage from the MSME pictures occur. Moreover, the STEAM NMR spectra of 40S, 40ST, 40T, and 31T show how the βCD concentration sharply decreases inside the gel after VPTT as the

P(NIPAM) undergoes a hydrophobic transition. The process becomes accelerated as βCD is squeezed out faster as temperature approaches the 40°C mark. The 2mm and 6mm voxels showcased the same behavior, but there is a slight delay as the diffusion rate of both water and the βCD becomes limited due to the dense layer that prevents the permeation the gel contents at the molecular level, as well as restricting their movement as the polymer network eventually collapsed. However, more testing should be conducted to validate and improve the results, as well as reduce the uncertaintity of the values obtained for the water D/D_0 analysis. Overall, the project has accomplished its goal of expanding the portfolio of both P(NIPAM), as well as βCD.

(9) References

[1] Staff.ustc.edu.cn. 2022. *NMR temperature calibration*. [online] Available at: <http://staff.ustc.edu.cn/~liuyz/methods/NMR_VT_calibration.htm> [Accessed 30 June 2022].

[2] Hoffman, R., 2022. *NMR Thermometer*. [online] Chem.ch.huji.ac.il. Available at: <http://chem.ch.huji.ac.il/nmr/software/thermometer.html> [Accessed 30 June 2022].

[3] Ammann, C., Meier, P. and Merbach, A., 1982. A simple multinuclear NMR thermometer. *Journal of Magnetic Resonance (1969)*, 46(2), pp.319-321.

[4] Wisniewska, M., 2017 *Characterizing mass transport in hydrogels using Nuclear Magnetic Resonance (NMR),* PhD thesis, University of Bergen, Bergen

[5] Kaplan, M., Bovey, F. and Cheng, H., 1975. Simplified method of calibrating thermometric nuclear magnetic resonance standards. *Analytical Chemistry*, 47(9), pp.1703-1705.

[6] Schopf, R., Schork, N., Amling, E., Nirschl, H., Guthausen, G. and Kulozik, U., 2020. Structural Characterisation of Deposit Layer during Milk Protein Microfiltration by Means of In-Situ MRI and Compositional Analysis. *Membranes*, 10(4), p.59.

[7] In vivo NMR and MRI using injection delivery of laser-polarized xenon - Scientific Figure on ResearchGate. Available from: https://www.researchgate.net/figure/The-radiofrequency-RF-and-gradient-G-pulse-sequences-for-the-FLASH-Fast-Low-Angle_fig2_13823914 [accessed 4 Jul, 2022]

[8] Mrimaster.com. 2022. *FLASH MRI | SPGR | T1 FFE | RSSG | STAGE | fast FE MRI sequence physics and image appearance*. [online] Available at: <https://mrimaster.com/characterise%20image%20spoiled%20gradient%20.html> [Accessed 4 July 2022].

[9] Mr-tip.com. 2022. *MRI Database: Fast Low Angle Shot*. [online] Available at: <https://www.mr-tip.com/serv1.php?type=db1&dbs=Fast%20Low%20Angle%20Shot> [Accessed 3 July 2022].

[10] Mrimaster.com. 2022. *Proton Density (PD) weighted MRI sequence physics and image appearance*.[online]Availableat:<https://mrimaster.com/characterise%20image%20pd.html#:~:text=Proton%20Density%20(PD)%20weighted%20MRI%20sequence%20physics%20and%20image%20appearance&text=When%20an%20MRI%20sequence%20is,the%20brightest%20on%20the%20image.> [Accessed 3 July 2022].

[11] Simultaneous Magnetic Resonance Imaging and Consolidation Measurement of Articular Cartilage - Scientific Figure on ResearchGate. Available from: https://www.researchgate.net/figure/An-MSME-imaging-sequence-simplified-for-further-detail-see-28-Read-phase-and-slice_fig6_262112129 [accessed 3 Jul, 2022]'

[12] Juchem, C. and de Graaf, R., 2017. B0 magnetic field homogeneity and shimming for in vivo magnetic resonance spectroscopy. *Analytical Biochemistry*, 529, pp.17-29.

[13] Brown, M. and Semelka, R., 2003. *MRI: Basic Principles and Applications*. 3rd ed. John Wiley & Sons, Inc.

[14] Philips. 2022. *MEGA MR Clinical application | Philips Healthcare*. [online] Available at: <https://www.usa.philips.com/healthcare/product/HCNMRF277/mega-mr-clinical-application> [Accessed 3 July 2022].

[15] Mullins, P., McGonigle, D., O'Gorman, R., Puts, N., Vidyasagar, R., Evans, C. and Edden, R., 2014. Current practice in the use of MEGA-PRESS spectroscopy for the detection of GABA. *NeuroImage*, 86, pp.43-52.

[16] 1D-spectral editing and 2D multispectral in vivo(1)H-MRS and (1)H-MRSI - Methods and applications - Scientific Figure on ResearchGate. Available from: https://www.researchgate.net/figure/The-MEGA-PRESS-sequence-is-commonly-used-for-J-editing-The-PRESS-localization-module-is_fig2_311993244 [accessed 3 Jul, 2022].

[17] Kovacs, H., Moskau, D. and Spraul, M., 2005. Cryogenically cooled probes—a leap in NMR technology. *Progress in Nuclear Magnetic Resonance Spectroscopy*, 46(2-3), pp.131-155.

[18] Teh, I., Maguire, M. and Schneider, J., 2016. Efficient gradient calibration based on diffusion MRI. *Magnetic Resonance in Medicine*, 77(1), pp.170-179.

[19] X.Z. Zhang, D.Q. Wu, and C.C. Chu. Synthesis, characterization and controlled drug release of thermosensitive ipn–pnipaam hydrogels. Biomaterials, 25(17):3793–3805, 2004.

[20] Y. Kaneko, K. Sakai, A. Kikuchi, R. Yoshida, Y. Sakurai, T. Okano
Influence of freely mobile grafted chains length on dynamic properties of comb-type grafted poly(*N*-isopropylacrylamide) hydrogels Macromolecules, 28 (1995), pp. 7717-7723

[21] Sato Matsuo, E.; Tanaka, T. J. Chem. Phys. 1988, 89, 1695.

[22] Kaneko, Y.; Yoshida, R.; Sakai, K.; Sakurai, Y.; Okano, T. J. Membr. Sci. 1995, 101, 13.

[23] Yoshida, R.; Sakai, K.; Okano, T.; Sakurai, Y. Ind. Eng. Chem. Res. 1992, 31, 2339.

[24] Larsson, A., Kuckling, D. and Schönhoff, M., 2001. 1H NMR of thermoreversible polymers in solution and at interfaces: the influence of charged groups on the phase transition. *Colloids and Surfaces A: Physicochemical and Engineering Aspects*, 190(1-2), pp.185-192.

[25] T. Tokuhiro, T. Amiya, A. Mamada, and T. Tanaka. Nmr study of poly (n-isopropylacrylamide)

[26] Su, J., Duncan, P., Momaya, A., Jutila, A. and Needham, D., 2010. The effect of hydrogen bonding on the diffusion of water in n-alkanes and n-alcohols measured with a novel single microdroplet method. *The Journal of Chemical Physics*, 132(4), p.044506.

[27] J. G. Lu, R. Kong, and T. C. Chan, J. Chem. Phys. 110, 3003 (1999).

[28] T. Tominaga, S. Tenma, and F. Watanabe, J. Chem. Soc., Faraday Trans. 92, 1863 (1996).

[29] S. H. Chen, D. F. Evans, and H. T. Davis AIChE J. 29, 640 (1983).

[30] Paduano, L., Sartorio, R., Vitagliano, V. and Costantino, L., 1990. Diffusion properties of cyclodextrins in aqueous solution at 25�C. *Journal of Solution Chemistry*, 19(1), pp.31-39.

[31] a) Y. Shrot, L. Frydman, J. Chem. Phys. 2009, 131, 224516; b) P. Pelupessy, L. Duma, G. Bodenhausen, J. Magn. Reson. 2008, 194, 169 – 174.

[32] Erdős, M., Frangou, M., Vlugt, T. and Moultos, O., 2021. Diffusivity of α-, β-, γ-cyclodextrin and the inclusion complex of β-cyclodextrin: Ibuprofen in aqueous solutions; A molecular dynamics simulation study. *Fluid Phase Equilibria*, 528, p.112842.

[33] a) Y. Shrot, L. Frydman, J. Chem. Phys. 2009, 131, 224516; b) P. Pelupessy, L. Duma, G. Bodenhausen, J. Magn. Reson. 2008, 194, 169 – 174.

[34] Gouilleux, B., Rouger, L., Charrier, B., Kuprov, I., Akoka, S., Dumez, J. and Giraudeau, P., 2015. Understanding J-Modulation during Spatial Encoding for Sensitivity-Optimized Ultrafast NMR Spectroscopy. *ChemPhysChem*, 16(14), pp.3093-3100.

[35] P.C. Griffiths, P. Stilbs, B.Z. Chowdhry, and M.J. Snowden. Pgse-nmr studies of solvent diffusion in poly (n-isopropylacrylamide) colloidal microgels. Colloid Polym. Sci., 273(4):405–411, 1995.

[36] J. Spevácek. NMR investigations of phase transition in aqueous polymer solutions and gels. Curr. Opin. Colloid Interface Sci, 14(3):184–191, 2009.

[37] N.C. Woodward, B.Z. Chowdhry, M.J. Snowden, S.A. Leharne, P.C. Griffiths, and A.L. Winnington. Calorimetric investigation of the influence of cross-linker concentration on the volume phase transition of poly(nisopropylacrylamide) colloidal microgels. Langmuir, 19(8):3202–3211, 2003.

[38] Langer R. Drug delivery and targeting. Nature. 1998; 392:5–10. [PubMed: 9579855]

[39] Hoare TR, Kohane DS. Hydrogels in drug delivery: Progress and challenges. Polymer. 2008; 49:1993–2007.

[40] Liechty WB, Kryscio DR, Slaughter BV, Peppas NA. Polymers for drug delivery systems. Ann Rev Chem Biomol Eng. 2010; 1:149–173. [PubMed: 22432577]

[41] Ford Versypt, A., Pack, D. and Braatz, R., 2013. Mathematical modeling of drug delivery from autocatalytically degradable PLGA microspheres — A review. *Journal of Controlled Release*, 165(1), pp.29-37.

[42] Bhowmik, D., Gopinath, H., Kumar, P., Duraivel, S. and Kumar, K., 2012. Controlled Release Drug Delivery Systems. *The Pharma Innovation Journal*, [online] 1(7725), pp.24-32. Available at: <http://www.thepharmajournal.com/> [Accessed 5 May 2020].

[43] J.F. Coelho, P.C. Ferreira, P. Alves, R. Cordeiro, A.C. Fonseca, J.R. Góis, and M.H. Gil. Drug delivery systems: Advanced technologies potentially applicable in personalized treatments. EPMA journal, 1(1):164–209, 2010.

[44] A. K. Bajpai, S. K. Shukla, S. Bhanu, and S. Kankane. Responsive polymers in controlled drug delivery. Prog. Polym. Sci., 33(11):1088–1118, 2008.

[45] Chiu, A., n.d. Characterizing hydrogels as drug carrier molecules for Controlled Release Drug Delivery Systems with NMR-based techniques.

[46] National Institute of Biomedical Imaging and Bioengineering. 2020. Drug Delivery Systems. [online] Available at: <https://www.nibib.nih.gov/science-education/science-topics/drug-delivery-systems-getting-drugs-their-targets-controlled-manner> [Accessed 4 May 2020].

[47] Bruschi, M., 2017. Strategies To Modify The Drug Release From Pharmaceutical Systems. Amsterdam [etc.]: Elsevier/Woodhead Publishing.

[48] Ratnaparkhi, M. and Gupta, J., 2013. Sustained Release Oral Drug Delivery System - An Overview. International Journal of Pharma Research & Review, 2(3), pp.11-21.

[49] Jethara, S., 2014. Pharmaceutical Controlled Release Drug Delivery Systems: A Patent Overview. Aperito Journal of Drug Designing and Pharmacology, 1(2).

[50] Perrie, Y. and Rades, T., 2012. *Fasttrack*. 2nd ed. London: Pharmaceutical Press, pp.11-13.

[51] Mejia-Oneto, J., Yee, N., Revilla, V. and Inc., S., 2020. *Localized Drug Delivery Promises To Improve Outcomes And Reduce Side Effects - Drug Discovery And Development*. Drug Discovery and Development. Available at: <https://www.drugdiscoverytrends.com/localized-drug-delivery-promises-to-improve-outcomes-and-reduce-side-effects/> [Accessed 4 May 2020].

[52] [Bhowmik, D., Gopinath, H., Kumar, P., Duraivel, S. and Kumar, K., 2012. Controlled Release Drug Delivery Systems. *The Pharma Innovation Journal*, [online] 1(7725), pp.24-32. Available at: <http://www.thepharmajournal.com/> [Accessed 5 May 2020].

[53] Li, J. and Mooney, D., 2016. Designing hydrogels for controlled drug delivery. *Nature Reviews Materials*, 1(12), pp.1-38.

[54] W. Hu, Z. Wang, Y. Xiao, S. Zhang, and J. Wang. Advances in crosslinking strategies of biomedical hydrogels. Biomater. Sci., 7(3):843–855, 2019.

[55] Vinogradov SV, Bronch TK, Kabanov AV. Nanosized cationic hydrogels for drug delivery preparation, properties and interactions with cells. Adv Drug Delivery Rev 2002;54:135–47.

[56] Peppas NA, Huang Y, Torres-Lugo M, Ward JH, Zhange J. Physiochemical foundation and structure design of hydrogel in medicine and biology. Annu Rev Biomed Eng 2000;2:9–29.

[57] Lingyun C, Zhigang T, Yumin D. Synthesis and pH sensitivity of carboxymethyl chitosan based polyampholyte hydro

[58] Hacker MC, Mikos AG. Synthetic polymers, principles of regenerative medicine. 2nd ed.; 2011. p. 587–622.

[59] Li Q, Wang J, Shahani S, Sun DDN, Sharma B, Elisseeff JH, et al. Biodegradable and photocrosslinkable polyphosphoester hydrogel. Biomaterials 2006;27:1027–34

[60] W. Hu, Z. Wang, Y. Xiao, S. Zhang, and J. Wang. Advances in crosslinking strategies of biomedical hydrogels. Biomater. Sci., 7(3):843–855, 2019.

[61] Lingyun C, Zhigang T, Yumin D. Synthesis and pH sensitivity of carboxymethyl chitosan based polyampholyte hydrogel for protein carrier matrices. Biomaterials 2004;25:3725– 32.

[62] Bearman, R. J. J. Phys. Chem. 1961, 65, 1961.

[63] Ganji F, Vasheghani-Farahani S and Vasheghani-Farahani E (2010). Theoretical description of hydrogel swelling: A review. Iranian Polymer Journal 19, 375–398.

[64] Porter TL, Stewart R, Reed J and Morton K (2007). Models of hydrogel swelling with applications to hydration sensing. Sensors 7,1980–1991.

[65] N.A. Peppas, P. Bures, W. Leobandung, and H. Ichikawa. Hydrogels in pharmaceutical formulations. Eur. J. Pharm. Biopharm., 50(1):27 – 46, 2000

[66] Polymerdatabase.com.2020. *Flory-Rehner Theory*. [online] Available at: <http://polymerdatabase.com/polymer%20physics/Flory%20Rehner.html> [Accessed 27 May 2020].

[67] Bodugoz-Senturk H, Macias CE, Kung JH, Muratoglu OK. Poly(vinyl alcohol)–acrylamide hydrogels as load-bearing cartilage substitute. Biomaterials. 2009; 30:589–596. [PubMed: 18996584]

[68] Hiemstra C, et al. In vitro and in vivo protein delivery from in situ forming poly(ethylene glycol)– poly(lactide) hydrogels. J Control Release. 2007; 119:320–327. [PubMed: 17475360]

[69] Silva EA, Kim ES, Kong HJ, Mooney DJ. Material-based deployment enhances efficacy of endothelial progenitor cells. Proc Natl Acad Sci USA. 2008; 105:14347–14352. [PubMed: 18794520]

[70] Zustiak, S. and Leach, J., 2010. Hydrolytically Degradable Poly(Ethylene Glycol) Hydrogel Scaffolds with Tunable Degradation and Mechanical Properties. *Biomacromolecules*, 11(5), pp.1348-1357.

[71] Canal T, Peppas NA. Journal of Biomedical Materials Research 1989;23:1183–1193. [PubMed: 2808463]

[72] Cruise GM, Scharp DS, Hubbell JA. Biomaterials 1998;19:1287–1294. [PubMed: 9720892]

[73] Mellott MB, Searcy K, Pishko MV. Biomaterials 2001;22:929–941. [PubMed: 11311012]

[74] N.A. Peppas, P. Bures, W. Leobandung, and H. Ichikawa. Hydrogels in pharmaceutical formulations. Eur. J. Pharm. Biopharm., 50(1):27 – 46, 2000.

[75] Amsden B. Solute diffusion within hydrogels. Mechanisms and models. Macromolecules. 1998.

[76] Bercea, M., 2022. Bioinspired Hydrogels as Platforms for Life-Science Applications: Challenges and Opportunities. *Polymers*, 14(12), p.2365.

[77] Hardy, R. and Cottington, R., 1949. Viscosity of deuterium oxide and water in the range 5 to 125 C. *Journal of Research of the National Bureau of Standards*, 42(6), p.573.

[78] Wu, V., 2022. *Diffusion — Supramolecular (Bio)Materials*. [online] Supramolecular (Bio)Materials. Available at: <http://www.supramolecularbiomaterials.com/msdm-calculator> [Accessed 9 August 2022].

[79] Bearman, R. J. J. Phys. Chem. 1961, 65, 1961.

[80] Fatin-Rouge, N.; Wilkinson, K. J.; Buffle, J. J. Phys. Chem. B 2006, 110, 20133.

[81] Atkins, Peter and de Paula, Julio, "Physical Chemistry for the Life Sciences", 2006

[82] Atkins, P. and De Paula, J., 2013. *Elements Of Physical Chemistry*. 7th ed. Oxford: Oxford University Press, pp.290-294.

[83] Matsukawa, S.; Yasunaga, H.; Zaho, C.; Kuroki, S.; Kurosu, H.; Ando, I. Prog. Polym. Sci. 1999, 24, 995

[84] H. Thérien-Aubin, X.X. Zhu, C.N. Moorefield, K. Kotta, and G.R. Newkome. Effect of ionic binding on the self-diffusion of anionic dendrimers and hydrophilic polymers in aqueous systems as studied by pulsed gradient nmr techniques. Macromolecules, 40 (10):3644–3649, 2007

[85] R. Valiullin. Diffusion NMR of Confined Systems: Fluid Transport in Porous Solids and Heterogeneous Materials. Royal Society of Chemistry, 2016.

[86] Bird, R. B.; Stewart, W. E.; Lightfoot, E. N. Transport Phenomena; John Wiley and Sons: Toronto, 1960.

[87] Ogston, A. G.; Preston, B. N.; Wells, J. D. Proc. R. Soc. LondonSer. A 1973, 333, 297-316.

[88] A.G. Ogston. The spaces in a uniform random suspension of fibres. Trans. Faraday Soc., 54:1754–1757, 1958.

[89] Gagnon, M. and Lafleur, M., 2009. Self-Diffusion and Mutual Diffusion of Small Molecules in High-Set Curdlan Hydrogels Studied by31P NMR. *The Journal of Physical Chemistry B*, 113(27), pp.9084-9091.

[90] Gandhi, A.; Paul, A.; Sen, S.O.; Sen, K.K. Studies on thermoresponsive polymers: Phase behaviour, drug delivery and biomedical applications. Asian J. Pharm. Sci. 2015, 10, 99–107. [CrossRef]

[91] Ashraf, S.; Park, H.-K.; Park, H.; Lee, S.-H. Snapshot of phase transition in thermoresponsive hydrogel PNIPAM: Role in drug delivery and tissue engineering. Macromol. Res. 2016, 24, 297–304. [CrossRef]

[92] Clark, E.A.; Lipson, J.E.G. LCST and UCST behavior in polymer solutions and blends. Polymer 2012, 53, 536–545. [CrossRef]

[93] Chatterjee, S.; Hui, P.C.; Kan, C.W. Thermoresponsive Hydrogels and Their Biomedical Applications: Special Insight into Their Applications in Textile Based Transdermal Therapy. Polymers 2018, 10, 480. [CrossRef]

[94] Karimi, M.; Sahandi Zangabad, P.; Ghasemi, A.; Amiri, M.; Bahrami, M.; Malekzad, H.; Ghahramanzadeh Asl, H.; Mahdieh, Z.; Bozorgomid, M.; Ghasemi, A.; et al. Temperature-responsive smart nanocarriers for delivery of therapeutic agents: Applications and recent advances. ACS Appl. Mater. Int. 2016, 8, 21107–21133. [CrossRef]

[95] S. Fujishige, K. Kubota, and I. Ando. Phase transition of aqueous solutions of poly(nisopropylacrylamide) and poly(n-isopropylmethacrylamide). J. Phys. Chem., 93(8): 3311–3313, 1989

[96] Y. Hirokawa and T. Tanaka. Volume phase transition in a nonionic gel. J. Chem. Phys., 81(12):6379–6380, 1984.¨

[97] M. Shibayama, T. Tanaka, and C.C. Han. Small angle neutron scattering study on poly(n-isopropyl acrylamide) gels near their volume-phase transition temperature. J. Chem. Phys., 97(9):6829–6841, 1992

[98] Rodkate, N.; Rutnakornpituk, M. Multi-responsive magnetic microsphere of poly(N-isopropylacrylamide)/carboxymethylchitosan hydrogel for drug controlled release. Carbohydr. Polym. 2016, 15, 251–259. [CrossRef] [PubMed]

[99] Wei, W.; Hu, X.; Qi, X.; Yu, H.; Liu, Y.; Li, J.; Zhang, J.; Dong, W. A novel thermo-responsive hydrogel based on salecan and poly(N-isopropylacrylamide): Synthesis and characterization. Colloids Surf. B Biointerfaces 2015, 125, 1–11. [CrossRef] [PubMed]

[100] Kim, A.R.; Lee, S.L.; Park, S.N. Properties and in vitro drug release of pH- and temperature-sensitive double cross-linked interpenetrating polymer network hydrogels based on hyaluronic acid/poly (N-isopropylacrylamide) for transdermal delivery of luteolin. Int. J. Biol. Macromol. 2018, 118, 731–740. [CrossRef] 28. Wang, B.; Xu, Q.; Ye, Z.; Liu, H.; Lin, Q.; Nan, K.; Li, Y.;

[101] Wang, Y.; Qi, L.; Chen, H. Copolymer brushes with temperature-triggered, reversibly switchable bactericidal and antifouling properties for biomaterial surfaces. ACS Appl. Mater. Int. 2016, 8, 27207–27217. [CrossRef] 29.

[102] Zhao, D.; Ma, W.; Wang, R.; Yang, X.; Li, J.; Qiu, T.; Xiao, X. The preparation of Green Fluorescence-Emissioned Carbon dots/poly(N-isopropylacrylamide) temperature-sensitive hydrogels and research on their properties. Polymers 2019, 11, 1171. [CrossRef]

[103] Hoffman, A.S. Stimuli-responsive polymers: Biomedical applications and challenges for clinical translation. Adv. Drug Deliv. Rev. 2013, 65, 10–16. [CrossRef] [PubMed]

[104] Klouda, L.; Mikos, A.G. Thermoresponsive hydrogels in biomedical applications. Eur. J. Pharm. Biopharm. 2008, 68, 34–45. [CrossRef]

[105] Haq, M.A.; Su, Y.; Wang, D. Mechanical properties of PNIPAM based hydrogels: A review. Mater. Sci. Eng. C 2017, 70, 842–855. [CrossRef] [PubMed]

[106] Klouda, L.; Mikos, A.G. Thermoresponsive hydrogels in biomedical applications. Eur. J. Pharm. Biopharm. 2008, 68, 34–45. [CrossRef]

[107] Cao, M.; Shen, Y.; Wang, Y.; Wang, X.; Li, D. Self-assembly of short elastin-like amphiphilic peptides: Effects of temperature, molecular hydrophobicity and charge distribution. Molecules 2019, 24, 202. [CrossRef] [PubMed]
[108] Zhao, Y.; Shi, C.; Yang, X.; Shen, B.; Sun, Y.; Chen, Y.; Xu, X.; Sun, H.; Yu, K.; Yang, B.; et al. pH- and temperature-sensitive hydrogel nanoparticles with dual photoluminescence for bioprobes. ACS Nano 2016, 10, 5856–5863. [CrossRef] [PubMed]

[109] Ziane, S.; Schlaubitz, S.; Miraux, S.; Patwa, A.; Lalande, C.; Bilem, I.; Lepreux, S.; Rousseau, B.; Le Meins, J.F.; Latxague, L.; et al. A thermosensitive low molecular weight hydrogel as scaffold for tissue engineering. Eur. Cells Mater. 2012, 23, 147–160. [CrossRef] [PubMed]

[110] Crini, G., 2014. Review: A History of Cyclodextrins. *Chemical Reviews*, 114(21), pp.10940-10975.

[111] Using cyclodextrin to stabilize and control colloidal micro-stickies to improve paper machine runnability - Scientific Figure on ResearchGate. Available from: https://www.researchgate.net/figure/Structure-for-a-beta-cyclodextrin-molecule-PROCEDURES-The-methods-used-for-this-work-are_fig1_283533569 [accessed 9 Jan, 2022]

[112] Arndt, K., Knörgen, M., Richter, S. and Schmidt, T., 2020. *NMR Imaging: Monitoring Of Swelling Of Environmental Sensitive Hydrogels*.

[113] Knörgen, M., Arndt, K., Richter, S., Kuckling, D. and Schneider, H., 2000. Investigation of swelling and diffusion in polymers by 1H NMR imaging: LCP networks and hydrogels. *Journal of Molecular Structure*, 554(1), pp.69-79.

[114] Liu, Y., Yu, Y., Tian, W., Sun, L. and Fan, X., 2020. *Preparation And Properties Of Cyclodextrin/Pnipam Microgels*.

[115] Viken, A., 2018. Bruk av MRI og NMR-spektroskopi for å karakterisere fukteigenskapar ved ulike magnetiske feltstyrkar. pp.5-10.

[116] Atkins, P. and De Paula, J., 2013. *Elements Of Physical Chemistry*. 7th ed. Oxford: Oxford University Press, pp.290-294.

[117] Atkins, P. and De Paula, J., 2013. *Elements Of Physical Chemistry*. 7th ed. Oxford: Oxford University Press, pp.524-537.

[118] Keeler, J., 2013. *Understanding NMR Spectroscopy*. Hoboken: Wiley.

[119] Friebolin, H., Basic One- and Two- Dimensional NMR Spectroscopy. 2013
[120] Chemistry LibreTexts. 2020. *Larmor Precession*. [online] Available at: <https://chem.libretexts.org/Bookshelves/Physical_and_Theoretical_Chemistry_Textbook_Maps/Supplemental_Modules_(Physical_and_Theoretical_Chemistry)/Spectroscopy/Magnetic_Resonance_Spectroscopies/Nuclear_Magnetic_Resonance/NMR__Theory/Larmor_Precession> [Accessed 28 May 2020].

[121] Chem.libretexts.org. 2020. *NMR: Introduction - Chemistry Libretexts*. [online] Availableat:<https://chem.libretexts.org/Bookshelves/Physical_and_Theoretical_Chemistry_Textbook_Maps/Supplemental_Modules_(Physical_and_Theoretical_Chemistry)/Spectroscopy/Magnetic_Resonance_Spectroscopies/Nuclear_Magnetic_Resonance/Nuclear_Magnetic_Resonance_II> [Accessed 28 May 2020].

[122] Chemistry LibreTexts. 2020. *Bloch Equations*. [online] Available at: <https://chem.libretexts.org/Bookshelves/Physical_and_Theoretical_Chemistry_Textbook_Maps/Supplemental_Modules_(Physical_and_Theoretical_Chemistry)/Spectroscopy/Magnetic_Resonance_Spectroscopies/Nuclear_Magnetic_Resonance/NMR_-_Theory/Bloch_Equations> [Accessed 28 May 2020].

[123] Bloch, F., 1946. Nuclear Induction. *Physical Review*, 70(7-8), pp.460-474.

[124] Mathur, A. and Scranton, A., 1996. Characterization of hydrogels using nuclear magnetic resonance spectroscopy. *Biomaterials*, 17(6), pp.547-557.

[125] Dunn, K. J., Bergman, D. J., Latorraca, G. A. , Nuclear Magnetic Resonance Petropysical and Logging Applications. Helbig, K.

[126] Freeman, R., A handbook of Nuclear Magnetic Resonance. Addison Wesley Longman: London, UK, 1997; Vol. 2.
[127] Bjørnerud, A., 2008. *The Physics of Magnetic Resonance Imaging*. Oslo: University of Oslo.
[128] Hahn, E., 1950. Spin Echoes. *Physical Review*, 80(4), pp.580-594.

[129] Tanner, J. and Stejskal, E., 1968. Restricted Self-Diffusion of Protons in Colloidal Systems by the Pulsed-Gradient, Spin-Echo Method. *The Journal of Chemical Physics*, 49(4), pp.1768-1777.

[130] Carr, H. and Purcell, E., 1954. Effects of Diffusion on Free Precession in Nuclear Magnetic Resonance Experiments. *Physical Review*, 94(3), pp.630-638.

[131] Questions and Answers in MRI. 2022. *Spin echo (SE)*. [online] Available at: <https://mriquestions.com/spin-echo1.html> [Accessed 1 March 2022].

[132] [166] Hoffman, R., 2022. *NMR Relaxation*. [online] Chem.ch.huji.ac.il. Available at: <http://chem.ch.huji.ac.il/nmr/techniques/other/t1t2/t1t2.html#T2star> [Accessed 17 February 2022].

[133] 2018. *BASIC PRINCIPLES OF CARDIOVASCULAR MRI*. [Place of publication not identified]: SPRINGER INTERNATIONAL PU.

[134] Mitsa, T., Parker, K., Smith, W., Tekalp, A. and Szumowski, J., 1990. Correction of periodic motion artifacts along the slice selection axis in MRI. *IEEE Transactions on Medical Imaging*, 9(3), pp.310-317.

[135] Chemistry LibreTexts. 2020. *Magnetic Resonance Imaging*. [online] Available at: <https://chem.libretexts.org/Bookshelves/Physical_and_Theoretical_Chemistry_Textbook_Maps/Supplemental_Modules_(Physical_and_Theoretical_Chemistry)/Spectroscopy/Magnetic_Resonance_Spectroscopies/Nuclear_Magnetic_Resonance/NMR%3A_Experimental/Magnetic_Resonance_Imaging> [Accessed 30 May 2020].

[136] Cis.rit.edu.2020. *CHAPTER-6.*[online]Available at: <https://www.cis.rit.edu/htbooks/mri/chap-6/chap-6.htm#top> [Accessed 30 May 2020].

[137] Brown, M. A. S., Richard C., MRI Basic Principles and Application. Wiley-iss: 2003.

[138] Bronzino JD. The Biomedical Engineering Handbook. 2nd edition. CRC Press, 2000.

[139] Moratal D, Brummer ME, Martí-Bonmatí L et al. NMR Imaging. In: Akay M, ed. Wiley Encyclopedia of Biomedical Engineering. Hoboken, New Jersey: John Wiley & Sons, Inc, 2006: 2590-606.

[140] Moratal, D., Valles-Luch, A., Marti-Bonmati, L. and Brummer, M., 2008. k-Space tutorial: an MRI educational tool for a better understanding of k-space. *Biomedical Imaging and Intervention Journal*, 4(1).

[141] Helm, L., Merbach, A. and Toth, E., 2014. *The Chemistry Of Contrast Agents In Medical Magnetic Resonance Imaging*. Hoboken, N.J.: Wiley.

[142] 2018. *BASIC PRINCIPLES OF CARDIOVASCULAR MRI*. [Place of publication not identified]: SPRINGER INTERNATIONAL PU.

[143] Themes, U., 2022. *Diffusion Kurtosis Imaging*. [online] Radiology Key. Available at: <https://radiologykey.com/diffusion-kurtosis-imaging/> [Accessed 10 August 2022].

[144] B. Amsden. Solute diffusion within hydrogels. mechanisms and models. Macromolecules, 31(23):8382–8395, 1998.

[145] Facey, G., 2022. *Shaped Pulses*. [online] U-of-o-nmr-facility.blogspot.com. Available at: <http://u-of-o-nmr-facility.blogspot.com/2011/05/shaped-pulses.html> [Accessed 25 February 2022].

[146] Questions and Answers in MRI. 2022. *Water suppression MRA*. [online] Available at: <https://mriquestions.com/water-suppression.html> [Accessed 7 March 2022].

[147] D.I. Hoult. Solvent peak saturation with single phase and quadrature fourier transformation.J. Magn. Reson., 21(2):337–347, 1976.

(10) Attachments

Attachment 1: Table summarization of various diffusion models and their respective hydrogels [75]

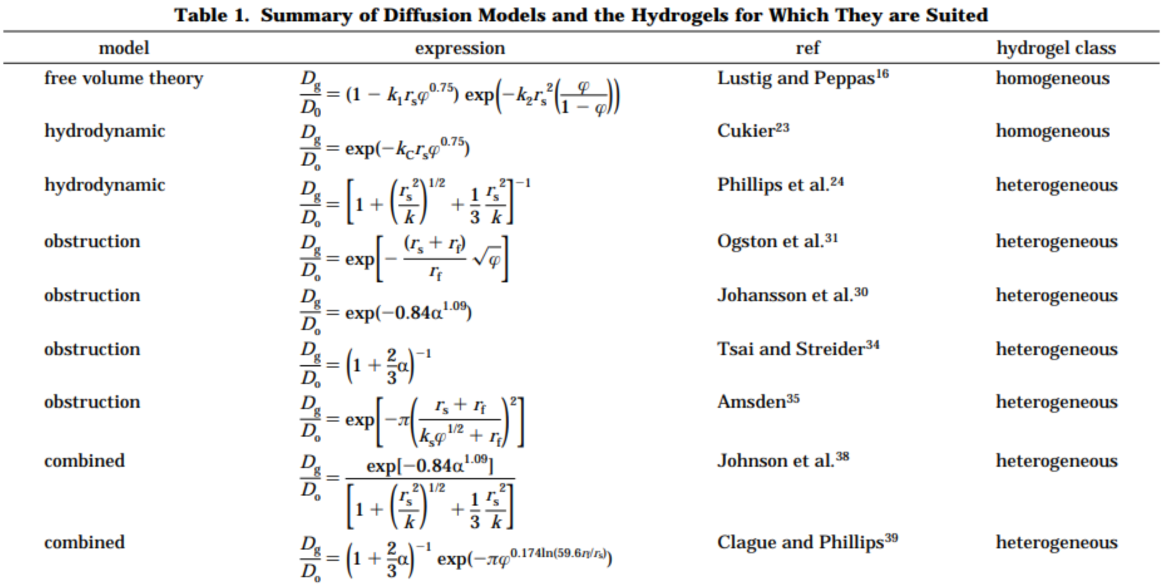

Table 1. Summary of Diffusion Models and the Hydrogels for Which They are Suited

model	expression	ref	hydrogel class
free volume theory	$\frac{D_g}{D_0} = (1 - k_1 r_s \varphi^{0.75}) \exp\left(-k_2 r_s^2 \left(\frac{\varphi}{1-\varphi}\right)\right)$	Lustig and Peppas[16]	homogeneous
hydrodynamic	$\frac{D_g}{D_o} = \exp(-k_C r_s \varphi^{0.75})$	Cukier[23]	homogeneous
hydrodynamic	$\frac{D_g}{D_o} = \left[1 + \left(\frac{r_s^2}{k}\right)^{1/2} + \frac{1}{3}\frac{r_s^2}{k}\right]^{-1}$	Phillips et al.[24]	heterogeneous
obstruction	$\frac{D_g}{D_o} = \exp\left[-\frac{(r_s + r_f)}{r_f}\sqrt{\varphi}\right]$	Ogston et al.[31]	heterogeneous
obstruction	$\frac{D_g}{D_o} = \exp(-0.84\alpha^{1.09})$	Johansson et al.[30]	heterogeneous
obstruction	$\frac{D_g}{D_o} = \left(1 + \frac{2}{3}\alpha\right)^{-1}$	Tsai and Streider[34]	heterogeneous
obstruction	$\frac{D_g}{D_o} = \exp\left[-\pi\left(\frac{r_s + r_f}{k_s\varphi^{1/2} + r_f}\right)^2\right]$	Amsden[35]	heterogeneous
combined	$\frac{D_g}{D_o} = \frac{\exp[-0.84\alpha^{1.09}]}{\left[1 + \left(\frac{r_s^2}{k}\right)^{1/2} + \frac{1}{3}\frac{r_s^2}{k}\right]}$	Johnson et al.[38]	heterogeneous
combined	$\frac{D_g}{D_o} = \left(1 + \frac{2}{3}\alpha\right)^{-1} \exp(-\pi\varphi^{0.174\ln(59.6 r_f/r_s)})$	Clague and Phillips[39]	heterogeneous

Attachment 2: βCD atomistics representation (a and b) and the incorporation of ibuprofen in two different orientations (c and d) [110]

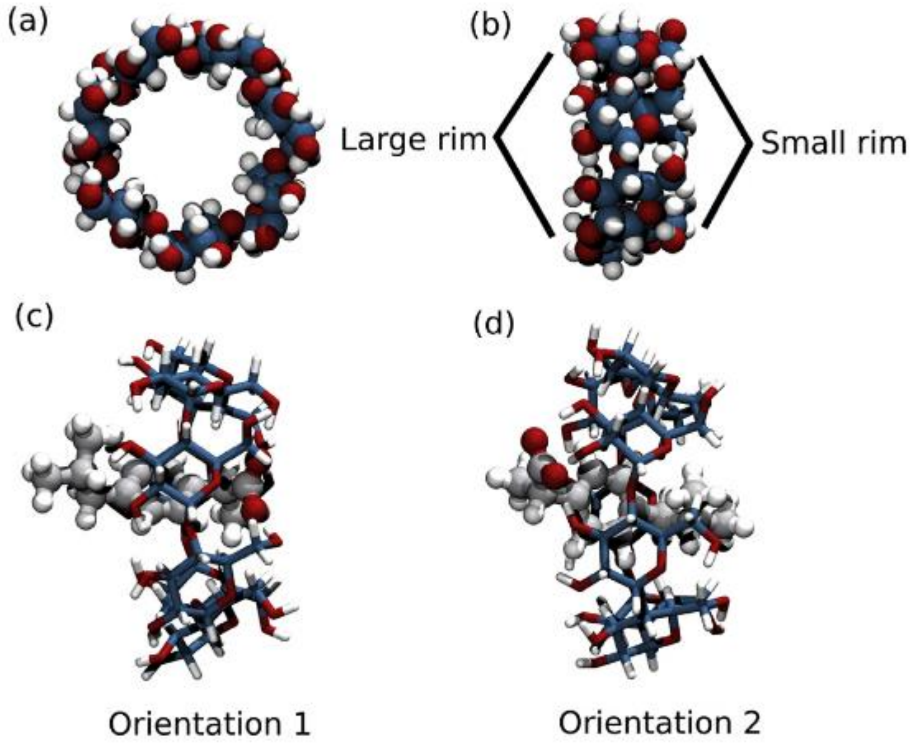

Fig. 1. (a) and (b) atomistic representations of the β-CD molecule. (c) and (d) the ibuprofen:β-CD inclusion complex in orientation 1 and orientation 2, respectively. In all simulations the q4md-CD [51] force field was used for modelling the α-, β- and γ-CDs, while the General AMBER force field [63] was used for ibuprofen.

Attachment 3 Table summarization of nuclear constitution and the nuclear spin quantum number [116]

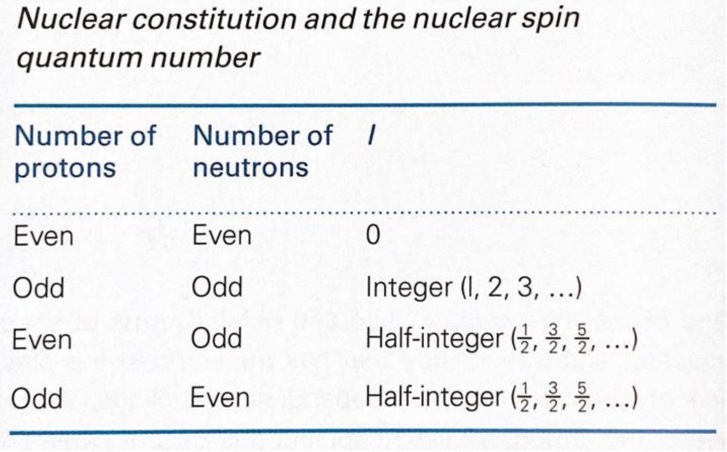

Nuclear constitution and the nuclear spin quantum number

Number of protons	Number of neutrons	I
Even	Even	0
Odd	Odd	Integer (l, 2, 3, …)
Even	Odd	Half-integer ($\frac{1}{2}$, $\frac{3}{2}$, $\frac{5}{2}$, …)
Odd	Even	Half-integer ($\frac{1}{2}$, $\frac{3}{2}$, $\frac{5}{2}$, …)

Attachment 4: Plotting A/A$_0$ against time for (a)40T, 31T and (b) 40S with increasing temperature [4]

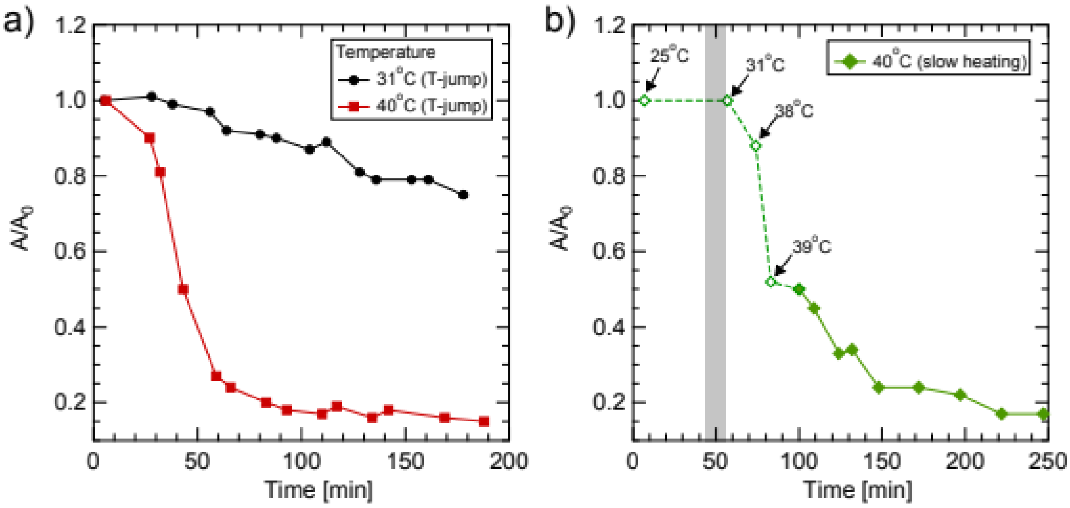

Figure 5: Time dependence of the degree of swelling of the P(NIPAM) hydrogels in water at (a) 31°C and 40°C obtained by the T-jump, (b) 40°C obtained by the slow heating. In (b) empty symbols refer to the data points recorded at the transition temperatures, between 25°C and 40°C. The transition temperatures are indicated with arrows. The gray rectangle represents the change of the temperature of the BCU20 controlling device.

Attachment 5: T_2/T_0 progression with time and increasing temperature for P(NIPAM) at various temperature conditions[4].

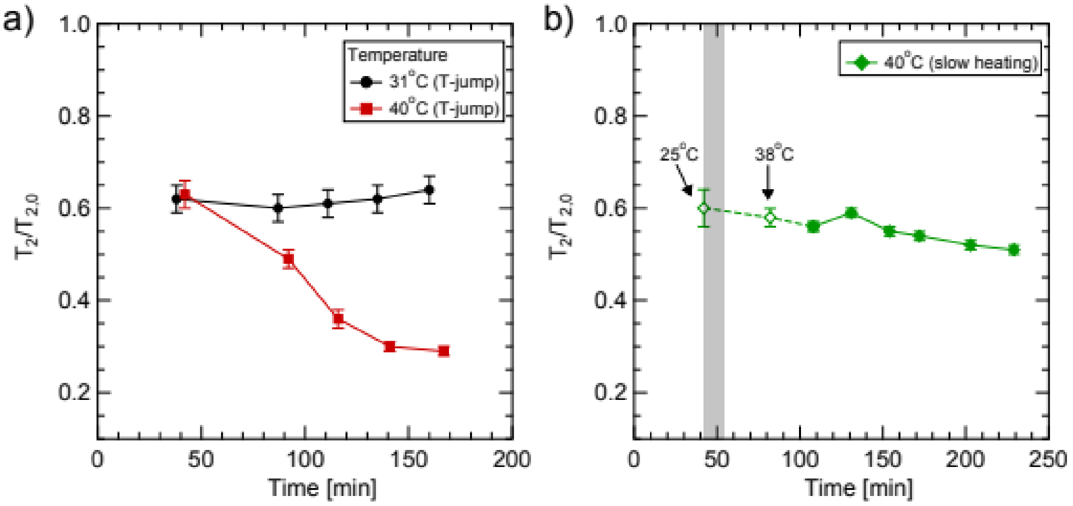

Figure 7: Time dependence of the normalized water T_2 relaxation time values measured in the hydrogel at (a) 31°C and 40°C obtained by the T-jump, (b) 40°C obtained by the slow heating. In (b) empty symbols refer to the data points recorded at the transition temperatures, between 25°C and 40°C. The transition temperatures are indicated with arrows. $T_{2,0}$ refers to bulk water T_2 relaxation time determined for different temperatures (Table 2). The gray rectangle represents the change of the temperature of the BCU20 controlling device.

Attachment 6: Broadening effect of P(NIPAM) from a swollen state [25]

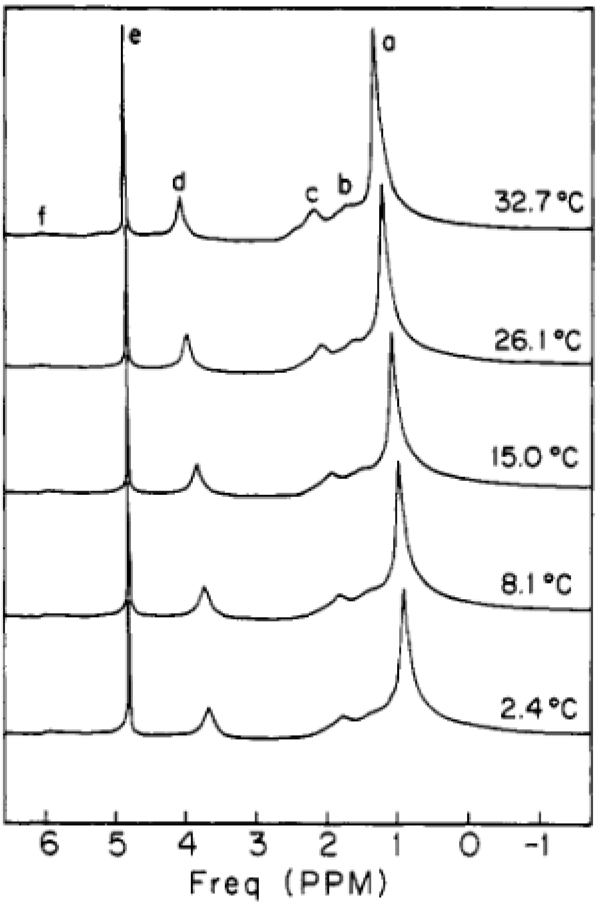

Figure 3. Temperature dependence of proton NMR spectra in the swollen state of a nonionic poly(*N*-isopropylacrylamide) gel.

Attachment 7: Absolute viscosity of ordinary water vs pure deuterium oxide [77]

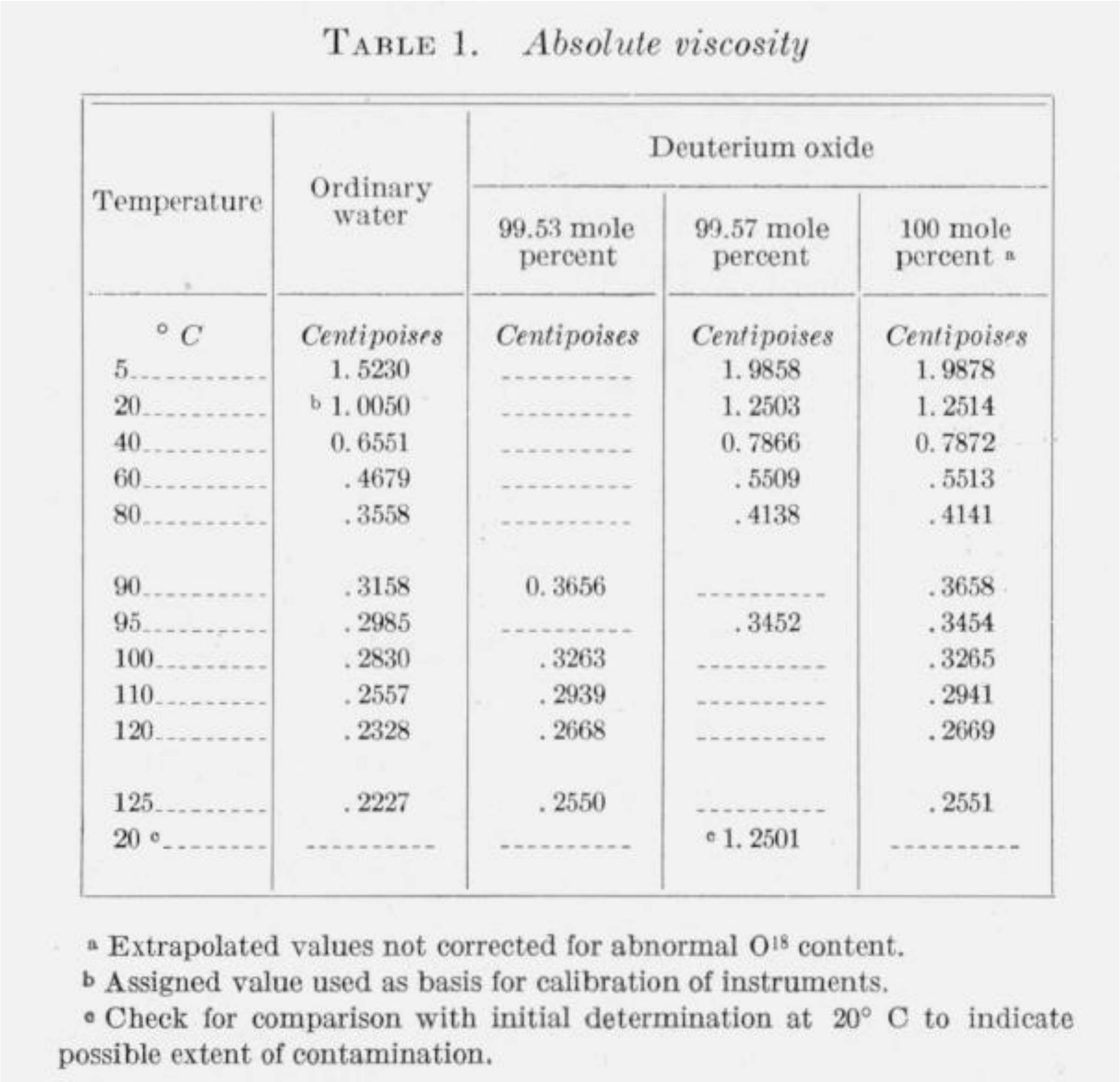

TABLE 1. *Absolute viscosity*

Temperature	Ordinary water	Deuterium oxide		
		99.53 mole percent	99.57 mole percent	100 mole percent [a]
° C	*Centipoises*	*Centipoises*	*Centipoises*	*Centipoises*
5	1.5230	----------	1.9858	1.9878
20	[b] 1.0050	----------	1.2503	1.2514
40	0.6551	----------	0.7866	0.7872
60	.4679	----------	.5509	.5513
80	.3558	----------	.4138	.4141
90	.3158	0.3656	----------	.3658
95	.2985	----------	.3452	.3454
100	.2830	.3263	----------	.3265
110	.2557	.2939	----------	.2941
120	.2328	.2668	----------	.2669
125	.2227	.2550	----------	.2551
20 [c]	----------	----------	[c] 1.2501	----------

[a] Extrapolated values not corrected for abnormal O^{18} content.

[b] Assigned value used as basis for calibration of instruments.

[c] Check for comparison with initial determination at 20° C to indicate possible extent of contamination.

Attachment 8: Computed self-diffusion coefficients, where (b) is βCD and is set up as a function of temperature and P=1atm. The color coding are force fields of water. The self-diffusion coefficients were corrected in the thermodynamic limit using the YH correction term($\boldsymbol{D_{self}^{YH}}$) [26]

$$D_{\mathrm{self}}^{\mathrm{YH}} = \frac{\xi k_B T}{6\pi \eta L}$$

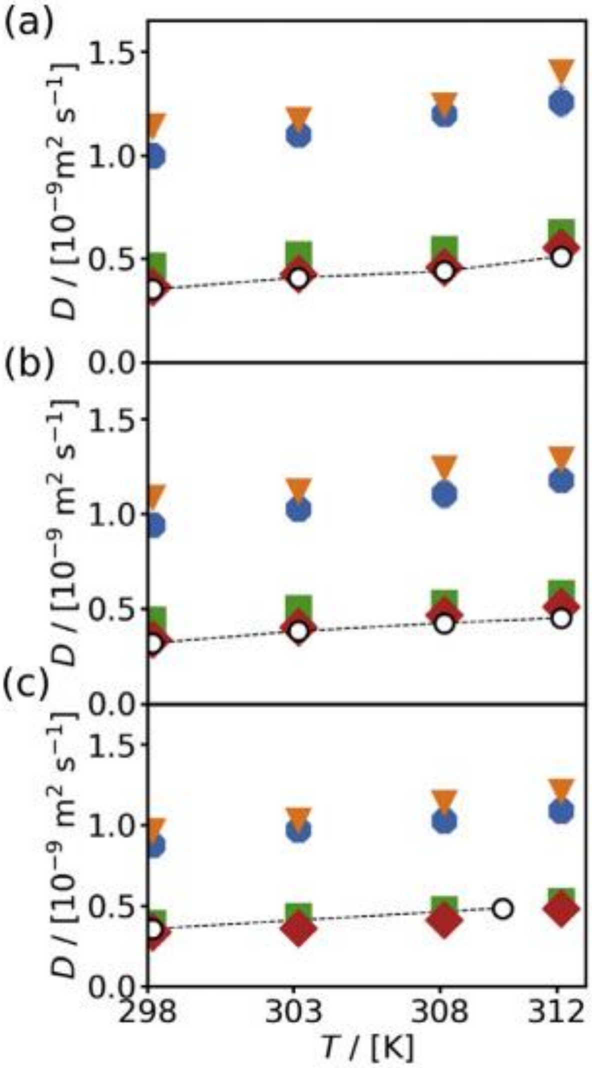

Attachment 9

Average number of hydrogen bonds for αCD, βCD and γCD with water as a function of temperature at P=1 bar. The color symbols represent the force field of water similar to **attachment 8** [26]

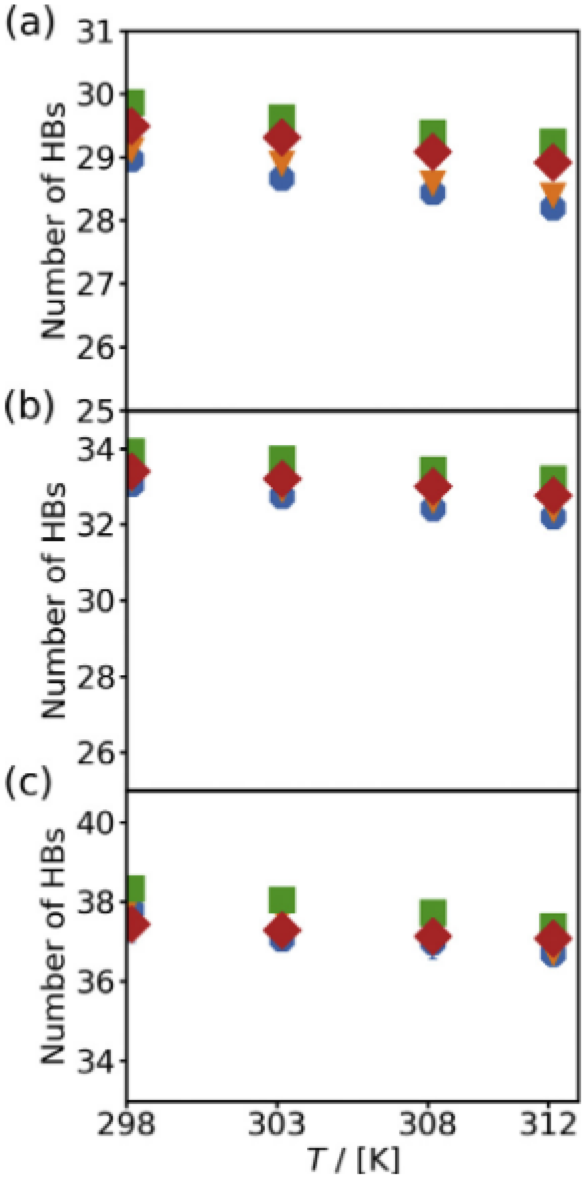

Fig. 4. The average number of hydrogen bonds (HBs) formed between the (a) α-CD, (b) β-CD and (c) γ-CD with water as a function of temperature at $P = 1$ bar. The symbols in blue, orange, green, and red colors indicate the use of TIP3P [56], Bind3P [34], SPC/E [57], and TIP4P/2005 [58] water force fields, respectively. The maximum statistical error in the computed number of HBs is 10%. The error bars are smaller than the symbol size.

Attachment 10: Diffusion data from [30] using He-Ne laser light source’

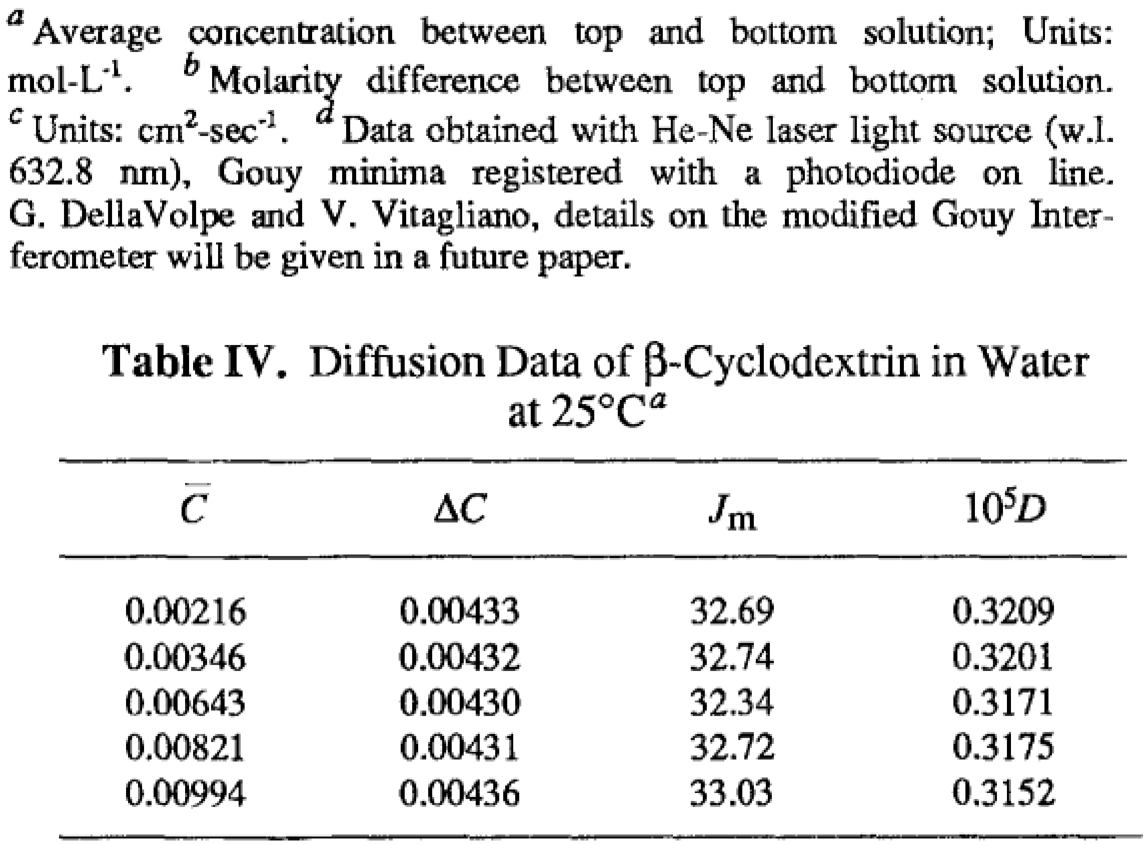

[a] Average concentration between top and bottom solution; Units: mol-L^{-1}. [b] Molarity difference between top and bottom solution. [c] Units: cm^2-sec^{-1}. [d] Data obtained with He-Ne laser light source (w.l. 632.8 nm), Gouy minima registered with a photodiode on line. G. DellaVolpe and V. Vitagliano, details on the modified Gouy Interferometer will be given in a future paper.

Table IV. Diffusion Data of β-Cyclodextrin in Water at 25°C[a]

$\bar{C}$	ΔC	J_m	$10^5 D$
0.00216	0.00433	32.69	0.3209
0.00346	0.00432	32.74	0.3201
0.00643	0.00430	32.34	0.3171
0.00821	0.00431	32.72	0.3175
0.00994	0.00436	33.03	0.3152

Attachment 11: Degree of swelling of P(NIPAM) [33]

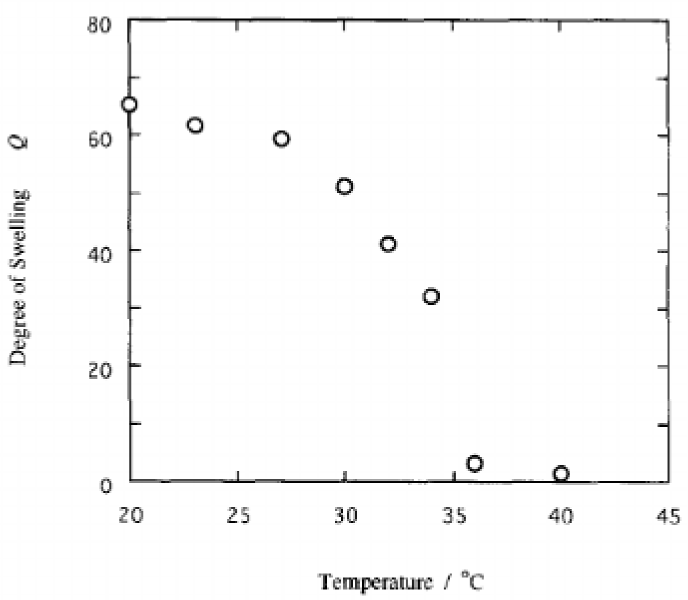

Figure 2 The temperature dependence of the degree of swelling Q under state of equilibrium for a PNIPAM gel

Attachment 11:Diffusion coefficient dependence on P(NIPAM) swelling [33]

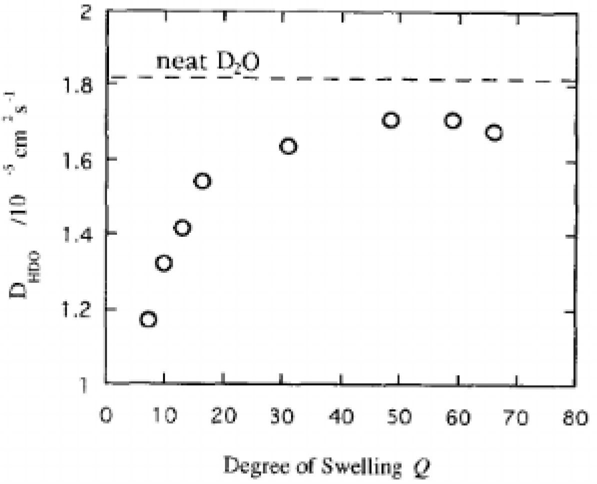

Figure 3 The dependence of diffusion coefficient for HDO, D_{HDO} on the degree of swelling (Q) in a PNIPAM gel. The dashed line indicates the diffusion coefficient of a small amount for HDO contained in neat D_2O

Attachment 12: Diffusion coefficient dependence on temperature for water [33]

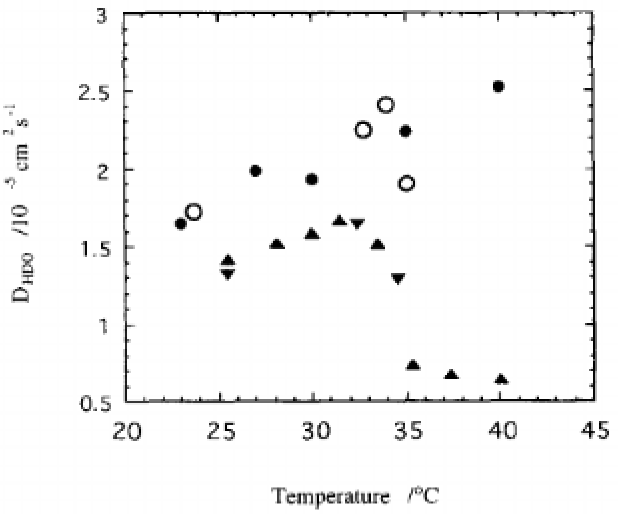

Figure 4 The temperature dependence of the diffusion coefficient for water molecule (D_{HDO}) in PNIPAM gel with equilibrated volumes (○), in NIPAM gel with a constant volume (Q = 4; heating (▲) and cooling (▼)) and in neat D_2O (●)

Attachment 13: D/D_0 against time for (a) 31T, 40T, and (b) 40S [4]

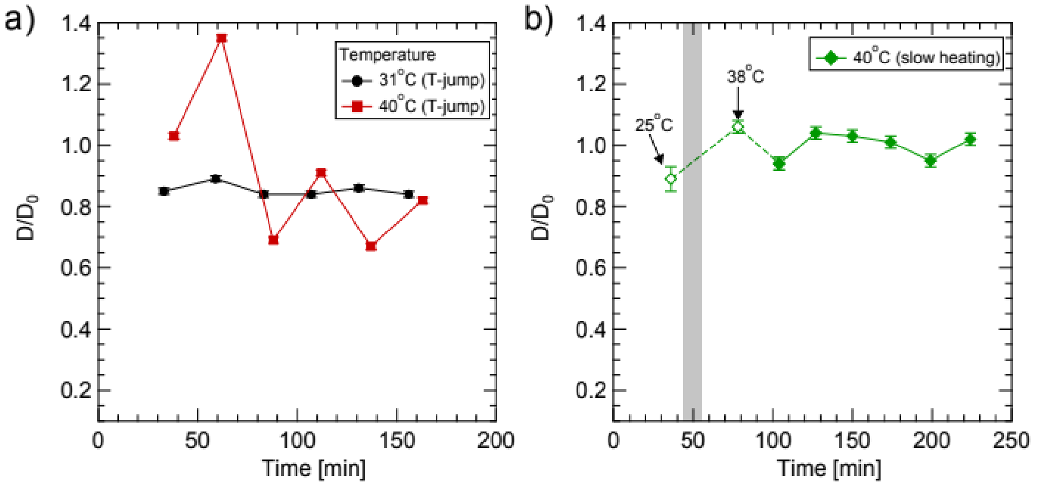

Figure 8: Time dependence of the normalized water self-diffusion coefficients measured in the hydrogel (D/D_0) measured at (a) 31°C and 40°C obtained by the T-jump, (b) 40°C obtained by the slow heating. In (b) empty symbols refer to the data points recorded at the transition temperatures, between 25°C and 40°C. The transition temperatures are indicated with arrows. D_0 refers to bulk water self-diffusion coefficients determined for different temperatures (Table 3). The gray rectangle represents the change of the temperature of the BCU20 controlling device.